Stage-dependent changes of the nuclear architecture, envelope and lamina during mammalian early embryonic development studied with a novel 3D structured illumination microscopy protocol

Dissertation

an der Fakultät für Biologie

der Ludwig-Maximilians-Universität München

vorgelegt von

Jens Popken

aus München

München, den 10. Februar 2015

Erstgutachter: Prof. Dr. med. Thomas Cremer

Zweitgutachter: Prof. Dr. Charles N. David

Tag der mündlichen Prüfung:
15. Januar 2016

Contents

Summary

Super-resolution fluorescence microscopy performed via 3D structured illumination microscopy (3D-SIM) features an 8-fold volumetric resolution improvement over conventional microscopy and is well established on flat, adherent cells. However, blastomeres in mammalian embryos are non-adherent, round and large. Scanning whole mount mammalian embryos with 3D-SIM is prone to failure due to non-adherent embryos moving during scanning and a large distance to the cover glass. The biggest challenge and achievement of this doctorate thesis was the development of a novel method to perform 3D-SIM on mammalian embryos ("3D structured illumination microscopy of mammalian embryos and spermatozoa" published in *BMC Developmental Biology*). The development and fine-tuning of this method took over two years due to the time-intense generation of embryos and the subsequent two day long embryo staining, embedding and scanning with steps that required novel techniques such as micromanipulation which was not associated with sample preparation prior to this protocol. Problem identification was time-intensive since each of the numerous steps necessary could negatively affect the image quality. This method was fine-tuned during three studies. The first study "Reprogramming of fibroblast nuclei in cloned bovine embryos involves major structural remodeling with both striking similarities and differences to nuclear phenotypes of *in vitro* fertilized embryos" (published in *Nucleus*) investigates the profound changes of nuclear architecture during cattle preimplantation development of embryos generated by somatic cell nuclear transfer (SCNT) and *in vitro* fertilization (IVF). Fibroblast nuclei in embryos generated by SCNT go through similar changes in nuclear architecture as embryos generated by IVF. In both embryo types the occurrence of a large, chromatin-free lacuna in the center of nuclei around major embryonic genome

activation (EGA) was noted. Similarly, the chromosome territory-interchromatin compartment (CT-IC) model applied to both types of embryos, featuring a lacuna or not, with an enrichment of RNA polymerase II and H3K4me3, a histone modification for transcriptionally competent chromatin, in less concentrated chromatin and an enrichment of H3K9me3, a transcriptionally restrictive histone modification, in more concentrated chromatin. However, large, highly concentrated H3K4me3 and H3K9me3 clusters were noted in both embryo types at chromatin concentrations that did not fit to the model. The chromatin-free lacunas were highly enriched in newly synthesized mRNA.

The second study “Remodeling of the Nuclear Envelope and Lamina during Bovine Preimplantation Development and Its Functional Implications” (published in *PLOS ONE*) presents the changes of the nuclear envelope and lamina during bovine preimplantation development. Before major EGA, chromatin-free areas of the nuclear periphery were also free of nuclear pore complexes (NPCs), whereas after major EGA, the entire nuclear periphery was equipped with at least a fine layer of chromatin and associated NPCs. Three types of nuclear invaginations were predominant at different stages. The most common invagination was lamin B and NUP153 positive and was most prominent between the 2-cell and 8-cell stages until the onset of major EGA. Lamin B positive, but NUP153 negative invaginations were most prominent during stages with large nuclear volume and surface reductions. The least common invagination was lamin B negative but NUP153 positive and occurred almost exclusively at the morula stage. RNA-Seq and 3D-SIM data showed large deposits of spliced *NUP153* mRNA and cytoplasmic NUP153 protein clusters until shortly after major EGA. NUP153 association with chromatin was initiated at metaphase.

The third study “Stage-dependent remodeling of the nuclear envelope and lamina during rabbit early embryonic development” (published in the *Journal of*

Reproduction and Development) demonstrated that rabbit embryonic nuclei feature a nuclear invagination type containing a large volume of cytoplasm that provides cytoplasmic proximity to nucleoli in addition to the small volume invaginations that were previously observed in bovine nuclei. The underlying mechanism for these two invaginations must differ from each other since small volume invaginations were frequently emanating from large volume invaginations emanating from the nuclear border but large volume invaginations were never emanating from small volume invaginations emanating from the nuclear border. Abundance of import/export competent invaginations featuring NPCs peaked at the 4-cell stage, which is the last stage before a drastic nuclear volume decline and also the last stage before major EGA is initiated at the 8- to 16-cell stage. Import/export incompetent invaginations positive for lamin B but not NUP153 peaked at the 2-cell stage. This was the stage with the largest variability in nuclear volumes. This may hint at an interphase nuclear surface reduction mechanism.

Additionally, previously generated but unpublished 3D-FISH data about the localization changes of a stably inserted reporter gene upon activation in cloned bovine embryos was analyzed and documented in the study “Positional changes of a pluripotency marker gene during structural reorganization of fibroblast nuclei in cloned early bovine embryos” (published in *Nucleus*). This study showed that the stably inserted *OCT-4* reporter gene *“GOF”* in bovine fetal fibroblasts was initially moved towards the nuclear interior in day 2 bovine embryos generated by SCNT of bovine fetal fibroblasts. However, in day 4 SCNT embryos the localization of *GOF* had moved towards the periphery while it was still activated. Its carrier chromosome territory did not significantly move differently compared with the non-carrier homolog. Constant proximity of *GOF* to its carrier chromosome territory ruled out a movement by giant loops.

In cooperation with the Department of Histology and Embryology of the Ege University (Izmir, Turkey) the destructive effects of cryopreservation on blastomere integrity were analyzed in the study “Ultra-Structural Alterations in In Vitro Produced Four-Cell Bovine Embryos Following Controlled Slow Freezing or Vitrification” (published in *Anatomia, Histologia, Embryologia*). The cryopreservation method slow freezing caused more damage to blastomeres and to the zona pellucida than its fast freezing alternative vitrification. This was most likely caused by ice crystal formation and the longer exposure to the toxic side effects of cryoprotectants before freezing was complete.

1. Introduction

1.1. Mammalian early embryonic development

Mammalian reproduction begins with the formation of a new embryo. During conception, the embryo is formed *in vivo*, when a paternal sperm cell fertilizes the maternal oocyte inside the mother animal’s oviducts (Rizos et al., 2002). Using assisted reproductive techniques (ART) extracted oocytes can be *in vitro* fertilized (IVF) with sperm cells (Parrish, 2014). Alternatively, after removal of the oocyte’s genomic content, oocytes can be fused via somatic cell nuclear transfer (SCNT) with somatic cells or embryonic stem cells (Ross and Cibelli, 2010). A newly formed fertilized embryo begins its development at the zygote stage with one cell (blastomere) containing two haploid pronuclei, whereas a newly generated SCNT embryo contains one diploid genome from the donor cell. The zygote cleaves repeatedly forming the 2-cell, 4-cell, 8-cell, 16-cell, morula and blastocyst stage (Figure 1). However, asynchronous divisions at any stages, differences in developmental speed between blastomeres or stopped blastomeres allow for

variations in the number of blastomeres after the zygote stage between embryos fertilized at the same time (Grisart et al., 1994).

The cleavages are not preceded by an equal increase in the cell size resulting in a reduction of blastomere and nuclear volumes from stage to stage until the blastocyst stage. The total size of the embryo is approximately maintained from the zygote stage until the early blastocyst stage. This size can vary greatly between species. For instance, the initial diameter of a mouse embryo is maintained until the early blastocyst stage at about 80-85 µm (Han et al., 2005; Zernicka-Goetz et al., 1997), whereas rabbit embryos can have an average diameter of about 125-130 µm (Meshreky et al., 2012) and bovine embryos can have a diameter of about 120-160 µm (Bó and Mapletoft, 2013).

Oocytes and early embryos are surrounded by the glycoprotein layer zona pellucida with a thickness of about 15 µm (Murayama et al., 2006). At the blastocyst stage the embryo's volume starts to fluctuate in order to break the zona pellucida and to ultimately escape from its confinements in a process called "hatching". This is facilitated by fluid intake into the cell-free areas inside the blastocyst called the blastocoel and can increase the volume of a blastocyst two- to threefold (Sathananthan et al., 2003). *In vivo* developing embryos leave the protective layer of the zona pellucida when entering the uterus. At the morula stage a differentiation between two cell types begins that culminates into the formation of the trophectoderm (TE) and the inner cell mass (ICM) at the blastocyst stage (Abe et al., 1999). The TE is the precursor of the placenta while the ICM continues its development into the growing animal. The stages up to blastocyst stage are called preimplantation development since a hatched blastocyst can implant into the endometrium of the uterus.

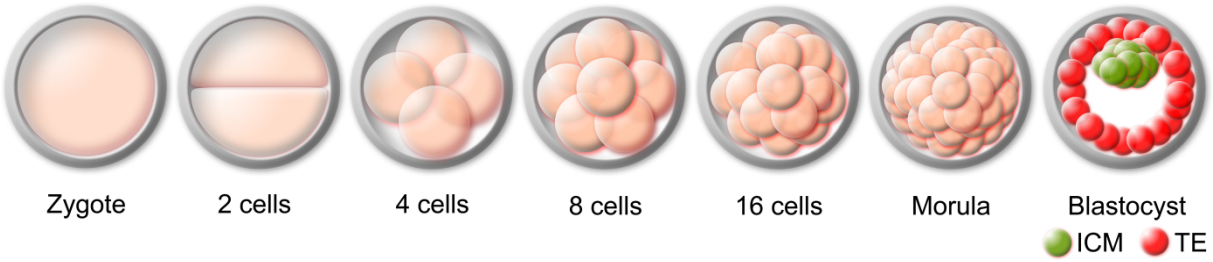

Figure 1. Stages of mammalian preimplantation embryonic development. Until the hatching of the blastocyst occurs, all blastomeres (light brown) are surrounded by the protective layer zona pellucida (grey). The blastocyst consists of the inner cell mass (ICM) further developing into the newly forming organism and the trophectoderm (TE) developing further into the placenta.

1.2. Activation of the embryonic genome

During oogenesis, the mother animal provides the developing oocyte with a large deposit of proteins and spliced mRNA to support initial embryonic development while the embryonic genome remains mostly inactive (Graf et al., 2014). Embryonic genome activation (EGA) occurs at species-specific stages and is required to replace the dependency on maternally provided proteins and mRNAs with a novel production based on the genome of the embryo (Tadros and Lipshitz, 2009). Normal development is only possible with a successful maternal-to-embryo transition (MET) (Li et al., 2013). The activation of the genome is achieved in two steps (Figure 2). In bovine embryos, a minor EGA is already detected at the end of the zygote stage (Pacheco-Trigon et al., 2002) or at the latest in 2-cell embryos, but restricted to the up-regulation of a few hundred genes when utilizing a two-fold threshold between subsequent stages (Kues et al., 2008). In contrast, RNA-Seq analyses revealed that major EGA affects the majority of genes activated during preimplantation development (Graf et al., 2014). Several reports described the 8- to 16-cell stage of bovine preimplantation embryos as the critical window for major EGA (Badr et al.,

2007; Camous et al., 1986; Memili and First, 2000; Misirlioglu et al., 2006; Vigneault et al., 2009). Deep RNA sequencing identified major EGA at the 8-cell stage (Graf et al., 2014). In the rabbit species, minor EGA occurs at the end of the zygote stage (Christians et al., 1994; Pacheco-Trigon et al., 2002). Genomic activation is occurring progressively with major EGA taking place at the 8- to 16-cell stage (Brunet-Simon et al., 2001; Leandri et al., 2009). In the mouse, minor EGA occurs at the end of the zygote stage (Pacheco-Trigon et al., 2002), whereas major EGA occurs at the 2-cell stage (Tadros and Lipshitz, 2009).

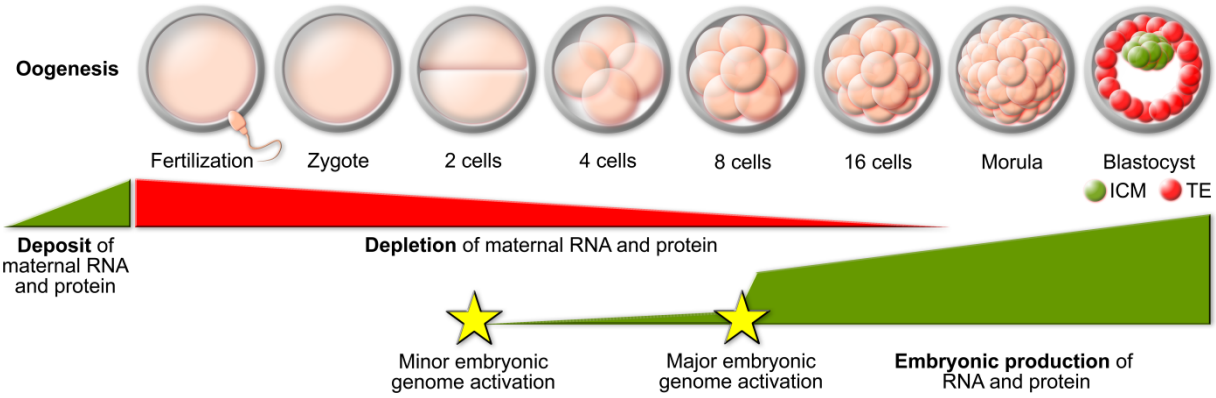

Figure 2. Activation of the bovine embryonic genome. Maternal RNA and protein deposited into the developing egg during oogenesis get gradually depleted during early embryonic development. Minor/major EGA initiate embryonic production of mRNA and protein. Green shapes symbolize the increase of mRNA and protein while the red shape symbolizes the reduction of mRNA and protein levels. Stars identify minor and major genome activation.

1.3. Gene activation and silencing

The activation or silencing of genes is achieved without changing the genetic code of the DNA itself. Instead, the transcription of genes into mRNA can be inhibited at the epigenetic level by multiple ways including small interfering RNAs (McManus and

Sharp, 2002), DNA methylation (Jaenisch and Bird, 2003) and histone modifications (Bannister and Kouzarides, 2011). 147 base pairs of DNA are wrapped approximately two times around nucleosomes (Campos and Reinberg, 2009). Nucleosomes are octamer protein complexes made up of 2 copies each of the histones H2A, H2B, H3 and H4 (Ramakrishnan, 1997). Specific peptides in the N-terminal peptide strings of these histones can have modifications such as acetylation, methylation, phosphorylation, ubiquitylation and sumoylation among others (Kouzarides, 2007). The methylation or acetylation of specific lysines on these peptide strings can act as markers for silenced or activated genomic areas (Bannister and Kouzarides, 2011). The acetylation of histones can be established by histone acetyltransferases (Roth et al., 2001) and removed by histone deacetylases (De Ruijter et al., 2003), whereas the methylation of histones can be facilitated by DNA methyltransferases (Pradhan and Esteve, 2003) and demethylation can be facilitated passively by preventing the establishment of novel methylation after DNA replication (Ooi and Bestor, 2008).

Transcription of the genetic code into RNA is performed by RNA polymerase II (Hahn, 2004). Histone 3 lysine 4 trimethylated (H3K4me3) is associated with transcriptionally competent chromatin (Bernstein et al., 2002), whereas histone 3 lysine 9 trimethylated (H3K9me3) is associated with transcriptionally repressive chromatin (Nakayama et al., 2001) (Figure 3). Histone acetylation in transcriptionally competent chromatin is associated with resulting in less condensed chromatin (Ridsdale et al., 1990). Antibodies against histone modifications can identify areas of the genome that are currently marked as transcriptionally active or silenced (Hebbes et al., 1988). Histone markers in transcriptionally competent or restrictive chromatin can regulate the RNA polymerase II activity (Stasevich et al., 2014). RNA polymerase II has a carboxyl-terminal domain made up of repeats of the peptide sequence

tyrosine-serine-proline-threonine-serine-proline-serine (Baskaran et al., 1993; Palancade and Bensaude, 2003). Phosphorylation of the serine at position 2 of the sequence is associated with elongation of the transcribed mRNA string while phosphorylation of the serine at position 5 of the sequence is associated with transcription initiation (Ahn et al., 2004).

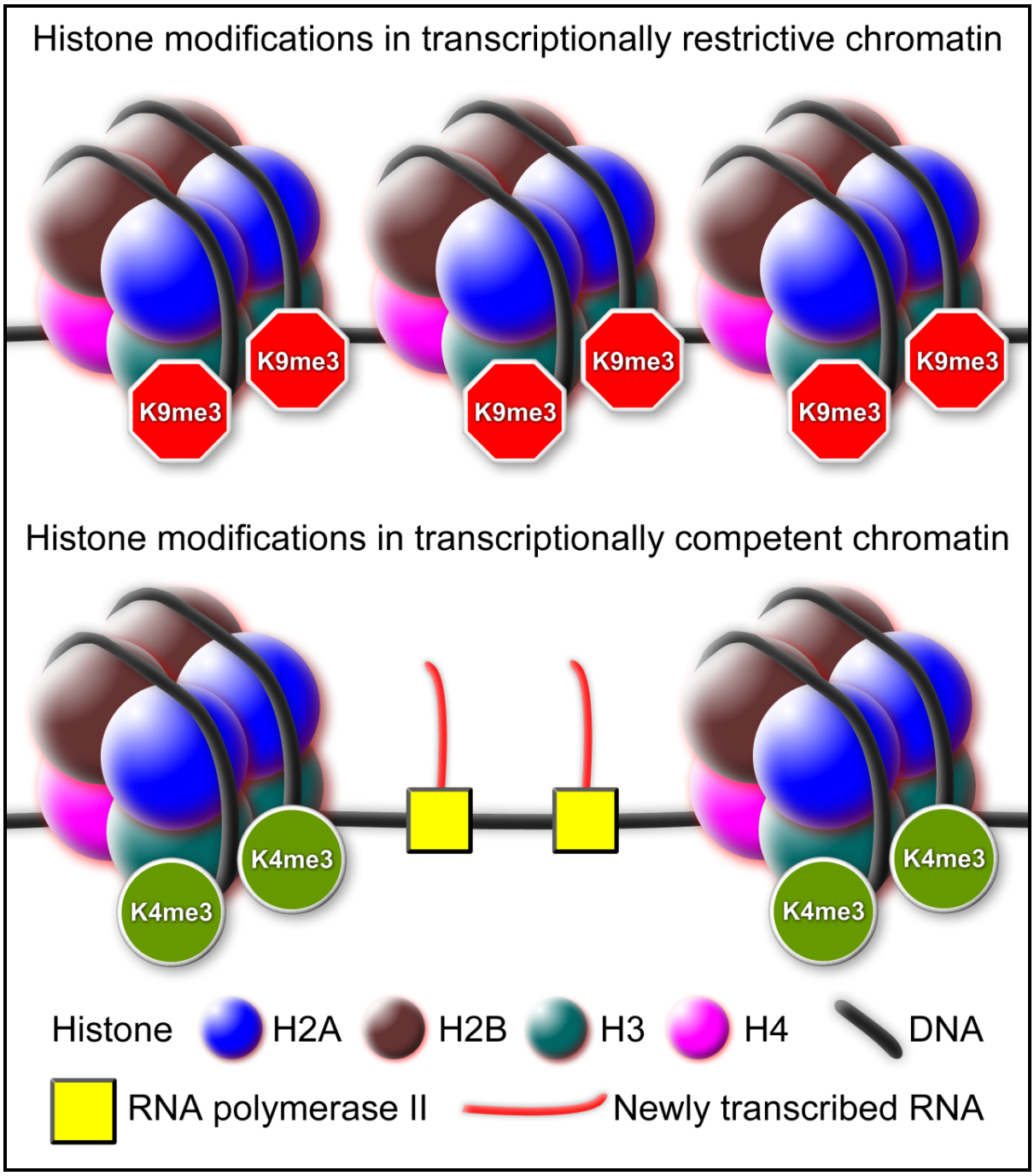

Figure 3. Chromatin concentration differences between transcriptionally

competent and restrictive chromatin. Transcriptionally competent chromatin marked by H3K4me3 is usually less condensed than transcriptionally restricted chromatin marked by H3K9me3. RNA polymerase II transcribes DNA into RNA preferably in transcriptionally competent, less condensed chromatin. This Figure is adapted from Figure 1 in (Croken et al., 2012). Spheres symbolize histones. Squares symbolize RNA polymerase II. Black lines symbolize DNA. Red lines symbolize RNA.

1.4. Chromosome territory-interchromatin compartment model

A territorial organization of chromosomes is a general feature of nuclear architecture (Figure 4). Chromosome territories (CTs) are built from a 3D network of chromatin domain clusters (CDCs). The CDC periphery carries loosely compacted chromatin, called the perichromatin region (PR), and is enriched in H3K4me3, a marker for transcriptionally competent chromatin, while the more densely compacted CDC interior predominantly carries markers for transcriptionally silent chromatin, such as H3K9me3 and H3K27me3 (Popken et al., 2014a; Smeets et al., 2014). The PR is the preferential, although not necessarily exclusive nuclear compartment, where transcription, co-transcriptional splicing, DNA-replication and DNA-repair occur (Rouquette et al., 2010). Interchromatin compartment channels (IC-channels) pervade the nuclear interior between CTs and the CT interior between CDCs (Markaki et al., 2010; Markaki et al., 2012; Schermelleh et al., 2008; Smeets et al., 2014). Channels frequently expand into larger IC-lacunas, carrying splicing speckles and other nuclear bodies. The IC should be considered as a highly organized nuclear subcompartment by itself. We have hypothesized that the IC system, in addition of being a nuclear subcompartment for the formation of nuclear bodies and macromolecular complexes necessary for transcription, splicing, replication and repair within the lining PR, allows for constrained movements of ribonucleoprotein

complexes with mRNA towards the nuclear pores (Mor et al., 2010) and possibly also for constrained movements of imported proteins. Based on the expectation of continuous, highly dynamic interaction between the PR and the IC, we have argued that they together form a functionally closely integrated system, termed the active nuclear compartment (aNC), whereas the interior of CDCs represents the transcriptionally inactive nuclear compartment (iNC) (Popken et al., 2014a; Smeets et al., 2014).

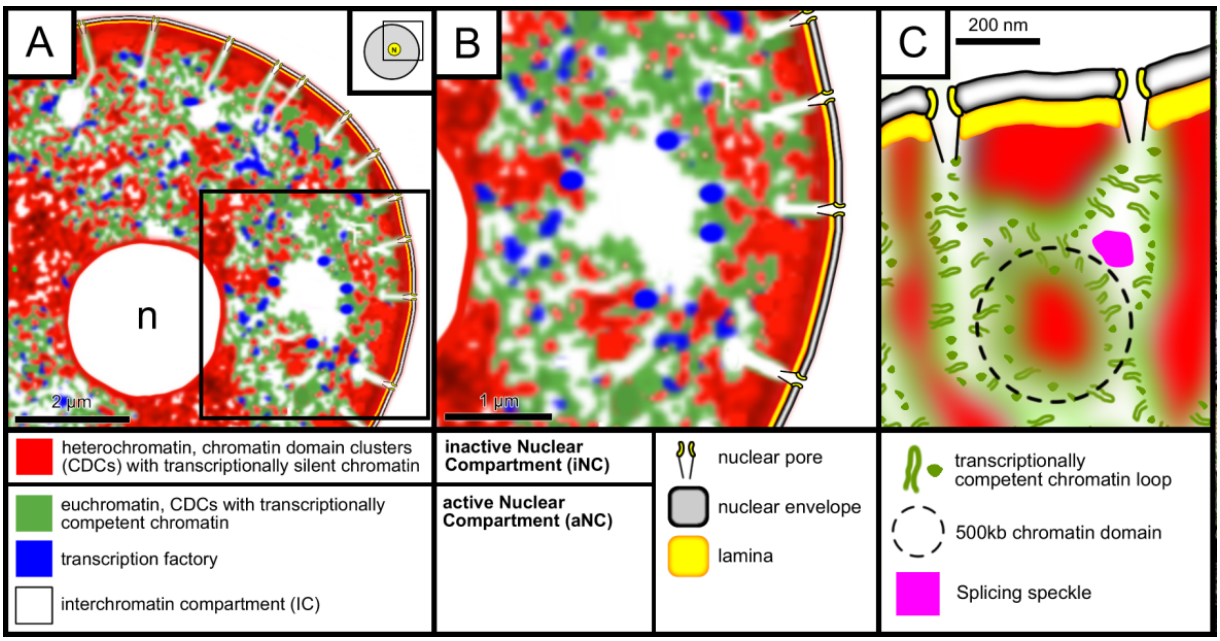

Figure 4. Chromosome territory-interchromatin compartment (CT-IC) model from (Popken et al., 2014a). A and B. Model of the eu- and heterochromatin distribution in a morula stage blastomere. B shows an enlargement of the boxed area in A. CTs are built up from chromatin domain clusters (CDCs). CDCs carry transcriptionally silent chromatin (red) in their interior. The less dense, transcriptionally competent chromatin (green) at the periphery of CDCs presents the perichromatin region (PR). It is enriched with transcription factories (blue) and represents the nuclear sub-compartment, where genes are transcribed. The PR lines the interchromatin compartment (IC), which starts with channels at nuclear pores and

forms a three-dimensional network throughout the nuclear interior. It extends between neighboring CTs but also throughout CTs. Considering the potential role of the IC in import-export functions, as well as functional interactions between nuclear bodies and machineries for transcription, co-transcriptional splicing, chromatin replication and repair acting within the PR, we propose that the PR and the IC provide the active nuclear compartment (aNC), whereas the compact interior of CDCs forms the inactive nuclear compartment (iNC). The nucleolus in A is marked with ‘n ’. **C.** This model presents a hypothetical topography at still higher resolution envisaged for a landscape at the nuclear periphery with nuclear pores connected to IC channels. Little chromatin loops invade these channels, their size and hypothetical arrangements minimize problems of chromatin entanglements in the perichromatin region and interchromatin compartment. At numerous sites the IC forms larger lacunas, which contain nuclear bodies, such as splicing speckles. A dotted circle comprises a chromatin domain with a DNA content of about 500 kbp. Chromatin domains attached to the nuclear lamina (yellow) are connected with domains extended into the nuclear interior.

1.5. Structural nuclear reorganization during pluripotency gene activation

Reprogramming of a differentiated cell nucleus in cloned embryos (Wilmut et al., 1997) is associated with major changes in its gene expression profile, including the activation of pluripotency genes (Shi et al., 2003). This pluripotency gene activation (PGA) apparently occurs together with major EGA (Wuensch et al., 2007), although causal relationships between PGA and major EGA are still not clear. While nuclei from terminally differentiated cells can support full term development of cloned animals, we still lack detailed information about the changes of nuclear architecture, which may be involved in the reprogramming of a somatic cell nucleus.

To study the time course of PGA in cloned early bovine embryos a reporter system was established (Wuensch et al., 2007), which makes it possible to follow *Oct4/Pou5f1* promoter activation in these embryos. This model system employs bovine fetal fibroblasts (BFF) carrying an *Oct4/Pou5f1*-EGFP reporter gene (*GOF*; Figure 5) (Niwa et al., 2000) on one of the two chromosomes 13. Expression of EGFP is controlled by a 9-kb fragment of the mouse *Pou5f1*/*Oct4* regulatory sequence with a deletion in the proximal enhancer (PE) (Yoshimizu et al., 1999). Downstream EGFP is flanked by a 9-kb fragment of the structural *Pou5f1* gene containing 5 exons. The reporter construct is silent in BFF nuclei, but is activated in nuclei of cloned embryos during major EGA at the fourth embryonic cell cycle (Wuensch et al., 2007). The localization of this reporter gene can be visualized via 3D-FISH. This method provides the possibility to study the correlation between *Oct4/Pou5f1* promoter activation and changes in the localization of the reporter gene, its carrier CT and, as a negative control, the homolog non-carrier CT in cloned bovine embryos.

Figure 5. The *Oct4/Pou5f1*-EGFP reporter gene (GOF) integrated into one of the two CTs 13 adapted from (Wuensch et al., 2007). Expression of EGFP is controlled by a 9-kb fragment of the mouse *Pou5f1*/*Oct4* regulatory sequence with a deletion in the proximal enhancer (PE) (Yoshimizu et al., 1999). Downstream EGFP is flanked by a 9-kb fragment of the structural *Pou5f1* gene containing 5 exons. This reporter gene was stably integrated into one of the two CTs 13 in bovine fibroblasts.

These fibroblasts were then used during somatic cell nuclear transfer to generate embryos carrying GOF.

1.6. Nuclear envelope, lamina and nuclear pore complexes (NPCs)

The nucleus containing the nucleoplasm is separated from its surrounding cytoplasm by the nuclear envelope on the outside and the nuclear lamina directly beneath it (Figure 6). The nuclear envelope consists of an outer and an inner lipid membrane (Watson, 1955) and contains at least 148 different proteins (Dreger et al., 2001). The nuclear lamina is made up of lamins B1 and B2 in developing cells and by lamins A and C in differentiated cells (Gruenbaum et al., 2005). Import/export of proteins and mRNA packaged as ribonucleoprotein (mRNP) complexes is facilitated through nuclear pore complexes (NPCs) (Carmody and Wente, 2009).

NPCs are constructed of eight similar nucleoporin aggregates in circular formation. 30 nucleoporins (NUPs) make up each of these eight clusters (Cronshaw et al., 2002). These eight clusters surround a tunnel with a diameter of ~50 nm (Doucet and Hetzer, 2010) connecting the cytoplasmic side at the outer to the nucleoplasmic side at the inner membrane of the nuclear envelope (Hinshaw et al., 1992). The area of the cytoplasmic side of this tunnel is called cytoplasmic ring and the nucleoplasmic area is called nuclear ring. Cytoplasmic filaments reaching into the cytoplasm are connected to the cytoplasmic ring. On the nucleoplasmic side, eight fibers connect the nuclear ring with another ring which is located further inside the nucleus called terminal ring. These eight fibers and the terminal ring form the nuclear basket (Arlucea et al., 1998). The 153kD nucleoporin NUP153 (Sukegawa and Blobel, 1993) has multiple localization options. It can localize at the nuclear ring or at the nuclear basket (Ball and Ullman, 2005).

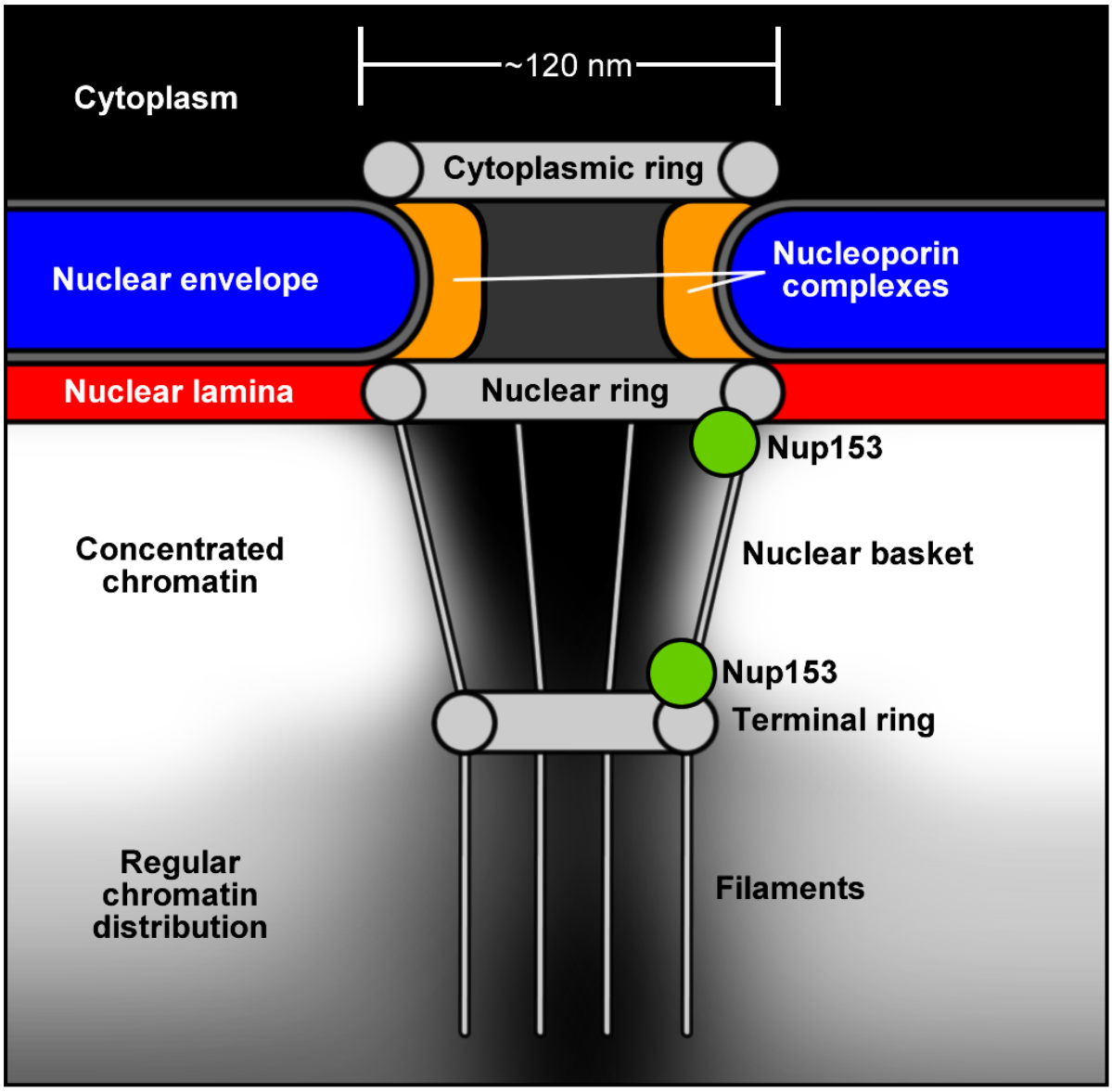

Figure 6. Nuclear pore complex at the nuclear border. The NPC creates a tunnel through the nuclear envelope and the nuclear lamina below the nuclear envelope. This tunnel serves as a connection for import/export between the cytoplasm above the nuclear pore and the nucleoplasm with the interchromatin compartment channel below. Chromatin is associated with the nuclear basket and the nuclear filaments attached to the nuclear basket. NUP153 (green circles) is localized at the NPC at the nuclear or the terminal ring. Cytoplasmic filaments are not depicted in this Figure in order to maintain simplicity and focus. This Figure is adapted from Figure 3 in (Strambio-De-Castillia et al., 2010).

1.7. Connection between nuclear pores and chromatin

Chromatin association with the nuclear basket and its attached intranuclear filaments has been shown in electron microscopic studies (Arlucea et al., 1998). NPCs are connected with the nuclear interior via the system of interconnected interchromatin compartment channels (Markaki et al., 2010; Markaki et al., 2012; Schermelleh et al., 2008; Smeets et al., 2014). The presence of NPCs at sites, where chromatin contacts the nuclear lamina provides opportunities for connections with interchromatin compartment channels, which start and end, respectively, at nuclear pores (Markaki et al., 2010; Rouquette et al., 2009; Schermelleh et al., 2008). The IC channel system connects nuclear pores with the nuclear interior, where IC channels expand both between and within CTs. This system may play a role both for a guided import of proteins entering the nucleus at NPCs into the nuclear interior and a guided mRNA export towards NPCs in the form of messenger ribonucleoprotein particles (mRNPs).

1.8. New nuclear pore assembly, disassembly and reassembly

New NPCs are assembled during G1- and S-phase in order to double the number of NPCs before the onset of the next mitosis by acquisition of structural components from both sides of the NE (Maul et al., 1972). The sites of nuclear pore assembly do not depend on components previously integrated into the NE (D'Angelo et al., 2006). NPCs require the lamina for their integration into the nuclear envelope (Smythe et al., 2000).

Disassembly of nuclear pore complexes (NPCs) starts at prophase (Lenart et al., 2003) and is initiated with the release of NUP98, followed by a first wave of partial NUP153 release, followed by the release of NUP50, followed by an approximately parallel release of NUP96, the release of the rest of NUP153 and the release of the nuclear basket protein Tpr, followed by the release of NUP107 and finally the release

of the transmembrane nucleoporin POM121 (Beaudouin et al., 2002; Dultz et al., 2008; Hase and Cordes, 2003).

Reassembly of nuclear pores is initiated during anaphase with the association of nucleoporin complexes with chromatin. During mitosis the NUP107/160 complex, NUP153 and NUP50 associate with chromosomes before the NE is re-established (Dultz et al., 2008; Franz et al., 2007; Kutay and Hetzer, 2008). Reassembly of NPCs begins with the incorporation of the NUP107/160 complex, POM121 and NDC1 (Antonin et al., 2005; Dultz et al., 2008; Kutay and Hetzer, 2008; Mansfeld et al., 2006), followed by the subcomplexes NUP93 and NUP62 (containing NUP53, NUP155 and others) (Dultz et al., 2008) and finally followed by the incorporation of NUP214, NUP153, nuclear basket protein Tpr, NUP50 and the membrane nucleoporin gp210 (Dultz et al., 2008; Kutay and Hetzer, 2008).

1.9. Nuclear invaginations

Invaginations of the nuclear envelope and the nuclear lamina featuring NPCs can extend the protein import and mRNP export functionality of NPCs to regions remote from the nuclear surface (Legartova et al., 2014; Malhas et al., 2011). Such a role may be especially important for large nuclei of early bovine preimplantation development, but has also been amply demonstrated for nuclear envelope invaginations in numerous normal and malignant somatic cell types (Garcia Verdugo et al., 1983; Storch et al., 2007; Sunba et al., 1980). During early embryonic development the volume and the surface of nuclei decline. Therefore, less invaginations or shorter invaginations are expected at the end of the embryonic development. Additionally, during spermiogenesis, vesicle-like excisions of the lamina into the nuclear interior have been associated with a reduction of the nuclear surface in interphase (Ndiaye and Mattei, 1993).

1.10. 3D structured illumination microscopy (3D-SIM) on embryos

3D-SIM improves the lateral optical resolution up to a factor of 2 (Cremer, 2012) and the volumetric resolution about eightfold compared with conventional microscopy (Schermelleh et al., 2010). This improvement requires multiple alterations to standard wide-field microscopy. Laser exposure of a grid in the optical illumination path produces a stripe-pattern in the object plane. The recorded images from samples illuminated with this stripe-pattern contain interference signals that can be used to calculate an image with a higher resolution than the resolution of the recorded image. The grid that generates this stripe-pattern is moved 5 times per angle with 3 angles per section to get interference data from all areas of the specimen from all sides of any signal giving location. This concept was introduced by Mats Gustafsson (Gustafsson, 1999, 2000) and Rainer Heintzmann and Christoph Cremer (Heintzmann and Cremer, 1999). The software calculating the final images is configured using point spread functions derived from signals produced by fluorescent beads solidly attached to a cover glass. Therefore, the software with such a configuration will provide optimal results with flat cell types attached to the cover glass whose nuclei resemble the situation of fluorescent beads directly attached to the cover glass as best as possible. However, blastomeres and their nuclei (Figure 7) are not flat and zygote stage blastomeres can have a diameter from about 80 µm (mouse) to about 140 µm (bovine) with nuclei mostly being located in the center of the blastomere (Iqbal et al., 2009). Furthermore, blastomeres are non-adherent and the standard staining protocol contains the use of bovine serum albumin which prevents surface attachments. Additionally, the phenomenon of artificial signal increases in cone-like shapes emanating from the sample is more pronounced in

large, round nuclei. 3D-SIM requires strong signals to reduce bleaching during the 15 scans per section. Strong bleaching reduces the final image quality significantly.

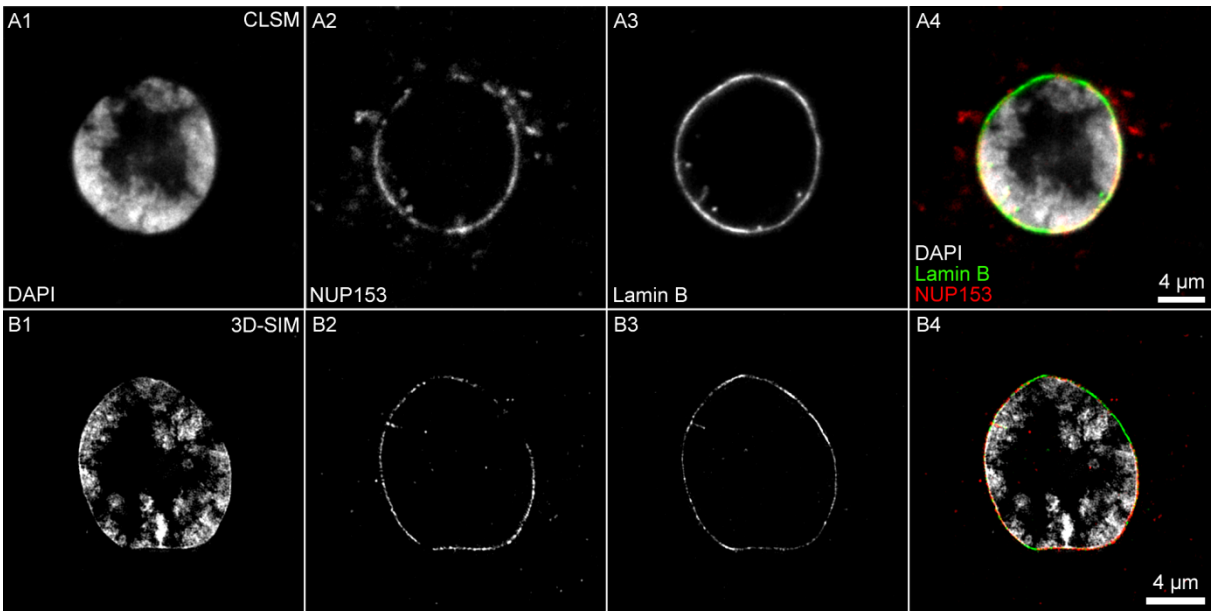

Figure 7. Resolution comparison of confocal laser scanning microscopy (CLSM; A) and 3D structured illumination microscopy (3D-SIM; B). Both nuclei were scanned in bovine 8-cell stage blastomers. **A1 and B1.** Chromatin stained with DAPI. **A2 and B2.** Nucleoporin NUP153 staining. **A3 and B3.** Lamin B staining. **A4 and B4.** Composite of DAPI (grey), lamin B (green) and NUP153 (red).

1.11. Cryopreservation of oocytes, spermatozoa or embryos

During cryopreservation oocytes, spermatozoa or embryos are frozen in liquid nitrogen to preserve their developmental potential for use at a later time-point. The two most common forms of cryopreservation are slow freezing and vitrification (Zander-Fox et al., 2013). Slow freezing was developed before vitrification (Saragusty and Arav, 2011). During slow freezing gametes and embryos are gradually cooled down in a programmable freezer and ultimately transferred to liquid nitrogen (Sommerfeld and Niemann, 1999). However, the gradual freezing can result in the formation of destructive ice crystals (Arav et al., 2002). The subsequently developed

vitrification procedure aims at reducing the ice crystal occurrence by chemically blocking ice formation and instant liquid nitrogen exposure (Wowk et al., 2000). On the economical side, vitrification renders expensive programmable freezers obsolete. Vitrification kits can be used in any lab featuring a gamete/embryo incubator and liquid nitrogen.

1.12. Aims of the studies combined in this doctorate thesis

This doctorate thesis combines multiple studies. In “3D structured illumination microscopy of mammalian embryos and spermatozoa” the aim was to develop a robust protocol to perform 3D structured illumination microscopy on blastomeres of mammalian preimplantation embryos, which was previously only established on adherent cells. The successful development of this protocol provided a super-resolution microscopy solution for three subsequent studies of mammalian early embryonic nuclear architecture and of the nuclear envelope and lamina. An initial study on bovine 8-cell embryos showed nuclei with a chromatin distribution exclusively limited to the nuclear periphery and a large chromatin-free lacuna in the center. Large H3K4me3 or H3K9me3 positive clusters were observed in this peripherally concentrated chromatin at the 8-cell stage. In “Reprogramming of fibroblast nuclei in cloned bovine embryos involves major structural remodeling with both striking similarities and differences to nuclear phenotypes of *in vitro* fertilized embryos“ the first aim was to investigate if this central lacuna was a regular occurrence both in *in vitro* fertilized and cloned embryos. The second aim was to check whether the CT-IC model applied to nuclei with and without a central lacuna. The third aim was to investigate if this lacuna may be filled with splicing factors and newly produced mRNA at major embryonic genome activation. The fourth aim was to

investigate whether the CT-IC model was applying to these large, concentrated H3K4me3 or H3K9me3 positive clusters as well.

During this investigation, a high abundance of small, chromatin-free regions were discovered at the nuclear periphery beneath the lamina. This prompted the initiation of the second investigation on the bovine embryonic nuclear envelope and lamina. In “Remodeling of the Nuclear Envelope and Lamina during Bovine Preimplantation Development and Its Functional Implications” the first aim was to identify the nature of these chromatin-free regions. Once these regions were confirmed to be nuclear invaginations the aim was to check whether alterations in the abundance of these invaginations occurred throughout embryonic development. In “Stage-dependent remodeling of the nuclear envelope and lamina during rabbit early embryonic development” the aim was to compare the results of the prior study with the scenario in rabbit, since rabbit nuclei have a profoundly different nuclear phenotype from bovine embryonic nuclei. While bovine embryonic nuclei usually feature a spherical shape with barely recognizable invaginations containing only a small volume of cytoplasm limited to the nuclear periphery, rabbit nuclei can feature a high abundance of invaginations containing a large volume of cytoplasm capable of crossing the entire nucleus.

In “Positional changes of a pluripotency marker gene during structural reorganization of fibroblast nuclei in cloned early bovine embryos” the aim was to investigate, whether a stably inserted pluripotency gene would alter its or its carrier CT’s location upon and during activation. Furthermore, the aim was to investigate whether a potential movement would be facilitated by a giant chromatin loop to locations remote from its carrier CT. In “Ultra-Structural Alterations in In Vitro Produced Four-Cell Bovine Embryos Following Controlled Slow Freezing or Vitrification” the aim was to compare the effects of the cryopreservation methods

slow freezing and vitrification on 4-cell bovine embryos. This comparison included quantifications of developmental rates as well as the effects on the blastomeres and the zona pellucida investigated with transmission electron microscopy.

2. Results

2.1. 3D structured illumination microscopy of mammalian embryos and spermatozoa

Popken et al. BMC Developmental Biology (2015) 15:46
DOI 10.1186/s12861-015-0092-7

BMC Developmental Biology

METHODOLOGY ARTICLE Open Access

3D structured illumination microscopy of mammalian embryos and spermatozoa

Jens Popken[1,2], Maik Dahlhoff[2], Tuna Guengoer[2], Eckhard Wolf[2] and Valeri Zakhartchenko[2,3*]

Abstract

Background: Super-resolution fluorescence microscopy performed via 3D structured illumination microscopy (3D-SIM) is well established on flat, adherent cells. However, blastomeres of mammalian embryos are non-adherent, round and large. Scanning whole mount mammalian embryos with 3D-SIM is prone to failure due to the movement during scanning and the large distance to the cover glass.

Results: Here we present a highly detailed protocol that allows performing 3D-SIM on blastomeres of mammalian embryos with an image quality comparable to scans in adherent cells. This protocol was successfully tested on mouse, rabbit and cattle embryos and on rabbit spermatozoa.

Conclusions: Our protocol provides detailed instructions on embryo staining, blastomere isolation, blastomere attachment, embedding, correct oil predictions, scanning conditions, and oil correction choices after the first scan. Finally, the most common problems are documented and solutions are suggested. To our knowledge, this protocol presents for the first time a highly detailed and practical way to perform 3D-SIM on mammalian embryos and spermatozoa.

Keywords: Super-resolution fluorescence microscopy, Mammalian embryos

Background

With an axial resolution of about 100 nm and a lateral resolution of about 300 nm 3D structured illumination microscopy (3D-SIM) features an 8-fold volumetric resolution improvement over confocal microscopy [1, 2]. This improvement is achieved by redirecting the laser beams through a mobile grid and scanning each section 15 times with a slightly altered grid location and orientation (3 angles with 5 phases each). The signals produced at the borders of this mobile grid allow a software to compute super-resolution images [3–6]. This scanning and calculating procedure has three requirements for specimens. Firstly, 15 scans per section require superior bleach resistant signal providing molecules. This is especially important when scanning thick objects since the total exposure time throughout all sections increases with the total number of z-sections scanned. Secondly, all signal providing molecules must remain at their 3D location during the entire scanning process, otherwise the calculation of the final image stack will fail. Since complete stacks are scanned for each angle before rotating the grid, even the slightest movement may reduce image quality markedly. Even individual signal providing molecules moving through the object such as particles can greatly interfere with the algorithm. Thirdly, 3D-SIM is a form of wide-field microscopy. This means that sharp images can only be acquired in an area at a certain distance to the cover glass. Signals outside the optimal range will appear less crisp and image artifacts such as artificial generation of signals can occur. This requires the use of the correct oil for a specific distance to the cover glass. Because of these three requirements flat and adherent cells are the optimal choice for 3D-SIM. However, blastomeres of mammalian embryos are non-adherent, large and surrounded by the zona pellucida. We have developed a protocol for 3D-SIM on mammalian embryos and generated high quality data for multiple studies [7, 8]. Here we present a detailed experimental protocol how to achieve

* Correspondence: v.zakhartchenko@gen.vetmed.uni-muenchen.de
[2]Chair for Molecular Animal Breeding and Biotechnology, and Laboratory for Functional Genome Analysis (LAFUGA), Gene Center, LMU Munich, Feodor-Lynen-Str. 25, D-81377 Munich, Germany
[3]Chair for Molecular Animal Breeding and Biotechnology, LMU Munich, Hackerstr. 27, D-85764 Oberschleissheim, Germany
Full list of author information is available at the end of the article

superior image quality of mammalian blastomeres using 3D-SIM.

Methods

Ethics statement

All animal procedures and experiments with embryos were approved by the Government of Upper Bavaria (permit number 55.2-1-54-2532-34-09) and performed in accordance with the German Animal Welfare Act and European Union Normative for Care and Use of Experimental Animals.

Recovery and culture of mouse embryos

Female mice were injected interperitoneally (IP) with pregnant mare's serum (PMS) between 1:00 and 4:00 PM of Day 1. On Day 3, forty-two hours after the PMS injection, the mice received an IP injection of human chorionic gonadotropin (HCG). Immediately following injection, females of the FVB/N inbred strain were mated with males of the same mouse strain. Ovulation occurs approximately 12 h after HCG injection, at which time the eggs can be fertilized. Females were screened every morning and evening for vaginal plugs to see if mating has occurred and sacrificed by cervical dislocation at the same day after finding a vaginal plug (0.5 dpc). For embryo recovery, females were euthanized by cervical dislocation under isoflurane anesthesia. The oviduct was removed and flushed with M2 medium (Sigma, Taufkirchen, Germany) containing 0.4 % bovine serum albumin (BSA) (Roth, Karlsruhe, Germany). Zygotes were collected under a stereo microscope (Zeiss, Jena, Germany) with 20x magnification and transferred to microdrops of M16 medium (Sigma) on a culture dish covered with paraffin oil (Roth). Embryos were cultivated at 37 °C and 5 % CO_2 in an incubator until the appropriate stage for fixation.

Recovery and culture of rabbit embryos

Recovery of embryos was performed as described [9]. Female Zika rabbits were first superovulated by injection of 100 IU (international units) of equine chorionic gonadotropin (ECG; Intergonan, Intervet) intramuscularly and 100 IU of human chorionic gonadotropin (HCG; Ovogest, Intervet) intravenously 72 h later. 18-20 h post-HCG injection and after natural mating *in vivo* fertilized zygotes were flushed from the explanted oviducts of rabbits in warm phosphate buffered saline (PBS) supplemented with 4 mg/ml bovine serum albumin. Rabbit embryos were cultured in Quinn's medium (SAGE, Trumbull, CT) containing 2.5 % fetal calf serum (FCS) in a humidified atmosphere of 5 % CO_2 in air at 38.5 °C until the appropriate stage for fixation.

Recovery and culture of bovine embryos

In vitro fertilization of bovine embryos was performed as described [10]. Cumulus-oocyte complexes (COCs) were obtained by aspiration from ovaries of slaughtered cows. COCs were matured in modified Parker's medium containing TCM199 supplemented with 5 % estrous cow serum (ECS) and 0.2 U/ml o-FSH (Ovagen; ICPbio) for 20–22 h at 39 °C, 5 % CO_2 in air and maximum humidity. Matured COCs were washed with the fertilization medium Tyrode's albumin lactate pyruvate (FERT-TALP) supplemented with sodium pyruvate (2.2 mg/ml), heparin sodium salt (2 mg/ml), and BSA (6 mg/ml) and transferred to 400-μl droplets of medium. Frozen spermatozoa were thawed at 38 °C. 100 μl thawed sperm suspension covered by 1 ml capacitation medium was subjected to the swim-up procedure for 60 min. The COCs and spermatozoa (2 x 10^6 cells/ml) were co-incubated for 18 h at 39 °C and 5 % CO_2 in humidified air. Presumptive zygotes were mechanically denuded by vortexing, washed 3x in SOF culture medium enriched with 5 % ECS, BME 100x (20 μl/ml; Invitrogen) and MEM (Minimum Essential Medium) 100x (10 μl/ml, Invitrogen), and transferred to 400-μl droplets of medium covered with mineral oil. Embryos were grown at 39 °C in a humidified atmosphere of 5 % CO_2, 5 % O_2, and 90 % N_2 until they reached the appropriate stage for fixation.

Cover glass preparation

Clean cover glasses were covered by polylysine (33 μl of a 1:100 Polylysine dilution in aqua bidest for 5 min) applying it in the exact center of each cover glass. If the covered area was too large the Vectashield applied to this prepared area at the final steps of the embedding procedure touched the constructed chamber's walls and could leave the blastomeres uncovered and dried out (see below). When finished with the last cover glass, but at least 5 min after the start with the first one, the drop of polylysine solution was rinsed off the cover glasses in the same order with 500 μl-1000 μl aqua bidest. No drops were left, since after drying they could leave marks. The polylysinated side in the same corner of each cover glass was marked with a permanent marker and with a character or number that can only be read correctly from one side (for example "1"). Even though no liquid was visible on the slides they were dried for at least 2 h.

Slide preparation

Clean glasses were covered with 4 layers of Tesa-Film. To cover a glass its center was pressed at a 45° angle against the sticky side of the film (Fig. 1a). Rotating a finger slowly in a circular pattern, the film was carefully pressed against the glass and attached onto the glass without generating bubbles. Then the film was cut off before and after the attached region on the glass. This procedure was repeated 3 more times to obtain 4 layers

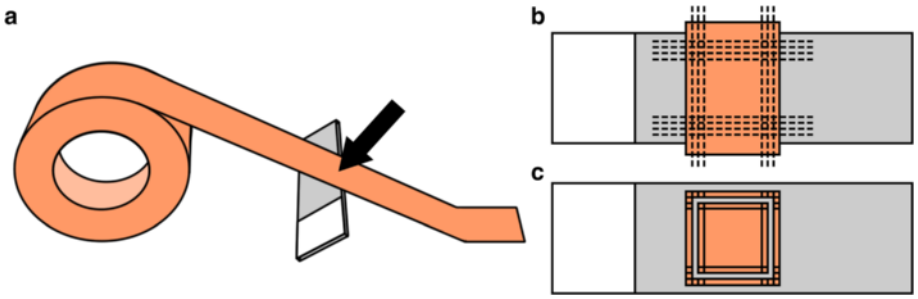

Fig. 1 Preparation of slides. **a** The film was attached to the slide. The black arrow marks the spot where the film was pressed against the slide in a circular motion. **b** The film layers were cut with a scalpel. The dashed lines mark the cutting positions. **c** The slide was prepared for storage. The grey areas inside the outer border mark Tesa-Film removed with 'tweezers'

of Tesa-Film exactly on the top of each other on the glass. The reason for building such a high chamber lies in the effect of the objective pressing down and thereby reducing the distance between the cover glass and the slide inside the chamber. According to the equation of continuity A1*v1 = A2*v2 (A1, A2 = cross-sectional areas before and after distance reduction; v1, v2 = speed of the embedding medium before and after distance reduction) the flow speed of the embedding medium inside the chamber will increase when pressing against the cover glass with the objective. A larger initial volume in the chamber equals a smaller relative volume decrease which equals a smaller speed increase under the pressure of the objective. Furthermore, the slide was placed under a stereo microscope and using a scalpel and tweezers the pattern shown in Fig. 1b was cut into all 4 layers. The central area should be as large as possible to prevent contact between embedding medium and film when placing the cover glass on top of this structure. The parts shown in Fig. 1c were removed with tweezers except for the center part. This central area of the film remained attached during storage and was removed shortly before placing the cover glass on top of this construct in order to minimize dust within the central chamber.

Fixation

Unless noted otherwise fixation of embryos and all subsequent steps were performed at room temperature (RT). For preservation of the 3D shape of embryos and nuclei it was necessary to avoid any deforming pressure and prevent embryos from drying out at any step of the following procedures. Embryos were briefly washed in 38 °C 1x phosphate buffered saline (PBS), fixed in 2 % paraformaldehyde (PFA) in PBS for 10 min, washed twice in PBS and then stored at 4 °C in PBS until further use. The maximum allowed storage duration depended on the concentration of target proteins for staining. Target proteins with a low concentration such as histones were stained and scanned shortly after fixation because the achievable signal strength diminishes with time. Target proteins with a high concentration such as nuclear lamins or nucleoporins were stained and scanned even after months of storage in PBS with acceptable signal strengths compared to the background signals.

Immunostaining

Background caused by PFA was quenched using 20 mM glycine in PBS for 10 min. After washing twice with PBS embryos were permeabilized with 0.5 % Triton-X 100 for 15-30 min. After washing twice with PBS unspecific background signals were reduced by incubation in 2 % BSA for 2-4 h at RT. When targeting proteins with a low concentration, such as histones, embryos were blocked before staining for 4 h or longer in 2 % BSA in PBS to differentiate actual signals from background more efficiently. Four hours of blocking could result in a more focused localization of the signals leading to a slightly altered appearance compared to blocking for 2 h. When targeting proteins with a high concentration such as nuclear lamins or nucleoporins embryos were blocked before staining for only 2 h since the background was relatively less intense. However, maximum image quality was achieved with a blocking for 4 h. Then embryos were sequentially incubated in 40 μl of primary and secondary antibody solutions contained within PCR-tube caps, diluted in PBS with 2 % BSA. The source of the first antibody was different from the species of the embryo or the zona pellucida to avoid staining problems (see Troubleshooting below). In the case of using the same source as the embryo's species, the zona pellucida was removed prior to staining as described below. Tables 1 and 2 show examples of primary and secondary antibodies used successfully with 3D-SIM. Specimens were incubated with primary antibodies overnight at 4 °C. After washing in PBS for 5 times with 2 % BSA the appropriate secondary antibodies, diluted in PBS with 2 % BSA, were applied for 1 h, again followed by washing in PBS for 5 times with 2 % BSA and 5 times without BSA. BSA had two effects. It blocked background signals and made embryos less sticky. While the first property was desired the second one was counter-effective when trying to attach blastomeres on a cover glass for minimal

Table 1 Examples of primary antibodies used successfully with 3D-SIM

Host	Target	Official name	Dilution	Company	ID
Goat	Epitope at C-terminus of Lamin B1. Detecting Lamin B1 and, to a lesser extent, Lamin B2	Lamin B Antibody (M-20)	1:100	Santa Cruz	SC-6217
Mouse	NUP153	Anti-NUP153 [QE5] antibody	1:200	Abcam	ab24700
Rabbit	H3K4me3	Anti-Histone H3 (tri methyl K4) antibody - ChIP Grade	1:100	Abcam	ab8580
Mouse	H3K9me3	Histone H3K9me3 antibody (mAb)	1:100	Active Motif	39285/6
Rat	RNAPII-S5p	Monoclonal antibody against CTD phosphoserine epitope 5	1:20	Gift from Dirk Eick (see Markaki et al. [23])	
Mouse	B23	Monoclonal Anti-B23 antibody produced in mouse	1:1000	Sigma	B0556

The host should be different from the species of the embryo. Otherwise, the zona pellucida should be removed prior to staining

movement. In order to maximize stickiness even after 5 times of washing away BSA with PBS the following fixation step was used to bind the remaining BSA. After washing away the PFA embryos were extremely sticky and in order to prevent their attachment to any surface PBS was constantly pumped under the embryos to keep them floating within the PBS and transporting the embryos not within the transferpettor's pipette but in a tiny drop at the tip of it. If the embryo has attached to a surface recovery was possible by blowing the embryo with the PBS very strongly against it. However, the pressure produced by a standard size opening of a pipette on a transferpettor may not suffice. In this case, the tip of a new glass pipette was melted until the opening was barely visible. Coating the pipette with silicone and the surfaces with silicone or agar may prevent embryos from attaching prior to the final embedding step. A cover glass with the polylysinated side upwards was put into the middle of the cover of a 3.5 cm well. A drop of 10-20 μl PBS was added in the center of the glass. Fixation of antibodies was performed with 4 % PFA in PBS for 10 min, followed by washing twice in PBS. PFA could cause increased background signals in the 488 nm channel. Therefore, fixing antibodies with only 2 % PFA in PBS was used to reduce such additional background signals. Chromatin was counterstained with DAPI (Life Technologies, Catalog No. D1306; 4′,6-diamidino-2-phenylindole) 25 μg/ml diluted in PBS for 15 min followed by washing twice in PBS.

Isolation of blastomeres and attachment to the cover glass

The 3.5 cm well containing the polylysinated cover glass, the drop of PBS and the embryo were transported to a microscope with at least one micromanipulator (two are preferred). An empty injection needle was mounted into the right micromanipulator holder. Similarly, a needle with a diameter smaller than an embryo was mounted into the left micromanipulator holder. This second needle was helpful to stabilize the position of the embryo but was not absolutely necessary for the subsequent steps. Once the embryo was placed inside the drop of PBS on top of the polylysinated cover glass adhesion forces attached the zona pellucida to the glass. An area of the zona pellucida slightly remote from the blastomeres was pressed against the cover glass with the injection needle. Then the needle was moved back and forth while keeping the zona pressed against the glass. The slit in the zona pellucida was enlarged by vibrating the needle via knocking against the micromanipulator with a finger (Fig. 2a). Afterwards the injection needle was inserted into the zona and stretched along the surface of the cover glass away from the embryo to open the zona even more. The embryo inside the open zona pellucida was rotated with the injection needle to line up the border between two blastomeres. Then the injection needle was placed along this border and moved back

Table 2 Examples of secondary antibodies used successfully with 3D-SIM

Host	Target	Fluorophore	Excitation [nm]	Dilution	Company	ID
Donkey	Mouse IgG (H + L)	Alexa	488	1:400	Invitrogen	A-21202
Donkey	Mouse IgG (H + L)	Alexa	594	1:500	Invitrogen	A-21203
Donkey	Goat IgG (H + L)	Alexa	488	1:400	Invitrogen	A-11055
Donkey	Goat IgG (H + L) preadsorbed	Alexa	594	1:400	Abcam	ab150136
Donkey	Rabbit IgG (H + L)	Dylight (Alexa bleaches less)	488	1:300	Jackson Immuno Research	711-485-152
Donkey	Rabbit IgG (H + L)	Dylight (Alexa bleaches less)	594	1:500	Jackson Immuno Research	711-505-152
Goat	Mouse IgG (H + L) preadsorbed	Alexa	594	1:300	Invitrogen	A-11032
Donkey	Rat IgG (H + L)	Alexa	594	1:300	Invitrogen	A-21209

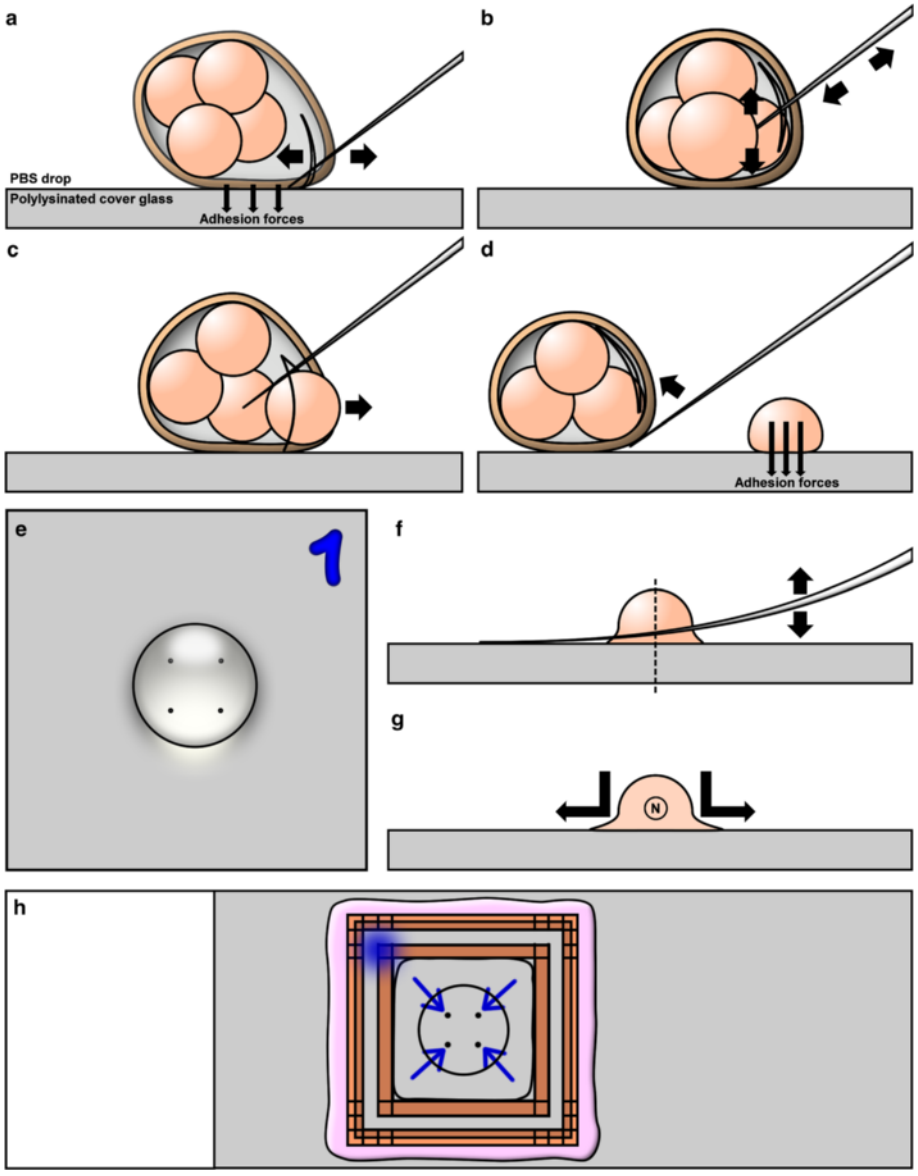

Fig. 2 Isolation and attachment of individual blastomeres. **a** The zona pellucida was cut open. **b** A blastomere was isolated. **c** The isolated blastomere was moved outside the zona pellucida through the cut. **d** The zona pellucida with the remaining blastomeres was moved to the target location for the next blastomere. **e** Positions of blastomeres on the cover glass were chosen as far away from each other as possible, but not too close to the border of the PBS drop. **f** Once all blastomeres had been placed on the cover glass their outermost parts were pressed against the glass. The dashed line marks the section shown in G. **g** The attachment surface was increased even further by stretching out the pressed down periphery of blastomeres by moving the pressed down needle away from the blastomere. The circled N marks the position of the nucleus in this blastomere. **h** The finalized slide with the reversed cover glass attached in the center chamber and sealed with nail polish. The marker "1" was dissolved by the nail polish

and forth to separate the blastomeres (Fig. 2b). Additional knocking against the micromanipulator could facilitate this process. A single blastomere was removed from the zona pellucida and the zona pellucida was moved with the remaining blastomeres away (Fig. 2c and d). The remaining blastomeres were moved inside the zona pellucida to a different remote location from the previous blastomere to prevent bleaching from scanning a neighbouring blastomere (Fig. 2e). The procedure was repeated for all blastomeres. The initial attachment of the blastomeres was automatically facilitated by the adhesion forces of the polylysinated surface. The attached blastomeres were left immobile otherwise this could lead to tearing and stretching artifacts. When working with blastocysts and the task was to scan only trophectoderm (TE) cells a blastocyst was

let to sink on the glass and the monolayer of cells closest to the glass was scanned (Fig. 3a). The cell-free space inside blastocysts (blastocoel) can be large enough so that TE cells on the far side of the blastocyst do not interfere with the scans. If there were multiple layers of TE cells then individual TE cells were isolated and placed next to each other in remote locations as a monolayer. If inner cell mass (ICM) and TE cells were scanned the layer(s) of TE cells were cut like the zona pellucida. Tearing and stretching of cells remote from the slit were avoided. TE cells were then gently attached to the glass while the sphere of ICM cells was residing on top of this monolayer. This ICM sphere was then detached from the monolayer of TE cells by gently pressing against it with the side of the injection needle (Fig. 3b). The ICM sphere was then moved to a remote location and individual cells were isolated as described above for other embryos (Fig. 3c). To maximize image quality it was necessary to attach single blastomeres to the glass not touching each other (Fig. 3d). After attachment of all blastomeres to their target location additional attachments were performed to prevent movements disabling 3D-SIM reconstruction (Fig. 2f and g). The outermost part of blastomeres was pressed down with the injection needle against the cover glass. Then the 3.5 cm well was carefully rotated by 90° and the newly accessible outermost parts were pressed down. The zona pellucida was moved outside the drop so that it could not swim through the medium while scanning. When scanning sperm cells attached to the zona pellucida after an IVF procedure the zona was cut in smaller parts and these parts were pressed against the glass for maximum adhesion.

Embedding

The closed well was transported back to the stereo microscope. The excess of PBS was removed from the cover glass while keeping all blastomeres covered with it. The cover glass was washed two times with 10-20 μl of PBS and covered slowly with 10-20 μl of Vectashield. The excess of Vectashield was removed from the cover glass while keeping all blastomeres covered with it. The slide with the removed central part of the Tesa-Film was placed under the stereo microscope. The cover glass with the drop facing down was put above the center part of the Tesa-Film frame and slowly lowered until the drop reached the slide avoiding the attachment of the drop with the Tesa-Film. The edges of the cover glass rested on the outer frame of the Tesa-Film. All sides of the outer frame were treated with a very small amount of nail polish using a fine brush. A contact between nail polish and Vectashield was avoided, while ensuring the complete sealing of the outer frame. After the nail polish had dried out the slide with the cover glass was held down at an angle under the stereo microscope and all blastomeres were marked with arrows on the back of the slide, but not on the cover glass (Fig. 2h). The slide was stored at 4 °C horizontally with the cover glass facing down to prevent movement of the Vectashield drop and detachment of the blastomeres.

Oil selection for microscopy

Selection of the correct oil required to produce crisp images at the desired distance to the cover glass was performed in two steps. Firstly, the oil was estimated using embryos at various stages of development based on empirical testing (Table 3). We found that smaller blastomeres required oils with lower refractive indexes. Secondly, the correct oil was determined by analyzing preview and reconstructed images provided by 3D-SIM and its accompanying software package.

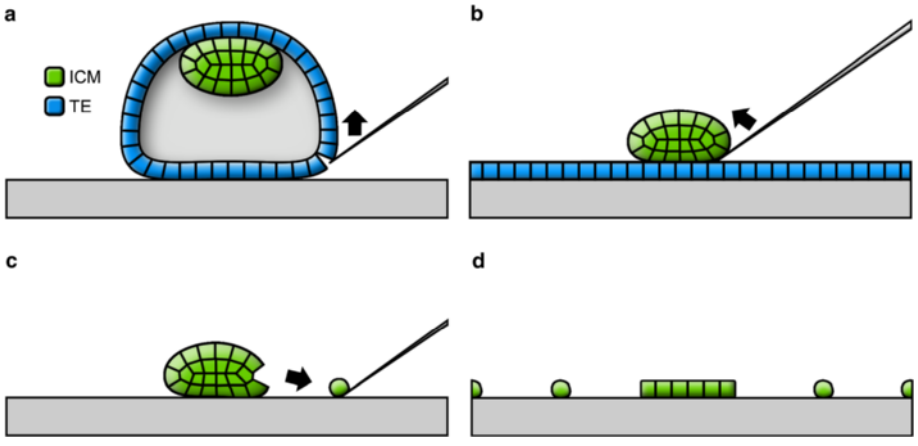

Fig. 3 Isolation of blastomeres from blastocysts. **a** The trophectoderm (TE) layer was cut open. **b** The inner cell mass was moved away from the TE layer. **c** Blastomere isolation. **d** Individual blastomeres were placed remotely from each other

Table 3 Optimal refractive indices of oils per stage based on empirical testing

Stage/cell type	Optimal refractive index of oil
Zygote (centrally located pronuclei)	>1.534
2-cell	1.528–1.534
4-cell	1.526–1.528
8-cell	1.518–1.526
16-cell, morula and blastocyst	1.512–1.518
Spermatozoa, fibroblasts and cell lines	1.512–1.514

Determination of the blastomere coordinates

A small drop of the estimated oil was applied on the clean cover glass. With the specimen localization microscope of the 3D-SIM setup the arrows in transmission light mode were found and the locations of the associated blastomeres were marked in the software.

Determination of the correct oil before scanning

The slide was transferred to the 3D-SIM microscope and the objective was moved in the z-direction at the position of the first blastomere. The z-position of the objective was compared before moving it towards the cover glass and afterwards. In our setup, smaller z-position values required oils with a higher refractive index, because the layer of the specimen was located at a greater distance from the cover glass. With this understanding, the preview image was used to predict the selection of the correct oil. In round specimens such as nuclei, wide-field microscopy apparently generates intense circular patterns that form cone shapes above and below the specimens (Fig. 4). The key to find the oil that provides a focused image in the vertical center of the specimen is to ensure that the distance of the upper and lower congregation points to the specimen is equal above and below the specimen (Fig. 4a–c). This can be assessed by moving in the z-direction above and below the specimen and counting sections between the top and bottom cone focal points and the first clearly visible grid on the nucleus' top and bottom side. If the distance of the upper and lower congregation points was equal above and below the specimen then the focal section of the oil was in the specimen center. This was verified by checking for sharp lines of the grid in the mid-section. If the distance was not the same, then the oil with a higher refractive index was used in the case when the side of the nucleus with the lower z-position had a shorter distance between the cone focal point and the first clearly visible grid on the nucleus compared to the side of the nucleus with the higher z-position. If this scenario was reversed then the oil with a lower refractive index was used.

3D structured illumination microscopy (3D-SIM) and quantitative image evaluation

3D-SIM of embryonic nuclei was performed on a DeltaVision OMX V3 system (Applied Precision Imaging/GE Healthcare) with a lateral (x,y) resolution of ~120 nm and an axial (z) resolution of ~300 nm. The system was equipped with a 100x/1.40 NA PlanApo oil immersion objective (Olympus), Cascade II:512 EMCCD cameras (Photometrics) and 405, 488 and 593 nm diode lasers. Image stacks were acquired with a z-distance of 125 nm and with 15 raw SIM images per plane (5 phases, 3 angles). The SI raw data were computationally reconstructed with channel specific measured OTFs using the softWoRX 4.0 software package (Applied Precision). Images from the different color channels were registered with alignment parameters obtained from calibration measurements with 0.2 μm diameter TetraSpeck beads (Invitrogen). The voxel size of the reconstructed images is 39.5 nm in x,y and 125 nm in z with 32-bit depth. For all subsequent image processing and data analysis, images were converted to 16-bit composite tiff-stacks. Image stacks were processed using ImageJ 1.45b (http://rsb.info.nih.gov/ij/).

Scanning

Before scanning the specimen was centered by comparing the distance of its border to the borders of the frame. This was also checked throughout all z-sections to use entire 3D-stacks. The key to great scans of perfectly immobile and clean specimens in clean Vectashield was to minimize bleaching during the scan. With highly concentrated target proteins such as lamins or nucleoporins a special property of the Alexa brand of secondary antibodies was used to not only reduce bleaching, but even stop or reverse bleaching. Alexa antibodies displayed two bleaching properties. Firstly, they bleached during a first intense scan (Table 4). Secondly, after such a first intense scan, their photon count was much more stable during a second less intense scan (Table 5). To obtain optimal results, Alexa stained specimens were scanned with a highly concentrated target protein in two steps. In the first step scanning was performed using the CCD camera with high laser intensity. This first reconstructed scan was inspected using the orthogonal viewer of the DV viewer software or with FIJI (ImageJ with appropriate plugins for viewing DV files) to check if the correct oil had been selected (Fig. 4). In that case, the two cones on the top and on the bottom of the sample had the same height. If the intensity of the signals did not allow for a second scan with the settings according to Table 5 then the first scan was repeated. The second scan was performed with a highly sensitive EMCCD camera with far less intense laser settings. A large photon count reduction was observed between the beginning and the end of the first, high intensity scan. The photon count stayed more stable in the second, low intensity scan. However, even the initial scan yielded very good results in many cases. This could be due to the fact that the bleaching of the fluorescent beads used to configure the algorithm of the software was proportional

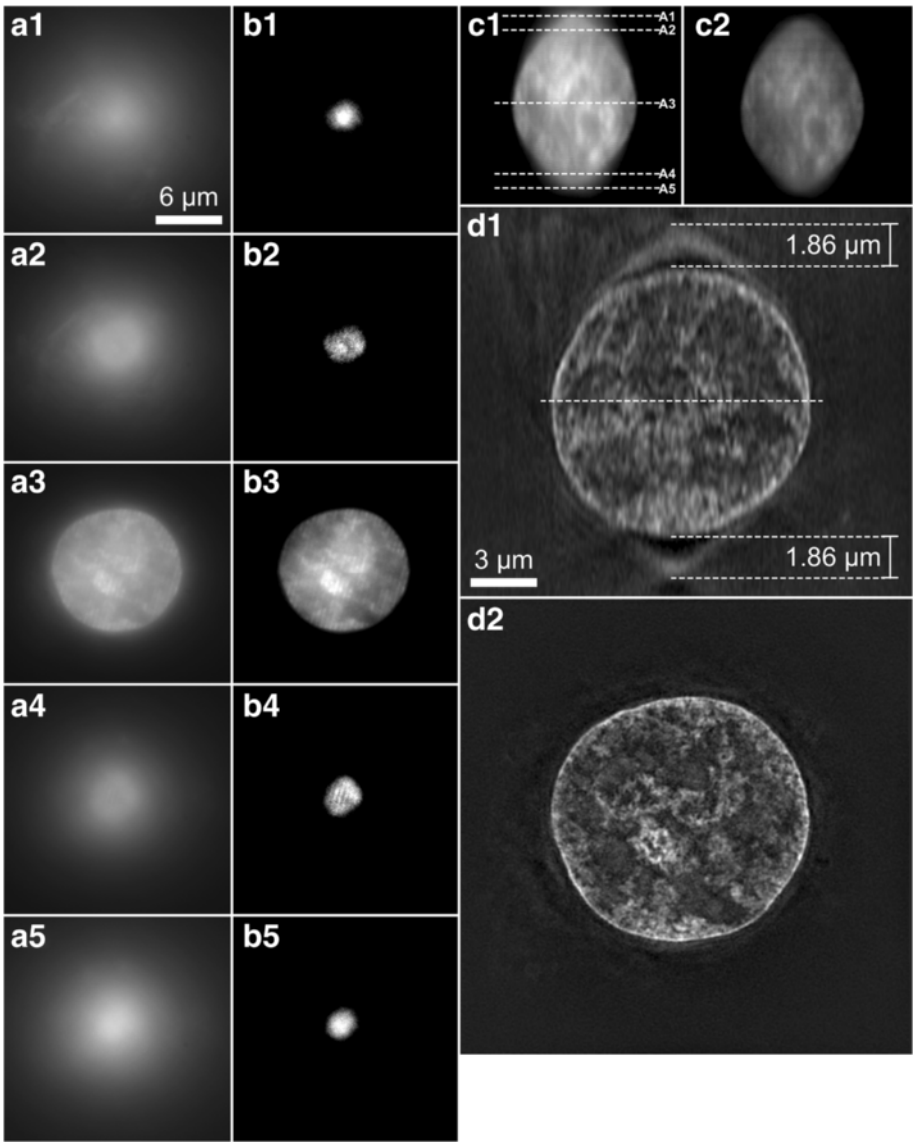

Fig. 4 Determination of the correct oil before the first scan. **a1–5** Preview images of the first focal point of grid-free signals (**a1**), the first occurrence of the grid on the specimen (**a2**), the mid-section (**a3**), the last occurrence of the grid (**a4**) and the second focal point of grid-free signals. **b1–5** show the same images as in (**a1–5**) with optimized contrast for improved visualization of the grid. **c1** Orthogonal view of the first of the three non-reconstructed scans with different angles. The dashed lines mark sections (**a1**–**a5**). **c2** Orthogonal view of the second of three non-reconstructed scans. Note the reduction of signal strength between the two scans caused by bleaching. **d1** Orthogonal view of the reconstructed scan. The central dashed line marks the section of D2. **d2** Reconstructed mid-section with full resolution

to the bleaching of the initial scan and therefore resembled the configured situation better than a reduced bleaching situation. Generally however, less bleaching was better than more bleaching. If the image quality was sub-optimal when scanning multiple wavelengths at the same time then those were scanned in separate runs and the channels were combined after the scans using FIJI or the DV software provided with the microscope. The reduced image quality in parallel scans could be due to fluorophores being bleached by other wavelengths as well, adding additional bleaching during parallel scanning. For optimal results each channel was bleached independently until the scenario described in Table 5 was achieved for all channels at the beginning of the final scan. If the target was not highly concentrated multiple scans were avoided. In this case each channel was scanned independently with the second scan settings.

Determination of the correct oil after the first scan

Not all objects generated cones of artificially increased signals above and below the object. Non-round nucleus-like objects observed in early stage rabbit embryos did

Table 4 Microscope settings and expected photon counts for the first scan

Fluorophor/staining	Mode	Exposure	Laser	Initial photon count
Alexa	CCD 5 MHz	25 ms	50 %	17000
DAPI	CCD 5 MHz	50 ms-120 ms (lower is better)	100 %	8000 - 16000

not generate intense cones (see the orthogonal views in Fig. 5). In this case, the correct oil was determined after the first scan. A highly concentrated target protein generating line-like signals along the z-axis like a nuclear lamina staining was the best indicator of whether to increase or lower the chosen oil refractive index and for this purpose orthogonal views of the first scan were generated. This was performed with the DV viewer software or with FIJI. Objects like nucleoli were identified in the stack and in the preview window to determine whether the top or the bottom of the z-stack were closer to the cover glass. To determine whether the top or the bottom of the scanned stack was closer to the cover glass the objective was moved up and down in the z-axis with the preview window and the z-position was compared with the objective's position when it was at a large distance to the cover glass before scanning. The area of the z-stack was identified in the orthogonal viewer with the highest signal intensity and the sharpest lines (Fig. 5). This focus area was moved further away from the glass by changing to oil with a higher refractive index or moved closer to the glass by changing to oil with a lower refractive index. Once the correct oil had been identified all channels were scanned.

Computing the final images

To ensure high quality scans the scanned stack was computed immediately after scanning. If the computed result was not optimal the same area was scanned again with different settings. In large scans the central area of 256 by 256 pixels was cut out and only this area was reconstructed for preview purposes. The final images were reconstructed with the optical transfer function (OTF) files generated using the optimal oil for fluorescent beads attached to the cover glass. In our case the refractive index of the oil optimal for beads was 1.512. Drift correction was activated to counteract any movements and produce images with a maximum quality. This setting did not have any negative effects on scans with perfectly still specimens.

List of materials and reagents

PMS: pregnant mare's serum
HCG: human chorionic gonadotropin
Isoflurane
BSA: bovine serum albumin
M2: medium
M16: medium
ECG: equine chorionic gonadotropin
Quinn's medium
FCS: fetal calf serum
Parker's medium
TCM199: medium
ECS: estrous cow serum
FSH: follicular stimulating hormone
FERT-TALP: fertilization medium Tyrode's albumin lactate pyruvate supplemented
Heparin: sodium salt
SOF: synthetic oviductal fluid
BME: Basal Medium Eagle
MEM: Minimum Essential Medium
Polylysine
Vectashield
PFA: paraformaldehyde
Glycine
Triton-X 100
DAPI: 4′,6-diamidino-2-phenylindole

Results and Discussion

Troubleshooting

In the case of a suboptimal image quality of scanned blastomeres we tested the staining and the microscope first using flat, adherent cells stained using the same conditions as stated above. If **channels were misaligned** (Fig. 6a) in adherent cells we recalibrated the microscope using fluorescent beads with the same temperature during scanning as for calibration. Misalignment could be checked best with prominent structures in multiple channels such as a lamin B and a nucleoporin staining or a nucleoli and a DAPI staining in nuclei with nucleoli lined by dense chromatin. If **antibodies for internuclear signals were also located at the nuclear periphery** (Fig. 6b) we used only 2 % BSA in PBS as blocking buffer since other additives could reduce accessibility of chromatin for antibodies. The antibody itself could also not be specific.

The wrong oil led to suboptimal results as described above. **Bleaching** was minimized by the pre-bleaching strategy outlined above. In the case of bleaching the top sections of a nucleus in an orthogonal view were

Table 5 Microscope settings and expected photon counts for the second scan

Fluorophor/staining	Camera	EMCCD gain	Exposure	Laser	Initial photon count
Alexa	EMCCD 5 MHz	2800-3300	30 ms	10 %	17000
DAPI	CCD 5 MHz	-	50 ms-120 ms (lower is better)	100 %	8000 – 16000

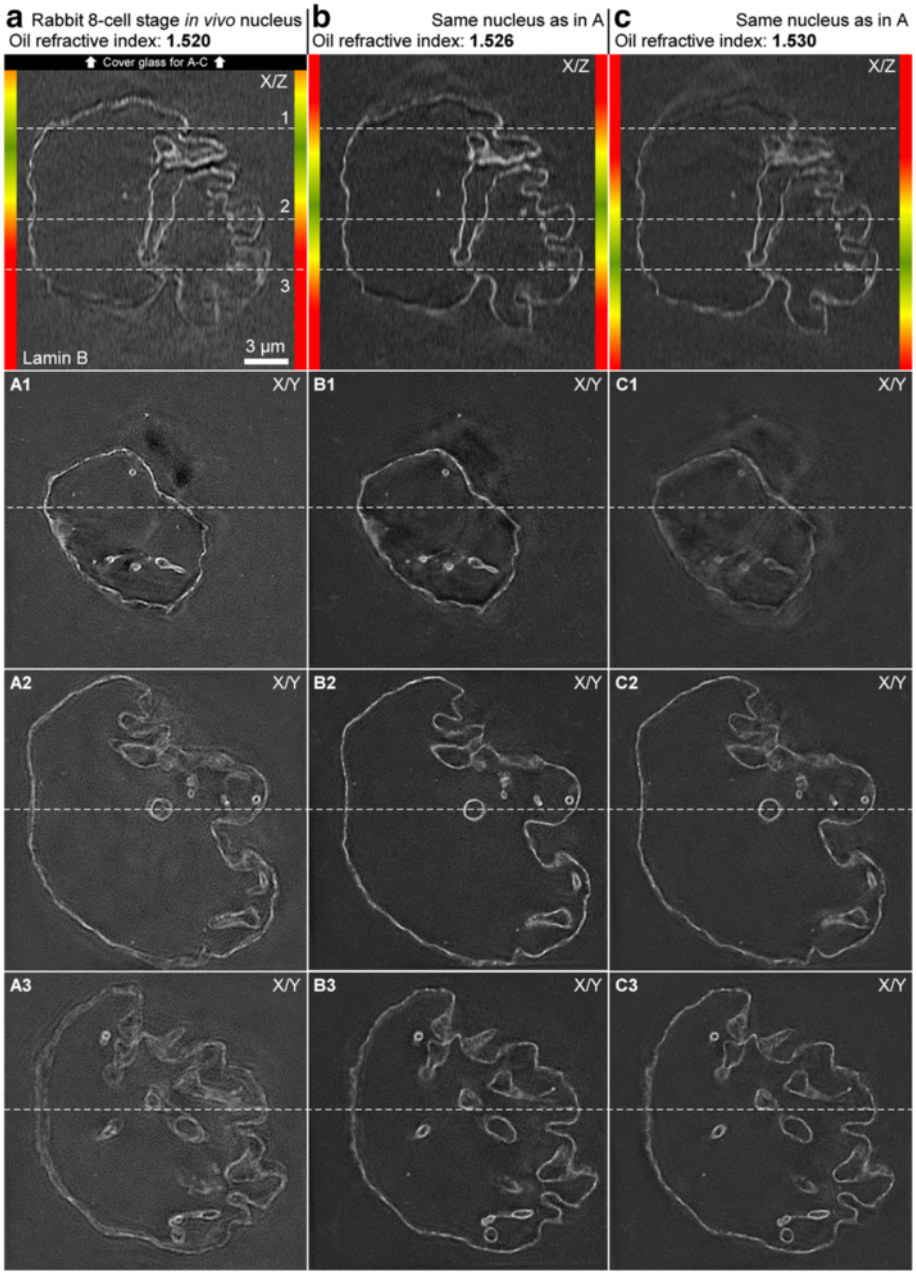

Fig. 5 Effect of oils with different refractive indices. The same nucleus stained for lamin B from a rabbit 8-cell stage *in vivo* embryo scanned with 1.520 (**a**), 1.526 (**b**) and 1.530 (**c**) oils. Note the movement of the optimal focal section away from the cover glass with higher oils. The sides of the orthogonal views are color-coded for high quality sections at around the optimal focal section (green), medium quality sections further away (yellow) and low quality sections even further away (red)

brighter than the bottom sections. **Artificial short lines emanating from the real signals** (Fig. 6c) indicated sample movement during scanning. This could be either due to an improper attachment of the sample to the cover glass or movements of other materials inside the sample (loose fluorophores or particles). The solution was to re-attach the specimen and to fix the specimen again. To achieve this with the same sample, PBS was added to the hardened nail polish seal while gently disconnecting the bond between the nail polish and the cover glass with very thin tweezers. Once the nail polish seal and the Tesa-Film were disconnected from the cover glass on all sides the cover glass was lifted up using tweezers, turned in the way that the drop of Vectashield faced up and then placed inside a 3.5 cm well. All subsequent steps were performed by exchanging chemicals on the cover glass with the blastomeres still attached. Vectashield was

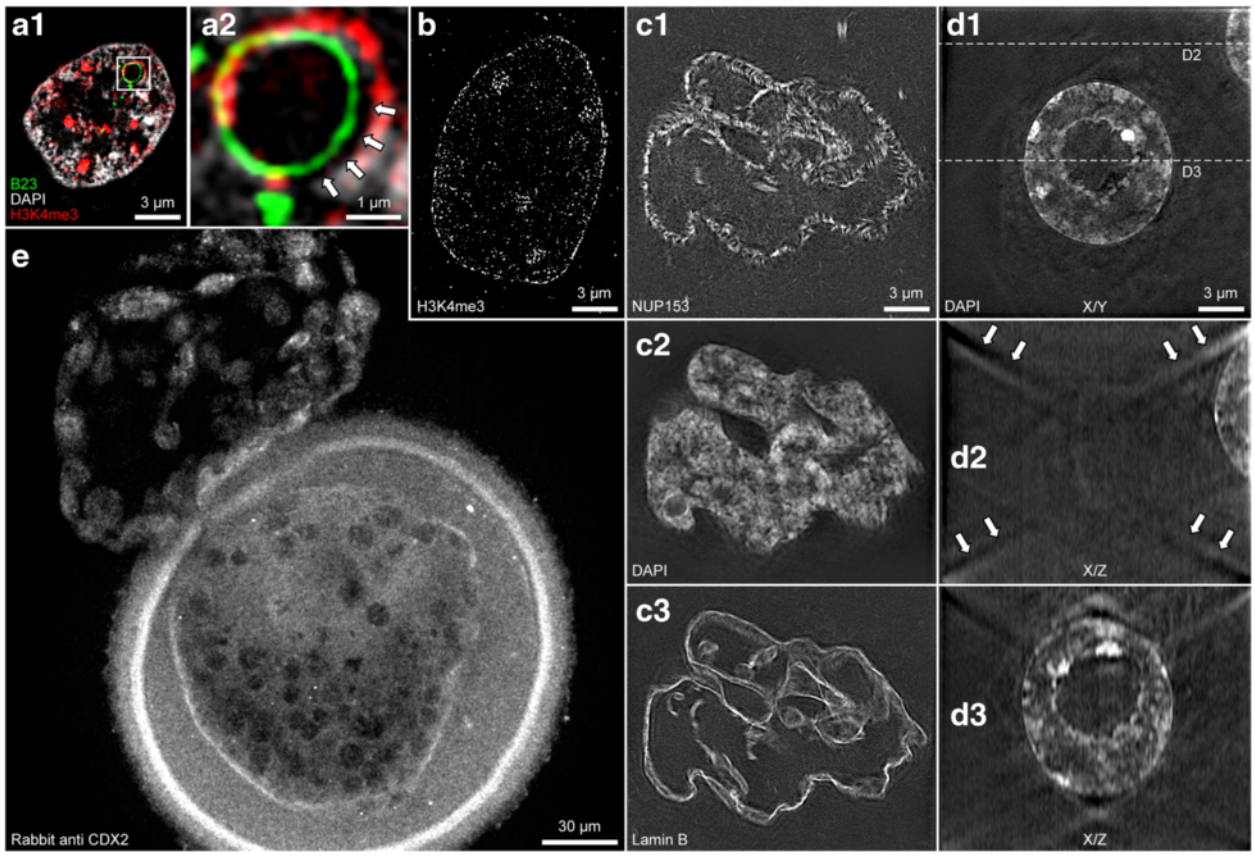

Fig. 6 Potential problems. **a1**. Misaligned B23 (green), H3K4me3 (red) and DAPI (grey) channel. **a2** shows an enlargement of the box in **a1**. Arrows mark the gap between the signals that should be aligned. **b**. H3K4me3 staining at the periphery occasionally caused by using the blocking buffer developed by Markaki et al. [21] and utilized by Huebner et al. [22] without such an effect. **c1**. Movement during scanning may have caused short lines instead of round nuclear pores as visualized by a NUP153 staining. **c2**. The DAPI channel from the same nucleus as shown in **c2** is blurry. **c3**. The lines of lamin B of the same nucleus as shown in **c1** and **c2** are duplicated. **d1**. Blurry X/Y section of a DAPI stained nucleus next to another DAPI stained nucleus at the right top border. **d2**. The X/Z section marked in D1 shows lines emanating from all four corners caused by the second nucleus (marked by arrows; compare with Figure 4 D1). **d3**. These lines interfere with the signals produced by the central nucleus. **e**. Rabbit anti CDX2 staining of a rabbit blastocyst recorded by confocal microscopy shows a normal staining pattern outside the zona pellucida, a strongly stained zona pellucida and an altered staining pattern of blastomeres inside the zona pellucida when compared with nuclei outside the zona pellucida

washed away gently but completely with PBS for 5 times while not blowing against the attached blastomeres. The specimen was fixed with 4 % PFA in PBS for 10 min, washed twice with PBS and restained with DAPI 25 µg/ml diluted in PBS for 15 min followed by washing twice in PBS. The well was moved to a microscope featuring micromanipulators. The periphery of blastomeres was pressed onto the cover glass with an injection needle attached to a micromanipulator as described above. The well was moved back to a stereo microscope and the sample was washed gently without blowing against the blastomeres with PBS for 5 times. The different light direction options of the stereo microscope were used to check the medium for floating particles. All particles were removed with a pipette. The specimens were washed twice with Vectashield and checked again for particles. All particles were removed with a pipette. The cover glass was turned in the way that the Vectashield was facing down and then was slowly lowered to a fresh clean slide while keeping it horizontally aligned. The slide was sealed with nail polish and scanned again. Another factor for optimal image quality was to ensure that there were **no additional nuclei in close vicinity** (Fig. 6d) to the nucleus scanned. Nuclei in the vicinity could cause artificial patterns reducing the image quality. If the **zona pellucida displayed strong signals** (Fig. 6e) while blastomeres within the zona pellucida had low to no signals the secondary antibody was most likely targeting the embryo's species. The zona pellucida could be saturated with target proteins. This is a common problem with mouse and rabbit embryos as most secondary antibodies are created in these species. The solution to this problem was to remove the zona

pellucida before the first contact with antibodies. Handling sticky embryos after removal of 2 % BSA in PBS without a zona pellucida could be challenging. This required constant blowing under the embryos to prevent attachment to the bottom of the Eppendorf tube cap. When moving embryos between caps it was necessary to keep embryos in a drop of liquid at the tip of the transferpettor's pipette to prevent attachment inside the pipette. In order to maximize stickiness even after 5 times of washing away BSA with PBS the following fixation step was used to bind the remaining BSA. After washing away the PFA embryos were extremely sticky and in order to prevent their attachment to any surface PBS was constantly pumped under the embryos to keep them floating within the PBS and transporting the embryos not within the transferpettor's pipette but in a tiny drop at the tip of it.

To avoid the stickiness of embryos with or without the zona pellucida a more simple solution than a complicated pipetting system could be the use of chambers/slides/dishes covered by agar or silicon and pipettes covered with silicon. However, such additional reagents in direct contact with the solutions containing the embryos may create particles disturbing the scanning and calculating procedure. It should also be noted that the embryo's stickiness is increased during prolonged storage of the fixed embryos at 4 °C, as prolonged storage can alter the surface of blastomeres and of the zona pellucida.

Examples of 3D-SIM and confocal microscopy scans

Figure 7 features 3D-SIM scans of nuclei in blastomeres from cattle, rabbit and mouse embryos and rabbit spermatozoa. A confocal scan shows the difference in resolution.

This figure showcases the image quality possible with our 3D-SIM protocol by resolving individual nuclear pores.

Comparison with alternative microscopy solutions

While 3D-SIM surpasses the image resolution of confocal imaging [11, 12], the stabilization of specimens, the determination of the correct oil, potentially increased bleaching by scanning each section far more often than during confocal microscopy and the requirement of reconstructing the final image make this method more demanding. Alternatively, confocal scanning without deconvolution may be the preferred method if signal intensities between multiple samples have to be compared, since algorithms can alter the signal intensity and create artifacts [13]. Wide-field microscopy also introduces new artifacts such as spherically increased signals to the specimens, which were not observed in confocal scans. GFP or RFP signals can get bleached too much with our setup and may require GFP or RFP boosters featuring Alexa fluorophores.

While the resolution of 3D-SIM is lower than the resolution achieved with electron microscopy [14, 15], 3D-SIM offers the advantage of using lasers with multiple wavelengths for multiple target co-localization studies not possible with electron microscopy. Additionally, embedding specimens in solid blocks and cutting/milling the blocks for scanning sections is necessary for electron microscopy and may introduce artifacts such as stretching of sections or cut marks [16, 17]. 3D-SIM can be performed in a liquid embedding medium that does not dry out and does not require cutting/milling and therefore does not change the morphology of specimens as demonstrated in completely spherical nuclei in 3D. However, liquid embedding media with a different density than PBS may potentially cause temporary deformation. A temporarily deformed zona pellucida was observed in earlier tests when embedding whole embryos with a zona pellucida in one step from PBS to Vectashield. Usually, the deformed zona pellucida recovered its original shape after some time. This temporary problem can be circumvented by washing embryos with increasing concentrations of the embedding medium in PBS before the final embedding step in pure embedding medium. Spherical nuclei in all dimensions prove that deformation based on medium density differences is either temporary or does not affect blastomeres. Earlier tests with embedding media that harden such as ProLong Gold led to alterations in morphology and an increased background signal and are therefore not recommended. This may be due to volume reductions during vaporization of the solvent.

Applicability to alternative super-resolution fluorescence microscopy solutions

This protocol essentially aims to simulate the stability of fluorescent molecule localizations of adherent cells by attaching blastomeres to polylysinated cover glasses. Furthermore, it aims to simulate their proximity to the cover glass by using the correct oil to work around the distance to the cover glass. Therefore, because this protocol essentially turns blastomeres into simulated adherent cells close to the cover glass, it is feasible that this protocol is also compatible with other super-resolution microscopy solutions proven to work with adherent cells such as photoactivated localization microscopy (PALM) [18], stochastic optical reconstruction microscopy (STORM) [19] and stimulated-emission-depletion microscopy STED [20].

Conclusions

To our knowledge, this protocol presents for the first time a highly detailed and practical way to perform super-resolution fluorescence microscopy on areas within blastomeres of mammalian embryos which can be remotely located from the cover glass. It underscores the importance of stabilizing the location of all

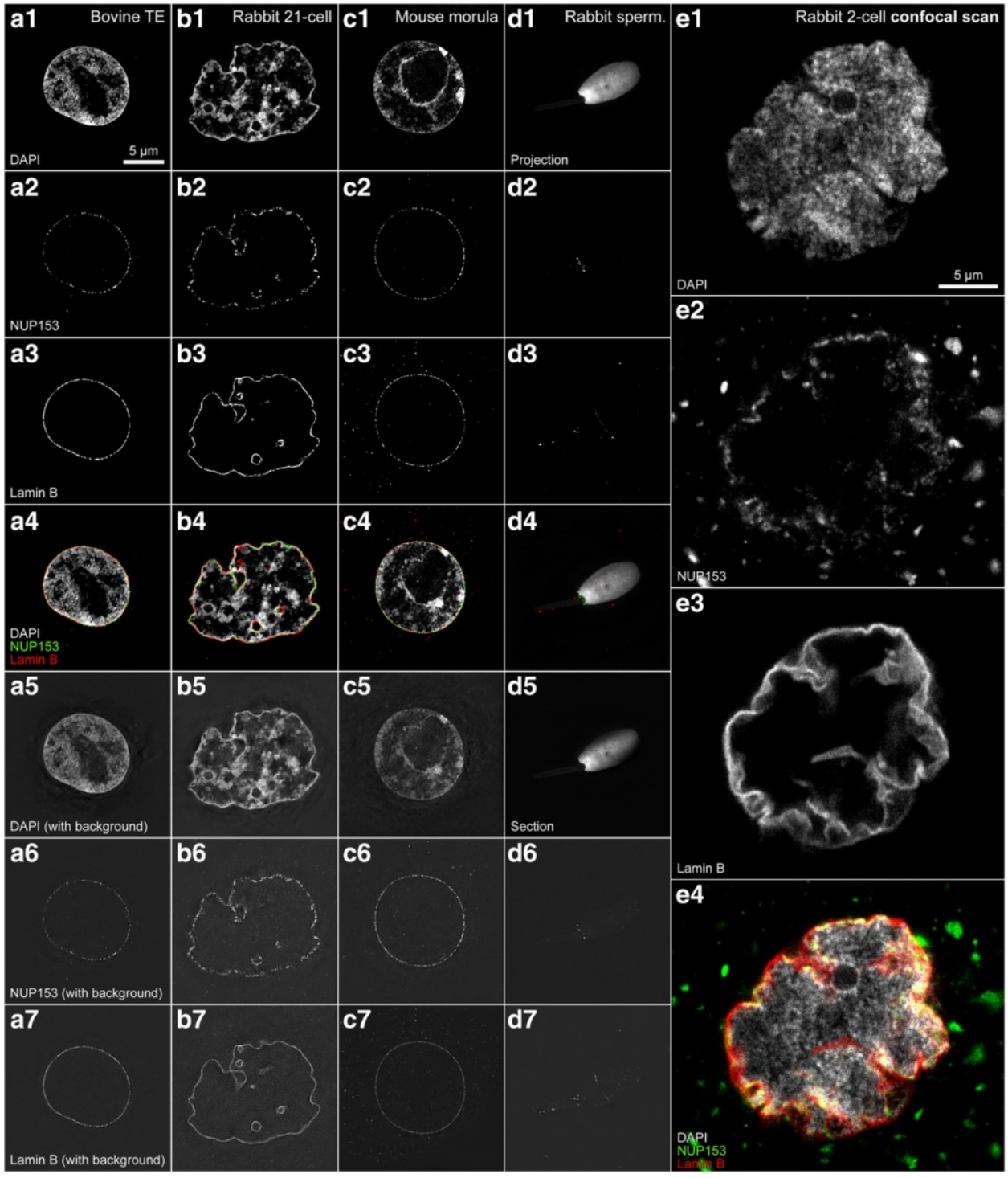

Fig. 7 Examples of 3D-SIM and confocal microscopy scans. **a**. 3D-SIM scans of a nucleus in a trophectoderm blastomere from a bovine blastocyst. **b**. 3D-SIM scans of a nucleus in a blastomere from a rabbit 21-cell embryo. **c**. 3D-SIM scans of a nucleus in a blastomere from a mouse morula. The background may have increased slightly since this morula was stored for 2 years in PBS under mineral oil between fixation and staining. **d**. 3D-SIM scans of a rabbit spermatozoon. **e**. Confocal microscopy scans of a nucleus in a blastomere from a rabbit 2-cell stage embryo. **a1**–**e1**. DAPI. **a2**–**e2**. NUP153. **a3**–**e3**. Lamin B. **a4**–**e4**. Composite of DAPI (grey), NUP153 (green) and lamin B (red). **a5**–**d5**. DAPI without a correction of the background signals. **a6**–**d6**. NUP153 without a correction of the background signals. **a7**–**d7**. Lamin B without a correction of the background signals

signal providing molecules throughout the scanning process and demonstrates the process of achieving stability in non-adherent cells. Furthermore, this protocol gives practical advice in selecting the oil with the correct refractive index before the first scan is performed. Selection of the correct oil is mandatory for performing high quality wide-field microscopy at large distances from the cover glass such as nuclei in large, round blastomeres of early mammalian embryos.

While the image resolution surpasses confocal imaging, the stabilization of specimens, the determination of the correct oil, potentially increased bleaching by scanning each section more often than in confocal microscopy and the requirement of reconstructing the final image make this method more demanding. The problem of bleaching is far greater in large blastomeres that require scanning of many z-sections than in flat adherent cells. This protocol gives practical advice on how to utilize the non-linear bleaching properties of Alexa fluorophores to minimize bleaching in large stacks.

Finally, this protocol serves as a guide to generate super-resolution fluorescence scans of areas within blastomeres in a highly robust and reliable way.

Abbreviations

3D: three-dimensional; B23: nucleolar phosphoprotein B23; BSA: Bovine serum albumin; CCD: Charge-coupled device; CDX2: Caudal-type homeobox 2; DAPI: 4′,6-diamidino-2-phenylindole; EMCCD: Electron multiplying charge coupled device; GFP: Green fluorescent protein; H3K4me3: Histone 3 lysine 4 trimethylated; ICM: Inner cell mass; IVF: *in vitro* fertilization; NUP153: Nucleoporin 153 kDa; PBS: Phosphate buffered saline; PFA: Paraformaldehyde; RFP: Red fluorescent protein; RT: Room temperature; SIM: Structured illumination microscopy; TE: Trophectoderm.

Competing interests

The authors declare that they have no competing interests.

Authors' contributions

Conceived and designed the experiments: JP VZ. Performed the experiments: JP TG VZ. Analyzed the data: JP. Wrote the paper: JP EW VZ. All authors read and approved the final manuscript.

Acknowledgements

We gratefully acknowledge the support provided by Thomas Cremer. This study was supported by grants from the Deutsche Forschungsgemeinschaft to E.W. and V.Z. (CR 59/26, FOR 1041, ZA 425/1-3). In addition, research of E.W. and V.Z. was supported by the EU grant Plurisys, HEALTH-F4-2009-223485 FP7 Health 534 project. The authors are members of COST Action BM1308 "Sharing Advances on Large Animal Models – SALAAM".

Author details

[1]Division of Anthropology and Human Genetics, Biocenter, LMU Munich, Grosshaderner Str. 2, D-82152 Planegg-Martinsried, Germany. [2]Chair for Molecular Animal Breeding and Biotechnology, and Laboratory for Functional Genome Analysis (LAFUGA), Gene Center, LMU Munich, Feodor-Lynen-Str. 25, D-81377 Munich, Germany. [3]Chair for Molecular Animal Breeding and Biotechnology, LMU Munich, Hackerstr. 27, D-85764 Oberschleissheim, Germany.

Received: 11 May 2015 Accepted: 31 October 2015
Published online: 26 November 2015

References

1. Schermelleh L, Heintzmann R, Leonhardt H. A guide to super-resolution fluorescence microscopy. J Cell Biol. 2010;190(2):165–75. doi:10.1083/jcb.201002018.
2. Cremer C, Masters BR. Resolution enhancement techniques in microscopy. EPJ H. 2013;38(3):281–344. doi:10.1140/epjh/e2012-20060-1.
3. Gustafsson MG. Surpassing the lateral resolution limit by a factor of two using structured illumination microscopy. J Microsc. 2000;198(2):82–7.
4. Heintzmann R, Cremer CG. Laterally modulated excitation microscopy: improvement of resolution by using a diffraction grating. International Society for Optics and Photonic; 1999. p. 185–96.
5. Gustafsson MG. Extended resolution fluorescence microscopy. Curr Opin Struct Biol. 1999;9(5):627–8.
6. Cremer C. Optics far beyond the diffraction limit. In: Traeger F, editor. Springer Handbook of Lasers and Optics: Springer Berlin Heidelberg; 2012. p. 1359–97.
7. Popken J, Brero A, Koehler D, Schmid VJ, Strauss A, Wuensch A, et al. Reprogramming of fibroblast nuclei in cloned bovine embryos involves major structural remodeling with both striking similarities and differences to nuclear phenotypes of *in vitro* fertilized embryos. Nucleus. 2014;5–5:542–54.
8. Popken J, Graf A, Krebs S, Blum H, Schmid VJ, Strauss A, et al. Remodeling of the nuclear envelope and lamina during bovine preimplantation development and its functional implications. PLoS One. 2015;10(5):e0124619.
9. Zakhartchenko V, Flisikowska T, Li S, Richter T, Wieland H, Durkovic M, et al. Cell-mediated transgenesis in rabbits: chimeric and nuclear transfer animals. Biol Reprod. 2011;84(2):229–37. doi:10.1095/biolreprod.110.087098.
10. Hiendleder S, Wirtz M, Mund C, Klempt M, Reichenbach HD, Stojkovic M, et al. Tissue-specific effects of in vitro fertilization procedures on genomic cytosine methylation levels in overgrown and normal sized bovine fetuses. Biol Reprod. 2006;75(1):17–23. doi:biolreprod.105.043919 [pii].
11. Schermelleh L, Carlton PM, Haase S, Shao L, Winoto L, Kner P, et al. Subdiffraction multicolor imaging of the nuclear periphery with 3D structured illumination microscopy. Science. 2008;320(5881):1332–6. doi:10.1126/science.1156947.
12. Huang B, Babcock H, Zhuang X. Breaking the diffraction barrier: super-resolution imaging of cells. Cell. 2010;143(7):1047–58. doi:10.1016/j.cell.2010.12.002.
13. Wallace W, Schaefer LH, Swedlow JR. A workingperson's guide to deconvolution in light microscopy. BioTechniques. 2001;31(5):1076–8. 80, 82 passim.
14. Wei D, Jacobs S, Modla S, Zhang S, Young CL, Cirino R, et al. High-resolution three-dimensional reconstruction of a whole yeast cell using focused-ion beam scanning electron microscopy. BioTechniques. 2012;53(1):41–8. doi:10.2144/000113850.
15. Huang B, Bates M, Zhuang X. Super-resolution fluorescence microscopy. Annu Rev Biochem. 2009;78:993–1016. doi:10.1146/annurev.biochem.77.061906.092014.
16. Mollenhauer HH. Artifacts caused by dehydration and epoxy embedding in transmission electron microscopy. Microsc Res Tech. 1993;26(6):496–512. doi:10.1002/jemt.1070260604.
17. Al-Amoudi A, Studer D, Dubochet J. Cutting artefacts and cutting process in vitreous sections for cryo-electron microscopy. J Struct Biol. 2005;150(1):109–21. doi:10.1016/j.jsb.2005.01.003.
18. Zhong H. Photoactivated localization microscopy (PALM): an optical technique for achieving ~10-nm resolution. Cold Spring Harb Protoc. 2010;2010(12):pdb top91. doi:10.1101/pdb.top91.
19. Rust MJ, Bates M, Zhuang X. Sub-diffraction-limit imaging by stochastic optical reconstruction microscopy (STORM). Nat Methods. 2006;3(10):793–5. doi:10.1038/nmeth929.
20. Hell SW, Wichmann J. Breaking the diffraction resolution limit by stimulated emission: stimulated-emission-depletion fluorescence microscopy. Opt Lett. 1994;19(11):780–2.
21. Markaki Y, Smeets D, Fiedler S, Schmid VJ, Schermelleh L, Cremer T, et al. The potential of 3D-FISH and super-resolution structured illumination microscopy for studies of 3D nuclear architecture: 3D structured illumination microscopy of defined chromosomal structures visualized by 3D (immuno)-FISH opens new perspectives for studies of nuclear architecture. Bioessays. 2012;34(5):412–26. doi:10.1002/bies.201100176.
22. Huebner B, Cremer T, Neumann J. Correlative Microscopy of Individual Cells: Sequential Application of Microscopic Systems with Increasing Resolution to

Study the Nuclear Landscape. Methods in Molecular Biology. 2013; 1042(Yaron Shav-Tal (ed.), Imaging Gene Expression: Methods and Protocols):299 - 336. doi:DOI 10.1007/978-1-62703-526-2_21.

23. Markaki Y, Gunkel M, Schermelleh L, Beichmanis S, Neumann J, Heidemann M, et al. Functional nuclear organization of transcription and DNA replication: a topographical marriage between chromatin domains and the interchromatin compartment. Cold Spring Harb Symp Quant Biol. 2010;75:475–92. doi:10.1101/sqb.2010.75.042.

2.2. Reprogramming of fibroblast nuclei in cloned bovine embryos involves major structural remodeling with both striking similarities and differences to nuclear phenotypes of *in vitro* fertilized embryos

RESEARCH PAPER

Nucleus 5:6, 555–589; November/December 2014; Published with license by Taylor & Francis

Reprogramming of fibroblast nuclei in cloned bovine embryos involves major structural remodeling with both striking similarities and differences to nuclear phenotypes of *in vitro* fertilized embryos

Jens Popken[1,2], Alessandro Brero[1], Daniela Koehler[1], Volker J Schmid[3], Axel Strauss[4], Annegret Wuensch[2], Tuna Guengoer[2], Alexander Graf[2], Stefan Krebs[2], Helmut Blum[2], Valeri Zakhartchenko[2,*], Eckhard Wolf[2,*], and Thomas Cremer[1,*]

[1]Division of Anthropology and Human Genetics; Biocenter; LMU Munich; Munich, Germany; [2]Chair for Molecular Animal Breeding and Biotechnology; and Laboratory for Functional Genome Analysis (LAFUGA); Gene Center; LMU Munich; Munich, Germany; [3]Institute of Statistics; LMU Munich; Munich, Germany; [4]Division of Genetics; Biocenter; LMU Munich; Munich, Germany

Keywords: bovine preimplantation development, chromosome territory, chromatin domain, embryonic genome activation, H3K4me3, H3K9me3, *in vitro* fertilization (IVF), interchromatin compartment, RNA polymerase II, somatic cell nuclear transfer (SCNT)

Abbreviations: 3D-CLSM, 3-dimensional confocal laser scanning microscopy; 3D-SIM, 3-dimensional structured illumination microscopy; B23, nucleophosmin B23; BTA, *Bos taurus*; CDC, chromatin domain cluster; CT, chromosome territory; major EGA, major embryonic genome activation; EM, electron microscopy; ENC, embryonic nuclei with conventional nuclear architecture; ENP, embryonic nuclei with peripheral CT distribution; H3K4me3, histone H3 with tri-methylated lysine 4; H3K9me3, histone H3 with tri-methylated lysine 9; H3S10p, histone H3 with phosphorylated serine 10; IC, interchromatin compartment; IVF, *in vitro* fertilization; MCB, major chromatin body; PR, perichromatin region; RNA polymerase II-S2p, RNA polymerase II with phosphorylated serine 2 of its CTD domain; RNA polymerase II-S5p, RNA polymerase II with phosphorylated serine 5 of its CTD domain; SC-35, splicing factor SC-35; SCNT, somatic cell nuclear transfer.

Nuclear landscapes were studied during preimplantation development of bovine embryos, generated either by *in vitro* fertilization (IVF), or generated as cloned embryos by somatic cell nuclear transfer (SCNT) of bovine fetal fibroblasts, using 3-dimensional confocal laser scanning microscopy (3D-CLSM) and structured illumination microscopy (3D-SIM). Nuclear landscapes of IVF and SCNT embryonic nuclei were compared with each other and with fibroblast nuclei. We demonstrate that reprogramming of fibroblast nuclei in cloned embryos requires changes of their landscapes similar to nuclei of IVF embryos. On the way toward the 8-cell stage, where major genome activation occurs, a major lacuna, enriched with splicing factors, was formed in the nuclear interior and chromosome territories (CTs) were shifted toward the nuclear periphery. During further development the major lacuna disappeared and CTs were redistributed throughout the nuclear interior forming a contiguous higher order chromatin network. At all stages of development CTs of IVF and SCNT embryonic nuclei were built up from chromatin domain clusters (CDCs) pervaded by interchromatin compartment (IC) channels. Quantitative analyses revealed a highly significant enrichment of RNA polymerase II and H3K4me3, a marker for transcriptionally competent chromatin, at the periphery of CDCs. In contrast, H3K9me3, a marker for silent chromatin, was enriched in the more compacted interior of CDCs. Despite these striking similarities, we also detected major differences between nuclear landscapes of IVF and cloned embryos. Possible implications of these differences for the developmental potential of cloned animals remain to be investigated. We present a model, which integrates generally applicable structural and functional features of the nuclear landscape.

*Correspondence to: Thomas Cremer; Email: Thomas.Cremer@lrz.uni-muenchen.de; Eckhard Wolf; Email: ewolf@lmb.uni-muenchen.de; Valeri Zakhartchenko; Email: V.Zakhartchenko@gen.vetmed.uni-muenchen.de

Submitted: 04/06/2014; Revised: 09/08/2014; Accepted: 10/02/2014

http://dx.doi.org/10.4161/19491034.2014.979712

Introduction

In 1985 Günter Blobel predicted that "the genome of a higher eukaryotic organism is organized into a number of distinct 3-dimensional (3D) structures, each characteristic for a given differentiated state. These discrete 3D structures are envisioned to develop in a hierarchical and largely irreversible manner from an omnipotent 3D structure of the zygotic genome."[1] Since then the nucleus has emerged as a biological system with an unexpectedly complex and dynamic higher order organization.[2-15] To test Günter Blobel's hypothesis further, it is necessary to explore how the 3D structure of the zygotic genome actually changes during early development. A number of groups, including ours, have made strong efforts to overcome the methodological obstacles, which have prevented detailed 3D analyses of nuclear architecture in space and time during preimplantation development of mammalian embryos.[16-22] Despite this progress, the connections between structural and functional changes of cell nuclei during development and differentiation must be counted among the great, unresolved problems of cell biology. For a comprehensive understanding of nuclear structure-function relationships it is important to decipher the rules of a dynamic higher order nuclear organization, including detailed information on changes of the nuclear architecture during development and differentiation at large, as well as positional changes of individual genes and chromosome territories (CTs). Changes of higher order chromatin arrangements correlated with transcriptional activation and silencing of genes may reflect a functional necessity of genes to adopt a nuclear environment favorable for their active or repressed state.[23,24]

As a model system we chose bovine embryos generated either by *in vitro* fertilization (IVF) or by somatic cell nuclear transfer (SCNT) of bovine fetal fibroblasts.[19,25] In bovine IVF embryos minor genome activation is already detected in 2-cell embryos, but restricted to a small number of genes.[26] In contrast, major embryonic genome activation (major EGA) affects a large number of genes and occurs at the 8-cell stage.[27] It marks the critical period when control of development is shifted from maternal to embryonic gene products and is essential for normal development.[28,29] Major EGA secures the embryo's further supply with proteins for the special needs of normal development. Several reports described the 8- to 16-cell stage of bovine preimplantation embryos as the critical window for major EGA.[30-34] A recent study based on deep RNA sequencing revealed the largest proportion of gene activation at the 8-cell stage, including the pluripotency genes *POU5F1* (previously known as *OCT4*) and *NANOG*.[27] This study was based on RNA sequencing and found that 58% of all genes activated between the 4-cell and the blastocyst stage were activated at the 8-cell stage. These genes can be classified as genes involved in major EGA. In cloned bovine preimplantation embryos the timing of reprogramming of gene expression is currently less well defined. In a previous study from our group[25] we studied the expression of a stably integrated *POU5F1-EGFP* reporter gene in cloned bovine embryos and found demonstrable EGFP fluorescence only in embryos carrying 9 and more cells. Based on this observation we tentatively assume that major EGA in *in vitro* fertilized and reprogramming of gene expression in cloned bovine embryos occurs within the same time window. For a quantitative analysis of positional changes of this pluripotency marker gene, the chromosome territory 13 harboring the transgene, as well as the homolog territory during structural reorganization of bovine fetal fibroblast nuclei in cloned early bovine embryos we refer readers to the accompanying article by Popken et al.[35]

Employing both the conventional light optical resolution of 3-dimensional confocal laser scanning microscopy (3D-CLSM) and the improved resolution of 3-dimensional structured illumination microscopy (3D-SIM), we demonstrate massive changes of the global nuclear architecture in both *in vitro* fertilized and cloned embryos passing through major EGA. With 3D-SIM we carried out an in-depth comparative analysis of nuclear landscapes in both types of bovine preimplantation embryos, as well as of nuclei from bovine fetal fibroblast cultures. We compare these landscapes with previously studied nuclear landscapes in mouse embryonic stem cells and somatic cell types from various mammalian species.[36-41] Notwithstanding major differences in the global nuclear architecture of different cell types with regard to nuclear shapes, volumes and chromatin arrangements at large, the results of all studies support the chromosome territory– interchromatin compartment (CT-IC) model of a functional nuclear architecture.[6,42,43] According to this model the IC represents an interconnected system of channels and larger lacunas. It harbors macromolecular complexes and factors necessary for transcription, splicing, replication and repair and may serve for the export of ribonucleoprotein complexes with mRNA.[6,44] IC-channels start/end at nuclear pore complexes (NPCs) and pervade the nuclear interior between ~1-Mbp chromatin domains and chromatin domain clusters (CDCs) as building blocks of CTs.[40] CDCs in turn give rise to chromosome band and arm domains yielding complete CTs, which typically form an interconnected higher order chromatin network attached to the nuclear lamina and expanding throughout the entire nuclear space.[6] At numerous sites channels expand into larger lacunas, which carry splicing speckles and other types of nuclear bodies. Electron microscopic (EM) evidence has shown that the periphery of CDCs, which lines the IC and has been termed the perichromatin region (PR), carries functionally competent chromatin, where transcription, co-transcriptional splicing, DNA replication and repair take place.[41] Evidence for the formation of nascent RNA in the PR was first provided in an EM study by Stan Fakan and colleagues, who pulse-labeled a human cancer cell line with BrUTP and demonstrated the enrichment of bromine-labeled RNA in the PR.[45,46] *In situ* hybridization with sense and anti-sense RNA probes derived from total cellular or cytoplasmic poly(A+) RNA in combination with immunoelectron microscopy demonstrated that most transcribed DNA is concentrated in the perichromatin region.[47] In another seminal EM study performed with a Chinese hamster cell line the Fakan group also observed the formation of nascent DNA within the PR.[48] Employing a pulse-chase-pulse labeling protocol with iododeoxyuridine and chlorodeoxyuridine, the authors were able to demonstrate that DNA replication was followed by movements of nascent DNA of about 100 nm into the interior of lining chromatin domains. The development of light optical super-resolution microscopy provided entirely new possibilities to investigate the 3D nuclear landscape with superior resolution.[36,37,40] These studies have led to

the view that the IC together with the PR forms an active nuclear compartment (aNC), located side-by-side with the inactive nuclear compartment (iNC), which is contributed by the core regions of the higher order CDC network.[40]

Our current study extends the aNC/iNC view of a functional nuclear landscape to nuclei studied during preimplantation development of *in vitro* fertilized and cloned embryos. Despite major differences of global architecture between pre- and post-major EGA embryos and even within the same embryo, all nuclei showed common basic features, including a highly significant enrichment of RNA polymerase II and of H3K4me3 in the peri-chromatin region. H3K4me3 is a marker for transcriptionally competent chromatin.[49] In contrast, H3K9me3 was enriched in the more densely DAPI-stained interior of chromatin domain clusters. H3K9me3 is enriched in a variety of (pericentromeric) repeats but also involved as a (mostly repressive) signature for fine tuning of expression levels at promoters, enhancers and gene bodies for large scale repression.[49] The striking similarities and differences of nuclear landscapes between fetal fibroblast nuclei and nuclei from cloned embryos provides insights into major structural events of nuclear reprogramming involved in cloning of mammals.

The following results are presented in 3 parts. In part 1 we describe nuclear landscapes from *in vitro* fertilized and cloned pre-implantation embryos observed with 3D confocal laser scanning microscopy, followed in part 2 by a comparison of the nuclear topography of DAPI-stained chromatin, H3K4me3, H3K9me3 and RNA polymerase II arrangements with the improved resolution of 3D structured illumination microscopy in such embryos, as well as in fetal fibroblasts employed for cloning. In part 3 we present a quantitative analysis of the changing frequencies of nuclear phenotypes described in part 1 and 2 and link topological chromatin density mapping of nuclear landscapes during preim-plantation development with local enrichments and depletions of H3K4me3, H3K9me3 and RNA polymerase II arrangements.

Results

Part 1. Studies of *in vitro* fertilized and cloned preimplantation embryos with 3D confocal laser scanning microscopy

Global reorganization of nuclear architecture accompanies the onset of major embryonic genome activation in in vitro fertilized and reprogramming in cloned embryos

Figure 1, Panels A1–A8 show top, midplane and bottom x/y-sections from a 3D-image stack recorded with 3D-CLSM from all nuclei of a typical IVF 8-cell embryo. In all nuclei large clusters of DAPI-stained chromatin, called major chromatin bodies (MCBs) surrounded a major lacuna with a mostly central or sometimes acentric location resulting in a markedly peripheral chromatin location. Accordingly, this nuclear phenotype was termed ENP (for Embryonic Nuclei with Peripheral chromatin location). The major lacuna did not contain detectable amounts of DAPI-stained DNA except for occasional clusters of chromatin which may represent MCBs retained in the nuclear interior during ENP formation.

Panels B1-B8 of **Figure 1** present top, midplane and bottom x/y-CLSM-sections of 8 representative nuclei from a 20-cell post-major EGA embryo. Panel B1 exemplifies one of 3 nuclei which had retained the ENP phenotype in this embryo. Panels B4-B8 are representative for 15 nuclei that had adopted a phenotype, called ENC (Embryonic Nuclei with Conventional architecture). In line with the architecture observed in numerous somatic cell types studied to date, ENCs are characterized by DAPI-stained chromatin expanded throughout the nuclear space and the absence of the major lacuna found in ENPs. The nuclear border of ENCs was marked by a rim of intensely DAPI-stained chromatin which was also observed around nucleoli. Other nuclei, termed ENP/Cs, apparently represent a transition stage between ENPs and ENCs. They contained a major lacuna, with a reduced size (Panels B2 and B3), in line with an invasion of chromatin into the nuclear interior. In ENP/Cs but not in ENPs we detected typical nucleoli, which were like nucleoli in ENCs surrounded by a rim of densely DAPI-stained chromatin (see below for further evidence).

Figure 2, Panels A1–A7, show top, midplane and bottom confocal sections from all nuclei of a cloned 7-cell bovine embryo obtained by somatic cell nuclear transfer (SCNT) of a bovine fetal fibroblast. Nuclear phenotypes in this embryo were strikingly similar to the ENP phenotype detected in *in vitro* fertilized embryos. In a cloned 25-cell embryo (**Fig. 2**, B1–B7) only one ENP persisted (Panel B1) and ENCs became the predominant phenotype (Panels B2–B7). Kinetochores, immunodetected by a kinetochore specific antibody, were strongly enriched in ENPs at the nuclear periphery with occasional exceptions of kinetochores associated with a rare chromatin cluster located inside the major lacuna. In ENCs kinetochores were distributed throughout the nuclear space, sometimes located directly beside a densely DAPI-stained chromatin cluster and sometimes at sites of modestly stained DNA (**Fig. 2**, bottom, Panels a and b). Notably, bovine chromosomes contain pericentromeric heterochromatin, which carries repetitive sequences with a high GC content.[50] The total numbers of kinetochore signals counted in 3D image stacks were consistently below the number of chromosomes ($2n = 60$) carried by a diploid bovine nucleus suggesting that signals may represent clusters of kinetochores from several spatially adjacent CTs (data not shown).

Chromosome painting experiments performed with a paint probe for BTA 13 in cloned embryos (see accompanying article by Popken et al.[35]) revealed that MCBs, isolated from each other by wide IC-channels in ENPs, represent individual CTs (**Fig. 3**, Panels B and C). In both fetal fibroblast nuclei and ENCs chromosome territories formed higher order networks expanding throughout the entire nuclear space. Accordingly, CTs could only be identified as discrete entities after chromosome painting (**Fig. 3**, Panels A and D). The striking differences of nuclear architecture between nuclei of embryos at major EGA at the 8-cell stage and nuclei of embryos both on their way toward major EGA and after major EGA are described in more detail using 3D-SIM in part 2 of Results.

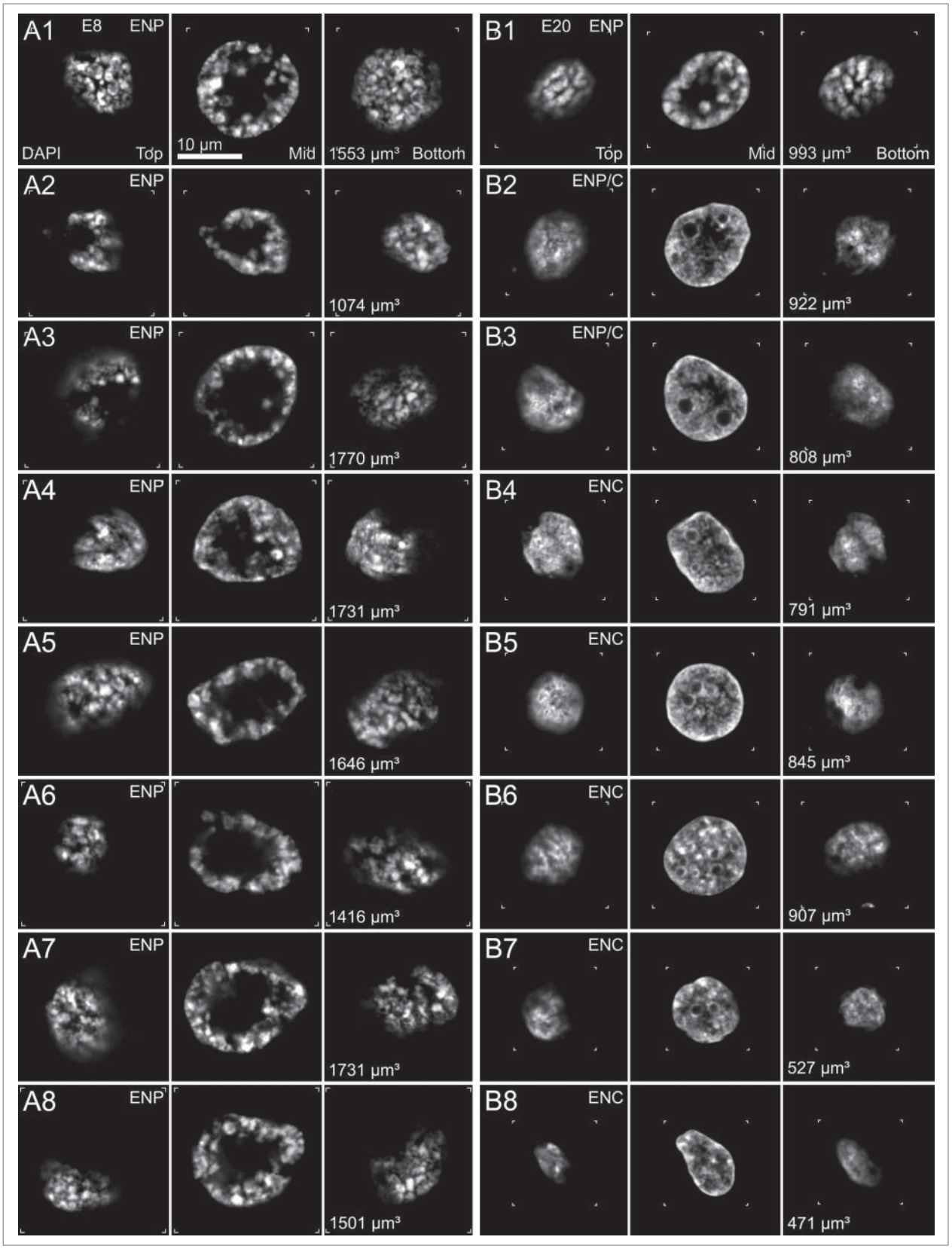

Figure 1. For figure legend, see page 559.

Splicing factors and RNA synthesis in nuclei of in vitro fertilized embryos passing through major genome activation and in cloned embryos at corresponding stages of preimplantation development

Immunostaining revealed an enrichment of the splicing factor SC-35 within the major lacuna of ENPs in IVF embryos (**Fig. 4**, Panel A), while numerous SC-35 positive splicing speckles were noted in ENCs (**Fig. 4**, Panel B). We suggest that the formation of this large lacuna represents a storage compartment for large amounts of splicing speckles and numerous other proteins and protein complexes, which help the embryo to comply with the demands of major genome activation. The expanding major lacuna may push CTs toward the nuclear periphery. *De novo* RNA synthesis was demonstrated in ENPs, ENP/Cs and ENCs of *in vitro* fertilized embryos (**Fig. 4**, Panels C–E). Strong RNA synthesis was noted in nucleoli of ENCs (**Fig. 4**, Panel E). The long labeling period with BrUTP or BrU precludes conclusions on the actual sites of nascent RNA synthesis in this experiment. The presence of bromine-labeled RNA within the major lacuna suggests movements of nascent RNA formed in peripheral MCBs into the nuclear interior. Evidence for remarkably similar patterns of RNA synthesized in ENP- and ENP/C-like nuclei as well as in ENCs of a cloned bovine embryo is presented in **Figure 4**, Panels F–I.

Since DAPI has a preference for AT-rich DNA, we considered the possibility that we missed GC-rich DNA located in the major lacuna of ENPs.[51] Staining of nuclear DNA with TO-PRO-3, a fluorescent dye without a DNA sequence preference, however, also revealed a lack of DNA in the major lacuna of ENPs except for occasional TO-PRO-3 stained chromatin clusters (**Fig. 4**, Panels A, C, G).[52] This finding argues against a major contribution of chromatin loops with GC-rich DNA extending from the nuclear periphery into its interior.

Topography of DNA replication, nucleolus development, and histone markers in nuclei of in vitro fertilized embryos passing through major genome activation

Figure 5 presents confocal midplane images recorded from ENPs, ENP/Cs and ENCs of early *in vitro* fertilized preimplantation embryos subjected to a variety of immunostainings. ENPs resembled to some extent the nuclear phenotype of cells during the G2/prophase transition. For a direct demonstration that ENPs were present in cells transversing through interphase and prophase, we treated pre-major EGA embryos with a 30-min pulse of the thymidine analog EdU and combined the immunocytochemical detection of incorporated EdU with the detection of phosphorylated H3S10, a marker strongly expressed in cells proceeding to prophase.[53] **Figure 5**, Panels A and B show ENPs from a 5-cell embryo. One of the 5 ENPs was strongly H3S10p positive and EdU negative, 4 ENPs were positive for EdU but barely showed H3S10p. As expected, ENCs presented conventional EdU pulse-labeling patterns during S-phase. For example, the ENC recorded from a 21-cell post-major EGA embryo (**Fig. 5**, Panel C) shows a pattern typical for mid S-phase with EdU labeled replication foci enriched at the nuclear periphery and around nucleoli but also noted throughout the nuclear space. **Figure 5**, Panel D exemplifies an ENP with nucleolar precursor bodies (NPBs) visualized by immunostaining of nucleophosmin B23.[54] NPBs were located at the interior side of the peripheral CTs, whereas the ENC shown in **Figure 5**, Panel E contained large nucleoli in the nuclear interior. **Figure 5**, Panels F and G, demonstrate an ENP and an ENP/C, respectively, with peripherally located major chromatin clusters, some strongly immunostained for transcriptionally competent chromatin (H3K4me3). This pattern of H3K4me3 was consistently found in ENPs of 5- to 8-cell embryos suggesting that chromatin reaches transcriptional competence prior to the 8-cell stage (**Fig. 5**, Panel F, see also part II below). It is not known yet whether MCBs strongly immunopositive for H3K4me3 in different ENPs comprise variable CTs from the entire chromosome complement or a specific subset of CTs. For comparison, **Figure 5**, Panels H–J, present typical examples of an ENP (Panel H), ENP/C (Panel I) and ENC (Panel J) from a 14-cell embryo with major chromatin clusters, which were immunopositive for H3K9me3, a histone marker for transcriptionally silent chromatin.

Major chromatin clusters will be described in more detail in part 2. We wish to make readers aware of the current lack of a generally accepted nomenclature to describe the range of higher order chromatin structures encountered at different scales of magnification. For this reason, a clarification of the terms used by us may be appropriate at this point for better comprehension of part 2 and part 3 of the present study. Major chromatin clusters may comprise a part of a single CT or a higher order structure composed from parts of several neighboring CTs with variable H3K4me3 and H3K9me3 labeling patterns, formed sometimes from modestly and sometimes from intensely DAPI-stained chromatin. As shown below, major chromatin clusters contribute to the variability, which distinguishes nuclear landscapes in *in vitro* fertilized and cloned embryos from each other and from somatic cell types, such as fetal fibroblasts used for animal cloning. Major chromatin clusters should neither be confused with major

Figure 1 (See previous page). Global reorganization of nuclear architecture during preimplantation development of *in vitro* fertilized bovine embryos studied with 3D confocal laser scanning microscopy. Panels A1–A8. Top, middle and bottom x/y-sections from image stacks of 8 DAPI-stained nuclei recorded with 3-dimensional confocal laser scanning microscopy (3D-CLSM) in an *in vitro* fertilized 8-cell embryo. All nuclei show the ENP phenotype (Embryonic Nucleus with a Peripheral chromatin arrangement; for a detailed description see Results). Panels B1–B8. Top, middle and bottom x/y-sections from representative DAPI-stained nuclei recorded with CLSM in an IVF 20-cell embryo. Panel B1 exemplifies one of 3 nuclei in this embryo with a persistent ENP phenotype. Panels B4–B8 provide examples for the nuclear phenotype, termed ENC, which was noted in 15 nuclei (Embryonic Nucleus with Conventional chromatin arrangement; for a detailed description see text). Two nuclei (Panels B2 and B3) apparently represent a transition stage between ENPs and ENCs, called ENP/C (for details see text). Bars: 10 μm in panel A1 is representative for all nuclei.

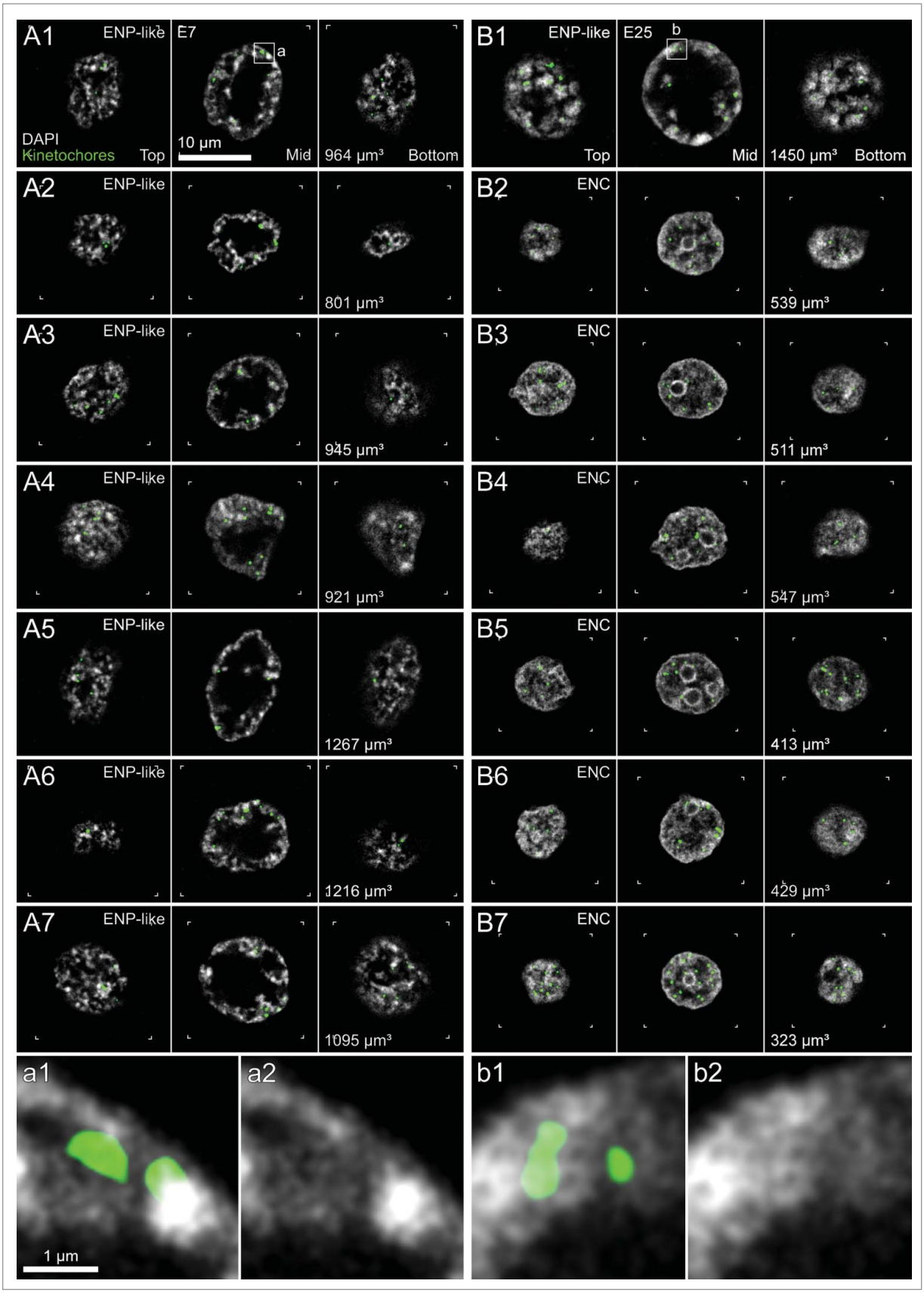

Figure 2. For figure legend, see page 561.

chromatin bodies in ENPs, representing an entire CT, nor with the much smaller chromatin domain clusters (CDCs) described in a previous study and below.[40]

Part 2.1 Nuclear landscapes in *in vitro* fertilized preimplantation embryos observed with 3D structured illumination microscopy (3D-SIM)

Compared with 3D-CLSM, 3D-SIM provides a superior resolution with an about twofold linear and eightfold volumetric improvement.[55,56] All 3D-SIM studies described below were based on over 1000 individually recorded images per nucleus. Despite its reported AT affinity we chose DAPI for DNA staining in our 3D-SIM studies because of its high photostability (tolerating the high number of exposures required for the recording of a single nucleus), its DNA specificity and spectral properties fitting to our 3D-SIM system configuration. From several dyes which we tested for this purpose, only DAPI fulfilled these requirements for our setup.[40]

The recording of high quality 3D image stacks with a high numerical aperture microscope objective is only possible from structures located very close to precision cover glasses using immersion oil with a refractory index carefully adapted after empirical testing (see also Supplementary Information: Extended Experimental Procedures). 3D-SIM is better suited for imaging of flat nuclei, such as fibroblast nuclei than for large roundish nuclei. The thickness of bovine preimplantation embryos in the order of 100 to 150 μm prevents high quality 3D-SIM studies of nuclei in structurally intact embryos. To overcome this limitation, we recorded only those nuclei from intact embryos, which were found close to the glass surface. Alternatively, we microdissected embryos into single cells, which were placed individually on appropriate, polylysine-coated glass slides for secure attachment.

The quality of SIM images is also reduced by noise originating from the Poisson distribution of the limited number of photons recorded for each image from a given immunostained structure and by a pattern of concentric rings (**Fig. 6**). To overcome this problem as best as possible, images of DAPI-stained nuclei were routinely thresholded for display with a threshold just sufficient to eliminate this pattern (**Fig. 6**).

Changes of higher order chromatin arrangements in nuclei of in vitro fertilized embryos studied with 3D structured illumination microscopy

Figure 7 shows sections from ENPs, ENP/Cs and ENCs recorded in IVF preimplantation embryos by 3D-SIM. The very large male and female pronuclei in an IVF zygote were recorded with 3D-CLSM (**Figs. 7A and B**) since they were positioned too far away from the glass surface to allow high quality imaging with 3D-SIM. Images from C to I demonstrate SIM sections from nuclei with phenotypes typical for IVF preimplantation embryos with increasing cell numbers: pre-ENPs from 2- and 4-cell embryos (C and D), an ENP from an 8-cell embryo (E) and ENCs from an embryo with 16 cells (F), a morula with around 30 cells (G) and the inner cell mass (H) and trophectoderm (I) of a blastocyst. Panels J–Q present midplane x/y-SIM sections (above) and x/z-SIM sections (below) from all nuclei of an 8-cell *in vitro* fertilized embryo. Seven nuclei (J–P) clearly show the major lacuna and peripheral localization of major chromatin bodies, characteristic for the ENP phenotype. One nucleus (Q) reveals major chromatin bodies isolated from each other by wide IC-lacunas, but lacks a major lacuna. **Supplementary Figure S1**, Panels A-H show the same DAPI stained nuclei in combination with immunostaining of H3K4me3. In line with findings described above (**Fig. 5**, Panel F), some MCBs were strongly immunostained, others modestly or weakly. For a more detailed inspection of the arrangements of DAPI-stained chromatin **Figures 7R1–10** provide midplane SIM sections from embryonic nuclei at higher magnification recorded from *in vitro* fertilized embryos prior, during and after major genome activation. Two nuclei from 4-cell embryos exemplify Pre-ENP phenotypes (R1, R2) with clustered chromatin still distributed throughout the nuclear interior. Two nuclei (R3, R4) exemplify transition stages from the pre-ENP to the ENP phenotype. Two nuclei from IVF 8-cell embryos represent typical ENPs (R5, R6) with a fully developed major lacuna and peripheral MCBs/CTs, isolated from their neighbors by wide IC-channels. Nuclei recorded from embryos after major genome activation represent examples of ENP/Cs (R7, R8) and ENCs (R9, R10), where a higher order chromatin network expanded throughout the entire nucleus. Typical nucleoli, surrounded by a rim of intensely DAPI-stained chromatin became apparent in ENP/Cs, but were absent in most nuclei of embryos prior to major genome activation. The improved resolution of 3D-SIM further revealed small chromatin domain clusters (CDCs) pervaded by numerous smaller IC-channels in these example nuclei, independent of their specific phenotype (compare the enlarged boxes a-c in R5, R6, R7 and R10). Supplementary Movies provide through view videos of 3D-SIM serial sections through DAPI-stained nuclei with typical phenotypes (movie 1: ENP (R4); movie 2: ENP (R6); movie 3: ENP/C (R8); movie 4: ENC (R10). **Figure 7S** provides a set of nuclear volume measurements based on 3D nuclear image stacks recorded with CLSM or 3D-SIM from *in vitro* fertilized embryos advancing from the 4-cell stage to >18 cells. Nuclei recorded in embryos consisting

Figure 2 (See previous page). Global reorganization of nuclear architecture during preimplantation development of cloned bovine embryos studied with 3D confocal laser scanning microscopy (3D-CLSM). Panels A1–A7. Top, mid and bottom x/y-sections from image stacks of 7 DAPI-stained nuclei recorded with 3D-CLSM in a cloned 7-cell embryo. All nuclei show an ENP-like phenotype (compare **Fig. 1**, Panels A1-A8). Panels B1–B7. Top, mid and bottom x/y-sections from representative DAPI-stained nuclei recorded with CLSM in a cloned 25-cell embryo. One nucleus (Panel B1) has retained the ENP phenotype. The other nuclei (Panels B2–B7) represent the ENC phenotype (compare **Fig. 1**, Panels B4–B8). Nucleoli surrounded with dense chromatin were noted in all ENCs but not in ENPs. Green signals in all Panels represent immunostained kinetochores. Enlarged views from boxed areas in Panels A1 and B1 with kinetochores are shown at the bottom of this Figure (Panels a and b). Note the location of kinetochore clusters in modestly DAPI-stained areas. Bars: 10 μm in panel A1 applies to all Panels A1-7 and B1-7; 1 μm for enlarged boxes a1/a2, and b1/b2.

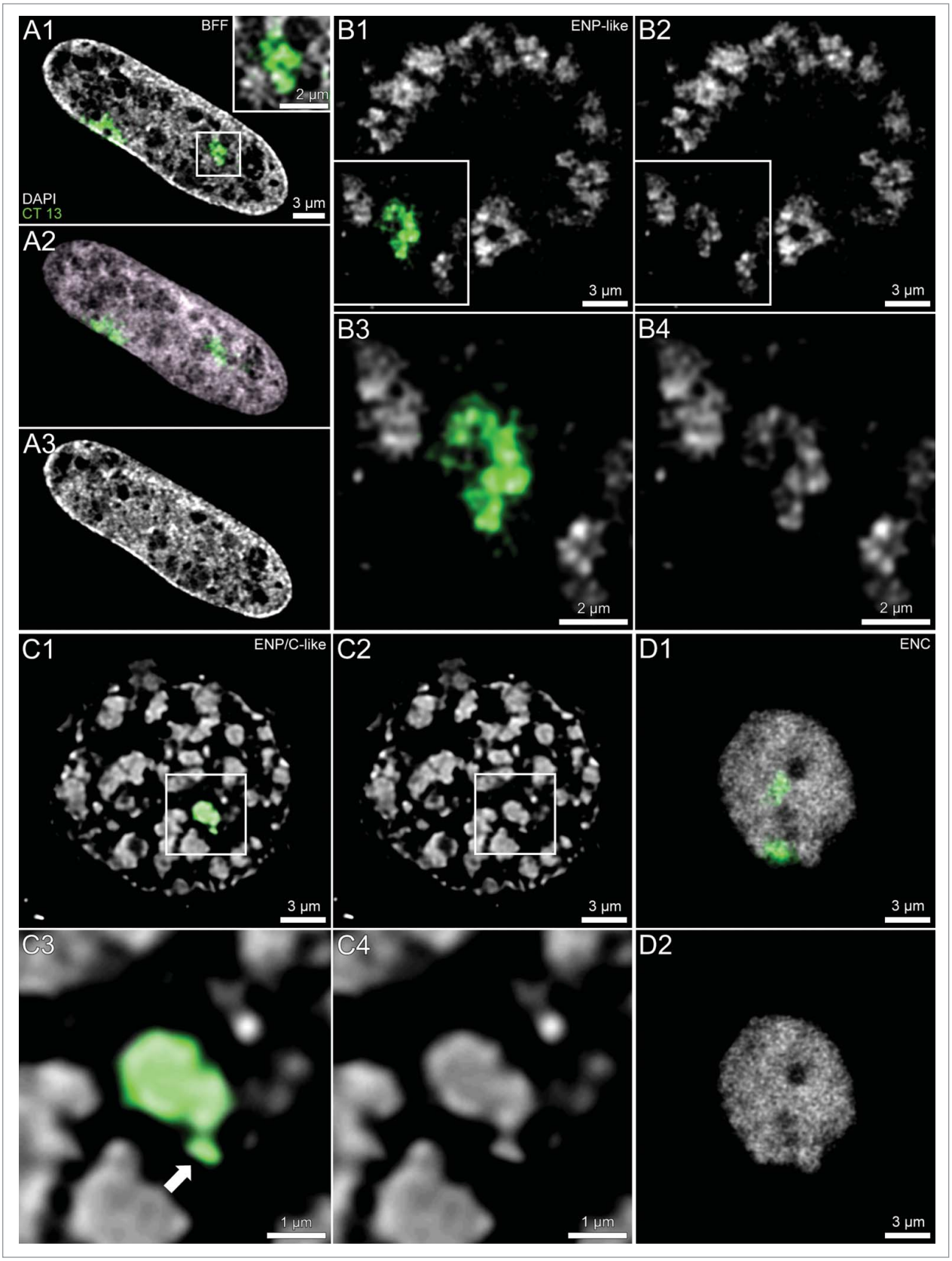

Figure 3. For figure legend, see page 563.

of 4 cells and 5–8 cells, respectively, did not show a significant difference of mean nuclear volumes ($p = 0.4$), whereas a highly significant volume decrease was detected for embryos with 5–8 cells advancing to 9–17 cells (passing through major EGA) ($p < 0.006$) and beyond (>18 cells) ($p < 0.0003$) indicating that volumes of ENCs with complete structural reconfiguration were highly significantly smaller than pre-ENPs, ENPs and ENP/Cs ($p < 10^{-6}$). Although the pronounced inter-cell variability of nuclear volumes for ENPs, ENP/Cs and ENCs may in part reflect fixation of cells at different stages of interphase, volume comparisons between nuclei classified as ENPs in 5- to 16-cell embryos with nuclei classified in embryos with more than 18 cells revealed a highly significant decrease of the mean nuclear volume of the latter ($p < 10^{-4}$). In contrast, the volumes of ENP/Cs did not differ significantly from the volumes of typical ENPs ($p = 0.08$), suggesting that the disappearance of the major lacuna was not simply enforced by nuclear volume reduction.

Nucleolus development and characterization of chromatin surrounding nucleoli during early preimplantation development of in vitro fertilized embryos studied with 3D structured illumination microscopy

As already noted in the preceding 3D-CLSM study (**Fig. 5**, Panel D), nucleolar precursor bodies lacked the rim of intensely DAPI-stained chromatin, noted as a typical feature of nucleoli in ENP/Cs and ENCs. Small precursor bodies in ENPs were entirely positive for nucleophosmin B23, whereas larger precursor bodies and mature nucleoli were characterized by a peripheral rim of B23. Based on the higher resolution of 3D-SIM, **Figure 8** provides further insights into the constitution of chromatin surrounding nucleoli. **Figure 8**, Panel A, shows an ENP with a particularly large nucleolar precursor or early nucleolus, which shows the peripheral B23 staining but lacks an intensely DAPI-stained rim. The typical "perinucleolar heterochromatic rim" harbors centromeric repeats and silenced (rRNA) genes and is enriched in repressive chromatin marks such as H3K9me3 and H3K27me3 and depleted in active marks such as H3K4me3.[57-59] ENP/Cs in contrast revealed heterogeneous patterns (**Fig. 8**, Panels B–E). Some rims revealed areas of strong H3K4me3 staining (Panels B and C), whereas others showed strong H3K9me3 staining (Panel E) or a mixture of H3K4me3 and H3K9me3 staining at different parts of the rim (Panel D). It may be speculated that H3K4me3 enriched perinucleolar chromatin represents (rRNA) genes poised for transcription.

Activation of ribosomal genes during preimplantation development of in vitro fertilized embryos

Figure 9 presents an evaluation of reads of intronic sequences from 83 genes coding for ribosomal proteins based on our recent transcriptome analysis of bovine oocytes and fertilized preimplantation embryos.[27] We calculated the ratio of intronic reads to intronic positions not covered by reads (RINP). This parameter can be used to detect embryonic activation of specific genes based on the presence of incompletely spliced primary transcripts, whereas maternal transcripts stored in oocytes are mostly spliced and thus have a significantly lower RINP value. In line with the formation of fully active nucleoli at the 8-cell stage, this analysis provided evidence for activation of expression of 61 genes coding for ribosomal proteins during early embryonic development, including 9 genes at the 4-cell stage, 47 genes at the 8-cell stage, 4 genes at the 16-cell stage, and 1 gene at the blastocyst stage. Columns in **Fig. 9** show average values of RINP for the entire pool of ribosomal protein genes. The 4-cell stage did not show a significant increase in the average RINP value in comparison with oocytes ($p = 0.3$). In contrast, a comparison between the 4-cell stage and the 8-cell stage indicates a massive and highly significant increase ($p < 0.001$) of the fraction of RNA synthesis provided on average by genes for ribosomal proteins in transcriptomes and a further rise at the 16-cell ($p < 0.001$) and blastocyst stage ($p < 0.001$). This finding is in line with the observation that typical nucleoli with intense RNA synthesis appear mostly in ENP/Cs after major genome activation, but are rarely observed in ENPs, which carry nucleolar precursor bodies or early nucleoli not yet surrounded by a rim of concentrated chromatin (compare (**Fig. 4**, Panels C, D, E, G, H, I; **Fig. 5**, Panels D and E; **Fig. 8**). The data, however, do not provide information on the average total amount of RNA synthesized from these genes per embryo or per cell at each stage.

RNA polymerase II, H3K4me3 and H3K9me3 arrangements in nuclei of in vitro fertilized preimplantation embryos

Figure 10, Panel A shows a midplane SIM section of a nucleus after immunodetection of H3K4me3 and RNA polymerase II, carrying a phosphorylated serine at position 5 (RNA polymerase II-S5p) of its C-terminal domain. This large nucleus was recorded in a 6-cell embryo and showed features of nuclei approaching the full ENP phenotype. It shows a central major lacuna surrounded by peripherally located, DAPI-stained chromatin peppered with RNA polymerase II clusters. In comparison with major chromatin bodies noted in fully developed ENPs at the 8-cell stage, chromatin appeared still more dispersed and individual MCBs separated by wide IC-channels could not yet be detected (compare **Figure 7**, panels J–Q, R5, R6). **Figure 10**, Panel B provides a typical example for the topography of H3K4me3 and RNA polymerase II-Ser5p in ENCs. In line with the distribution of a DAPI-stained higher order chromatin network focal signals of both RNA polymerase II and H3K4me3 are dispersed throughout the nuclear space. Boxed areas in the ENP (panel A) and ENC (Panel B) are shown as enlarged images (A1, A3, A5, A7 and B1, B3, B5, B7) on the right side of

Figure 3 (See previous page). Comparison of painted chromosome territories in nuclei of bovine fetal fibroblasts and cloned embryos. Panels A–D. Midplane nuclear sections from imaging stacks recorded with CLSM from a bovine fetal fibroblast nucleus (panel A), an ENP (panel B), an ENP/C (panel C) and an ENC (panel D) from cloned embryos after 3D-FISH with a BTA 13 paint probe (green). Chromosome painting demonstrates that individual CTs 13 correspond to individual major chromatin bodies (MCBs) with variable configurations, occasionally including nearby chromatin clusters (arrow). Three further MCBs painted with the BTA 13 probe were detected in other light optical sections from this nucleus (see Supplementary **Fig. S1** in accompanying article by Popken et al.[35]). Bars: 3 μm for A1–3, B1, B2, C1, C2, D1, D2; 2 μm for the enlarged box in A1 and for B3, B4; 1 μm for C3, C4.

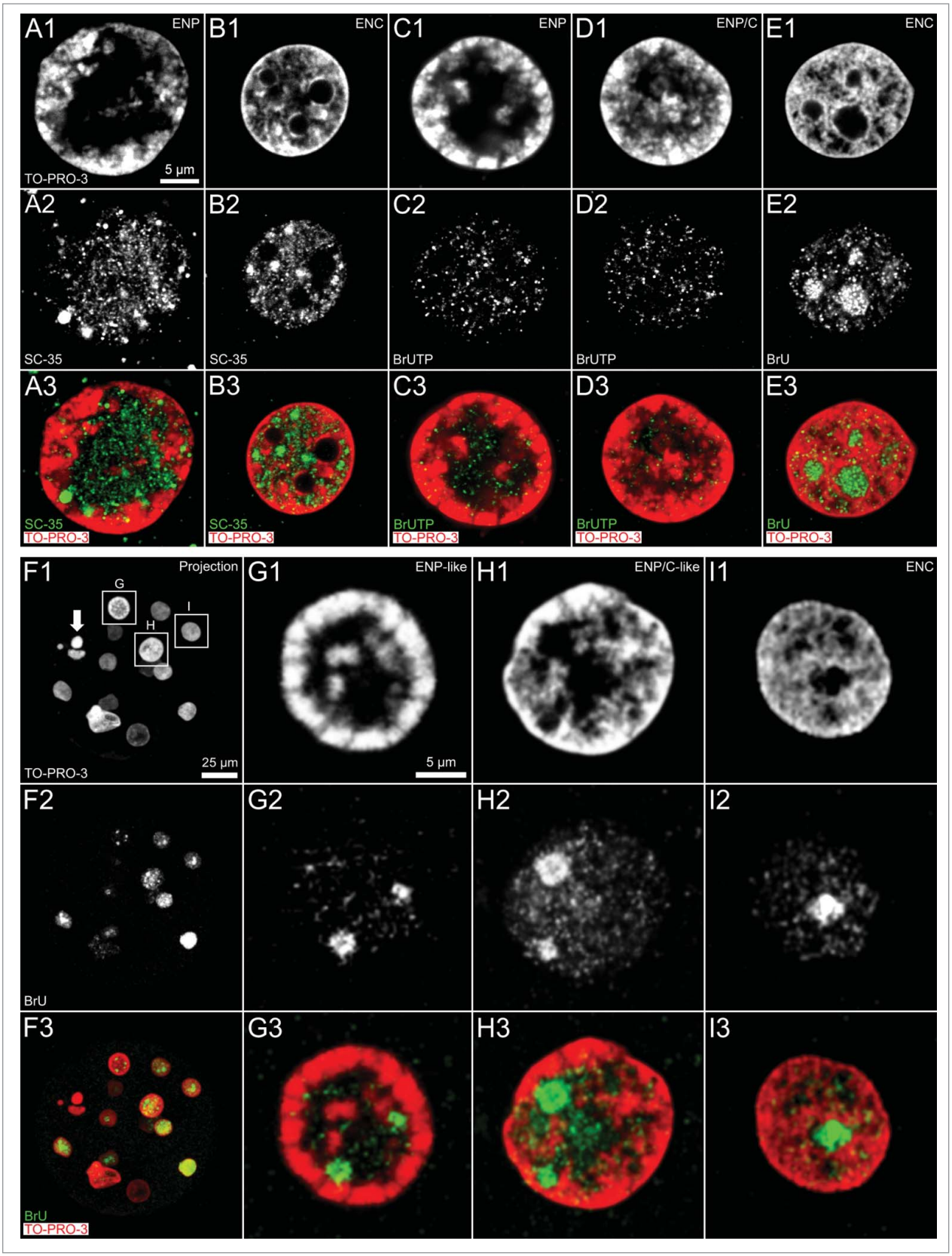

Figure 4. For figure legend, see page 565.

Figure 10. Boxes framed in these enlarged images are further enlarged in images A2, A4, A6, A8 and B2, B4, B6, B8 to provide insight into the topographical relationships of DAPI-stained chromatin, H3K4me3 and RNA polymerase II at the level of individual pixel clusters representing DAPI positive, RNA polymerase II and H3K4me3 signals. Although we noted occasional spatial overlap between RNA polymerase II clusters and H3K4me3 labeled chromatin (see black pixels in **Figures 10** A7, A8 and B7, B8), numerous RNA polymerase II foci were observed without demonstrable contact to H3K4me3 positive chromatin suggesting that RNA polymerase II-S5p foci were either formed prior to their spatial association with transcriptionally competent chromatin or persisted after their spatial dissociation from transcribed chromatin.[60]

It should be noted that the choice of a threshold necessary to distinguish between background and true signals inevitably reflects to some extent a subjective decision. Our choice was based on the rationale that we expected little, if any true signal for RNA polymerase II or epigenetic marks outside the nucleus. Accordingly, the threshold was set with the goal to maintain signal inside the nucleus, while decreasing presumptive background outside the nucleus. The size and abundance of immunopositive RNA polymerase II and H3K4me3 signals was affected by the choice of a low, medium or high threshold (**Supplementary Figs. S2 and** S3). For each threshold, however, we noted a preferential localization of both markers at the periphery of chromatin domain clusters. For a quantitative assessment of the topography between higher order chromatin arrangements and the localization of RNA polymerase II, H3K4me3 and H3K9me3 see Part 3 below.

Next, we used 3D-SIM to analyze nuclear arrangements of epigenetic marks of transcriptionally competent (H3K4me3) and silent chromatin (H3K9me3), respectively, with regard to the arrangements of DAPI-stained DNA in ENPs and ENCs of IVF embryos. Striking changes in the patterns of these epigenetic marks were observed during ENP-ENP/C-ENC transitions of nuclei in embryos passing major genome activation. In typical ENPs (**Fig. 11**, Panel A) some MCBs were predominantly labeled with H3K4me3, others with H3K9me3, whereas still others showed only sparse evidence for the presence of either marker. H3K4me3 was frequently extended directly to the nuclear border. **Figure 11**, Panel B, presents an ENP/C at an early stage of post-major EGA structural transformation. Inspection of 3D-SIM image stacks revealed nucleoli surrounded by a rim of densely DAPI-stained chromatin in this ENP/C (see box c in **Figure 11** B2). **Figure 11**, Panel C, shows an example of the arrangements of H3K9me3 and H3K4me3 marked chromatin typical for ENCs. Large H3K9me3 positive chromatin clusters were maintained in the interior of ENCs, whereas large H3K4me3 clusters had mostly disappeared. In further contrast to ENPs, H3K4me3 was barely detected at the nuclear border but nearly exclusively restricted to the nuclear interior. Several boxed areas in these nuclei are enlarged in the images on the right side of **Figure 11** (Panels A, B, D, E, G, H) and provide insight into the topographical relationships of DAPI-stained chromatin, H3K4me3 and H3K9me3, employing the highest informative magnification possible. For comparison, images A1, B1, D1, E1, G1 and H1 represent only the DAPI-stained chromatin, whereas images A2, B2, D2, E2, G2 and H2 add H3K4me3 and H3K9me3 positive pixels, displayed without an attempt to distinguish between pixel intensities. We noted a nearly complete, mutual exclusion of chromatin clusters marked by H3K4me3 and clusters marked by H3K9me3. For further details see legend to **Figure 11**.

Part 2.2. Nuclear landscapes in fibroblasts and cloned preimplantation embryos observed with 3D structured illumination microscopy

Higher order arrangements of DAPI-stained chromatin studied by 3D structured illumination microscopy in bovine fetal fibroblast nuclei and cloned embryos

Next we employed 3D-SIM for a comparison of nuclear landscapes in bovine fetal fibroblasts and cloned embryos (**Fig. 12**). Our observations confirm and expand observations made with 3D-CLSM (compare **Figs. 1 and 2**). Changing nuclear landscapes during preimplantation development of cloned bovine embryos show striking similarities with the landscapes described above for *in vitro* fertilized embryos but also notable differences. The flat-ellipsoidal shape of bovine fetal fibroblast nuclei (**Fig. 12**, Panels A1 to A8) was transformed into a roundish shape in all nuclei of the cloned 8-cell embryo shown in (**Fig. 12**, Panels B1 to B8. Compared with bovine fetal fibroblast nuclei, visual inspection of nuclei in this embryo also suggested a more pronounced clustering of chromatin with a corresponding increase of the IC, including a major, sometimes irregularly shaped lacuna, which clearly exceeded the size of the largest IC-lacunas noted in fetal fibroblast nuclei, but which was generally smaller than major lacunas discovered in *in vitro* fertilized 8-cell embryos (compare **Figures 1 and 2**; **Figure 12** B1 to B8; **Supplementary Figure S1**). IC-lacunas in bovine fetal fibroblast nuclei should not be confused with their large, irregularly shaped nucleoli stained with B23 (**Fig. 12** A1, A3, A5, A7). Roundish nuclei

Figure 4 (See previous page). Arrangements of splicing speckles and *de novo* synthesized RNA in nuclei of *in vitro* fertilized and cloned embryos. Panels A and B. Midplane sections recorded by 3D-CLSM in an ENP (panel A) and an ENC (panel B) from IVF embryos stained with TO-PRO-3 DNA (red) show the enrichment of the splicing factor SC-35 (green) in splicing speckles both in the major lacuna of the ENP and distributed throughout the interchromatin compartment of the ENC. Panels C–E. Immunocytochemical detection of bromine-labeled RNA after incubation for 45 minutes with BrUTP or BrU precursors. Panel F. Projection of a confocal image stack from a 15-cell cloned embryo stained with TO-PRO-3 (red) following 45 minutes incubation with BrU shows nuclei with strikingly different phenotypes, including a pyknotic nucleus (arrow). Note that the visibility of all nuclei in this projection is precluded by nuclear overlays. Panels G–I. Enlarged views of nuclei, framed in F1 by boxes G, H and I, include an ENP-like nucleus (G), an ENP/C-like nucleus (H) and an ENC (I) (for definition of these nuclear phenotypes see Results and compare **Figs. 1 and 2**). These Panels also present evidence for *de novo* RNA synthesis in nuclei of this cloned embryo independent of differences between nuclear phenotypes. Note strong RNA synthesis in nucleoli of ENCs of both fertilized (panel E) and cloned embryos (panel I). Bars: 5 μm in A1 representative for Panels A–E, 25 μm in Panel F; 5 μm in G1 for Panels G–I.

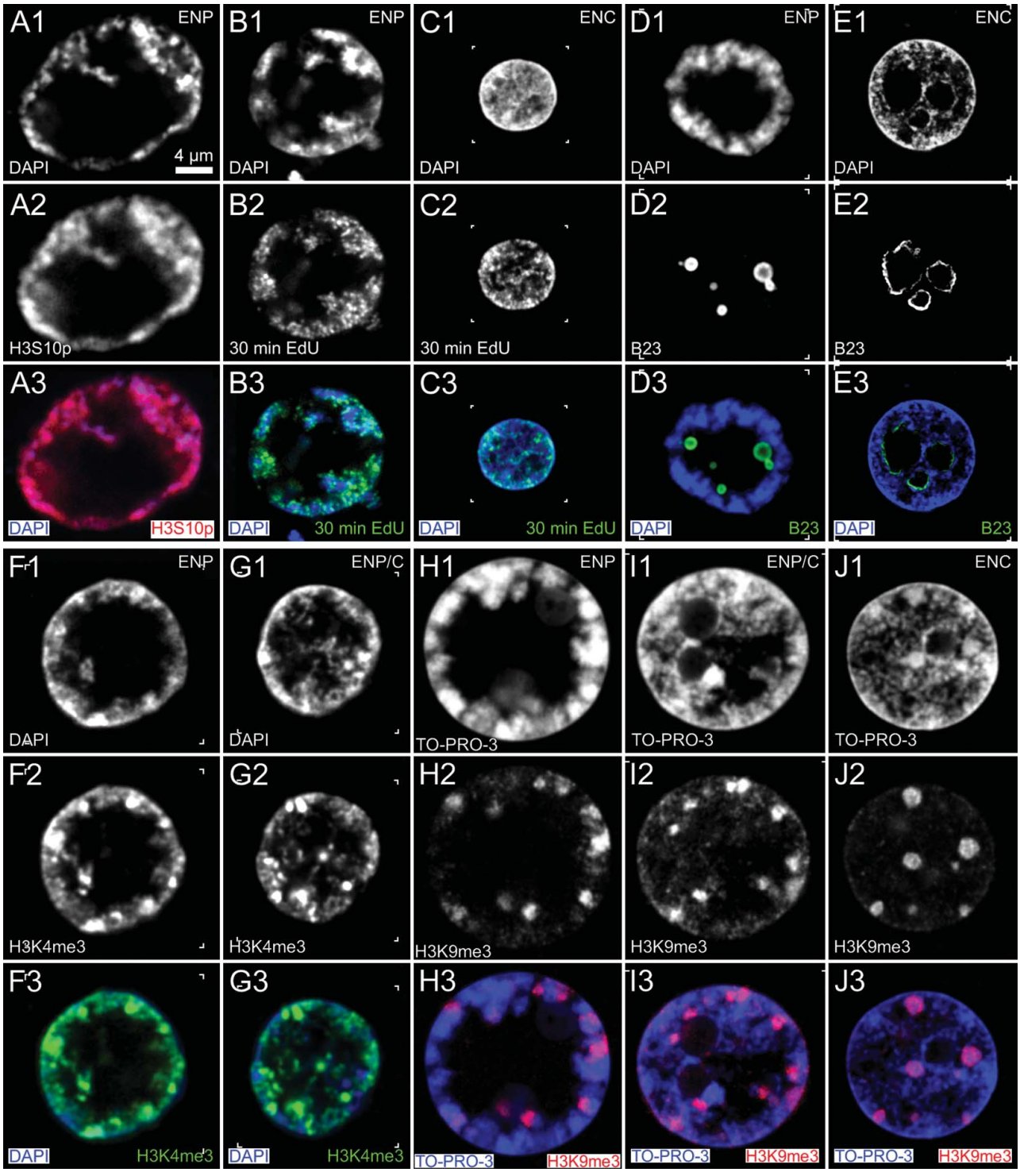

Figure 5. Representative confocal midplane sections demonstrate essential features of ENPs and ENCs in *in vitro* fertilized embryos. Panel A. ENP at G2/prophase, characterized by strong immunostaining of H3S10p. Panel B. ENP in S-phase, characterized by pulse-labeling (30 min) of replication foci with EdU. Panel C. EdU pulse labeling pattern of a typical ENC in mid S-phase. Panel D. ENP with several nucleolar precursor bodies (NPBs), immunostained with the nucleolar marker B23. Panel E. Large nucleoli lined with B23 in the interior of an ENC. Panels F, G. ENP (F) and ENP/C (G) with positive H3K4me3 immunostaining of chromatin, clearly enriched in some MCBs (compare Supplementary **Fig. S1**). Panels H, I, J. Immunocytochemical detection of H3K9me3 in an ENP (H), an ENP/C (I) and an ENC (J). Bar: 4 µm in A1 representative for all Panels.

with a major lacuna were classified as ENP-like. Occasional nuclei presented small, round nucleoli with an intensely stained rim of DAPI-stained DNA (see **Figure 12,** B5 for example). This nucleolar phenotype resembled nucleoli noted in nuclei of *in vitro* fertilized embryos but was starkly different from the very large, irregularly shaped nucleoli in fetal fibroblast nuclei, indicating a major structural reconfiguration of such nucleoli in cloned preimplantation embryos. At this point, we do not know whether nucleoli carried by the fibroblast nucleus are dissolved and replaced by new nucleoli emerging during major genome activation of cloned embryos. For comparison, **Figure 12** C1–4 and D1–4 show 8 nuclei from trophectodermal cells recorded by 3D-SIM from a non-hatched (C1–4) and a hatched (D1–4) cloned blastocyst fixed at day 8. Large nucleoli, resembling nucleoli of bovine fetal fibroblasts with an irregularly shaped rim of DAPI dense DNA, were frequently seen in nuclei of cloned blastocysts and the large majority had adopted a typical ENC phenotype with higher order chromatin networks expanding throughout the nuclear space. A comparison of volumes of bovine fetal fibroblast nuclei with nuclei from cloned embryos shows a several-fold mean volume increase of embryonic nuclei, when embryos approached

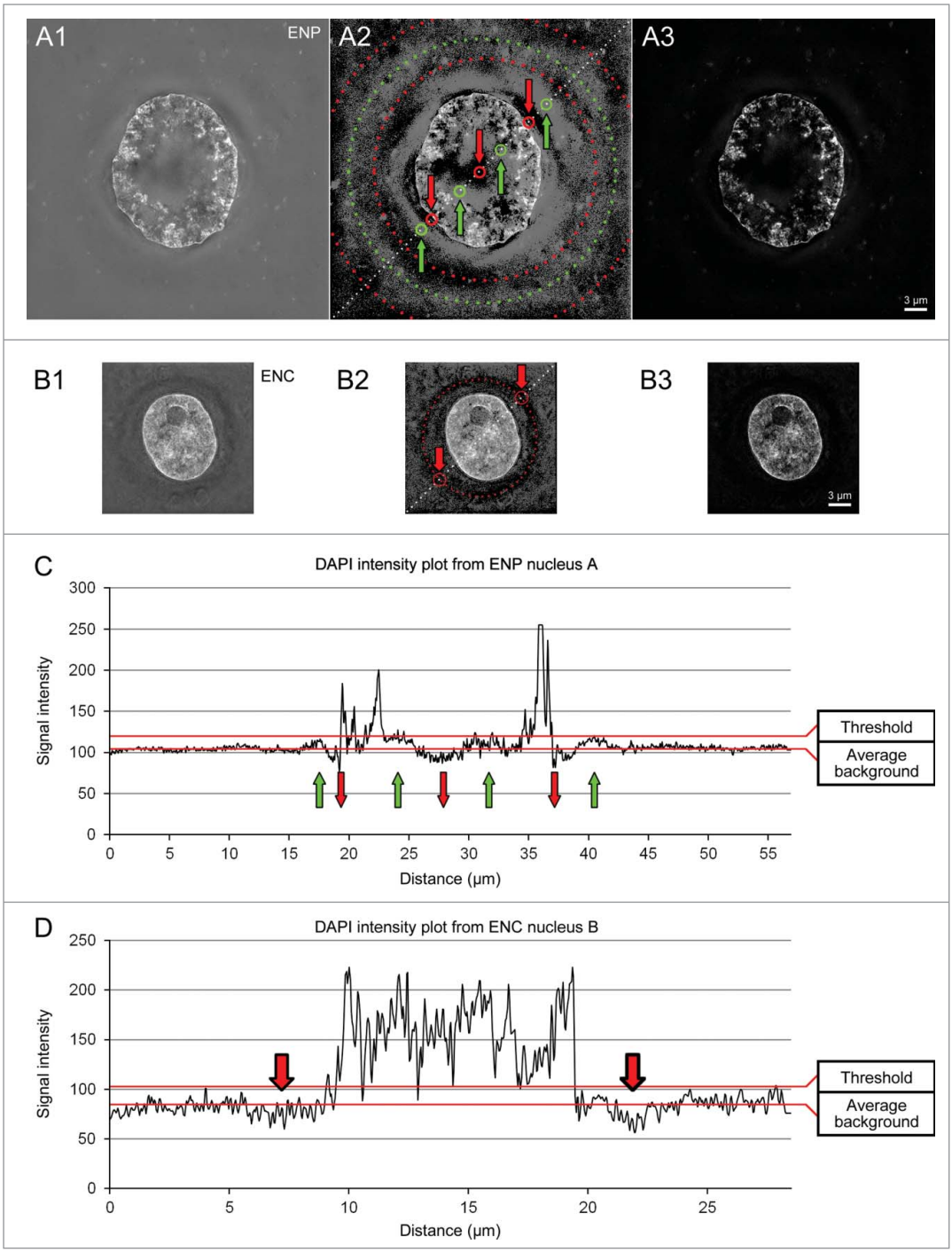

Figure 6. Problems and consequences of image thresholding in 3D structured illumination microscopy. Mid-plane SIM sections from a DAPI-stained ENP (panel A) and an ENC (panel B) without any threshold (A1, B1) and after application of a moderate threshold (A2, A3 and B2, B3). Contrast and brightness of images A2, B2 was chosen to emphasize a pronounced pattern of concentric rings, which represents an artifact of structured illumination microscopy. C and D. DAPI intensity profiles recorded along dashed lines in A2 and B2. Maintenance of these patterns in unthresholded images resulted in erroneous local increases (A2, C, green dotted line, circles and arrows) or decreases (A2, B2, C, D, red dotted line, circles and arrows) of DAPI intensities. Application of a threshold just above average background (C and D) largely removed the cocentric-ring like patterns, but at the expense that part of the real DAPI signal was also lost (A3, B3). See Supplementary **Figures S2 and S3** for problems and consequences of threshold application to immunostained signals. Bars: 3 µm in A3 representative for all Panels.

major genome activation at day 2 after SCNT, followed by a strong volume reduction during post-major EGA development at day 4 (accompanying publication Popken et al.[35]).

A comparison of all nuclei from the 2 cloned 8-cell embryos shown in **Figs. 2 and 12** emphasizes the pronounced variability of nuclear phenotypes in different cloned embryos with identical cell numbers. Whereas all nuclei of the cloned embryo presented in **Fig. 2** show – in close correspondence with ENPs of the *in vitro* fertilized embryo in **Figure 1** – a major lacuna, surrounded by compact and well demarcated major chromatin bodies, nuclei of the cloned embryo in **Figure 12** failed to show this complete ENP morphology, although most nuclei presented an ENP-like phenotype. The more pronounced variability of nuclear landscape changes during the development of cloned embryos may reflect problems of a proper structural remodeling of bovine fetal fibroblast nuclei, as well as the higher frequency of chromosomal

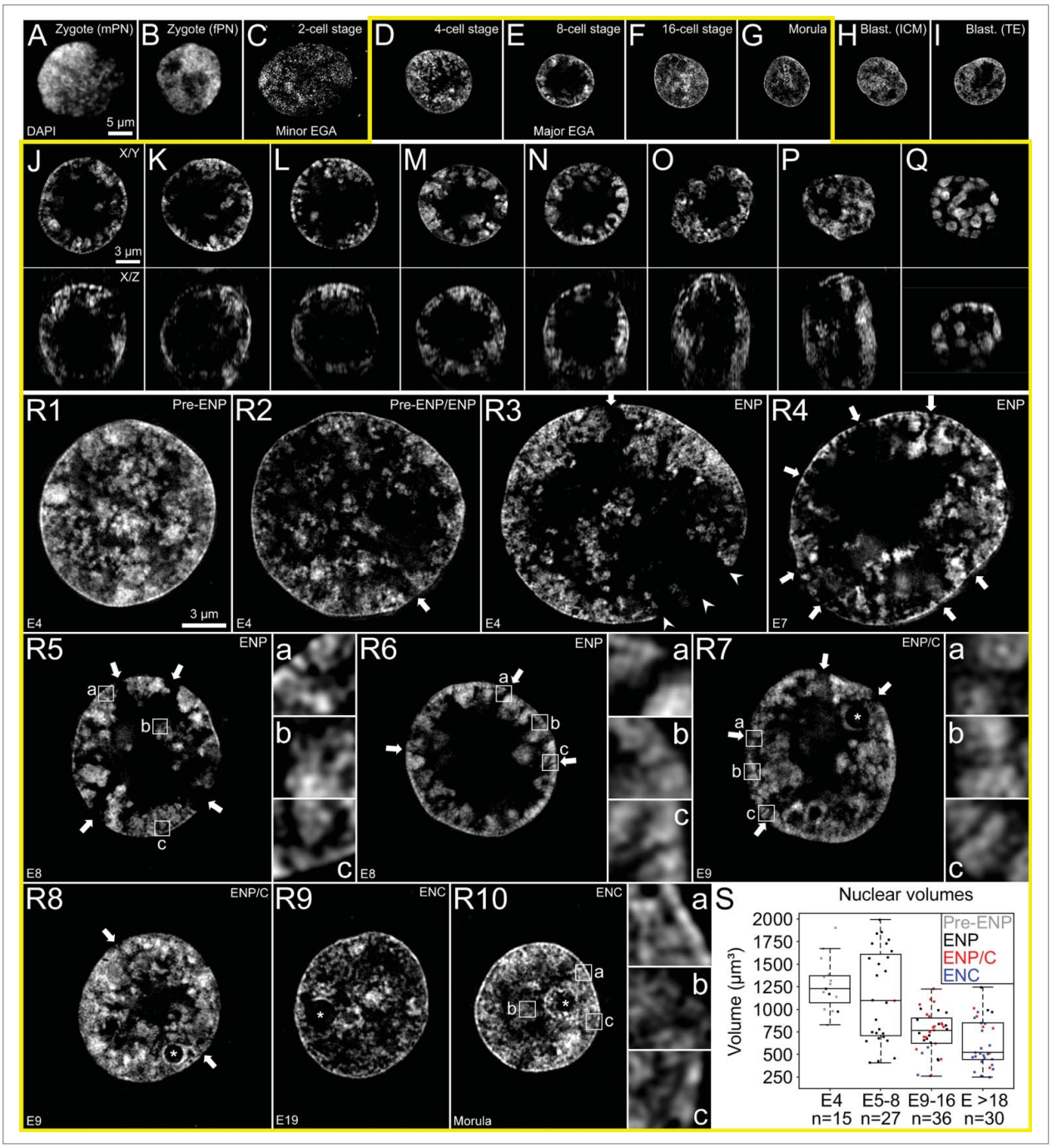

Figure 7. For figure legend, see page 569.

missegregation events during early preimplantation development of cloned versus *in vitro* fertilized embryos (accompanying article by Popken et al.[35]).

H3K4me3, H3K9me3 and RNA polymerase II arrangements in fetal fibroblast nuclei

Fig. 13 presents typical SIM midplane sections of DAPI-stained bovine fibroblast nuclei together with immunostainings of H3K4me3 (green) and nucleophosmin B23 (red) (Panel A), of H3K4me3 and RNA polymerase II-Ser2p (red) (Panel B) and of H3K4me3 and H3K9me3 (red) (Panel C). H3K4me3 labeled chromatin appeared dispersed throughout the nuclear interior. This epigenetic mark was enriched in chromatin lining IC-lacunas together with RNA polymerase II (Panels A/a and B/b) but not detected in the interior of nucleoli (Panel A) and only occasionally noted in the layer of intensely DAPI-stained DNA contacting the nuclear lamina. In addition to dispersed H3K9me3 labeled chromatin, we observed large H3K9me3 positive major chromatin clusters (Panels C/c/d). They often revealed a rim, which was intensely DAPI and H3K9me3 stained (c1, d1). These clusters may represent chromocenters and should not be confused with major chromatin bodies, which likely represent CTs (see above).[61] Notably, H3K4me3 labeling inside and outside these clusters had approximately the same intensity, whereas RNA polymerase II-Ser2p was absent inside these clusters (b2). The variation of the intensity of H3K4me3 signals inside and outside these clusters was more pronounced in cloned blastocysts (see below). The intensely DAPI-stained rims of these clusters were generally connected to the intensely DAPI-stained chromatin beneath the nuclear envelope. Clusters located in the nuclear interior were connected to the nuclear border by a highly concentrated chromatin bridge (yellow boxes in B2/B4). Lining of fibroblast nucleoli with B23 was interrupted at sites, where major chromatin clusters were in direct contact with nucleoli (a2).

H3K4me3, H3K9me3 and RNA polymerase II arrangements in nuclei of cloned preimplantation embryos

Fig. 14 shows midplane SIM sections of 2 nuclei from a cloned 8-cell embryo (Panels A and B) and 2 nuclei from a cloned, hatched blastocyst (Panels C and D) and exemplifies topographical relationships between DAPI-stained chromatin (gray), H3K4me3 (green) and H3K9me3 (red), which were typically noted in ENP-like and ENP/C-like nuclei (Panels A and B) and in ENCs (Panels C and D). The 4 representative nuclei show prominent major chromatin clusters, all prominently labeled with H3K9me3, but some of them intensely, others only modestly stained with DAPI (for examples see Panels a to h). In intensely DAPI-stained major chromatin clusters seen in ENP- and ENP/C-like nuclei we noted very little H3K4me3 label, whereas in modestly DAPI-stained clusters additional H3K4me3 labeling appeared more pronounced (compare DAPI intensities with chromatin clusters in Panel c). Intensely DAPI-stained major chromatin clusters observed in ENCs of the cloned, hatched blastocyst showed little H3K4me3 label. In remarkable contrast, however, weakly DAPI-stained major chromatin clusters showed a strong enrichment of both H3K4me3 and H3K9me3 (compare DAPI intensities with chromatin clusters in Panel h).

Figure 15 shows SIM midplane sections recorded in 2 ENP-like nuclei from a cloned, DAPI-stained 8-cell embryo with immunostaining of H3K4me3 and RNA polymerase II-Ser2p (Panels A and B), as well as 2 nuclei from a non-hatched cloned blastocyst (Panels C and D). Enlarged images of boxed areas in these nuclei (Panels a-h) demonstrate an enrichment of RNA polymerase II together with H3K4me3 in chromatin lining IC-lacunas, in line with observations described above for fetal fibroblast nuclei (**Fig. 13**, Panels B/b), as well as for ENPs and ENCs of *in vitro* fertilized embryos (**Fig. 10**). The observation of major chromatin clusters strongly labeled with H3K4me3 but not with RNA polymerase II in the ENC of the cloned, non-hatched

Figure 7 (See previous page). Nuclear phenotypes in *in vitro* fertilized preimplantation embryos studied with 3D structured illumination microscopy. A–I. Midplane sections from typical DAPI-stained nuclei recorded with 3D-SIM at different preimplantation stages, male pronucleus from a zygote (A), female pronucleus from the same zygote (B), 2-cell stage (C), 4-cell stage (D), 8-cell stage (E), 16-cell stage (F), morula (G), and blastocyst (H from inner cell mass (ICM) and I from trophectoderm (TE)). The 2 pronuclei in a zygote were recorded with 3D confocal laser scanning microscopy (3D-CLSM) due to their distance to the cover glass. J–Q. Top row: Midplane-SIM sections from all DAPI-stained nuclei recorded in an IVF 8-cell embryo. Bottom row: Corresponding x/z-sections. With rare exceptions nuclei have a roundish shape and show the ENP phenotype (for definition see Results and **Fig. 1**). R1-R10. Midplane SIM sections present typical phenotypes of DAPI-stained nuclei at higher magnification taken from embryos with 4 cells (R1 – R3), 7 cells (R4), 8 cells (R5, R6), 9 cells (R7, R8), 19 cells (R9) and a morula with about 32 cells (R10). These nuclei were classified as pre-ENP (R1), transition state from the pre-ENP phenotype to ENP phenotype (R2) or early ENPs (R3, R4), fully developed ENPs (R5, R6), ENP/Cs (R7, R8), and ENCs (R9, R10). Typical nucleoli surrounded by intensely DAPI-stained chromatin (examples marked by asterisks in R7 – R10) were typically noted in ENP/Cs and in all ENCs. Arrows in R2 – R8 point to wide interchromatin compartment (IC) channels, pervading from the major lacuna toward the nuclear envelope between major chromatin bodies. They were first noted during the pre-ENP/ENP transition (R2), prominent in ENPs and ENP/Cs (see enlargements of boxed areas a-c in R6, R7) and disappeared together with the major lacuna during the development of ENCs (R9, R10). Major lacunas often adopted a central position in the nuclear interior of ENPs (R6), but acentric positions were also observed resulting in broad regions of direct contact of a major lacuna with the nuclear envelope (R3, arrowheads). At all stages of preimplantation development major chromatin bodies likely representing individual chromosome territories (compare **Fig. 3**) were built up from smaller chromatin domain clusters (CDCs) pervaded by small IC channels (see enlargements of boxed areas a-c in R5 and R10). S. Volumes recorded for a sample of nuclei recorded with 3D-CLSM or 3D-SIM from embryos with 4-cells (E4; 15 nuclei), 5 to 8 cells (E5–8; 27 nuclei), 9–16 cells (E9–16; 36 nuclei) and more than 18 cells (E > 18; 30 nuclei). Scatter plots are combined with box plots presenting mean values, quartiles and whiskers. Each dot respresents the volume of an individual nucleus. Black dots respresent ENPs, red dots ENP/Cs and blue dots ENCs. A highly significant volume decrease ($P < 0.006$) was noted for nuclei in embryos advancing from 5–8 cells to 9–16 cells. Bars: 5 μm in I representative for A–I; 3 μm in J representative for J–Q; 3 μm in R1 representative for R1-R10; 1 μm side length of enlarged boxes a, b and c in R5-R7, R10.

blastocyst shown in **Figure 15**, panel D, however, suggests that this epigenetic mark can be enriched in chromatin, which is not or not yet actively transcribed. **Fig. 16** shows that major chromatin clusters with a strong enrichment of H3K4me3 were consistently detected in nuclei (n = 17) recorded by 3D-SIM in this non-hatched blastocyst, whereas we did not observe this type in fetal fibroblast nuclei (n = 57) and only rarely in another cloned blastocyst studied after hatching (1 from 11 nuclei). Similar to fibroblasts, most nuclei in this hatched blastocyst did not show an increased H3K4me3 labeling intensity inside clusters marked strongly with H3K9me3 compared to areas outside these clusters. More studies of non-hatched and hatched blastocysts are

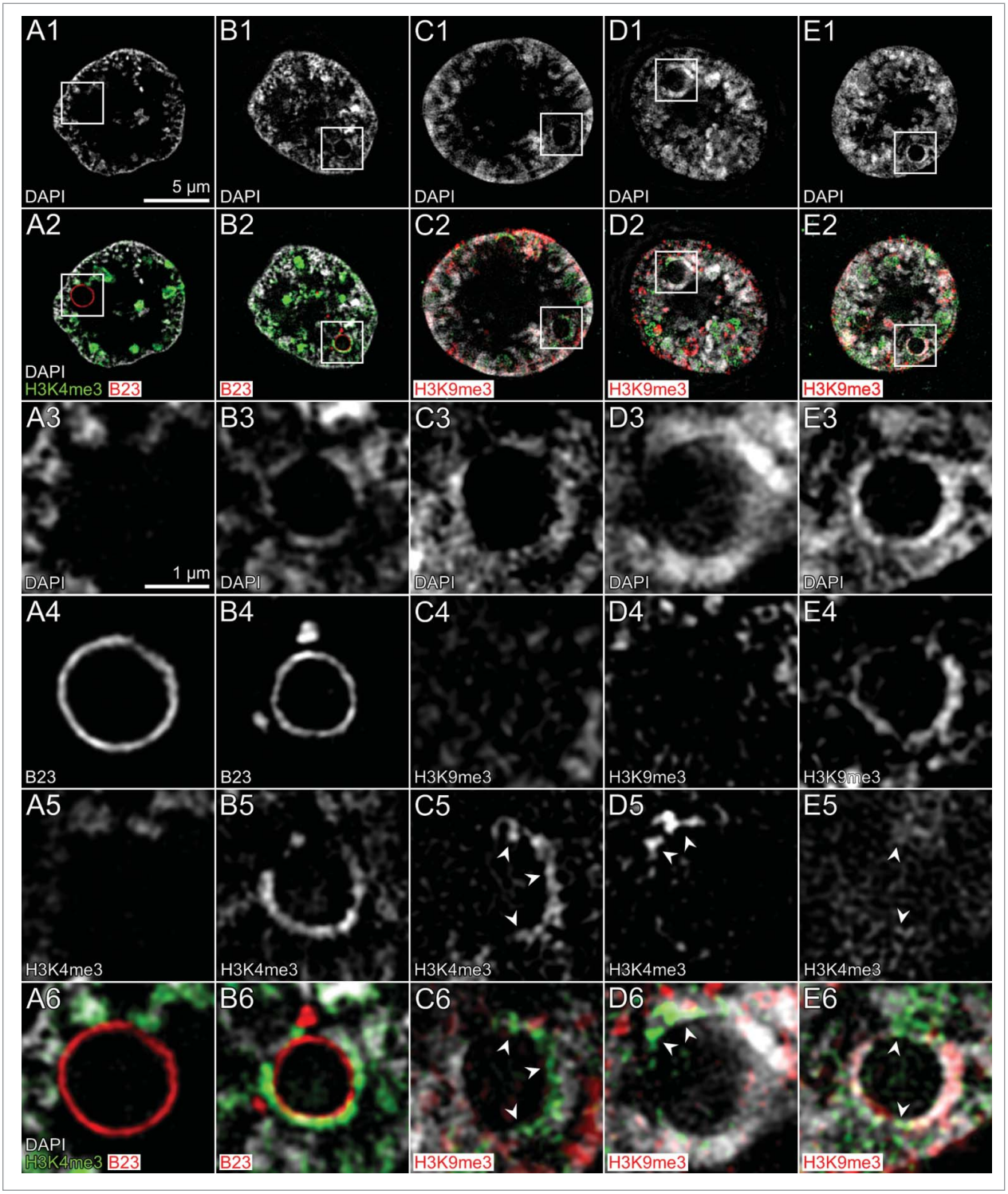

Figure 8. For figure legend, see page 571.

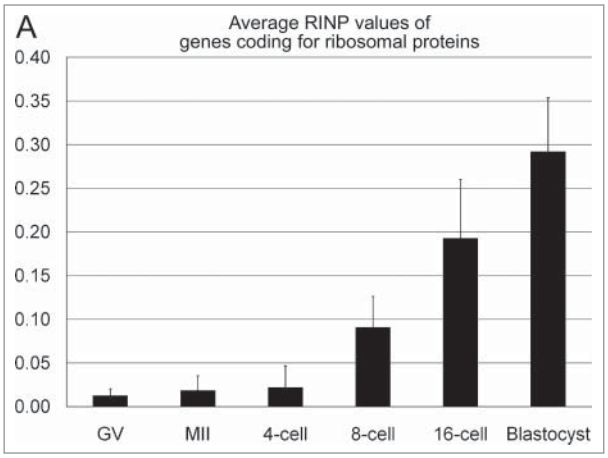

Figure 9. A transcriptome analysis suggests a major increase of intronic sequences from genes coding for ribosomal proteins at the 8-cell stage of *in vitro* fertilized embryos. Columns present the results of a transcriptome analysis of 83 genes coding for ribosomal proteins at germinal vesicle (GV) and at metaphase II stage bovine oocytes, as well as in IVF embryos with 4, 8 and 16 cells and in blastocysts.[27] For all genes the parameter RINP was determined individually as a measure for the coverage of all intronic sequences in transcripts from each gene. RINP indicates the ratio of intronic read counts to not-covered intronic positions. A fold change ≥10 in RINP between subsequent replicates of the embryonic stages was considered as indicative of nascent transcription. Background was defined as the 75th percentile of RINP in the oocyte stages (for further details see Graf et al. 2014).[27] A fold change ≥10 could only be confirmed for a fraction of ribosomal protein genes at each stage (for details see Results). Columns show average values of RINP for the entire pool of ribosomal protein genes.

necessary in order to decide whether the observed differences represent a differentiation event correlated with embryo hatching or whether these differences reflect a strong variability of major chromatin complexes between different cloned embryos, possibly correlated with differences in their developmental potentials.

Part 3. Quantitative analysis of similarities and differences between nuclear landscapes of *in vitro* fertilized embryos, cloned embryos and fetal fibroblasts

Frequencies of distinguished nuclear phenotypes in in vitro fertilized and cloned preimplantation embryos

Figure 17A provides a quantitative analysis of the frequencies of pre-ENPs, ENPs, ENP/Cs and ENCs analyzed in a total of 259 nuclei recorded with 3D-SIM in IVF embryos, including 9 embryos with 2 cells, 6 embryos with 3–4 cells, 7 embryos with 7–8 cells, 8 embryos with 9–15 cells and 6 embryos with more than 18 cells up to the morula stage (~30 cells). In 17 nuclei recorded from 2-cell embryos pre-ENPs were the predominant phenotype (82%), although 18% of nuclei showed already a major lacuna and were classified accordingly as ENPs. In 22 nuclei recorded from embryos with 3–4 cells the percentage of pre-ENPs decreased to 27% and ENPs became predominant (73%). In addition to a major lacuna, 10% of nuclei also presented nucleoli, demarcated by a rim of intensely DAPI-stained DNA. This nucleolar phenotype was rarely noted in classical ENPs but marked the beginning of the transition from ENP to ENC after major genome activation (ENP/C). In 56 nuclei recorded from embryos with 7–8 cells 89% represented the ENP phenotype. After major embryonic genome activation the fraction of ENPs determined in 66 nuclei from embryos with 9 to 15 cells dropped to 48%, while the fraction of ENP/Cs and ENCs rose to 38% and 13%. Only one nucleus with the pre-ENP like phenotype was observed at this stage of preimplantation development. In 98 nuclei recorded from embryos with more than 18 cells to morula stage ENCs presented by far the dominant fraction (87%) and only few nuclei still showed an ENP or ENP/C phenotype. **Figure 17B** presents a quantification of pre-ENP-like, ENP-like and ENP/C-like nuclear phenotypes recorded in 40 nuclei from 5 cloned 8-cell embryos and 28 nuclei from 2 cloned blastocysts. The ENP-like phenotype was predominant at the 8-cell stage (48%), followed by the ENP/C-like phenotype (32%) and the pre-ENP like phenotype (20%). All nuclei studied at the blastocyst showed the ENC phenotype.

Linking topological chromatin density mapping of the nuclear landscape with H3K4me3, H3K9me3 and RNA polymerase II arrangements

For a quantitative comparison of the nuclear topography of the functionally relevant hallmarks H3K4me3, H3K9me3 and RNA polymerase II with the topography of DAPI-stained chromatin, we employed a segmentation algorithm, previously developed for DAPI-stained nuclei.[37,40] DAPI positive pixels in SIM sections were segmented into 7 DAPI intensity classes with equal intensity variance. This classification provided a clear visualization of nuclear landscapes shaped by color-coded DAPI intensity classes and allowed for a statistical comparison both between individual nuclei and between different areas within individual nuclei.

Figure 8 (See previous page). Nucleolar precursor bodies and nucleoli in nuclei of *in vitro* fertilized embryos. A1–E1. Midplane SIM sections of a DAPI-stained nucleus approaching ENP (A1) and of 4 ENP/Cs (B1–E1). A2–E2. Corresponding sections with immunostained H3K4me3 (green) and B23 (red) in A2 and B2 or H3K4me3 (green) and H3K9me3 (red) in C2 – E2. Boxed areas in Panel A frame a nucleolar precursor body or early nucleolus and likely mature nuclei in Panels B–E. Enlarged images of boxed areas are presented below: A3–E3, DAPI; A4, B4, B23; C4–E4, H3K9me3; A5–E5, H3K4me3; A6, B6, colored overlays of DAPI, H3K4me3 and B23; C6–E6, colored overlays of DAPI, H3K4me3 and H3K9me3. Note that the nucleolar precursor body or early nucleolus shown in Panel A is lined by B23 (A4) but lacks a surrounding rim of intensely DAPI-stained DNA (A3) in contrast to mature nucleoli (B3–E3). Unexpectedly, most of the nucleoli shown in Panels B, D and E present variable parts of their DAPI-stained rims labeled with H3K4me3 (B5, C5, D5, see arrow heads in C5 and D5), considered as a marker for transcriptionally competent chromatin, but little detectable staining with H3K9me3, considered as a marker for silent chromatin (C4, D4). The DAPI-stained rim of the nucleolus shown in Panel E is strongly marked by H3K9me3 (E4) but shows little H3K4me3 staining (E5, arrow heads). Bars: 5 μm in A1 is representative for A1–E2, 1 μm in A3 is representative for enlarged boxes A3–E6.

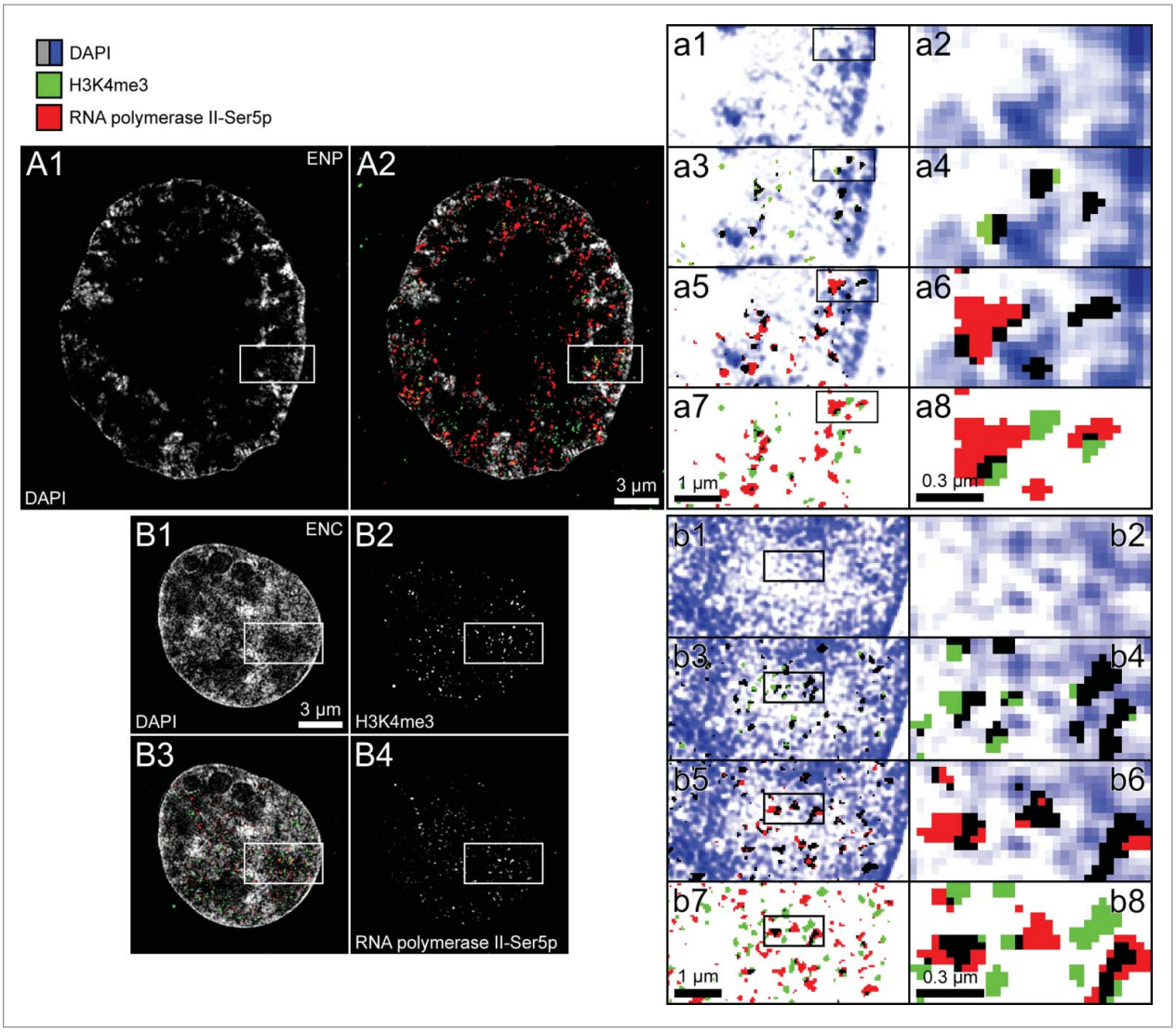

Figure 10. Topography of DAPI-stained chromatin, RNA polymerase II-S5p and H3K4me3 in nuclei from in vitro fertilized preimplantation embryos recorded with 3D structured illumination microscopy. Panels A and B. Midplane SIM sections from an ENP (panel A) and ENC (panel B). A1 and B1. Patterns of DAPI-stained DNA (gray). A2 and B3. Overlay of H3K4me3 (green) and RNA polymerase II-S5p signals (red) on the DAPI images. B2 shows only the H3K4me3 pattern, B4 only the RNA polymerase II-S5p pattern of this ENC. Rectangular boxes of the same size area marked in A1, A2, B1–B4 are presented as enlarged views in images a1, a3, a5, a7 and b1, b3, b5, b7. To allow a more detailed visual inspection at the level of individually recognizable pixels (39.5 nm^2 pixel size) rectangular boxes marked in these views are further enlarged in a2, a4, a6, a8 and b2, b4, b6, b8. An increase in color intensity of DAPI positive pixels (blue) is tentatively considered as a reflection of a local increase in the compaction of chromatin stained with DAPI (a1, a2, b1, b2). Black pixels in a3, a4 and b3, b4 denote a colocalization of DAPI positive pixels with H3K4me3 positive pixels. Green colored H3K4me3 positive pixels were noted in DAPI negative areas of thresholded images (compare **Fig. 6**) (tentatively considered as interchromatin compartment channels). Red colored pixels in a5, a6 and b5, b6 are taken as an indication for RNA polymerase II-S5p positive pixels located within the interchromatin compartment, whereas black pixels in these images denote a colocalization of RNA polymerase II-S5p positive pixels with DAPI positive pixels. Black pixels in a7, a8 and b7, b8 indicate a colocalization of H3K4me3 positive pixels with RNA polymerase II-S5p positive pixels, whereas green and red pixel clusters hint to separate H3K4me3 and RNA polymerase II-S5p signals. Note the predominance of positive pixels for H3K4me3 and RNA polymerase II-S5p clusters at the periphery of chromatin clusters stained with DAPI often expanding into the IC (white). RNA polymerase II-S5p clusters show side-by-side associations with clusters of H3K4me3 labeled chromatin, but are also frequently located remote from each other. Bars: 3 µm for A1, A2, B1–B4; 1 µm for a1, a3, a5, a7 and b1, b3, b5, b7; 300 nm for a2, a4, a6, a8 and b2, b4, b6, b8.

Fig. 18 presents midplane sections with color-coded DAPI intensity classes from typical nuclear phenotypes recorded with 3D-SIM from *in vitro* fertilized embryos (Panels A–E) and cloned embryos (Panels F–J). As noted above, images of DAPI-stained nuclei were routinely displayed after thresholding to remove artifacts due to patterns of concentric rings (see **Fig. 6**). All pixels below the chosen threshold are counted as class 1 pixels. Panels A-J show nuclear arrangements of color-coded DAPI intensity classes for both thresholded (A1–J1) and unthresholded nuclei (A2–J2).

Linking of DAPI density mapping with H3K4me3, H3K9me3 and RNA polymerase II arrangements was performed with unthresholded nuclei (exemplified in **Fig. 18A2–J2**). This approach stretched DAPI intensity classes over the widest possible range (compare Supplementary **Figure S4**). In non-thresholded DAPI images classes 1–3 apparently represented the interchromatin compartment, classes 4 and 5 preferentially the less intensely DAPI-stained periphery of chromatin domain clusters (CDCs), called the perichromatin region (PR) (see Introduction and Discussion) and classes 6 and 7 preferentially the intensely DAPI-stained core regions of CDCs. Class 1 (blue) is strongly increased in the thresholded nuclei.

Fig. 19 shows the results of a quantitative high-resolution analysis of RNA polymerase II, H3K4me3 and H3K9me3 positive pixels attributed to the 7 DAPI intensity classes from unthresholded ENPs and ENCs of *in vitro* fertilized embryos (including a few early stages of ENP/Cs) (**Fig. 19A and B**), ENP-like nuclei and ENCs from cloned embryos (**Fig. 19C and D**) and fetal fibroblast nuclei (**Fig. 19E**). Care was taken to correct for any shifts between the channels used for recording DAPI and the additional pairwise recording of H3K4me3 and H3K9me3 or H3K4me3 and RNA polymerase II. In each sample 3 – 6 sequential, mid-nuclear SIM sections were evaluated from a total of 20 nuclei, including 10 nuclei with immunostained H3K4me3/H3K9me3 (cloned ENP-like n = 7) and 10 nuclei with immunostained H3K4me3/RNA polymerase II (cloned ENP-like n = 8; for further details see Supplementary Information: Extended Experimental Procedures). We tested the

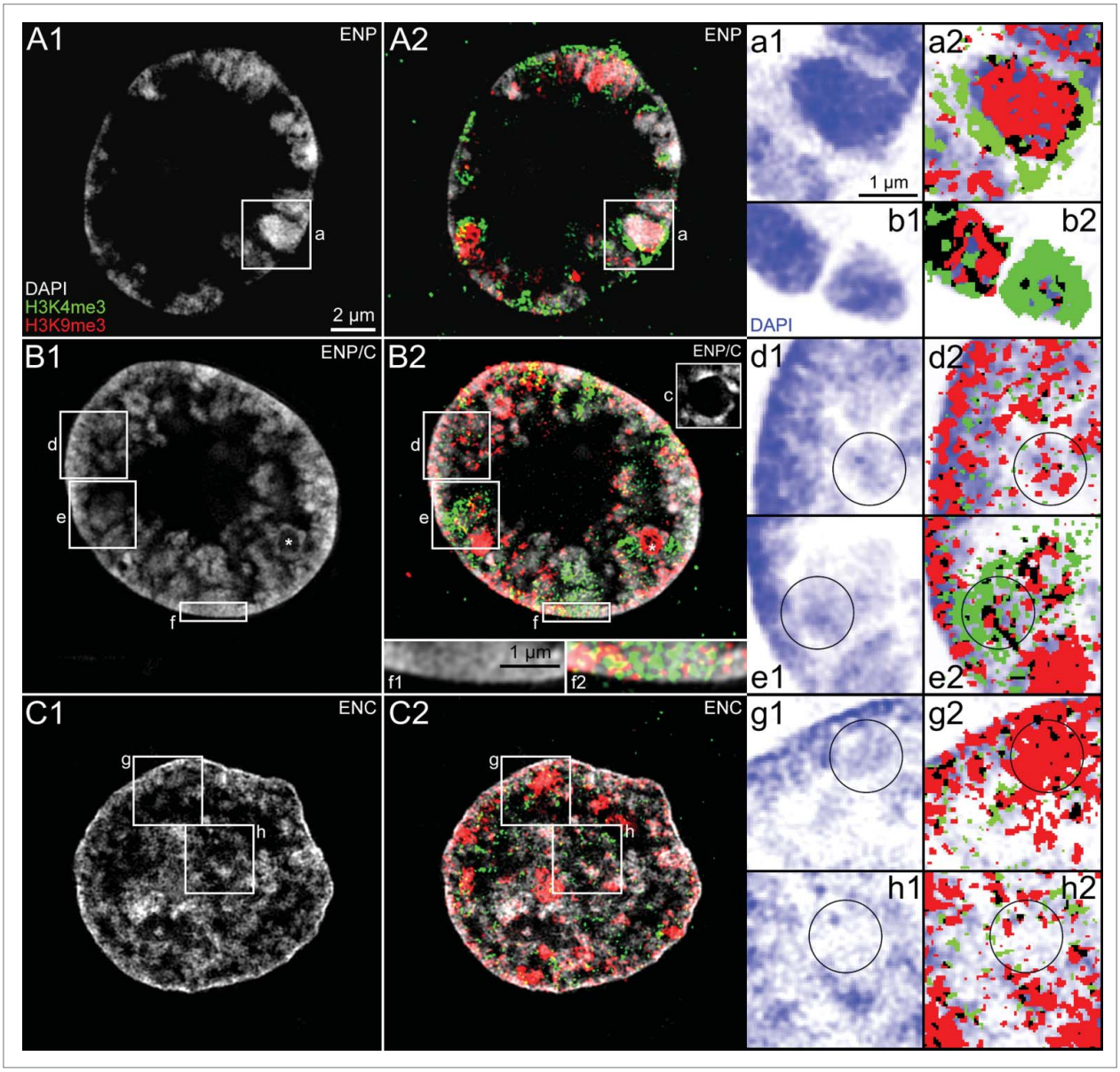

Figure 11. For figure legend, see page 574.

null hypothesis of a random distribution of H3K4me3, H3K9me3 and RNA polymerase II positive pixels across the 7 DAPI intensity classes. For a random distribution the fraction of marker pixels should equal the fraction of DAPI positive pixels representing each class. In all samples the null hypothesis could be rejected with a very high probability ($P < 10^{-15}$).

Figure 19 demonstrates a highly non-random and consistent pattern of RNA polymerase II, H3K4me3 and H3K9me3 in all samples despite the strikingly different global nuclear landscapes of ENPs and ENP-like nuclei compared with ENCs and fibroblast nuclei. DAPI intensity classes 6 and 7 showed a significant enrichment of H3K9me3 with a higher accumulation in class 6, whereas a distinct depletion was typically found in class 7 for H3K4me3 and RNA polymerase II. These 2 markers were consistently enriched in class 4. In contrast, all 3 markers were depleted in class 1. In our analyses of *in vitro* fertilized embryos we studied RNA polymerase II with a phosphorylated serine 5 of its CTD domain, while analyses of cloned embryos and fetal fibroblasts were carried out with RNA polymerase II carrying a phosphorylated serine 2. A noticeable difference between the nuclear arrangements of the 2 enzyme modifications was not detected. The patterns described in **Figure 19** were robustly supported for a range of thresholds applied to SIM sections of immunostained markers (Supplementary **Fig. S4**; for further details see Extended Experimental Procedures) despite the fact that the size and abundance of immunopositive pixel clusters for RNA polymerase II, H3K4me3 and H3K9me3 was affected by the choice of low, medium and high thresholds (Supplementary **Figs. S2 and S3**).

The comparison of nuclear samples from *in vitro* fertilized and cloned embryos was complicated by major chromatin clusters strongly marked with H3K4me3, H3K9me3 or both. We noted such clusters in both types of embryos but they appeared particularly prominent relative to the nuclear volume in the small ENCs of cloned blastocysts. Supplementary **Figure S5** presents a separate analysis of immunopositive pixels present in individual strongly H3K9me3 decorated major chromatin clusters to the 7 DAPI intensity classes. Supplementary **Figure S6** provides such an analysis for major chromatin clusters decorated with H3K4me3. These Supplementary Figures indicate a pronounced variability of the topography of H3K9me3 and H3K4me3 in different major chromatin clusters even within the same nucleus. For the evaluation of ENPs and ENCs from *in vitro* fertilized embryos and ENP-like presented in **Figure 19A, B** entire SIM sections were used, since the modest presence of major chromatin clusters did not make any important difference relative to the nuclear volume. For the evaluation of ENCs from cloned blastocysts shown in **Figure 19C, D** we deliberately analyzed sections with few if any major chromatin clusters to ensure that the analysis represents the signal distribution in the interchromatin compartment, perichromatin region and core regions of CDCs (see above).

In summary, despite major differences of the global landscapes the detailed inspection of SIM-images (**Figs. 10–15**) and quantitative image analyses (**Fig. 19**) indicate for all types of nuclei a local accumulation of H3K9me3 in the core of chromatin domain clusters and of H3K4me3 and RNA polymerase II in the less intensely DAPI-stained periphery of these clusters, whereas these markers were depleted in the interchromatin compartment.

Figure 11 (See previous page). Topography of DAPI-stained chromatin, H3K4me3 and H3K9me3 in nuclei from *in vitro* fertilized preimplantation embryos recorded with 3D structured illumination microscopy. Panels A–C. Midplane SIM sections from an ENP (A), an ENP/C (B) and an ENC (C) present typical examples of the topography of DAPI-stained DNA (gray, A1–C1) together with overlays of DAPI-stained DNA with H3K4me3 (green) and H3K9me3 (red) (A2–C2). Enlargements of boxed areas a, d, e, g and h in these nuclei are shown on the right with DAPI-stained chromatin in blue (a1, d1, e1, g1 and h1) and corresponding overlays of DAPI images with pixels (pixel size 39.5 nm^2) classified as immunopositive for H3K4me3 (green) or H3K9me3 (red) (a2, d2, e2, g2 and h2). Pixels and pixel clusters positive for both H3K4me3 and H3K9me3 are denoted in black. Circles in the corresponding images d1/d2, e1/e2, g1/g2, h1/h2 were drawn into these enlarged images either to mark areas of special interest (see below) or to facilitate comparisons between images showing only the DAPI pattern (left) and their corresponding counterpart showing additional immunolabeling of epigenetic markers (right). Panel A. In this ENP most of the core parts of the strictly peripherally located DAPI-stained major chromatin bodies (MCBs) are labeled with H3K9me3. In the periphery of some of these MCBs we note intensive labeling with H3K4me3 (compare a1 and a2). H3K4me3 positive clusters can be noted directly at the nuclear border. The MCB presented at the right side of b1 and b2 exemplifies a case, strongly labeled with H3K4me3 throughout with very little additional staining of H3K9me3, whereas the MCB on the left side of b1 and b2 shows overlapping signals of H3K4me3 and H3K9me3. Panel B. This nucleus was identified as ENP/C. Nucleoli surrounded by densely DAPI-stained chromatin were noted in other sections of the 3D-SIM image stack (for an example see box c). In comparison with the ENP shown in Panel A, the size of the major lacuna is apparently reduced by the invasion of MCBs toward the nuclear interior. A clear separation of neighboring MCBs by wide IC channels is no longer possible in this nucleus. Potential MCBs or alternatively major chromatin domain clusters with contributions from several neighboring CTs were preferentially labeled with H3K4me3, while others were preferentially labeled with H3K9me3 (see boxed area e in Panel B and enlarged views e1 and e2 on the right). Enlarged boxes d1/d2 show a peripheral nuclear region with intensely DAPI-stained chromatin enriched at the nuclear border. H3K9me3 labeled chromatin is noted in clusters both at the nuclear border and away from the border. These clusters, however, colocalize only in part with the densely DAPI-stained chromatin but also extend into modestly DAPI-stained regions. Clusters of H3K4me3 labeled chromatin are distributed between the H3K9me3 labeled clusters. The enlarged views f1/f2 show that not only H3K9me3 but also H3K4me3 positive clusters can be noted directly at the nuclear border (compare with a2). Panel C. Midplane SIM section from a typical ENC nucleus. In contrast to the ENP and ENP/C, the major lacuna has disappeared. Chromatin at the nuclear border is nearly exclusively marked with H3K9me3 and extends as an interconnected chromatin network throughout the nuclear interior with numerous large and small H3K9me3 labeled clusters, whereas enrichment of H3K4me3 label is only noted in dispersed small clusters (compare g1/g2 and h1/h2). Although these enlarged views suggest a preference of H3K9me3 for regions more densely stained with DAPI, whereas H3K4me3 appears preferentially located in less densely stained regions, detailed inspection shows an occasional extension of H3K9me3 positive pixels also into regions with weakly DAPI-stained chromatin and on the contrary an extension of H3K4me3 positive pixels into intensely DAPI-stained regions (see Results part 3 for quantitative analysis). Bars: 2 μm for A1–C2 and c; 1 μm for a1–b2 and d1–h2.

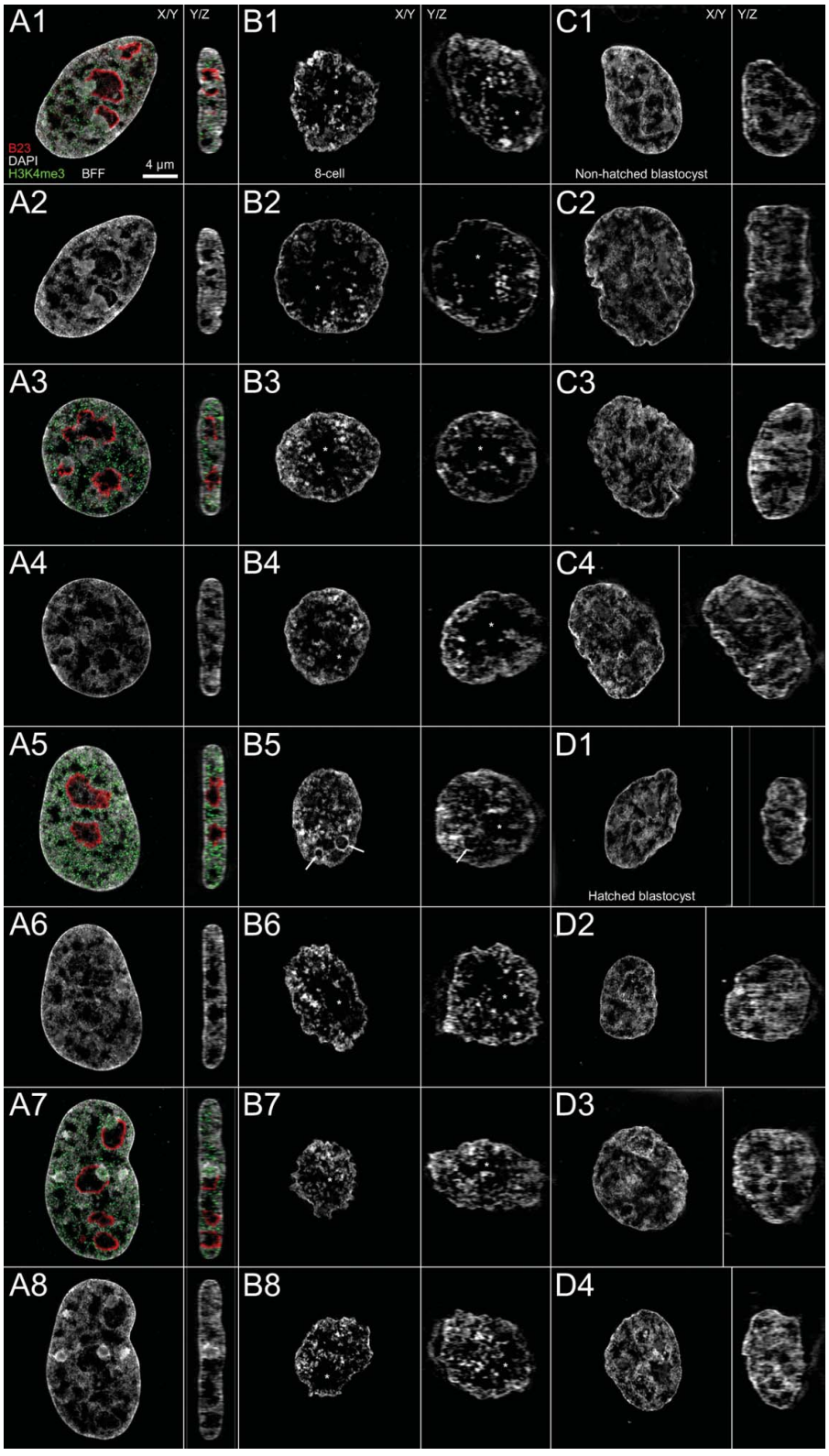

Figure 12. Comparison of nuclear phenotypes from bovine fetal fibroblasts and cloned preimplantation embryos studied with 3D structured illumination microscopy. Panels A1–A8. Midplane SIM x/y-sections (left) and y/z-sections (right) from DAPI-stained fetal fibroblast nuclei indicate their common flat-ellipsoidal shape. DAPI-stained sections are shown together with immunostaining of nucleophosmin B23 (red) and of H3K4me3 (green) in A1, A3, A5 and A7. Corresponding sections with DAPI staining alone are presented in A2, A4, A6 and A8. Panels B1–B8. Midplane SIM x/y-sections (left) and y/z-sections (right) from DAPI-stained nuclei in a cloned 8-cell embryo demonstrate the transformation of the flat-ellipsoidal shape of fibroblast nuclei into a roundish shape with a more pronounced clustering of chromatin and the formation of a major lacuna, marked by asterisks (compare **Figure 7**, Panels J-Q). Panels C1–C4 and D1–D4. Four nuclei recorded by 3D-SIM from a cloned, non-hatched blastocyst (C1–C4) and 4 nuclei from a cloned, hatched blastocyst (D1–D4). These nuclei were present in cells, which maintained their connection during microdissection of the embryos for 3D-SIM (see Results and Extended Experimental Procedures) and likely represent trophectoderm nuclei. Bar: 4 µm in A1 representative for all Panels.

Discussion

Preimplantation development of *in vitro* fertilized and cloned embryos is accompanied by massive changes of nuclear landscapes

Major embryonic genome activation occurs at the 8-cell stage of *in vitro* fertilized bovine embryos.[27] A major change of the gene expression status may also occur in cloned 8-cell bovine embryos as suggested by the activation of pluripotency genes at this stage.[25] *In vitro* fertilized and cloned bovine embryos approaching the 8-cell stage were characterized by the formation of a major lacuna, enriched in splicing factors, and presumably many other storage factors, whose nuclear topography was not tested in the present study. Occasional DAPI or TO-PRO-3 stained chromatin bodies were found in the interior of the major lacuna, but otherwise current evidence suggests that these lacunas constitute a rather DNA-free space. DNA staining with these compounds may, however, not suffice to exclude occasional giant chromatin loops, penetrating from peripheral CTs deep into the major lacuna. The peripheral chromatin surrounding major lacunas presented itself as major chromatin bodies (MCBs), separated from each other by wide

interchromatin compartment (IC) channels, whereas smaller IC-channels pervaded the interior of MCBs as well. Chromosome painting experiments identified individual MCBs as distinct chromosome territories (CTs).[19] For nuclei with this phenotype we introduced the term **ENP** (for Embryonic Nucleus with Peripheral distribution of CTs). Although typical ENPs were also noted in cloned 8-cell embryos, the major lacuna was often smaller and the corresponding shift of chromatin toward the

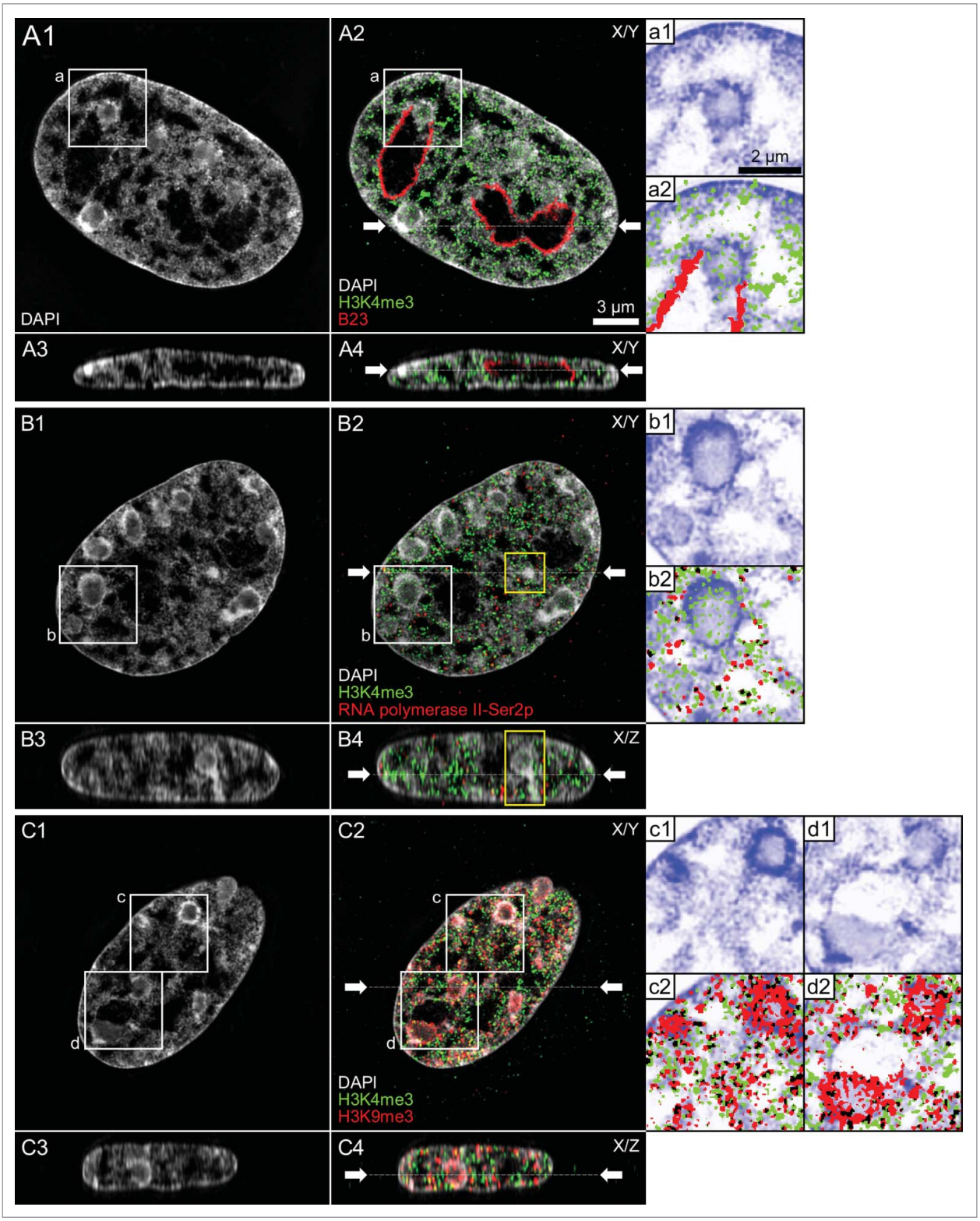

Figure 13. For figure legend, see page 577.

nuclear periphery, as well as chromatin compaction was less pronounced. To account for such differences – notwithstanding the striking similarities of these nuclear phenotypes in *in vitro* fertilized and cloned embryos – we designated the phenotype of such nuclei as ENP-like.

Preimplantation development after major EGA was characterized in both *in vitro* fertilized and cloned embryos by the disappearance of the major lacuna and the formation of much smaller nuclei with a 3D higher order chromatin network expanding throughout the entire nuclear space. We called nuclei with this phenotype **ENCs** (for **E**mbryonic **N**uclei with **C**onventional architecture), because they adopted common features of nuclear landscapes, previously described for a variety of somatic cell types.[6,40]

To our best knowledge, the ENP phenotype was first described in an EM study of 8-cell bovine IVF embryos.[62] The authors argued for a difference in the distribution of major chromatin bodies between nuclei from IVF embryos and nuclei from conventionally fertilized embryos obtained from cows at slaughter. In these *in vivo* embryos they observed a distribution of MCBs throughout the nuclear space. It is not clear, whether a systematic difference between nuclear phenotypes in IVF and *in vivo* embryos truly exists or whether this difference reflects slightly different developmental stages of IVF and *in vivo* generated embryos.

The observed coincidence of major embryonic genome activation and the formation of rather compact CTs, separated by wide IC-channels, in *in vitro* fertilized 8-cell embryos was an unexpected finding.[27] We would rather have expected a correlation of major EGA with a more decondensed state of CTs. Surprisingly, the rather compact CTs detected in ENPs share structural similarities with senescence associated heterochromatic foci (SAHF) observed in human fibroblast cultures at the end of their replicative life span as well as in CTs driven into a senescence-like state after exposure with the thiodioxopiperazine metabolite chaetocin.[63,64] Like ENPs, senescent fibroblasts formed CTs separated from each other by wide IC-channels but lacked a major central lacuna. A functional compartmentalization with transcriptionally competent chromatin at the periphery and silenced chromatin in the compact interior of SAHFs and SAHF-like chromatin bodies was consistently observed.[63,64] The picture in ENPs is more heterogeneous. Some major chromatin bodies observed in ENPs of *in vitro* fertilized embryos and ENP-like nuclei of cloned embryos presented a compact core with H3K9me3, surrounded by H3K4me3 labeled, peripheral chromatin, others were highly enriched in H3K4me3 distributed throughout the entire territory and still others revealed little H3K4me3 and H3K9me3 immunopositive labeling.

Incorporation of BrUTP or BrU demonstrated *de novo* RNA synthesis both in ENPs of *in vitro* fertilized embryos and ENP-like nuclei of cloned embryos. Notably, previous studies have demonstrated *de novo* RNA synthesis already during minor genome activation, which occurs in bovine embryos already at the 2-cell stage. The total amounts of such RNA may be even larger than *de novo* RNA synthesis at the 8-cell stage.[65] Major embryonic genome activation at the 8-cell stage is characterized by a steep increase in the number of transcribed genes.[27] From 6848 genes, which were found to be switched on from the 4-cell to the blastocyst stage, 3965 (58%) were activated at the 8-cell stage.

Functional nucleoli, characterized by a surrounding rim of compact chromatin and intense RNA synthesis, were common in nuclei of both *in vitro* fertilized and cloned embryos, which had passed the 8-cell stage, i.e. studied during post-major EGA development. They were rarely noted in ENPs of *in vitro* fertilized embryos, though more frequently in ENP-like nuclei of cloned embryos. Data available from our recently published transcriptome analysis[27] were further analyzed in the present study with a focus on genes involved in the formation of ribosomal proteins. This analysis confirmed a major rise of intronic sequences from such genes from the 8-cell stage to the blastocyst stage.

We found impressive differences in the clustering of H3K4me3 and H3K9me3 in both *in vitro* fertilized and cloned preimplantation embryos, but are not able to decide to which extent these differences may reflect true changes in the topography of the respective epitopes or effects of differential epitope masking. In any case, the extent of such changes and internuclear variability, observed even between nuclei of the same embryo, emphasize the importance to study the dynamics of nuclear architecture in space and time at the single cell level.

For a quantitative comparison of the nuclear topography of transcriptionally competent chromatin (H3K4me3), transcriptionally silent chromatin (H3K9me3) and RNA polymerase II with regard to the topography of DAPI-stained chromatin, we defined 7 DAPI intensity classes. This classification provided a clear visualization of nuclear landscapes shaped by color-coded

Figure 13 (See previous page). Topography of DAPI-stained chromatin, nucleophosmin B23, RNA polymerase II-Ser2p, H3K4me3 and H3K9me3 in nuclei of bovine fetal fibroblasts studied with 3D structured illumination microscopy. Panels A–C. SIM midplane x/y-sections of DAPI-stained bovine fibroblast nuclei (A1, B1, C1) and x/z-sections (A3, B3, C3) are shown together with corresponding immunostainings of H3K4me3 (green) and nucleophosmin B23 (red) (A2, A4), H3K4me3 and RNA polymerase II-Ser2p (red) (B2, B4), H3K4me3 and H3K9me3 (red) (C2, C4). A fine line marked by pairs of arrows in A2/A4, B2/B4 and C2/C4 indicates the sites of the respective x/z- and x/y-sections. All nuclei contain major chromatin domain clusters with a modestly DAPI-stained core and an intensely DAPI-stained periphery. Examples are framed by white boxes. The yellow boxes in B2 and B4 indicate a major chromatin cluster in the nuclear interior connected to chromatin at the nuclear border. Panels a-d. Enlargements of white boxed areas in the 3 nuclei show major chromatin clusters with a modestly DAPI-stained core (light blue) and an intensely DAPI-stained periphery (dark blue) (a1–d1), overlays of pixels representing immunostained markers are shown in the corresponding images a2–d2. Black pixels represent colocalization of the 2 immunostained markers. Panel a presents a major chromatin cluster, which interrupts the B23 stained rim of a nucleolus. Note also the lining of an IC lacuna with H3K4me3. Panel b indicates that the core part of the chromatin domain cluster is modestly labeled with H3K4me3 but lacks RNA polymerase II-Ser2p. IC-lacunas are lined with both H3K4me3 and RNA polymerase II-Ser2p. Panel c and d show intense H3K9me3 label enriched at the intensely DAPI-stained periphery of major chromatin clusters. Bars: 3 μm for A1–C4; 2 μm for a1–d2.

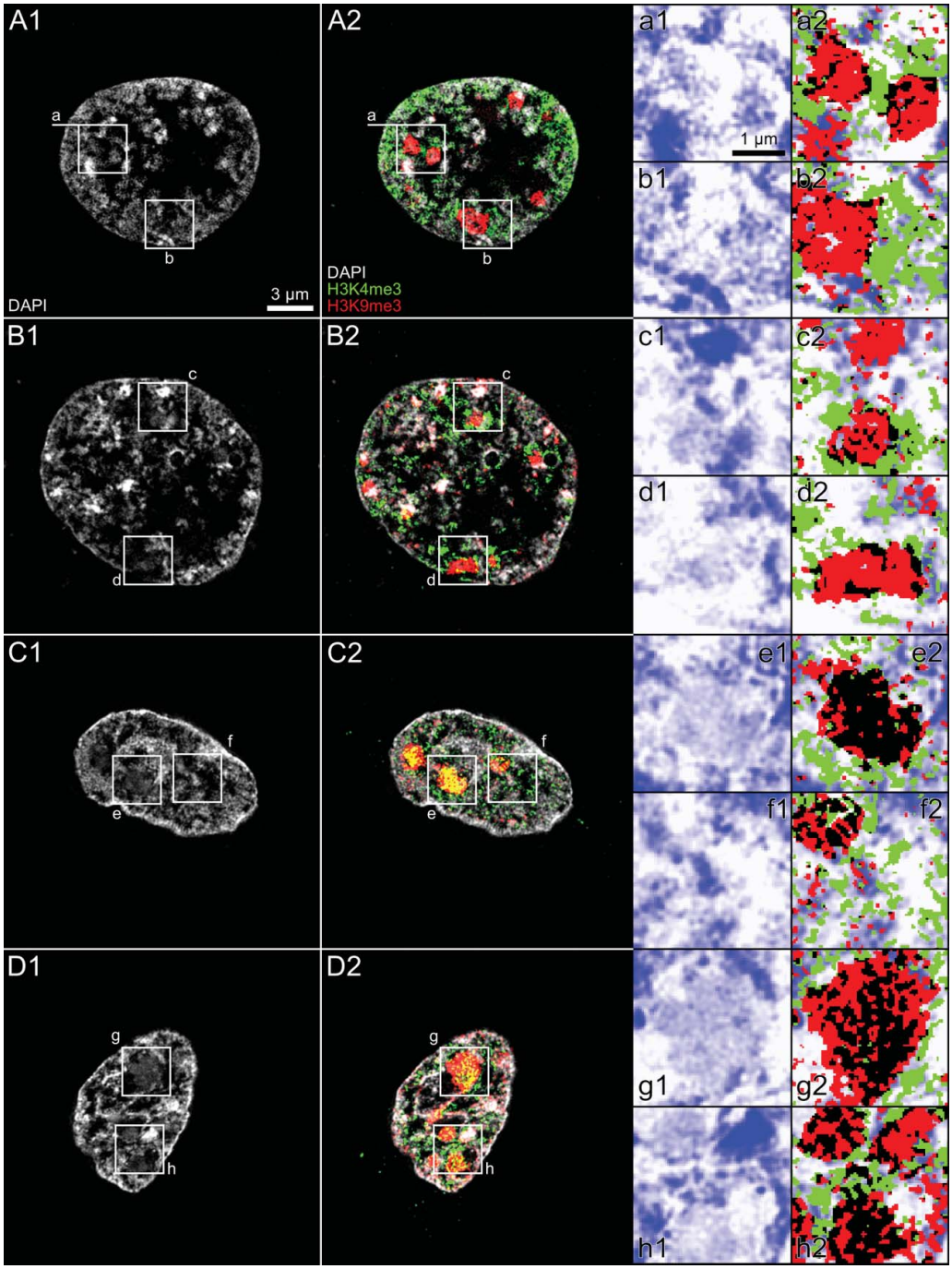

Figure 14. Topography of H3K4me3 and H3K9me3 observed with 3D structured illumination microscopy in nuclei from a cloned 8-cell embryo and a cloned blastocyst. Panels A and B. Midplane SIM sections from an ENP-like (Panel A) and an ENP/C-like nucleus (Panel B) recorded from a cloned 8-cell embryo with DAPI-stained chromatin (gray), H3K4me3 (green) and H3K9me3 (red). Panels C and D. Midplane SIM sections from 2 DAPI-stained ENCs of a cloned, hatched blastocyst with immunostaining of the 2 epigenetic markers. The 4 example nuclei show prominent major chromatin clusters, some of them intensely, others modestly stained with DAPI, but all prominently labeled with H3K9me3. Panels a to h. Enlargements of boxed areas demonstrate strongly H3K9me3 labeled major chromatin clusters, which cover both modestly and strongly DAPI-stained chromatin. In ENP- and ENP/C-like nuclei such clusters are surrounded by H3K4me3 labeled chromatin, but contain little H3K4me3 in their interior (Panels a-d). Black pixels denote colocalization events of H3K4me3 and H3K9me3 positive pixels, which mostly occurred at the periphery of a given major chromatin cluster. In ENCs of the cloned, hatched blastocyst we found numerous major chromatin clusters, modestly stained with DAPI and strongly labeled with both H3K4me3 and H3K9me3 (for examples compare e1/e2 and g1/g2). Panel h1/h2 shows 3 major chromatin clusters. Black pixels indicate colocalization of H3K4me3 and H3K9me3 throughout the interior of 2 modestly DAPI-stained clusters (upper left corner and bottom). An intensely DAPI-stained major chromatin cluster (upper right corner) shows only few black pixels indicating colocalization of H3K4me3 and H3K9me3 in its interior, and an enrichment at the periphery. Bars: 3 µm for A1-D2; 1 µm for a1–h2.

DAPI intensity classes and allowed for a statistical comparison both between different areas of individual nuclei and different samples of nuclei. These analyses demonstrate major similarities and differences between nuclear landscapes of *in vitro* fertilized and cloned preimplantation embryos, as well as fetal fibroblasts used for somatic cell nuclear transfer. Notably, the overall patterns of relative enrichments and depletions of H3K4me3, H3K9me3 and RNA polymerase II positive pixels over the 7 DAPI intensity classes were similar for ENPs, ENP-like nuclei, ENCs studied in *in vitro* fertilized and cloned embryos as well as for nuclei of fetal fibroblasts. In all samples, DAPI intensity classes 6 and 7, representing the core of chromatin domain clusters (CDCs), showed an enrichment of H3K9me3. In contrast, H3K4me3 and RNA polymerase II were consistently enriched in class 4, representing the less

intensely DAPI-stained periphery of these CDCs, whereas all 3 markers were consistently depleted in class 1, representing the rather DNA-free parts of the interchromatin compartment.

Our study provides robust evidence for highly significant enrichments of H3K4me3 and RNA polymerase II clusters at the periphery of CDCs, whereas H3K9me3 was enriched in their interior. Multiple RNA polymerases II have been described as integrative parts of transcription factories.[66] For immunodetection of RNA polymerase II we used antibodies detecting either a phosphorylated serine 2 (S2p) or serine 5 (S5p) in its C-terminal domain. The S2p modification is considered as a marker for RNA polymerase II involved in elongation, whereas RNA polymerase II-S5p occurs early in the transcription cycle.[67,68] Independent of whether RNA polymerase II carried the S2p or S5p modification, we consistently found an enrichment at the periphery of CDCs. This observation, however, does not exclude the presence of some RNA polymerase II at numerous other locations, including heterochromatic regions.

Major chromatin clusters showed a pronounced variability of their labeling patterns. We observed major chromatin clusters in ENPs from *in vitro* fertilized embryos that were predominantly labeled either with H3K4me3 or H3K9me3, whereas others showed only sparse

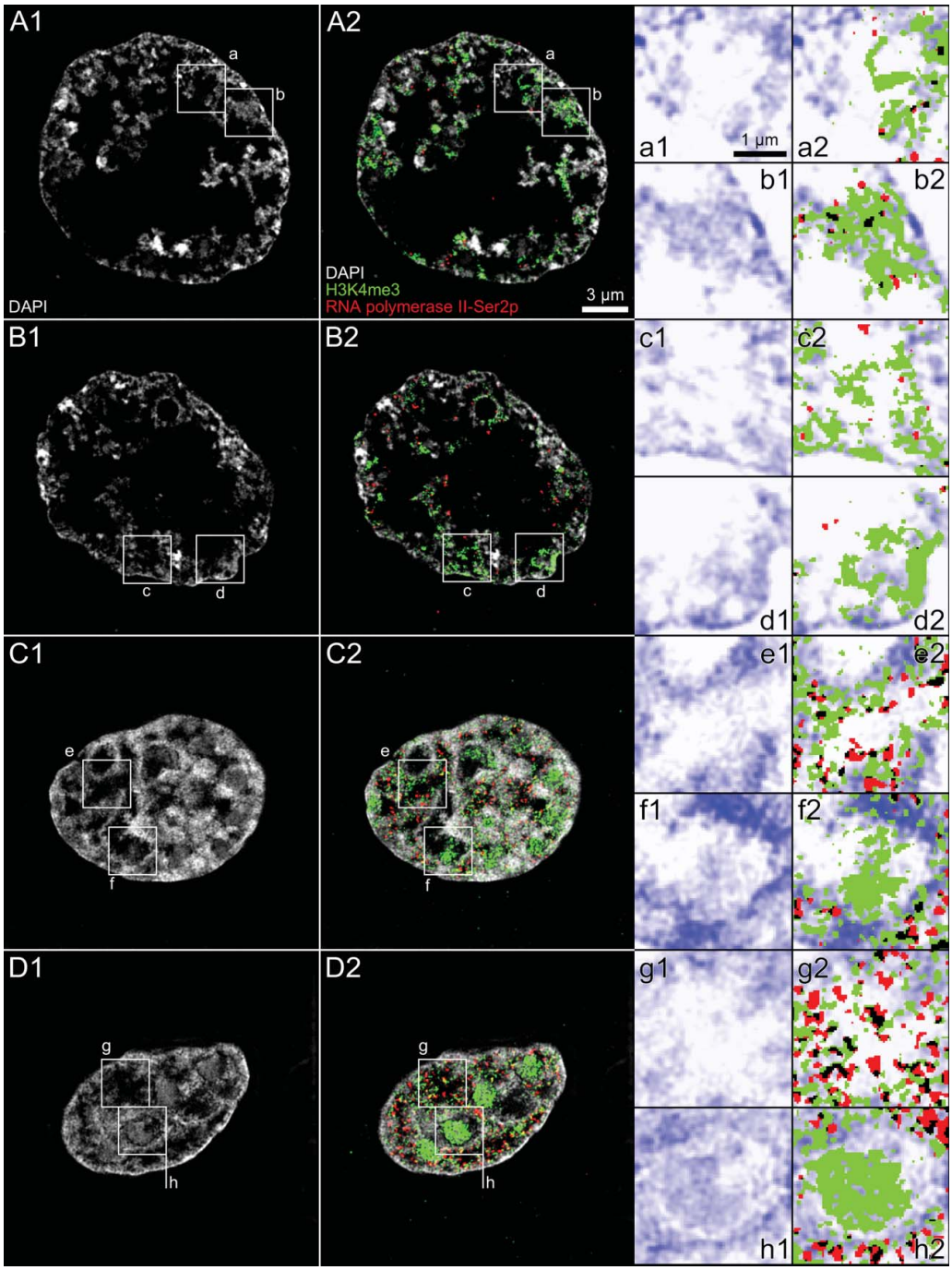

Figure 15. H3K4me3 and RNA polymerase II-Ser2p arrangements observed with 3D structured illumination microscopy in nuclei from a cloned 8-cell embryo and a cloned, non-hatched blastocyst. Panels A and B. SIM midplane sections recorded from an ENP-like nucleus (panel A) and an ENP/C-like nucleus (panel B) of a cloned, DAPI-stained (A1, B1) 8-cell embryo following immunostaining of H3K4me3 (green) and RNA polymerase II-Ser2p (red) (A2, B2). Panels C and D. SIM midplane sections from 2 DAPI-stained nuclei (C1, C2) from a cloned, non-hatched blastocyst demonstrate dispersed RNA polymerase II-Ser2p together with dispersed H3K4me3, as well as large, H3K4me3 labeled chromatin clusters (C2, D2), particularly prominent in D2 (compare **Fig. 14**, Panels D, G and H). Enlarged images of boxed areas in these nuclei (Panels a-h) show major chromatin clusters strongly marked with H3K4me3 but lacking RNA polymerase II-Ser2p. An enrichment of RNA polymerase II-Ser2p together with H3K4me3 is noted in chromatin lining IC-channels/lacunas. Bars: 3 µm for A1–D2; 1 µm for a1–h2.

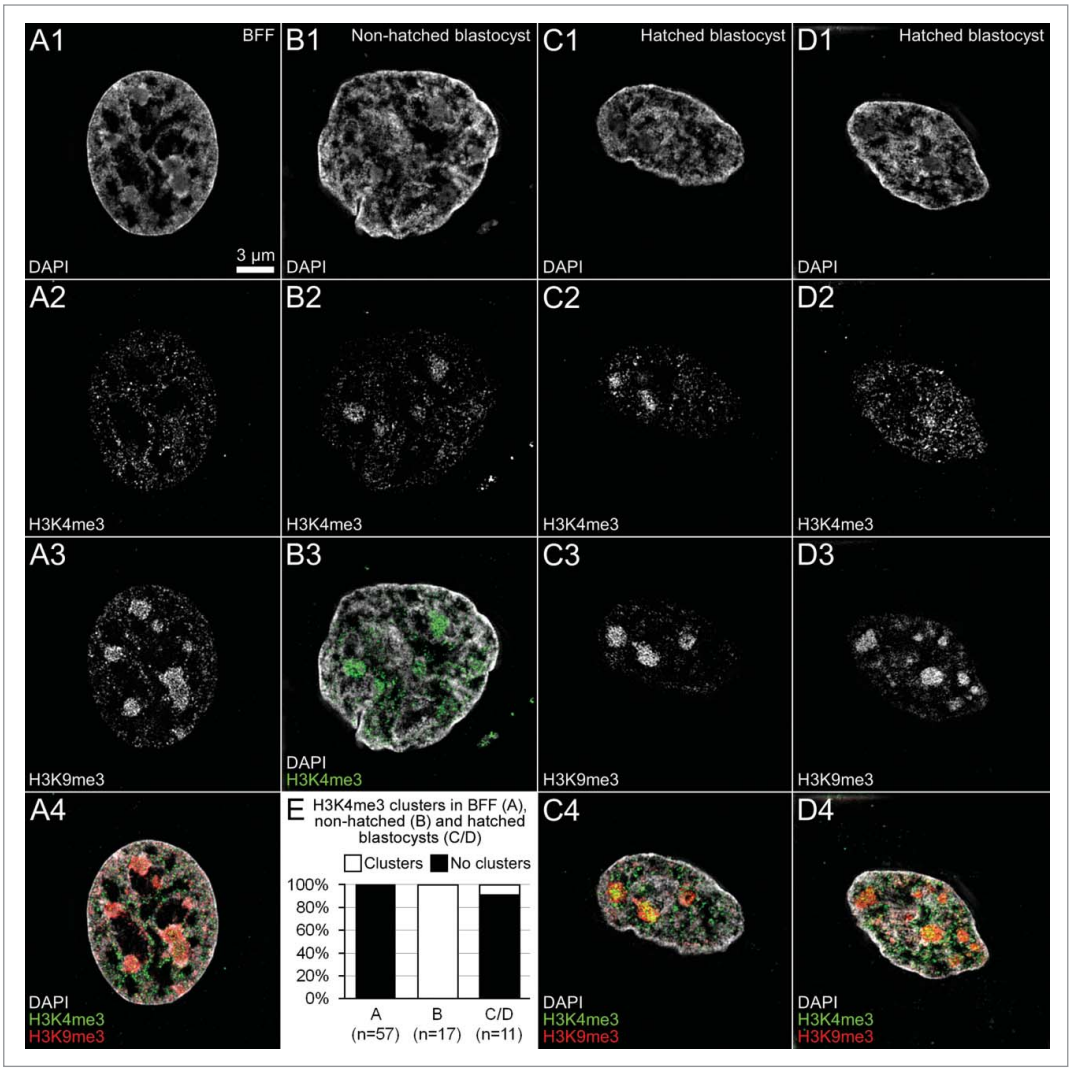

Figure 16. Differences between major chromatin clusters observed with 3D structured illumination microscopy in fetal fibroblast nuclei and nuclei from cloned, non-hatched and hatched blastocysts. Panel A. Corresponding midplane SIM sections from a typical DAPI-stained (A1) bovine fetal fibroblast nucleus with immunostained H3K4me3 (A2) and H3K9me3 (A3), overlay (A4; H3K4me3 green; H3K9me3 red) demonstrate numerous major chromatin domain clusters strongly labeled with H3K9me3 and sparsely with H3K4me3. Panel B. In contrast, the ENC recorded from a cloned, non-hatched blastocyst presents major chromatin domain clusters, strongly labeled with H3K4me3. Panels C and D. Two DAPI-stained ENCs (C1, D1) from a cloned, hatched blastocyst reveal major chromatin clusters strongly labeled with H3K9me3 (C3, D4), but differ with regard to H3K4me3 (C2, D2). Whereas this marker is apparently enriched in 2 of 3 clusters noted in one ENC (Panel C), no enrichment of H3K4me3 was detected in the major chromatin clusters present in the other ENC (panel D) similar to the pattern noted in the fibroblast nucleus (panel A). E. A quantitative assessment of the labeling patterns of major chromatin clusters in 57 fibroblast nuclei (A), 17 nuclei from cloned, non-hatched blastocysts (B) and 11 nuclei from cloned, hatched blastocysts (C, D) demonstrates the reproducibility of the similarities and differences of patterns described for the 4 example nuclei. Bar: 3 µm in A1 representative for all Panels.

evidence for the presence of either marker. It is not clear whether clustering of these epigenetic marks occurs as a transient phenomenon in all CTs or only in specific CTs or whether clusters may also represent chromatin from several neighboring CTs. The reconfiguration of nuclear landscapes during post-major EGA development of in vitro fertilized embryos into ENCs was characterized by a dispersed distribution of H3K4me3 throughout the nuclear space, while large H3K9me3 positive chromatin clusters were maintained. ENP-like nuclei in cloned embryos also showed major clusters labeled with either H3K9me3 or H3K4me3, though the latter were less pronounced compared with ENPs. Large clusters with both H3K4me3 and H3K9me3 label were also observed in ENCs of cloned embryos, in contrast to fetal fibroblast nuclei which consistently showed H3K9me3 labeled major chromatin clusters and a dispersed pattern for H3K4me3. The highly variable patterns of these histone modifications in particular in ENPs may reflect their impact on fine tuning of rapidly changing expression levels in multiple genes at this developmental stage. An attempt of a functional interpretation of such differences has also to take into account the high frequency of chromosome missegregations, which occurs during preimplantation development (see accompanying article by Popken et al.[35]). Even for mammalian embryos, which develop normally beyond the preimplantation period, this period is marked by the frequent failure of individual cells to grow and divide properly.[69] The elimination of such cells by apoptosis or mitotic cell death is a typical part of normal embryonic development, but occurs at much higher frequencies in cloned embryos (see accompanying article by Popken et al.[35]).[70-72] It will be interesting to investigate, whether some of the structural features described in this study have predictive value for the normal or abnormal development of a given embryonic cell, but it is not possible at this point to describe the sequence of structural events, which are connected with a normal development at the single cell level.

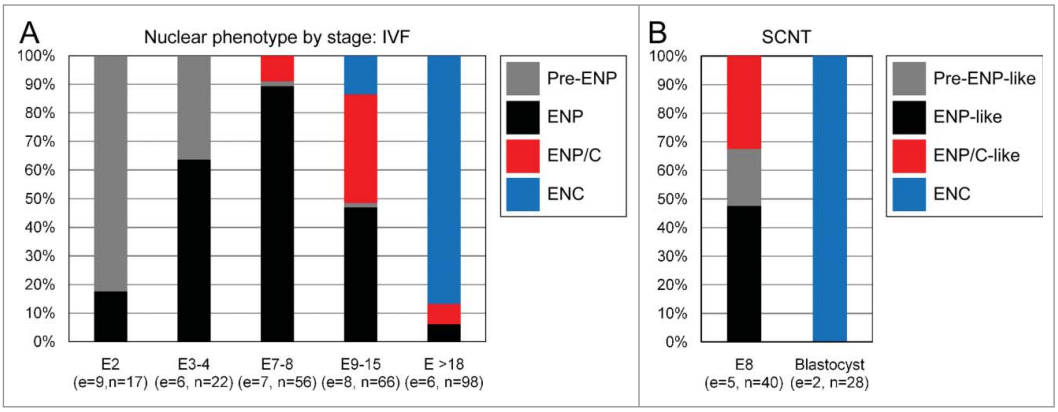

Figure 17. Quantitative assessment of different nuclear phenotypes recorded with 3D structured illumination microscopy during preimplantation development of in vitro fertilized and cloned embryos. A. Nuclei from 9 fertilized embryos with 2 cells (E2; 17 nuclei), 6 embryos with 3 or 4 cells (E3–4; 22 nuclei), 7 embryos with 7 or 8 cells (E7–8; 56 nuclei), 8 embryos between 9 and 15 cells (E9–15; 66 nuclei) and 6 embryos with more than 18 cells on their way toward the morula stage (about 32 cells) (E >18; 98 nuclei) were classified as pre-ENP, ENP, ENP/C and ENC according to the criteria described in Results and the examples presented in **Figure 7**. B. Classification of nuclei from 5 cloned 8-cell stage embryos (E8; 40 nuclei) and 2 blastocysts (28 nuclei) as pre-ENP-like, ENP-like, ENP/C-like and ENC was performed as described in Results.

The global structural transformation of the large ENPs into smaller ENCs may be correlated or even causally connected with the long-term replicative potential of embryonic cells. Notably, ENPs were rarely seen at the blastocyst stage and it was observed that cells carrying a persistent ENP phenotype during post-major EGA development became TUNEL positive, a hallmark for apoptosis.[73] The massive reorganization of nuclei during preimplantation development of *in vitro* fertilized and cloned embryos with large scale movements of CTs extends current evidence for major differentiation-dependent changes of nuclear landscapes. Mammalian rod cell nuclei provide a case for a massive reorganization during postmitotic-terminal cell differentiation during the course of several weeks.[74] Other studies report large scale movements of specific chromatin segments in interphase nuclei within time scales of several minutes.[75-78] The mechanisms necessary for these movements have not yet been clarified and may act both from inside and outside the nucleus.[79,80]

A model for a functional nuclear architecture based on co-aligned, 3-dimensional networks of inactive and active nuclear compartments

In **Figure 20A–C** we make an attempt to integrate both our current observations and findings reported in the literature into a refined version of the chromosome territory-interchromatin compartment (CT-IC) model (see Introduction).[42,43] While chromosome territories are now generally accepted as a basic feature of nuclear landscapes in animals and plants, this is not the case for the interchromatin compartment. Since an interchromatin space exists between any local chromatin configuration, be it a cluster of chromatin fibers or neighboring domains, it is a question of definition what fraction of the entire interchromatin space in a given cell nucleus is attributed to the interchromatin compartment. In the model shown in **Figure 20** we consider only the channels expanding between CDCs as part of the interchromatin compartment. Such a distinction depends on functional considerations and is open to modifications, when further methodological advancements will help to study the structure-function conundrums of chromatin domains with increased resolution. We propose a structurally highly ordered active nuclear compartment (aNC) with closely integrated functional interactions between the interchromatin compartment and the perichromatin region of chromatin domain clusters, whereas the interior of these clusters represents the transcriptionally inactive nuclear compartment (iNC). The active NC and iNC are structurally and functionally interconnected. The co-aligned 3D networks of the iNC and aNC may be compared with a natural landscape, where brushwood growing at the shore zone invades the interior of an interconnected system of little streams and ponds (**Fig. 20D**). This comparison seems more appropriate than a system of tubes with sharply defined borders. Small chromatin loops may expand from the perichromatin region into the interior of these channels or even penetrate throughout entire channels. Although we lack evidence, how big such loops may be and how they may be ordered within the aNC, a topography, which minimizes problems of chromatin entanglements was likely favored by natural selection during the evolution of larger genomes. Similarly, like the shore zone interacts with the land outside, dynamic interactions occur between the aNC and iNC, including local repositioning of chromatin between the aNC and iNC during transcription, replication and repair. Continuous, constrained movements of clustered chromatin at all levels from nucleosomes, individual ~1 Mbp CDs to entire CTs enforce continuous changes of intermediary spaces, including the width of IC-channels and lacunas, and provide possibilities for dynamic changes of chromatin interactions.[81-83] The concept of an interchromatin compartment as a major player by itself in the functional organization, which interacts structurally and functionally with the perichromatin region should not be confused with the trivial notion of an interchromatin space between all sorts of chromatin fibers.

In line with microscopic studies, recent high-resolution chromosome conformation capture (Hi-C) studies demonstrate the clustering of chromatin from the level of entire CTs down to megabase-sized chromatin domains.[9,84] These studies identified megabase-sized, topological domains (TDs) as an evolutionary

conserved property of mammalian higher order chromatin architecture.[84] Individual topological domains are characterized by extensive interactions, whereas fewer interactions were found between neighboring domains.[9,84] We take also into account the evidence for megabase-sized, gene-rich and gene-poor isochores found across a wide range of eukaryote species.[85] Linked TDs may generate larger gene-rich, transcriptionally active and DNase hypersensitive compartments, as well as gene-poor, transcriptionally silent, and DNase I insensitive compartments.[86] It is tempting to speculate that TDs, isochores and microscopically observed megabase-sized chromatin domains (~1 Mbp-CDs) represent at least to some extent the same basic units of CT architecture. For TDs a median size of several hundred kb was calculated, while a small remaining fraction with a size of <50 kb was termed 'boundary regions'.[84] In case of an allocation of a diploid mammalian genome into ~1 Mbp-CDs we would expect a total number of roughly 6000 domains. Remarkably, a study with improved optical 3D resolution identified 3- to 5-fold more distinct replication foci than previously reported suggesting an average DNA content of a few hundred kbp rather than the ~1 Mbp chromatin domains suggested from previous studies.[87] Foci varied in size from 210 nm down to 40 nm with an average size of 125 nm that was conserved throughout S-phase.[87] We conclude that current estimates for the size of TDs and replication foci are in close agreement and predict that these domains form larger chromatin domain clusters (CDCs), which are integrated into chromosome band domains, chromosome arm domains and finally into entire CTs.[6] We postulate a non-random, radial positioning of regulatory and transcribed sequences toward the periphery of chromatin domain clusters (CDCs) to ensure direct access to the finest branches of the interchromatin compartment. The fractions of the nuclear volume, occupied by CDCs and the interchromatin compartment vary widely in different cell types.

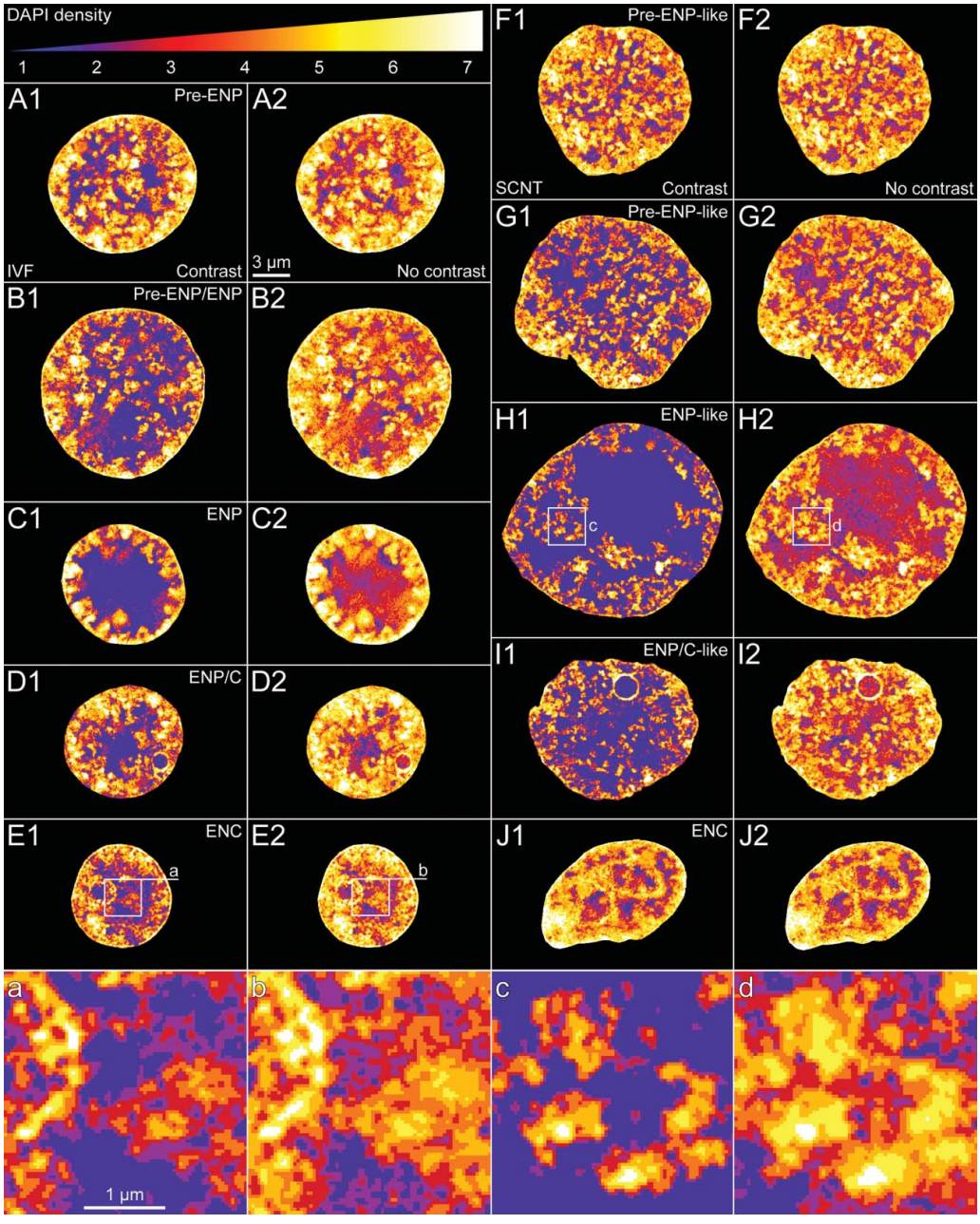

Figure 18. For figure legend, see page 583.

Differences between nuclei with regard to the space occupied by the interchromatin compartment reflect to some extent differences of chromatin compaction.[38,88] This was experimentally verified by showing that a brief incubation of living, cultured cells in hyperosmolar medium triggered the

formation of hypercondensed chromatin with a corresponding increase of the interchromatin compartment, although nuclear volumes even decreased in this case.[88] This effect was fully reversible, when cells were again incubated in normotonic medium. The most extreme case of chromatin domain compaction has been predicted by the polymer melt model, which has put doubts on the role of 30 nm thick chromatin loops in the formation of chromatin domains.[89,90] Whatever the true organization of CDCs and chromatin domains may be, we expect that a dynamic organization of these structures is required by functional necessity. Given the constrained movements of CTs, CDCs and chromatin domains, which occur continuously in the nucleus of a living cell, the width of IC-channels also changes continuously establishing numerous opportunities for transient spatial interactions between individual higher order structures. In line with dynamic changes we expect the formation of more or less space even between chromatin located in the interior of CDCs.

Differences in chromatin compaction, however, do not suffice to explain the huge variation in the size of the interchromatin compartment. We assume that the formation of a major lacuna as part of the interchromatin compartment of ENPs was prompted by a necessity of a large storage capacity for factors important for the survival of embryos at a time, when the further development of embryos depends on proteins and RNAs provided by the oocyte.[27] Accordingly, differences of the extent and width of IC-channels and lacunas between ENPs and ENCs likely reflect different amounts of macromolecules stored in the interchromatin compartment. The formation of a major lacuna may generate a mechanic force yielding a shift of CTs toward the nuclear periphery and possibly also to a higher overall compaction of CTs. However, the occasional observation of nuclei in embryos approaching major EGA, which failed to generate a major lacuna, but showed compact and well separated CTs, rather suggests that chromatin compaction is regulated by mechanisms acting directly on chromatin. Increased chromatin compaction can enforce a relative expansion of the interchromatin compartment.

In view of the limitations of current evidence the model shown in **Figure 20** should be regarded as an inevitable oversimplification. In addition to densely compacted silent chromatin the interior of chromatin domain clusters may still contain some transcriptionally competent chromatin. In order to become transcriptionally active, relocation of such chromatin into the PR may be required. Alternatively, finest IC-channels may expand and guide factors relevant for transcription and other functions into the interior of CDCs. The resolution of the current 3D-SIM study does not suffice to describe how chromatin domain clusters are organized in detail. We also wish to emphasize that this view is static and does not explain dynamic interactions between the aNC and the iNC. Despite these limitations, this view has the benefit to provide a coherent interpretation for a wide set of data presented both in this study and the literature, and may stimulate further experimental tests (see below, Perspectives).

Perspectives

Efforts to understand the structure and interactions of individual macromolecules (DNAs, RNAs and proteins) must be complemented by efforts to understand the large scale organization of the cell nucleus. The CT-IC model and other current models should be understood as attempts to provide a coherent view of structural and functional aspects of nuclear organization, including the structural organization and functional interactions of CTs.[84,91-99] We have attempted to provide a model view, drawn to scale, but given the methodological limitations of our study, this view may turn out to be misleading or even flatly wrong in some aspects – the usual fate of models in science. Understanding the functional nuclear organization in space and time requires advancements in understanding structure-function interactions at all levels of nuclear organization from molecules to the entire system. The long term goal of these efforts is the decipherment of universally valid, as well as species and cell-type-specific rules of nuclear architecture and their evolutionary origins. Evidence for conserved features throughout the whole range of eukaryotes, including comparisons with nucleoids in

Figure 18 (See previous page). Typical examples of nuclei with color-coded DAPI intensity classes recorded with 3D structured illumination microscopy in *in vitro* fertilized and cloned embryos. Panels A–E. Midplane SIM sections with color-coded DAPI intensity classes 1 to 7 from typical nuclear phenotypes observed in *in vitro* fertilized embryos (A, pre-ENP; B, transition from pre-ENP to ENP; C, ENP; D, ENP/C; E, ENC). Classes 1 to 7 present increasing DAPI intensity. The color code is presented at the top. Class 1 coded blue, class 2 purple, class 3 dark red, class 4 light red, class 5 orange, class 6 yellow and class 7 white. A1-E1 provide color-coded SIM sections after thresholding to remove patterns of concentric rings and diffuse background (see **Fig. 6**). A2–E2 show the same sections before thresholding. Note that the size of the areas occupied by the lowest DAPI density classes, in particular class 1, are strongly increased in thresholded compared to non-thresholded sections. For quantitative assessments of the nuclear topography of RNA polymerase II, H3K4me3 and H3K9me3 arrangements presented in **Figure 19** with respect to these DAPI intensity classes we used non-thresholded, color-coded SIM sections (for further details see Supplementary **Fig. S4**, Results and Extended Experimental Procedures). Panels F–J. Midplane SIM sections with color-coded DAPI intensity classes from typical nuclear phenotypes observed in cloned embryos (F, pre-ENP-like; G, transition from pre-ENP to ENP-like state; H, ENP-like; I, ENP/C-like; J, ENC), F1–J1 and F2–J2, color-coded SIM sections after and before thresholding. Panels a-d. Enlarged views of boxed areas depicted in 2 example nuclei (E1/E2, H1/H2) are presented in panels a/b and c/d. The enlarged box from the ENP-like nucleus shown in c demonstrates particularly well chromatin domain clusters (CDCs), separated by IC-channels (blue). Red color in the periphery of CDCs signifies less compact DAPI-stained chromatin, yellow and white colors more compacted DAPI-stained chromatin in the core part of CDCs. The strong difference between thresholded and corresponding non-thresholded images emphasizes limitations of our current approach with regard to the resolution achieved with 3D-SIM and the sensitivity of DAPI staining to distinguish unequivocally between chromatin and DNA-free parts of the interchromatin compartment. Bars: 3 μm for A1–J2; 1 μm for a-d.

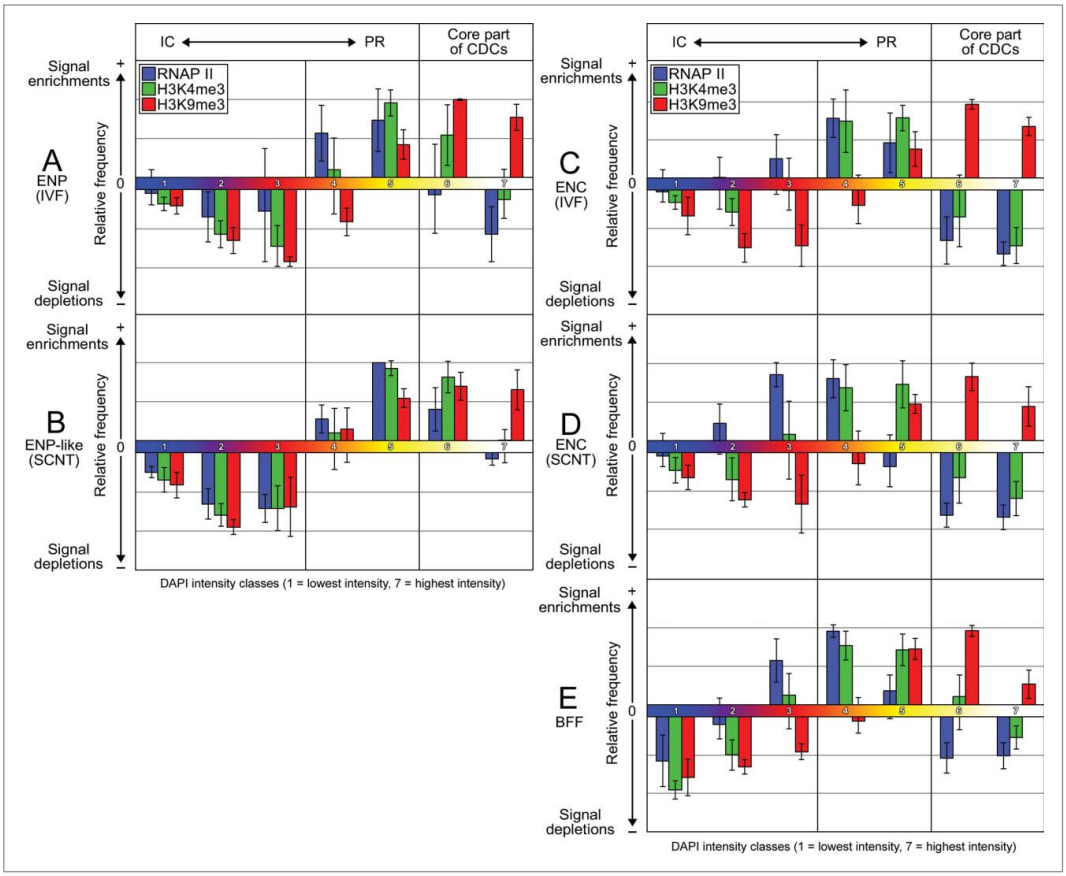

Figure 19. Quantitative analysis of topographical relationships between DAPI-stained chromatin, H3K4me3, H3K9me3 and RNA polymerase II in nuclei from *in vitro* fertilized embryos, cloned embryos and fetal bovine fibroblasts. A. ENPs from *in vitro* fertilized embryos (n = 20). B. ENCs from *in vitro* fertilized embryos (n = 20). C. ENP-like nuclei from cloned embryos (n = 15). D. ENCs from cloned embryos (n = 20). E. Nuclei from growing, non-synchronized fetal bovine fibroblast cultures (n = 20). For each sample A – E our analysis comprised 10 nuclei immunostained for H3K4me3 and H3K9me3 (cloned ENP-like n=7) and 10 nuclei immunostained for H3K4me3 and RNA polymerase II (cloned ENP-like n=8). In each nucleus 3 to 6 consecutive mid-nuclear SIM sections were analyzed. For each nucleus 7 DAPI intensity classes were distinguished in unthresholded midplane sections covering the entire range from lowest to highest pixel intensity values (**Fig. 18**; for details see Supplementary Information: Extended Experimental Procedures). The height of columns presents a relative measure for the overrepresentation (+) or underrepresentation (-) of H3K4me3 (green), H3K9me3 (red) and RNA polymerase II (blue) positive pixels, respectively, calculated as the relative frequency of such pixels in comparison to the number of DAPI positive pixels attributed to classes 1 to 7. For all tested combinations of DAPI, H3K4me3 and RNA Polymerse II thresholds (compare Supplementary **Figs. S2, S3 and S4**) the null-hypothesis of a random class assignment was rejected ($P < 10^{-15}$). A comparison of A-E indicates striking similarities of local RNA polymerase II, H3K4me3 and H3K9me3 assignments to the 7 DAPI intensity classes despite the striking differences between the global nuclear architectures of ENPs and ENP-like nuclei compared with ENCs and fibroblast nuclei. The overrepresentation of RNA polymerase II signals in class 4 ($P < 10^{-14}$) of ENPs, ENP-like nuclei, ENCs and fibroblast nuclei supports the hypothesis that the major transcriptionally active nuclear compartment is located at the periphery of chromatin domain clusters, called the perichromatin region (PR) (compare **Fig. 18**). In ENPs and ENCs of *in vitro* fertilized embryos (A, B) the immunostained RNA polymerase II carried a C-terminal domain (CTD) with a phosphorylated serine 5 (Ser5p), whereas the polymerase immunodetected in ENP-like nuclei and ENCs from cloned embryos (C, D), as well as fibroblast nuclei (E) carried a CTD with a phosphorylated serine 2 (S2P). The topography of RNA polymerase II in relation to the 7 DAPI intensity classes was essentially the same for both serine 2 and 5 phosphorylations.

prokaryotes as outgroups, should pave the way for the discovery of major selective constraints during the evolution of large genomes.

A solid descriptive basis of nuclear landscapes during development and differentiation sets the stage for studies of molecular mechanisms involved in the space-time organization of nuclei adapted to their functioning in a large set of cell types. Profound changes of nuclear architecture during early mammalian embryonic development (our present study) and terminal cell differentiation demonstrate the complexity of nuclear dynamics and their adaptive benefits for different functional tasks.[74] Clearly, changes of nuclear landscapes do not follow a simple deterministic pattern, but show an unexpected amount of variation even among cells of the same, distinct cell type. This variation may to some extent be of a stochastic nature but also reflect environmental influences starting with local influences from neighboring cells to general influences exerted within and outside a given organism. Single cell analyses are indispensable to explore this variability. Efforts to generate 1D maps of chemical modifications of nucleotides and histones along the genome and the direct or indirect binding of numerous proteins involved in transcription, splicing, replication and repair are indispensable. It is, however, equally important to understand the changing geometry of the nucleus and its structural compartmentalization starting from global parameters, such as size and shape, down to the space-time interactions at the low nanometer scale. Issues, such as the heterogeneity of local molecule concentrations, crowding effects, phase separation and entropic forces are coming to the forefront of research.[100-102] A scientific enterprise toward a full understanding of nuclear functions, such as gene regulation, DNA replication and repair,

requires understanding of the space-time dynamics of nuclear organization and necessitates a paradigmatic shift in research – from nuclear biochemistry to nuclear biophysics.

The resolution, currently achieved with 3D-SIM is still far away from the space-time resolution needed for an understanding of how macromolecules and macromolecular complexes interact and function within the aNC and how a reconfiguration of chromatin domain clusters may be triggered to expose DNA sequences embedded in compact core regions of CDCs within the perichromatin region and *vice versa* on functional demands. New possibilities to visualize specific proteins, RNAs and genes in the nucleus of living cells, together with advancements of light optical super resolution microscopy (for reviews see Cremer and Masters[103] and Renz[104]) provide a glimpse on future possibilities to study nuclear organization.[46,105,106] Whereas structured illumination microscopy currently allows a lateral resolution in the order of 100 nm and an axial resolution in the order of 300 nm, single molecule localization microscopy provides opportunities for a 3D resolution in the order of 30 nm and possibly even better in the future. A recent study demonstrated that DAPI (and other fluorescent dyes for DNA staining), can be effectively employed in single molecule localization microscopy.[107] Sheet microscopy combined with the ultra high resolution of localization microscopy bears the promise to study large numbers of nuclei in structurally intact organisms such as embryos or in thick tissue sections.[108] Such an approach avoids the disadvantages of microdissection of embryos in order to place each single cell directly on a cover glass. Methods of correlative microscopy are currently implemented for sequential imaging of one and the same nucleus first in the living cell and after fixation with increasing resolution, employing both super-resolution fluorescence microscopy and electron microscopy with its still unsurpassed resolution.[39,109]

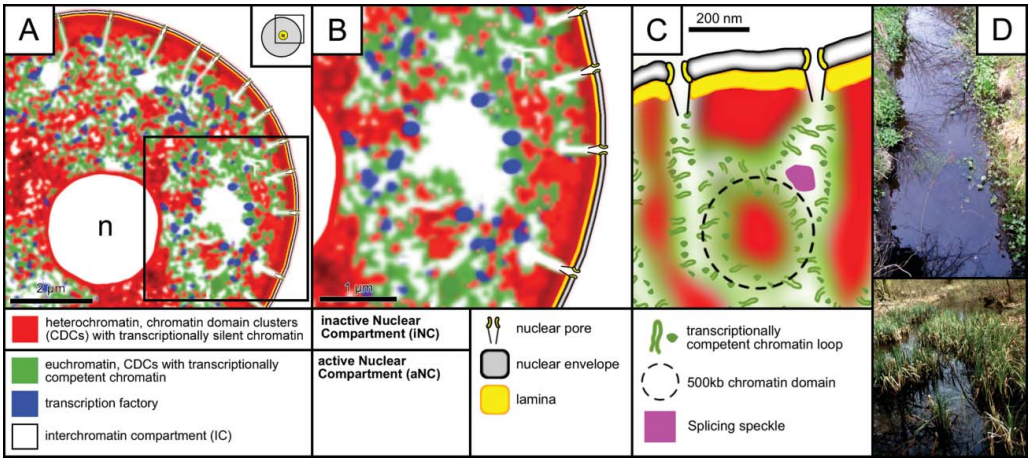

Figure 20. A high-resolution model view of the functional nuclear landscape. Evidence stems in part from the present study and in part from the literature (see Discussion). (**A** and **B**) Representative landscape of an ENC. B shows an enlargement of the boxed area in A. CTs are built up from interconnected basic chromatin domains with a DNA content in the order of a few hundred kbp, which form higher order chromatin structures, such as chromatin domain clusters (CDCs), chromosome arm and band domains (for further details see Discussion). Identification of individual structures in microscopic images requires their individual visualization. CDCs carry transcriptionally silent chromatin (red) in their interior. The less dense, transcriptionally competent chromatin (green) at the periphery of CDCs presents the perichromatin region (PR). It is enriched with transcription factories (blue) and represents the nuclear sub-compartment, where genes are transcribed. The PR lines the interchromatin compartment (IC), which starts with channels at nuclear pores and forms a 3-dimensional network throughout the nuclear interior. It extends between neighboring CTs but also throughout CTs. At numerous sites the IC forms larger lacunas, which contain nuclear bodies, such as splicing speckles. Considering the potential role of the IC in import-export functions, as well as functional interactions between nuclear bodies and machineries for transcription, co-transcriptional splicing, chromatin replication and repair acting within the PR, we propose that the PR and the IC provide the active nuclear compartment (aNC), whereas the compact interior of CDCs forms the inactive nuclear compartment (iNC). The nucleolus in A is marked with 'n'. (C). This model presents a hypothetical topography at still higher resolution envisaged for a landscape at the nuclear periphery with nuclear pores connected to IC channels. Little chromatin loops invade these channels, their size and hypothetical arrangements minimize problems of chromatin entanglements in the perichromatin region and interchromatin compartment. A dotted circle comprises a chromatin domain with a DNA content of about 500 kbp. Chromatin domains attached to the nuclear lamina (yellow) are connected with domains extended into the nuclear interior (D). Comparison of the nuclear landscape shown in C with little streams and ponds pervading a natural landscape. Note some vegetation expanding from embankments into the inner part of streams and ponds (images recorded in the Spreewald southeast of Berlin and provided by courtesy of Marion Cremer). Bars: 2 μm for A; 1 μm for B; 200 nm for C.

Future attempts to solve the structure-function conundrums of nuclear organization in space and time require a combination of advanced microscopic and biochemical approaches. So far, Hi-C based genome-wide studies of 3D genome organization with one exception yielded data only for cell populations.[110] Strong efforts, however, are made to increase their sensitivity to the point, where studies at the single cell level become feasible.[110] The combination of these methods with advanced 4D imaging methods will help to overcome the limitations of each method performed in isolation.

Experimental Procedures

See Supplementary Information for detailed descriptions of materials and protocols.

Ethics statement

No animal experiments were conducted. Oocytes for SCNT were recovered from ovaries of heifers and cows slaughtered for meat production.

Cultivation of early bovine embryos

In vitro fertilized and cloned bovine preimplantation embryos were generated as described.[19,35]

DNA and RNA synthesis in embryonic cell nuclei

DNA synthesis was studied by pulse labeling experiments with EdU.[37] BrUTP or BrU incorporation and immunodetection for the detection of RNA synthesis was performed using modifications of protocols described previously.[111,112]

Immunostainings

Immunodetection of histone modifications H3K4me3, H3K9me3 and H3S10p, RNA polymerase II-Ser2p, RNA polymerase II-Ser5p, SC-35 and B23, as a marker for nucleoli was performed as described.[36,37] A complete list of primary and secondary antibodies used in this study is provided in Extended Experimental Procedures.

3D confocal laser scanning microscopy (3D-CLSM)

Light optical serial sections from embryonic nuclei were obtained with a Leica TCS SP5 confocal laser scanning microscope using 10×, 20× or 63× objectives. Fluorochromes were excited using blue diode, argon, and helium-neon lasers with 405 nm, 488 nm and 594 nm laser lines, respectively.[19]

3D structured illumination microscopy (3D-SIM) and quantitative image evaluation

3D-SIM of embryonic nuclei was performed on a DeltaVision OMX V3 system (Applied Precision Imaging/GE Healthcare) with a lateral (x/y) resolution of ~120 nm and an axial (z) resolution of ~300 nm.[37] The system was equipped with a 100×/1.40 NA PlanApo oil immersion objective (Olympus), Cascade II:512 EMCCD cameras (Photometrics) and 405, 488 and 593 nm diode lasers. Image stacks were acquired with a z-distance of 125 nm and with 15 raw SIM images per plane (5 phases, 3 angles). The SI raw data were computationally reconstructed with channel specific measured OTFs using the softWoRX 4.0 software package (Applied Precision). Images from the different color channels were registered with alignment parameters obtained from calibration measurements with 0.2 μm diameter TetraSpeck beads (Invitrogen). The voxel size of the reconstructed images is 39.5 nm in x/y and 125 nm in z with 32-bit depth. For all subsequent image processing and data analysis, images were converted to 16-bit composite tif-stacks. Image stacks were processed using ImageJ 1.45b (http://rsb.info.nih.gov/ij/). DAPI intensity classes were established as described.[37] The statistical comparison of the localization of positive pixels for histone modifications H3K4me3, H3K9me3, RNA polymerase II-Ser2p and RNA polymerase II-Ser5p signals within these DAPI intensity classes was achieved with dedicated software written by V.S. and A.S. on the basis of the software package for scientific computing R 2.15 (http://www.r-project.org/).

RNA-Seq data analysis

Raw data files generated by Graf et al.[27] available at GEO (GSE52415). Data analysis performed as described in Graf et al.[27]

Assembly of images and graphs

Image stacks were processed using ImageJ 1.45b (http://rsb.info.nih.gov/ij/). Figures were prepared with Adobe Photoshop CS4 (http://www.adobe.com/). Combined box-/scatterplots were generated using the software package R 2.15 and bar charts with Microsoft Excel 2003/2007.

Statistical analyses

Chi-square goodness-of-fit tests were employed to assess the significancy levels of over- and underrepresentation of signals compared to the DAPI intensity levels. All other significancy levels were determined by Wilcoxon rank-sum test.

Author Contributions

T.C., J.P., V.Z., and E.W. designed research, J.P., V.Z., A.B., D.K., T.G., and A.W. performed experiments, J.P., A.B., V.S., and A.S. analyzed data, T.C., J.P., E.W., and V.Z. wrote the paper.

Disclosure of Potential Conflicts of Interest

No potential conflicts of interest were disclosed.

Acknowledgments

We are grateful for expert assistance of Myriam Reichenbach, Andrea Beck and Nicolas Saucedo in the generation of IVF embryos used in the present study. We also gratefully acknowledge numerous discussions with Marion Cremer and her critical reading of preliminary versions of the manuscript.

Funding

This study was supported by grants from the Deutsche Forschungsgemeinschaft to T.C, E.W. and V.Z. (CR 59/26, FOR 1041, ZA 425/1–3). In addition, research of E.W. and V.Z. was supported by the EU grant Plurisys, HEALTH-F4-2009-223485 FP7 Health 534 project.

Supplemental Material

Supplemental data for this article can be accessed on the publisher's website: http://www.tandfonline.com/kncl

References

1. Blobel G. Gene gating: a hypothesis. Proc Nat Acad Sci U S A 1985; 82:8527-9; PMID:3866238; http://dx.doi.org/10.1073/pnas.82.24.8527
2. Bickmore WA, van Steensel B. Genome architecture: domain organization of interphase chromosomes. Cell 2013; 152:1270-84; PMID:23498936; http://dx.doi.org/10.1016/j.cell.2013.02.001
3. Cardoso MC, Schneider K, Martin RM, Leonhardt H. Structure, function and dynamics of nuclear subcompartments. Curr Opin Cell Biol 2012; 24:79-85; PMID:22227228; http://dx.doi.org/10.1016/j.ceb.2011.12.009
4. Cavalli G, Misteli T. Functional implications of genome topology. Nat Struct Mol Biol 2013; 20:290-9; PMID:23463314; http://dx.doi.org/10.1038/nsmb.2474
5. de Graaf CA, van Steensel B. Chromatin organization: form to function. Curr Opin Genet Dev 2013; 23:185-90; PMID:23274160; http://dx.doi.org/10.1016/j.gde.2012.11.011
6. Cremer T, Cremer M. Chromosome territories. Cold Spring Harb Perspect Biol 2010; 2:a003889; PMID:20300217; http://dx.doi.org/10.1101/cshperspect.a003889
7. Cremer T, Zakhartchenko V. Nuclear architecture in developmental biology and cell specialisation. Reprod, Fert Dev 2011; 23:94-106; PMID:21366985; http://dx.doi.org/10.1071/RD10249
8. Ghirlando R, Felsenfeld G. Chromatin structure outside and inside the nucleus. Biopolymers 2013; 99:225-32; PMID:23348669; http://dx.doi.org/10.1002/bip.22157
9. Gibcus JH, Dekker J. The hierarchy of the 3D genome. Mol Cell 2013; 49:773-82; PMID:23473598; http://dx.doi.org/10.1016/j.molcel.2013.02.011
10. Hubner MR, Spector DL. Chromatin dynamics. Annu Rev Biophys 2010; 39:471-89; PMID:20462379; http://dx.doi.org/10.1146/annurev.biophys.093008.131348
11. Lanctot C, Cheutin T, Cremer M, Cavalli G, Cremer T. Dynamic genome architecture in the nuclear space: regulation of gene expression in three dimensions. Nat Rev Genet 2007; 8:104-15; PMID:17230197; http://dx.doi.org/10.1038/nrg2041
12. Meister P, Mango SE, Gasser SM. Locking the genome: nuclear organization and cell fate. Curr Opin Genet Dev 2011; 21:167-74; PMID:21345665; http://dx.doi.org/10.1016/j.gde.2011.01.023
13. Pederson T. The spatial organization of the genome in mammalian cells. Curr Opin Genet Dev 2004; 14:203-9; PMID:15196468; http://dx.doi.org/10.1016/j.gde.2004.02.008
14. Rapkin LM, Anchel DR, Li R, Bazett-Jones DP. A view of the chromatin landscape. Micron 2012; 43:150-8; PMID:22172345; http://dx.doi.org/10.1016/j.micron.2011.11.007
15. Zhang J, Poh HM, Peh SQ, Sia YY, Li G, Mulawadi FH, Goh Y, Fullwood MJ, Sung WK, Ruan X, et al. ChIA-PET analysis of transcriptional chromatin interactions. Methods 2012; 58:289-99; PMID:22926262; http://dx.doi.org/10.1016/j.ymeth.2012.08.009
16. Ahmed K, Dehghani H, Rugg-Gunn P, Fussner E, Rossant J, Bazett-Jones DP. Global chromatin architecture reflects pluripotency and lineage commitment in the early mouse embryo. PloS One 2010; 5:e10531; PMID:20479880; http://dx.doi.org/10.1371/journal.pone.0010531
17. Aguirre-Lavin T, Adenot P, Bonnet-Garnier A, Lehmann G, Fleurot R, Boulesteix C, Debey P, Beaujean N. 3D-FISH analysis of embryonic nuclei in mouse highlights several abrupt changes of nuclear organization during preimplantation development. BMC Dev Biol 2012; 12:30; PMID:23095683; http://dx.doi.org/10.1186/1471-213X-12-30
18. Brero A, Hao R, Schieker M, Wierer M, Wolf E, Cremer T, Zakhartchenko V. Reprogramming of active and repressive histone modifications following nuclear transfer with rabbit mesenchymal stem cells and adult fibroblasts. Cloning Stem Cells 2009; 11:319-29; PMID:19508112; http://dx.doi.org/10.1089/clo.2008.0083
19. Koehler D, Zakhartchenko V, Froenicke L, Stone G, Stanyon R, Wolf E, Cremer T, Brero A. Changes of higher order chromatin arrangements during major genome activation in bovine preimplantation embryos. Exp Cell Res 2009; 315:2053-63; PMID:19254712; http://dx.doi.org/10.1016/j.yexcr.2009.02.016
20. Merico V, Barbieri J, Zuccotti M, Joffe B, Cremer T, Redi CA, Solovei I, Garagna S. Epigenomic differentiation in mouse preimplantation nuclei of biparental, parthenote and cloned embryos. Chromosome Res: Int J Mol Supramol Evolut Aspects Chromosome Biol 2007; 15:341-60; PMID:17447149
21. Salvaing J, Aguirre-Lavin T, Boulesteix C, Lehmann G, Debey P, Beaujean N. 5-Methylcytosine and 5-hydroxymethylcytosine spatiotemporal profiles in the mouse zygote. PloS One 2012; 7:e38156; PMID:22693592; http://dx.doi.org/10.1371/journal.pone.0038156
22. Yang CX, Liu Z, Fleurot R, Adenot P, Duranthon V, Vignon X, Zhou Q, Renard JP, Beaujean N. Heterochromatin reprogramming in rabbit embryos after fertilization, intra-, and inter-species SCNT correlates with preimplantation development. Reproduction 2013; 145:149-59; PMID:23221012; http://dx.doi.org/10.1530/REP-11-0421
23. Harmon B, Sedat J. Cell-by-cell dissection of gene expression and chromosomal interactions reveals consequences of nuclear reorganization. PLoS Biol 2005; 3:e67; PMID:15737020; http://dx.doi.org/10.1371/journal.pbio.0030067
24. Kosak ST, Groudine M. Form follows function: The genomic organization of cellular differentiation. Genes Development 2004; 18:1371-84; PMID:15198979; http://dx.doi.org/10.1101/gad.1209304
25. Wuensch A, Habermann FA, Kurosaka S, Klose R, Zakhartchenko V, Reichenbach HD, Sinowatz F, McLaughlin KJ, Wolf E. Quantitative monitoring of pluripotency gene activation after somatic cloning in cattle. Biol Reprod 2007; 76:983-91; PMID:17314316; http://dx.doi.org/10.1095/biolreprod.106.058776
26. Kanka J, Kepkova K, Nemcova L. Gene expression during minor genome activation in preimplantation bovine development. Theriogenology 2009; 72:572-83; PMID:19501393; http://dx.doi.org/10.1016/j.theriogenology.2009.04.014
27. Graf A, Krebs S, Zakhartchenko V, Schwalb B, Blum H, Wolf E. Fine mapping of genome activation in bovine embryos by RNA sequencing. Proc Nat Acad Sci U S A 2014; 111:4139-44; PMID:24591639
28. Tadros W, Lipshitz HD. The maternal-to-zygotic transition: a play in two acts. Development 2009; 136:3033-42; PMID:19700615; http://dx.doi.org/10.1242/dev.033183
29. Li L, Lu X, Dean J. The maternal to zygotic transition in mammals. Mol Aspects Med 2013; 34:919-38; PMID:23352575; http://dx.doi.org/10.1016/j.mam.2013.01.003
30. Badr H, Bongioni G, Abdoon AS, Kandil O, Puglisi R. Gene expression in the in vitro-produced preimplantation bovine embryos. Zygote 2007; 15:355-67; PMID:17967215; http://dx.doi.org/10.1017/S0967199407004315
31. Camous S, Kopecny V, Flechon JE. Autoradiographic detection of the earliest stage of [3H]-uridine incorporation into the cow embryo. Biol Cell 1986; 58:195-200; PMID:2436695; http://dx.doi.org/10.1111/j.1768-322X.1986.tb00506.x
32. Memili E, First NL. Zygotic and embryonic gene expression in cow: a review of timing and mechanisms of early gene expression as compared with other species. Zygote 2000; 8:87-96; PMID:10840878; http://dx.doi.org/10.1017/S0967199400000861
33. Misirlioglu M, Page GP, Sagirkaya H, Kaya A, Parrish JJ, First NL, Memili E. Dynamics of global transcriptome in bovine matured oocytes and preimplantation embryos. Proc Nat Acad Sci U S A 2006; 103:18905-10; PMID:17142320; http://dx.doi.org/10.1073/pnas.0608247103
34. Vigneault C, Gravel C, Vallee M, McGraw S, Sirard MA. Unveiling the bovine embryo transcriptome during the maternal-to-embryonic transition. Reproduction 2009; 137:245-57; PMID:18987256; http://dx.doi.org/10.1530/REP-08-0079
35. Popken J, Koehler D, Brero A, Wuensch A, Guengoer T, Thormeyer T, Wolf E, Cremer T, Zakhartchenko V. Positional changes of a pluripotency marker gene during structural reorganization of fibroblast nuclei in cloned early bovine embryos. Nucleus 5:6; http://dx.doi.org/10.4161/19491034.2014.979712 (Under Review) 2014.
36. Markaki Y, Gunkel M, Schermelleh L, Beichmanis S, Neumann J, Heidemann M, Leonhardt H, Eick D, Cremer C, Cremer T. Functional nuclear organization of transcription and DNA replication: a topographical marriage between chromatin domains and the interchromatin compartment. Cold Spring Harbor Symposia Quant Biol 2010; 75:475-92; PMID:21467142; http://dx.doi.org/10.1101/sqb.2010.75.042
37. Markaki Y, Smeets D, Fiedler S, Schmid VJ, Schermelleh L, Cremer T, Cremer M. The potential of 3D-FISH and super-resolution structured illumination microscopy for studies of 3D nuclear architecture: 3D structured illumination microscopy of defined chromosomal structures visualized by 3D (immuno)-FISH opens new perspectives for studies of nuclear architecture. BioEssays: News Reviews Mol Cell Dev Biology 2012; 34:412-26; PMID:22508100; http://dx.doi.org/10.1002/bies.201100176
38. Rouquette J, Genoud C, Vazquez-Nin GH, Kraus B, Cremer T, Fakan S. Revealing the high-resolution three-dimensional network of chromatin and interchromatin space: a novel electron-microscopic approach to reconstructing nuclear architecture. Chromosome Res: Int J Mol Supramol Evol Aspects Chromosome Biol 2009; 17:801-10; PMID:19731052; http://dx.doi.org/10.1007/s10577-009-9070-x
39. Huebner B, Cremer T, Neumann J. Correlative microscopy of individual cells: sequential application of microscopic systems with increasing resolution to study the nuclear landscape. Methods Mol Biol 2013; 1042:299-336; PMID:23980016; http://dx.doi.org/10.1007/978-1-62703-526-2_21
40. Smeets D, Markaki Y, Schmid VJ, Kraus F, Tattermusch A, Cerase A, Sterr M, Fiedler S, Demmerle J, Popken J, et al. Three-dimensional super-resolution microscopy of the inactive X chromosome territory reveals a collapse of its active nuclear compartment harboring distinct Xist RNA foci. Epigenetics Chromatin 2014; 7:8; PMID:25057298; http://dx.doi.org/10.1186/1756-8935-7-8
41. Rouquette J, Cremer C, Cremer T, Fakan S. Functional nuclear architecture studied by microscopy: present and future. Int Rev Cell Mol Biol 2010; 282:1-90; PMID:20630466; http://dx.doi.org/10.1016/S1937-6448(10)82001-5
42. Cremer T, Kreth G, Koester H, Fink RH, Heintzmann R, Cremer M, Solovei I, Zink D, Cremer C. Chromosome territories, interchromatin domain compartment, and nuclear matrix: an integrated view of the functional nuclear architecture. Crit Rev Eukaryotic Gene Exp 2000; 10:179-212; PMID:11186332; http://dx.doi.org/10.1615/CritRevEukarGeneExpr.v10.i2.60
43. Cremer T, Cremer C. Chromosome territories, nuclear architecture and gene regulation in mammalian cells. Nat Rev Genet 2001; 2:292-301; PMID:11283701; http://dx.doi.org/10.1038/35066075
44. Mor A, Suliman S, Ben-Yishay R, Yunger S, Brody Y, Shav-Tal Y. Dynamics of single mRNP nucleocytoplasmic transport and export through the nuclear pore in living cells. Nat Cell Biol 2010; 12:543-52;

PMID:20453848; http://dx.doi.org/10.1038/ncb2056
45. Cmarko D, Verschure PJ, Martin TE, Dahmus ME, Krause S, Fu XD, van Driel R, Fakan S. Ultrastructural analysis of transcription and splicing in the cell nucleus after bromo-UTP microinjection. Mol Biol Cell 1999; 10:211-23; PMID:9880337; http://dx.doi.org/10.1091/mbc.10.1.211
46. Maharana S, Sharma D, Shi X, Shivashankar GV. Dynamic organization of transcription compartments is dependent on functional nuclear architecture. Biophys J 2012; 103:851-9; PMID:23009834; http://dx.doi.org/10.1016/j.bpj.2012.06.036
47. Niedojadlo J, Perret-Vivancos C, Kalland KH, Cmarko D, Cremer T, van Driel R, Fakan S. Transcribed DNA is preferentially located in the perichromatin region of mammalian cell nuclei. Exp Cell Res 2011; 317:433-44; PMID:21056558; http://dx.doi.org/10.1016/j.yexcr.2010.10.026
48. Jaunin F, Visser AE, Cmarko D, Aten JA, Fakan S. Fine structural in situ analysis of nascent DNA movement following DNA replication. Exp Cell Res 2000; 260:313-23; PMID:11035926; http://dx.doi.org/10.1006/excr.2000.4999
49. Zhou VW, Goren A, Bernstein BE. Charting histone modifications and the functional organization of mammalian genomes. Nat Rev Genet 2011; 12:7-18; PMID:21116306; http://dx.doi.org/10.1038/nrg2905
50. Schnedl W, Breitenbach M, Stranzinger G. Mithramycin and DIPI: a pair of fluorochromes specific for GC-and AT-rich DNA respectively. Hum Genet 1977; 36:299-305; PMID:67077; http://dx.doi.org/10.1007/BF00446280
51. Kapuscinski J. DAPI: a DNA-specific fluorescent probe. Biotechnic Histochem: Off Pub Biol Stain Comm 1995; 70:220-33; http://dx.doi.org/10.3109/10520299509108199
52. Bink K, Walch A, Feuchtinger A, Eisenmann H, Hutzler P, Hofler H, Werner M. TO-PRO-3 is an optimal fluorescent dye for nuclear counterstaining in dual-colour FISH on paraffin sections. Histochem Cell Biol 2001; 115:293-9; PMID:11405057
53. Prigent C, Dimitrov S. Phosphorylation of serine 10 in histone H3, what for? J Cell Sci 2003; 116:3677-85; PMID:12917355; http://dx.doi.org/10.1242/jcs.00735
54. Chan PK, Liu QR, Durban E. The major phosphorylation site of nucleophosmin (B23) is phosphorylated by a nuclear kinase II. Biochem J 1990; 270:549-52; PMID:2400401
55. Cremer C. Optics far beyond the diffraction limit. In: Traeger F, ed. Springer Handbook of Lasers and Optics, Berlin,: Springer, 2012:1359-97.
56. Schermelleh L, Heintzmann R, Leonhardt H. A guide to super-resolution fluorescence microscopy. J Cell Biol 2010; 190:165-75; PMID:20643879; http://dx.doi.org/10.1083/jcb.201002018
57. Guetg C, Santoro R. Formation of nuclear heterochromatin: the nucleolar point of view. Epigenetics: Off J DNA Methylation Soc 2012; 7:811-4; PMID:22735386; http://dx.doi.org/10.4161/epi.21072
58. Nemeth A, Conesa A, Santoyo-Lopez J, Medina I, Montaner D, Peterfia B, Solovei I, Cremer T, Dopazo J, Langst G. Initial genomics of the human nucleolus. PLoS Genet 2010; 6:e1000889; PMID:20361057; http://dx.doi.org/10.1371/journal.pgen.1000889
59. Zinner R, Albiez H, Walter J, Peters AH, Cremer T, Cremer M. Histone lysine methylation patterns in human cell types are arranged in distinct three-dimensional nuclear zones. Histochem Cell Biol 2006; 125:3-19; PMID:16215742; http://dx.doi.org/10.1007/s00418-005-0049-1
60. Mitchell JA, Fraser P. Transcription factories are nuclear subcompartments that remain in the absence of transcription. Genes Dev 2008; 22:20-5; PMID:18172162; http://dx.doi.org/10.1101/gad.454008
61. Probst AV, Almouzni G. Heterochromatin establishment in the context of genome-wide epigenetic reprogramming. Trends Genet: TIG 2011; 27:177-85; PMID:21497937; http://dx.doi.org/10.1016/j.tig.2011.02.002
62. Kopecny V, Fakan S, Pavlok A, Pivko J, Grafenau P, Biggiogera M, Leser G, Martin TE. Immunoelectron microscopic localization of small nuclear ribonucleoproteins during bovine early embryogenesis. Mol Reprod Dev 1991; 29:209-19; PMID:1834097; http://dx.doi.org/10.1002/mrd.1080290302
63. Chandra T, Kirschner K, Thuret JY, Pope BD, Ryba T, Newman S, Ahmed K, Samarajiwa SA, Salama R, Carroll T, et al. Independence of repressive histone marks and chromatin compaction during senescent heterochromatic layer formation. Mol Cell 2012; 47:203-14; PMID:22795131; http://dx.doi.org/10.1016/j.molcel.2012.06.010
64. Illner D, Zinner R, Handtke V, Rouquette J, Strickfaden H, Lanctot C, Conrad M, Seiler A, Imhof A, Cremer T, et al. Remodeling of nuclear architecture by the thiodioxopiperazine metabolite chaetocin. Exp Cell Res 2010; 316:1662-80; PMID:20302859; http://dx.doi.org/10.1016/j.yexcr.2010.03.008
65. Memili E, Dominko T, First NL. Onset of transcription in bovine oocytes and preimplantation embryos. Mol Reprod Dev 1998; 51:36-41; PMID:9712315; http://dx.doi.org/10.1002/(SICI)1098-2795(199809)51:1%3c36::AID-MRD4%3e3.0.CO;2-X
66. Papantonis A, Cook PR. Transcription factories: genome organization and gene regulation. Chem Rev 2013; 113:8683-705; PMID:23597155; http://dx.doi.org/10.1021/cr300513p
67. Eick D, Geyer M. The RNA polymerase II carboxy-terminal domain (CTD) code. Chem Rev 2013; 113:8456-90; PMID:23952966; http://dx.doi.org/10.1021/cr400071f
68. Heidemann M, Hintermair C, Voss K, Eick D. Dynamic phosphorylation patterns of RNA polymerase II CTD during transcription. Biochimica et Biophysica Acta 2013; 1829:55-62; PMID:22982363; http://dx.doi.org/10.1016/j.bbagrm.2012.08.013
69. Fragouli E, Alfarawati S, Spath K, Jaroudi S, Sarasa J, Enciso M, Wells D. The origin and impact of embryonic aneuploidy. Hum Genet 2013; 132:1001-13; PMID:23620267; http://dx.doi.org/10.1007/s00439-013-1309-0
70. Demyda-Peyras S, Dorado J, Hidalgo M, Anter J, De Luca L, Genero E, Moreno-Millan M. Effects of oocyte quality, incubation time and maturation environment on the number of chromosomal abnormalities in IVF-derived early bovine embryos. Reprod Fertility Dev 2013; 25:1077-84; PMID:23182337; http://dx.doi.org/10.1071/RD12140
71. Viuff D, Rickords L, Offenberg H, Hyttel P, Avery B, Greve T, Olsaker I, Williams JL, Callesen H, Thomsen PD. A high proportion of bovine blastocysts produced in vitro are mixoploid. Biol Reprod 1999; 60:1273-8; PMID:10330080; http://dx.doi.org/10.1095/biolreprod60.6.1273
72. Leidenfrost S, Boelhauve M, Reichenbach M, Gungor T, Reichenbach HD, Sinowatz F, Wolf E, Habermann FA. Cell arrest and cell death in mammalian preimplantation development: lessons from the bovine model. PloS One 2011; 6:e22121; PMID:21811561; http://dx.doi.org/10.1371/journal.pone.0022121
73. Leidenfrost S. Zellentwicklung, Zelltod und die Expression Apoptose-assoziierter Gene in der frühen Embryogenese beim Rind. Lehrstuhl für Allgemeine Anatomie, Histologie und Embryologie. Munich: Ludwig-Maximilians-University, http://edoc.ub.uni-muenchen.de/11663/, 2009.
74. Solovei I, Kreysing M, Lanctot C, Kosem S, Peichl L, Cremer T, Guck J, Joffe B. Nuclear architecture of rod photoreceptor cells adapts to vision in mammalian evolution. Cell 2009; 137:356-68; PMID:19379699; http://dx.doi.org/10.1016/j.cell.2009.01.052
75. Chuang CH, Carpenter AE, Fuchsova B, Johnson T, de Lanerolle P, Belmont AS. Long-range directional movement of an interphase chromosome site. Curr Biol 2006; 16:825-31; PMID:16631592; http://dx.doi.org/10.1016/j.cub.2006.03.059
76. Osborne CS, Chakalova L, Mitchell JA, Horton A, Wood AL, Bolland DJ, Corcoran AE, Fraser P. Myc dynamically and preferentially relocates to a transcription factory occupied by Igh. PLoS Biol 2007; 5:e192; PMID:17622196; http://dx.doi.org/10.1371/journal.pbio.0050192
77. Roukos V, Voss TC, Schmidt CK, Lee S, Wangsa D, Misteli T. Spatial dynamics of chromosome translocations in living cells. Science 2013; 341:660-4; PMID:23929981; http://dx.doi.org/10.1126/science.1237150
78. Bridger JM, Arican-Gotkas H, Foster H, Godwin L, Harvey A, Kill IR, Knight M, Mehta IS, Ahmed M. The non-random repositioning of whole chromosomes and individual gene loci in interphase nuclei and its relevance in disease, infection, aging, and aancer. In: Schirmer EC, de las Heras JI, eds. Cancer Biology and the Nuclear Envelope, New York: Springer, 2014, 263-79.
79. Mehta IS, Eskiw CH, Arican HD, Kill IR, Bridger JM. Farnesyltransferase inhibitor treatment restores chromosome territory positions and active chromosome dynamics in Hutchinson-Gilford progeria syndrome cells. Genome Biol 2011; 12:R74; PMID:21838864; http://dx.doi.org/10.1186/gb-2011-12-8-r74
80. Strickfaden H, Zunhammer A, van Koningsbruggen S, Kohler D, Cremer T. 4D chromatin dynamics in cycling cells: theodor boveri's hypotheses revisited. Nucleus 2010; 1:284-97; PMID:21327076; http://dx.doi.org/10.4161/nucl.1.3.11969
81. Walter J, Schermelleh L, Cremer M, Tashiro S, Cremer T. Chromosome order in HeLa cells changes during mitosis and early G1, but is stably maintained during subsequent interphase stages. J Cell Biol 2003; 160:685-97; PMID:12604593; http://dx.doi.org/10.1083/jcb.200211103
82. Hihara S, Pack CG, Kaizu K, Tani T, Hanafusa T, Nozaki T, Takemoto S, Yoshimi T, Yokota H, Imamoto N, et al. Local nucleosome dynamics facilitate chromatin accessibility in living mammalian cells. Cell Rep 2012; 2:1645-56; PMID:23246002; http://dx.doi.org/10.1016/j.celrep.2012.11.008
83. Bornfleth H, Edelmann P, Zink D, Cremer T, Cremer C. Quantitative motion analysis of subchromosomal foci in living cells using four-dimensional microscopy. Biophys J 1999; 77:2871-86; PMID:10545385; http://dx.doi.org/10.1016/S0006-3495(99)77119-5
84. Dixon JR, Selvaraj S, Yue F, Kim A, Li Y, Shen Y, Hu M, Liu JS, Ren B. Topological domains in mammalian genomes identified by analysis of chromatin interactions. Nature 2012; 485:376-80; PMID:22495300; http://dx.doi.org/10.1038/nature11082
85. Bernardi G. The genome: an isochore ensemble and its evolution. Ann N Y Acad Sci 2012; 1267:31-4; PMID:22954213; http://dx.doi.org/10.1111/j.1749-6632.2012.06591.x
86. Lieberman-Aiden E, van Berkum NL, Williams L, Imakaev M, Ragoczy T, Telling A, Amit I, Lajoie BR, Sabo PJ, Dorschner MO, et al. Comprehensive mapping of long-range interactions reveals folding principles of the human genome. Science 2009; 326:289-93; PMID:19815776; http://dx.doi.org/10.1126/science.1181369
87. Baddeley D, Chagin VO, Schermelleh L, Martin S, Pombo A, Carlton PM, Gahl A, Domaing P, Birk U, Leonhardt H, et al. Measurement of replication structures at the nanometer scale using super-resolution light microscopy. Nucleic Acids Res 2010; 38:e8; PMID:19864256; http://dx.doi.org/10.1093/nar/gkp901
88. Albiez H, Cremer M, Tiberi C, Vecchio L, Schermelleh L, Dittrich S, Kupper K, Joffe B, Thormeyer T,

von Hase J, et al. Chromatin domains and the interchromatin compartment form structurally defined and functionally interacting nuclear networks. Chromosome Res: Int J Mol Supramol Evol Aspects Chromosome Biol 2006; 14:707-33; PMID:17115328; http://dx.doi.org/10.1007/s10577-006-1086-x

89. Joti Y, Hikima T, Nishino Y, Kamada F, Hihara S, Takata H, Ishikawa T, Maeshima K. Chromosomes without a 30-nm chromatin fiber. Nucleus 2012; 3:404-10; PMID:22825571; http://dx.doi.org/10.4161/nucl.21222
90. Eltsov M, Maclellan KM, Maeshima K, Frangakis AS, Dubochet J. Analysis of cryo-electron microscopy images does not support the existence of 30-nm chromatin fibers in mitotic chromosomes in situ. Proc Nat Acad Sci U S A 2008; 105:19732-7; PMID:19064912; http://dx.doi.org/10.1073/pnas.0810057105
91. Munkel C, Eils R, Dietzel S, Zink D, Mehring C, Wedemann G, Cremer T, Langowski J. Compartmentalization of interphase chromosomes observed in simulation and experiment. J Mol Biol 1999; 285:1053-65; PMID:9887267; http://dx.doi.org/10.1006/jmbi.1998.2361
92. Kreth G, Finsterle J, von Hase J, Cremer M, Cremer C. Radial arrangement of chromosome territories in human cell nuclei: a computer model approach based on gene density indicates a probabilistic global positioning code. Biophys J 2004; 86:2803-12; PMID:15111398; http://dx.doi.org/10.1016/S0006-3495(04)74333-7
93. Dehghani H, Dellaire G, Bazett-Jones DP. Organization of chromatin in the interphase mammalian cell. Micron 2005; 36:95-108; PMID:15629642; http://dx.doi.org/10.1016/j.micron.2004.10.003
94. Branco MR, Pombo A. Intermingling of chromosome territories in interphase suggests role in translocations and transcription-dependent associations. PLoS Biol 2006; 4:e138; PMID:16623600; http://dx.doi.org/10.1371/journal.pbio.0040138
95. Mirny LA. The fractal globule as a model of chromatin architecture in the cell. Chromosome Res: Int J Mol Supramol Evol Aspects Chromosome Biol 2011; 19:37-51; PMID:21274616; http://dx.doi.org/10.1007/s10577-010-9177-0
96. Halverson JD, Smrek J, Kremer K, Grosberg AY. From a melt of rings to chromosome territories: the role of topological constraints in genome folding. Rep Prog Phys Phys Soc 2014; 77:022601; PMID:24472896; http://dx.doi.org/10.1088/0034-4885/77/2/022601
97. Jerabek H, Heermann D. How chromatin looping and nuclear envelope attachment affect genome organization in eukaryotic cell nuclei. Int Rev Cell Mol Biol 2014; 307:351-81; PMID:24380599; http://dx.doi.org/10.1016/B978-0-12-800046-5.00010-2
98. Maeshima K, Imai R, Tamura S, Nozaki T. Chromatin as dynamic 10-nm fibers. Chromosoma 2014; 123:225-37; PMID:24737122; http://dx.doi.org/10.1007/s00412-014-0460-2
99. Barbieri M, Fraser J, Lavitas LM, Chotalia M, Dostie J, Pombo A, Nicodemi M. A polymer model explains the complexity of large-scale chromatin folding. Nucleus 2013; 4:267-73; PMID:23823730; http://dx.doi.org/10.4161/nucl.25432
100. Pederson T. Chapter one-the nuclear physique. Int Rev Cell Mol Biol. 2014; 307:1-13. doi: 10.1016/B978-0-12-800046-5.00001-1
101. Hancock R, Jeon KW. Preface. New models of the cell nucleus: crowding, entropic forces, phase separation, and fractals. Int Rev Cell Mol Biol 2014; 307:xiii; PMID:24380603
102. Woringer M, Darzacq X, Izeddin I. Geometry of the nucleus: a perspective on gene expression regulation. Curr Opin Chem Biol 2014; 20C:112-9; PMID:24981829; http://dx.doi.org/10.1016/j.cbpa.2014.05.009
103. Cremer C, Masters BR. Resolution enhancement techniques in microscopy. EPJ H 2013; 38:281-344; http://dx.doi.org/10.1140/epjh/e2012-20060-1
104. Renz M. Fluorescence microscopy-a historical and technical perspective. Cytometry A 2013; 83:767-79; PMID:23585290; http://dx.doi.org/10.1002/cyto.a.22295
105. Chen B, Gilbert LA, Cimini BA, Schnitzbauer J, Zhang W, Li GW, Park J, Blackburn EH, Weissman JS, Qi LS, et al. Dynamic imaging of genomic loci in living human cells by an optimized CRISPR/Cas system. Cell 2013; 155:1479-91; PMID:24360272; http://dx.doi.org/10.1016/j.cell.2013.12.001
106. Ma H, Reyes-Gutierrez P, Pederson T. Visualization of repetitive DNA sequences in human chromosomes with transcription activator-like effectors. Proc Nat Acad Sci U S A 2013; 110:21048-53; PMID:24324157; http://dx.doi.org/10.1073/pnas.1319097110
107. Szczurek AT, Prakash K, Lee HK, Zurek-Biesiada DJ, Best G, Hagmann M, Dobrucki JW, Cremer C, Birk U. Single molecule localization microscopy of the distribution of chromatin using Hoechst and DAPI fluorescent probes. Nucleus 2014; 5:331-340; PMID:24945151; http://dx.doi.org/10.4161/nucl.29564
108. Hu YS, Zimmerley M, Li Y, Watters R, Cang H. Single-molecule super-resolution light-sheet microscopy. Chemphyschem: Eur J Chem Phys Phys Chem 2014; 15:577-86; PMID:24615819; http://dx.doi.org/10.1002/cphc.201300732
109. Kruhlak MJ. Correlative fluorescence and EFTEM imaging of the organized components of the mammalian nucleus. Methods Mol Biol 2013; 950:397-416; PMID:23086887
110. Nagano T, Lubling Y, Stevens TJ, Schoenfelder S, Yaffe E, Dean W, Laue ED, Tanay A, Fraser P. Single-cell Hi-C reveals cell-to-cell variability in chromosome structure. Nature 2013; 502:59-64; PMID:24067610; http://dx.doi.org/10.1038/nature12593
111. Kageyama S, Nagata M, Aoki F. Isolation of nascent messenger RNA from mouse preimplantation embryos. Biol Reprod 2004; 71:1948-55; PMID:15286032; http://dx.doi.org/10.1095/biolreprod.104.031906
112. Waksmundzka M, Debey P. Electric field-mediated BrUTP uptake by mouse oocytes, eggs, and embryos. Mol Reprod Dev 2001; 58:173-9; PMID:11139229; http://dx.doi.org/10.1002/1098-2795(200102)58:2%3c173::AID-MRD6%3e3.0.CO;2-2

Legends to Supplementary Figures

Supplementary Figure 1. DAPI-stained ENPs with immunostained H3K4me3 recorded by 3D structured illumination microscopy in an IVF 8-cell embryo.

Panels A-H. Midplane SIM sections from each of the eight nuclei: DAPI-stained section (1), corresponding section with immunostained H3K4me3 (2), overlay of DAPI (grey) and H3K4me3 (green) (3). Enlargements of boxed areas in each nucleus are shown in 4 (DAPI), 5 (H3K4me3) and 6 (overlay). H3K4me3 labeled chromatin extends to the nuclear border at numerous sites. Note major chromatin bodies or clusters intensely labeled with H3K4me3 and the correspondence of H3K4me3-stained clusters with less intensely DAPI-stained nuclear regions. Bars: 3 µm for 1-3; 1 µm for 4-6.

Supplementary Figures 2 and 3. Effects of low, medium and high thresholds on the abundance and topography of H3K4me3 and RNA polymerase II-S5p signals in nuclei from IVF embryos.

Panels Aa-Ac. Midplane SIM sections from an ENP (Supplementary Figure 2) and an ENC (Supplementary Figure 3) with DAPI-stained chromatin (grey) and immunostained H3K4me3 (green) and RNA polymerase II-S5p (red) are displayed after application of a low (A), medium (B) and high threshold (C). The same threshold was applied to the enlarged images shown in each vertical column below each nuclear section: **a1-a6**, low threshold; **b1-b6**, medium threshold; **c1-c6**, high threshold. Images of the b-column in Supplementary Figure 2 are identical with images shown in Figure 10a. In all images the same moderate threshold was applied for DAPI to remove the pattern of concentric rings (compare Figure 6). Comparison of images in each horizontal row demonstrates the effects of the different thresholds applied to H3K4me3 (rows 1 and 2) and RNA polymerase II signals (rows 3 and 4) on the relative abundance of these signals and their topography with respect to DAPI-stained chromatin. Black pixels in rows 1 and 2 suggest the colocalization of H3K4me3 positive signals with DAPI-stained chromatin. Clusters of green signals in areas DAPI negative after thresholding (white) suggest an extension of H3K4me3 signals into an interchromatin compartment channel (although technical artifacts should be emphasized as an important issue). In rows 3 and 4 clusters of black pixels suggest the co-localization of RNA polymerase II positive signals with DAPI-stained chromatin. Clusters of red pixels hint to the presence of RNA polymerase II in interchromatin compartment channels. Rows 5 and 6 show topographical relationships between H3K4me3 and RNA polymerase II signals. Black pixel clusters suggest partial overlap of green H3K4me3 and red RNA polymerase II signals. In rows 1-4 we note a preference for black pixels at the less densely DAPI-stained periphery of chromatin domain clusters (CDCs), termed the perichromatin region (compare Figure 18). For a quantitative analysis see Figure 19. The evident threshold dependence of the size and abundance of H3K4me3 and RNA polymerase II signals illustrates a caveat, which should be taken into account, when quantitative measurements of such parameters are attempted. Bars: 3 µm in C is representative for A-C; 1 µm in c1 is representative for rows 1, 3 and 5; 0.3 µm in c2 is representative for rows 2, 4 and 6.

Supplementary Figure 4. Threshold effects on quantitative 3D image analysis.

Panels A-D. The left column shows midplane SIM sections of the ENP and ENC shown in Figure 10 and Supplementary Figures 2 and 3. A and C present color-coded DAPI intensity classes (see Figure 18) prior to thresholding, B and D after thresholding (Figure

6). Thresholding of DAPI-stained nuclei results in a strong increase of the number of DAPI pixels with DAPI intensities below the chosen threshold (attributed to class 1 and color-coded with blue). Boxed areas marked in each nucleus are further enlarged in the right column (A1-3, B1-3, C1-3, D1-3) with individual pixels of 39.5 nm. Enlargements 2 represent color-coded pixels of the 7 DAPI intensity classes. Enlargements 1 show color-coded DAPI pixels, which colocalize with H3K4me3 positive pixels. Enlargements 3 present color-coded DAPI pixels, which colocalize with RNA polymerase II positive pixels. The right side of this Supplementary Figure shows the result of quantitative analyses of topographical relationships between color-coded DAPI-stained chromatin, H3K4me3 and RNA polymerase II (compare Figure 19). Positive values for the height of columns (>0 and ≤1) provide a relative measure for the overrepresentation (+) of positive pixels for H3K4me3 (green columns) and RNA polymerase II (red columns) in the 7 DAPI intensity classes. The height of the column, which represents the DAPI intensity class with the highest excess of H3K4me3 or RNA polymerase II pixels was set at +1. Green and red columns with negative values provide a relative measure for the underrepresentation of H3K4me3 and RNA polymerase II positive pixels. For low, medium and high thresholds an underrepresentation of H3K4me3 and RNA polymerase II positive pixels was noted in the two highest DAPI intensity classes 6 and 7. For both the ENP and ENC nucleus the use of unthresholded DAPI sections yielded an excess of H3K4me3 and RNA polymerase II positive pixels in classes 4 and 5 and an underrepresentation in classes 1 and 2. For thresholded DAPI sections the analysis yielded an underrepresentation in classes 5, 6 and 7, whereas an overrepresentation was noted (with few exceptions) in classes 1 to 4. For all combinations of DAPI, H3K4me3 and RNA polymerase II thresholds the null-hypothesis of a random association between the 7 classes of color-coded DAPI pixels and pixels indicating the presence of H3K4me3 or RNA polymerase II was rejected with a very high probability ($p < 10^{-15}$). Under all conditions a relative depletion of H3K4me3 and RNA polymerase II signals was noted in the dense interior of chromatin domain clusters. Bars: 3 µm for A-D; pixel size 39.5 nm² for 1-3.

Supplementary Figure 5. **A-E**. **SIM sections with strongly H3K9me3 marked major chromatin clusters**. Sections are displayed after thresholding (compare Figure 6) from DAPI-stained nuclei with distinct phenotypes (A, ENP; B, ENC; C, ENP-like; D, ENC; E, bovine fetal fibroblast nucleus) recorded from *in vitro* fertilized embryos (A, B) and cloned embryos (C, D) generated by transfer of bovine fibroblasts. Boxed areas 1 and 2 in each SIM section are enlarged at the right side. **A1a – E1a (box 1) and A2a – E2a (box 2)**. Enlargements show color-coded DAPI intensity classes derived from a classification of the entire unthresholded nuclear section carrying a given major chromatin cluster (compare the code shown at the right side of A and Figure 18). **A1b/A2b – E1b/E2b.** Immunolabeling of H3K9me3 shown in corresponding enlargements of the two boxes. **A1c/A2c – E1c/E2c**. A mask identifies the strongly H3K9me3 labeled major chromatin cluster framed by each box. **A1d/A2d – E1d/E2d**. Quantitative analyses of H3K9me3 pixels present in each masked chromatin cluster with regard to seven color-coded DAPI intensity classes. The height of each column reflects the relative overrepresentation (+) or underrepresentation (-) of H3K9me3 pixels in each class (compare Figure 19). A comparison of these profiles demonstrates a large variation of H3K9me3 assignments between different major chromatin clusters, even for clusters present in the same nucleus. Bars: 3 µm for A-E; 1 µm for A1a–E2c.

Supplementary Figure 6. A-D. SIM sections with strongly H3K4me3 marked, major chromatin clusters. Sections are displayed after thresholding (compare Figure 6) from DAPI-stained nuclei with distinct phenotypes (A, ENP; B, ENC; C, ENP-like; D, ENC) recorded from *in vitro* fertilized embryos (A, B) and cloned embryos (C, D). Boxed areas 1 and 2 in each section are enlarged at the right side. **A1a – D1a (box 1) and A2a – D2a (box 2)**. Enlargements show color-coded DAPI intensity classes derived from a classification of the entire unthresholded nuclear section carrying a given major chromatin cluster (compare the code shown at the right side of A and Figure 18). **A1b/A2b – D1b/D2b.** Corresponding enlargements show immunolabeling of H3K4me3. **A1c/A2c – D1c/D2c.** Selective masks for the strongly H3K4me3 labeled major chromatin cluster framed by each box. **A1d/A2d – D1d/D2d.** Quantitative analyses of H3K4me3 pixels present in each masked chromatin cluster with regard to seven color-coded DAPI intensity classes obtained for entire nuclear sections shown in A – D. The height of each column reflects the relative overrepresentation (+) or underrepresentation (-) of H3K4me3 pixels in each class (compare Figure 19). A comparison of these profiles demonstrates a large variation of H3K4me3 assignments between different H3K4me3 labeled major chromatin clusters, even for clusters present in the same nucleus. Note that major chromatin clusters strongly labeled with H3K9me3 in bovine fibroblast nuclei (Supplementary Figure 5, Panel E) typically showed minor H3K4me3 labeling as well (compare Figure 13b1/b2). However, major chromatin clusters strongly labeled with H3K4me3 were not observed in the sample of bovine fibroblast nuclei studied with 3D-SIM (n = 57). Bars: 3 µm for A-D; 1 µm for A1a–D2c.

Supplementary Information

Supplementary Movies of 3D-SIM serial sections through bovine embryonic nuclei. Movie 1. DAPI-stained chromatin in an ENP from an *in vitro* fertilized 7-cell stage embryo (Figure 7R4). **Movie 2.** DAPI-stained chromatin in an ENP from an *in vitro* fertilized 8-cell stage embryo (Figure 7R6). **Movie 3.** DAPI-stained chromatin in an ENP/C from an *in vitro* fertilized 9-cell stage embryo (Figure 7R8). **Movie 4.** DAPI-stained chromatin in an ENC from an *in vitro* fertilized morula stage embryo (Figure 7R10). **Movie 5.** DAPI-stained chromatin in an ENP-like nucleus from a cloned 8-cell stage embryo. **Movie 6.** DAPI-stained chromatin in an ENC from a cloned blastocyst stage embryo.

Extended Experimental Procedures

***In vitro* fertilization and cultivation of IVF embryos.** *In vitro* fertilization of bovine oocytes was performed essentially as previously described.[1] In brief, cumulus-oocyte complexes (COCs) were obtained by aspiration of ovarian follicles from slaughtered cows and matured in TCM 199 supplemented with 10% estrous cow serum (ECS) containing 0.2 U/ml o-FSH (Ovagen; ICPbio) for 20–22 hours at 39°C in an atmosphere of 5% CO_2 in humidified air.. Matured COCs were washed in fertilization medium (Tyrode's albumin lactate pyruvate) supplemented with sodium pyruvate (2.2 mg/ml), heparin sodium salt (2 mg/ml) and BSA (6 mg/ml) and transferred to 400-µl droplets of medium. Frozen-thawed spermatozoa were subjected to swim-up procedure for 90 min. Then the COCs and spermatozoa (2 x 10^6 cells/ml) were co-incubated for 18 hours at 39°C, 5% CO_2 in humidified air, The presumptive zygotes were mechanically denuded by vortexing, washed 3x in synthetic oviductal fluid (SOF) culture medium enriched with

5% ECS, BME 100x (20 µl/ml; Invitrogen) and MEM (Minimum Essential Medium) 100x (10 µl/ml, Invitrogen), and transferred to 400-µl droplets of medium covered with mineral oil. Embryos were cultured at 39°C in a humidified atmosphere of 5% CO_2, 5% O_2 and 90% N_2 until they reached the appropriate stage for fixation.

Generation and cultivation of cloned early bovine embryos. Cloned early bovine embryos were generated by somatic cell nuclear transfer (SCNT) of bovine fetal fibroblasts BFF as previously described.[2] Frozen aliquots from vigorously growing BFF cultures were thawed approximately one week before SCNT and grown in a 24-well plate in DMEM, supplemented with 20% FCS. Fibroblasts from confluent cultures were used for SCNT. Cloned embryos were cultured in 100-µl drops of synthetic oviduct fluid supplemented with 5% (v/v) ECS at 39°C in a humidified atmosphere of 5% CO_2, 5% O_2 and 90% N_2 covered by mineral oil.

Fixation and handling of embryos during experimental procedures. Unless noted otherwise fixation of embryos and all subsequent steps were performed at room temperature. For preservation of the 3D shape of embryos and nuclei care was taken to avoid any deforming pressure and to prevent embryos from drying out at any step of the following procedures. Embryos were briefly washed in 38°C 1x phosphate buffered saline (PBS), fixed in 2% paraformaldehyde (PFA) in PBS, washed twice in PBS and then stored at 4°C in PBS until further use.

Fluorescence in situ hybridization experiments. For visualization of BTA 13 we used a chromosome specific paint probe for sheep (*Ovis aries*) chromosome 13, which is homologous to bovine chromosome 13.[3, 4] For FISH experiments the chromosome paint probe was labeled with DIG (digoxigenin)-11-dUTP. Fixed embryos were incubated in 0.1N HCl between 30 sec and 2 min until the zona pellucida disappeared, washed again 2x each for 10 min in 0.05% Triton X-100/1x PBS containing 0.1% BSA, permeabilized for 60 min in 0.5% Triton X-100/1x PBS containing 0.1% BSA, washed again 2x in 0.05% Triton X-100 in 1x PBS plus 0.1% BSA, incubated in 0.1N HCl for 2 min, washed as above and finally washed 2x for 10 min in 0.01% Triton X-100 in 2x SSC plus 0.1% BSA. Prior to 3D-FISH embryos were incubated in 50% formamide/2x SSC containing 0.1% BSA (pH=7.0) for at least two days and nights. FISH experiments were carried out as described by Cremer et al.[5] and Koehler et al.[6]. Hybridization mixtures contained 50% formamide, 2x SSC, 10% dextran sulfate. For 3D-FISH experiments with BFF cultures probe concentrations of 20-40 ng/µl were used for BTA 13. For 3D-FISH experiments on embryos the hybridization mixture contained about 170 ng/µl of the paint probe to compensate probe dilution due to medium adherent to the embryo. Embryos were pipetted into a 5 µl drop of hybridization mixture placed in the middle of a metal ring (diameter 2 cm, height 1 mm; Brunel Microscopes Ltd.) sealed with Fixogum (Marabu GmbH & Co. KG) on the surface of a glass slide. The droplet of hybridization mixture was overlaid with mineral oil to avoid air-drying. After at least 2 hours of equilibration of the hybridization mixture with the embryo in a humid environment the glass slide was put on a hot block for 3 min at 76°C to denature nuclear DNA of embryos and probe DNA simultaneously. Hybridization was performed for 2-3 days at 37°C in a humidified atmosphere. For all subsequent washing and probe detection steps, individual embryos were transferred between 1 ml wells carrying the appropriate solutions (for details see Koehler[7]). Embryos were washed twice in 2x SSC followed by stringent washings in 50% formamide/2x SSC and in 0.1% SSC, each for 10 min. After a short incubation in

4x SSC/0.02% Tween 20 (4x SSCT) embryos were placed in 4% BSA for 10 min for blocking unspecific antibody binding sites. Embryos were then incubated overnight at 4℃ with monoclonal mouse-anti-digoxigenin (1:500, Sigma). After two washings in 4x SSCT secondary goat-anti-mouse antibodies conjugated to Alexa 488 (1:200, Molecular Probes/Invitrogen) were applied for 90 min at room temperature. After two additional 10 min washings in 4x SSCT, embryos were transferred into 0.1 µg/ml DAPI/4x SSCT for 30 min. Embryos were then subjected to an increasing glycerol dilution series (20%, 40% and 60% in 4x SSCT), each for 5 min, and incubated in Vectashield antifade medium (Vector Laboratories) supplemented with DAPI (0.1 µg/ml) and transferred to polylysinated, 18-well "µ-slides" (Ibidi, Martinsried, Germany).

Immunostaining procedures. Background caused by PFA was quenched using 20 mM glycine in PBS for 10 min. After washing twice with PBS embryos were permeabilized with 0.5% Triton-X 100 for 15-30 min. After washing twice with PBS unspecific background signals were reduced by incubation in 2% BSA for 2-4 hours. Embryos were sequentially incubated in 40 µl of primary and secondary antibody solutions contained within PCR-tube caps, diluted in PBS with 2% BSA (as described in **Supplementary Tables 1 and 2**). Specimens were incubated with primary antibodies overnight at 4℃. After washing 5x in PBS with 2% BSA the appropriate secondary antibodies, diluted in PBS with 2% BSA, were applied for 1 hour, again followed by 5x washing in PBS with 2% BSA and 5x without. Thereafter fixation of antibodies was performed with 4% PFA in PBS for 10 min, followed by washing twice in PBS and twice in PBS with 0.05% Tween 20 (PBST). Before the removal of the zona pellucida chromatin was counterstained with DAPI (Life Technologies, Catalog No. D1306; 4′,6-diamidino-2-phenylindole) 2.5 µg / ml diluted in PBST for 10 min or by TO-PRO-3 (Life Technologies, Catalog No. T3605; CAS name and number: Quinolinium, 4-[3-(3-methyl-2(3H)-benzothiazolylidene)-1-propenyl]-1-[3-(trimethylammonio)propyl]-, diiodide/ 157199-63-8) 2 mM also diluted in PBST for 5 min, followed by washing twice in PBS.

DNA replication studied with EdU labeling experiments. Live embryos were incubated in EdU (5-Ethynyl-2'-deoxyuridine) diluted 1:1000 in SOF culture medium enriched with 5% ECS, BME and MEM for 30 min at 38℃.[8] After briefly washing in PBS (38℃), fixation was performed for 10 min with 2% PFA in PBS at room temperature followed by washing twice in PBS. Background caused by PFA was quenched using 20 mM glycine in PBS for 10 min. After washing twice with PBS embryos were permeabilized with 0.5% Triton-X 100 for 10 min. After washing twice with PBS unspecific background signals were reduced by incubation in 4% BSA in PBS for 30 min. EdU detection was performed for 40 min using the detection kit provided by Invitrogen (Click-iT EdU Cell Proliferation Assay Kit, catalog No. C10337: 206.4 µl Click it reaction buffer, 9.6 µl $CuSO_4$, 0.58 µl Az488, 2.4 µl 10x reaction buffer additive and 21.6 µl ddH_2O). 4x washing in PBS was followed by 45 min of blocking in 2% BSA in PBS. Subsequent antibody stainings were performed as described above and embedding for microscopy as described below.

RNA synthesis studied with BrUTP or BrU labeling experiments. For BrUTP labeling embryos were washed twice in electroporation buffer (EB; see Kageyama et al.[9]) and once in EB with 10 mM BrUTP. Embryos were incubated for 5 min at room temperature in EB with 10 mM BrUTP, transferred in this dilution to an Eppendorf micro fusion chamber with a electrode distance of 200 µm and electroporated 2x (interval 2

min) with an Eppendorf Multiporator with 30 V for 200 µs. Embryos were incubated for 2 min in EB with 10 mM BrUTP and washed in SOF culture medium enriched with 5% ECS, BME and MEM, and briefly washed in PBS (37°C). Fixation and staining were performed as described for BrU incorporation staining experiments below. For BrU incorporation embryos were incubated for 45 min with 10 mM BrU in SOF culture medium enriched with 5% ECS, BME and MEM, and briefly washed in PBS (37°C), fixed for 10 min in 3.7% formaldehyde in PBS, washed 3x in PBS, permeabilized in 0.5% Triton-X 100 in PBS for 10 min. After blocking for 30 min in 4% BSA in PBST, embryos were incubated overnight at 4°C with mouse anti-BrdU (Roche 1170376 1:500) in 2% BSA in PBS, washed 4x in PBST, incubated with goat anti-mouse Alexa 488 (Invitrogen A11029 1:400) for 1 hour at room temperature and washed 5x in PBST. DNA was counterstained with DAPI (see above).

Embedding. Whole early bovine embryos are relatively thick (with a diameter of roughly 150-190 µm).[10] Prior to inverted 3D confocal laser scanning microscopy (3D-CLSM) or 3D structured illumination microscopy (3D-SIM) entire embryos, or individual embryonic cells obtained by microdissection (see below), were mounted on polylysinated precision cover glasses in a drop of the antifade embedding medium Vectashield (Vector Laboratories). To avoid uncontrolled changes of the refractive index of Vectashield due to dilution with PBS specimens were washed twice with Vectashield before embedding.

Three-dimensional confocal laser scanning microscopy. Light optical serial sections from nuclei in whole mounted embryos were recorded with a Leica TCS SP5 using a high aperture, oil immersion objective (63x/1.4 NA) with a pixel length/height of 30–120 nm and distances of 200 nm between sections. If the working distance of this objective was insufficient to reach nuclei located at a greater distance from the cover glass or entire embryos were to be recorded in one stack, a lower aperture and longer working distance oil immersion objective (20x/0.7 NA) with a pixel length/height of 30-400 nm and distances of 500-1000 nm between consecutive sections was used. Fluorochromes were excited with blue diode, argon and helium-neon lasers using laser lines at 405 nm, 488 nm, 594 nm and 633 nm, respectively.

Three-dimensional structured illumination microscopy: problems and pitfalls. 3D-SIM was performed with a DeltaVision OMX V3 system (Applied Precision Imaging/GE Healthcare) equipped with a 100x/1.4 NA Oil PSF Olympus UPlanSApo objective (UPLSAPO100XOPSF). The concept of SIM was introduced by Mats Gustafsson and Rainer Heintzmann and Christoph Cremer.[11-13] Compared with conventional wide-field microscopy the effective lateral optical resolution of SIM was improved up to a factor of 2 and the volumetric resolution of 3D-SIM about eightfold.[14, 15] The imaging quality of thick nuclei is impaired by a pattern of concentric rings (see main text, **Figure 6**). Readers not familiar with the practical issues, which arise in studies of nuclear architecture with 3D-SIM, are referred to Markaki et al.[16, 17] In thick, highly scattering specimens, such as entire early bovine embryos, 3D-SIM could only be performed with nuclei located next to the surface of the cover glass. Alternatively, embryos were microdissected with fine needles to obtain single cells, which were placed directly on polylysinated, high precision microscope cover glasses (18 x 18 mm; 170 ± 5 µm; Carl Roth, Germany; LH22.1). In freshly fixed embryos these cells had a higher tendency to stick together than in embryos stored for days or weeks after fixation in PBS at 4°C. Dedicated software was

used for a Fourier transformation of a high number of serial images recorded at a z-distance of 125 nm with 15 raw SI images per plane (5 phases, 3 angles). Image quality can be impaired by noise originating from the Poisson distribution of the limited number of photons recorded for a given immunostained structure. In comparison with 3D-CLSM, the preparation of immunostained cells for 3D-SIM is technically more demanding.[16, 17]

Quantitative analysis of immunostained SIM sections. Application of a threshold just sufficiently high to remove both average background and patterns of concentric rings (**Figure 6**) had the unavoidable consequence that a certain fraction of specific signal was also lost. **Supplementary Figures 2 and 3** show that size and number of signal counts for H3K4me3 and RNA polymerase II-S5p were threshold dependent. It is important to take into consideration that background cannot be completely avoided in immunostaining procedures and may vary depending on the primary antibodies available for an epitope of choice and the protocol applied. In case that a diffuse signal is considered as background, it can be removed by application of a proper threshold, In this case only structured signals remain with the caveat that the presence of a lot of a given immunostained protein diffusely distributed at other sites is neglected. It can be difficult, if not impossible, to distinguish dotted background from structured signals of similar size (compare Supporting Figures 4A-D in Markaki et al.[16]).

To deal with these concerns in the best possible way, we have only taken results into account for a biological interpretation, which turned out to be robust in repeated experiments and under a variety of threshold conditions. For signal intensity classification in SIM sections of DAPI-stained nuclei at the voxel level a hidden Markov random field model classification was implemented using the open-source statistics software R.[18] This approach combines a finite Gaussian mixture model with a spatial model (Potts model) and allows a classification, which is not only based on the intensity of an individual voxel, but also takes into account the classification of surrounding voxels (for a detailed description see Zhang et al.[19]). Prior to segmentation, 3D masks were generated in ImageJ to define the nuclear space according to the DAPI signal. Dedicated software written by V.S. and A.S. on the basis of the software package for scientific computing R 2.15 was used for a statistical comparison of the localization of positive pixels for histone modifications H3K4me3, H3K9me3 and RNA polymerase II-S2p/S5p signals within the range of DAPI intensity classes achieved for unthresholded and thresholded DAPI images.[18] As shown in **Figure 6** for the case of 3D-SIM of DAPI-stained nuclei thresholding is indicated to remove general background and concentric rings, which represent imaging artifacts. **Supplementary Figures 2 and 3** provide evidence that the size and abundance of immunopositive signals depends on the chosen threshold. **Supplementary Figure 4** shows how thresholding of SIM-sections recorded for DAPI, RNA polymerase II and H3K4me3 affects the outcome of such a quantitative analysis. The higher the chosen DAPI threshold, the more DAPI signal pixels fall into class 1 with the consequence that immunopositive signals originally attributed to higher DAPI intensity classes appear now in lower DAPI intensity classes as well. Notably, the underrepresentation of H3K4me3 and RNA polymerase II-S5p signals in DAPI intensity classes 6 and 7 combined with an overrepresentation in lower DAPI intensity classes was a robust finding seen at low, moderate and high thresholds subjected to SIM sections with RNA polymerase II and H3K4me3. The analyses presented in the main text (**Figure 19**) were performed with unthresholded DAPI images based on the rationale that the seven DAPI intensity classes in such images cover the

whole range of DAPI intensities as best as possible (compare **Supplementary Figure 4**). Our main conclusion that H3K4me3 and RNA polymerase II-S5p signals were relatively enriched at the periphery whereas H3K4me3 and RNA polymerase II-S5p were relatively depleted in the core part of chromatin domain clusters (CDCs) remained valid for the entire range of thresholds tested (**Supplementary Figure 4**). This result, however, does not exclude small amounts of signals of RNA polymerase II-S5p and H3K4me3 still present in the interior of CDCs (see main Discussion).

References

1. Hiendleder S, Wirtz M, Mund C, Klempt M, Reichenbach HD, Stojkovic M, Weppert M, Wenigerkind H, Elmlinger M, Lyko F, et al. Tissue-specific effects of in vitro fertilization procedures on genomic cytosine methylation levels in overgrown and normal sized bovine fetuses. Biology of reproduction 2006; 75:17-23.

2. Wuensch A, Habermann FA, Kurosaka S, Klose R, Zakhartchenko V, Reichenbach HD, Sinowatz F, McLaughlin KJ, Wolf E. Quantitative monitoring of pluripotency gene activation after somatic cloning in cattle. Biology of reproduction 2007; 76:983-91.

3. Ansari HA, Bosma AA, Broad TE, Bunch TD, Long SE, Maher DW, Pearce PD, Popescu CP. Standard G-, Q-, and R-banded ideograms of the domestic sheep (Ovis aries): homology with cattle (Bos taurus). Report of the committee for the standardization of the sheep karyotype. Cytogenetics and cell genetics 1999; 87:134-42.

4. Burkin DJ, O'Brien PC, Broad TE, Hill DF, Jones CA, Wienberg J, Ferguson-Smith MA. Isolation of chromosome-specific paints from high-resolution flow karyotypes of the sheep (Ovis aries). Chromosome research : an international journal on the molecular, supramolecular and evolutionary aspects of chromosome biology 1997; 5:102-8.

5. Cremer M, Grasser F, Lanctot C, Muller S, Neusser M, Zinner R, Solovei I, Cremer T. Multicolor 3D fluorescence in situ hybridization for imaging interphase chromosomes. Methods in molecular biology 2008; 463:205-39.

6. Koehler D, Zakhartchenko V, Ketterl N, Wolf E, Cremer T, Brero A. FISH on 3D preserved bovine and murine preimplantation embryos. Methods in molecular biology 2010; 659:437-45.

7. Koehler D. Cloning in Cattle: Nuclear architecture and epigenetic status of chromatin during reprogramming of donor cell nuclei. Faculty of Biology, Department II. Munich: Ludwig-Maximilians-University, http://edoc.ub.uni-muenchen.de/9915/, 2009.

8. Chehrehasa F, Meedeniya AC, Dwyer P, Abrahamsen G, Mackay-Sim A. EdU, a new thymidine analogue for labelling proliferating cells in the nervous system. Journal of neuroscience methods 2009; 177:122-30.

9. Kageyama S, Nagata M, Aoki F. Isolation of nascent messenger RNA from mouse preimplantation embryos. Biology of reproduction 2004; 71:1948-55.

10. Bó G, Mapletoft R. Evaluation and classification of bovine embryos. Anim Reprod 2013; 10:344-8.

11. Gustafsson MG. Extended resolution fluorescence microscopy. Curr Opin Struct Biol 1999; 9:627-34.

12. Gustafsson MG. Surpassing the lateral resolution limit by a factor of two using structured illumination microscopy. J Microsc 2000; 198:82-7.

13. Heintzmann R, Cremer CG. Laterally modulated excitation microscopy: improvement of resolution by using a diffraction grating. BiOS Europe'98: International Society for Optics and Photonics, 1999:185-96.

14. Cremer C. Optics Far Beyond the Diffraction Limit. In: Traeger F, ed. Springer Handbook of Lasers and Optics: Springer Berlin Heidelberg, 2012:1359-97.

15. Schermelleh L, Heintzmann R, Leonhardt H. A guide to super-resolution fluorescence microscopy. The Journal of cell biology 2010; 190:165-75.

16. Markaki Y, Smeets D, Fiedler S, Schmid VJ, Schermelleh L, Cremer T, Cremer M. The potential of 3D-FISH and super-resolution structured illumination microscopy for studies of 3D nuclear architecture: 3D structured illumination microscopy of defined chromosomal structures visualized by 3D (immuno)-FISH opens new perspectives for studies of nuclear architecture. BioEssays : news and reviews in molecular, cellular and developmental biology 2012; 34:412-26.

17. Markaki Y, Smeets D, Cremer M, Schermelleh L. Fluorescence in situ hybridization applications for super-resolution 3D structured illumination microscopy. Methods in molecular biology 2013; 950:43-64.

18. Team RCD. R: A Language and Environment for Statistical Computing. R Foundation for Statistical Computing, Vienna, Austria, 2012. ISBN 3-900051-07-0, 2012.

19. Zhang Y, Brady M, Smith S. Segmentation of brain MR images through a hidden Markov random field model and the expectation-maximization algorithm. IEEE Trans Med Imaging 2001; 20:45-57.

20. Markaki Y, Gunkel M, Schermelleh L, Beichmanis S, Neumann J, Heidemann M, Leonhardt H, Eick D, Cremer C, Cremer T. Functional nuclear organization of transcription and DNA replication: a topographical marriage between chromatin domains and the interchromatin compartment. Cold Spring Harbor symposia on quantitative biology 2010; 75:475-92.

Supplementary Tables to Extended Experimental Procedures

Supplementary Table 1: list of primary antibodies

Host	Target	Official name	Dilution	Company	ID
Rabbit	H3K4me3	Anti-Histone H3 (tri methyl K4) antibody - ChIP Grade	1:100	Abcam	ab8580
Mouse	H3K9me3	Histone H3K9me3 antibody (mAb)	1:100	Active Motif	39285/6
Rat	RNA polymerase II-S2p	Monoclonal antibody against CTD phosphoserine epitope 2	1:20	Gift from Dirk Eick (see Markaki et al.[20])	
Rat	RNA polymerase II-S5p	Monoclonal antibody against CTD phosphoserine epitope 5	1:20	Gift from Dirk Eick (see Markaki et al.[20])	
Mouse	B23	Monoclonal Anti-B23 antibody produced in mouse	1:1000	Sigma	B0556
Mouse	SC-35	Anti-SC35 (phospho) antibody [SC-35] - Nuclear Speckle Marker	1:1500	Abcam	ab11826
Rabbit	H3S10p	Anti-Histone H3 (phospho S10) antibody - ChIP Grade	1:200	Abcam	ab5176
Human	Kinetochores (CREST)	Antibody against cell nuclei (ANA control), centromere pattern	1:5	Euroimmune	CA1611-0101

Supplementary Table 2: list of secondary antibodies

Host	Target	Fluorophore	Excitation [nm]	Dilution	Company	ID
Donkey	Rabbit IgG (H+L)	Dylight	488	1:300	Jackson ImmunoResearch	711-485-152
Donkey	Rabbit IgG (H+L)	Dylight	594	1:500	Jackson ImmunoResearch	711-505-152
Donkey	Mouse IgG (H+L)	Alexa	488	1:400	Invitrogen	A-21202
Donkey	Mouse IgG (H+L)	Alexa	594	1:500	Invitrogen	A-21203
Goat	Mouse IgG (H+L) preadsorbed	Alexa	594	1:300	Invitrogen	A-11032
Donkey	Rat IgG (H+L)	Alexa	594	1:300	Invitrogen	A-21209
Donkey	Human IgG (H+L)	Cy5	650	1:200	Jackson ImmunoResearch	709-176-149

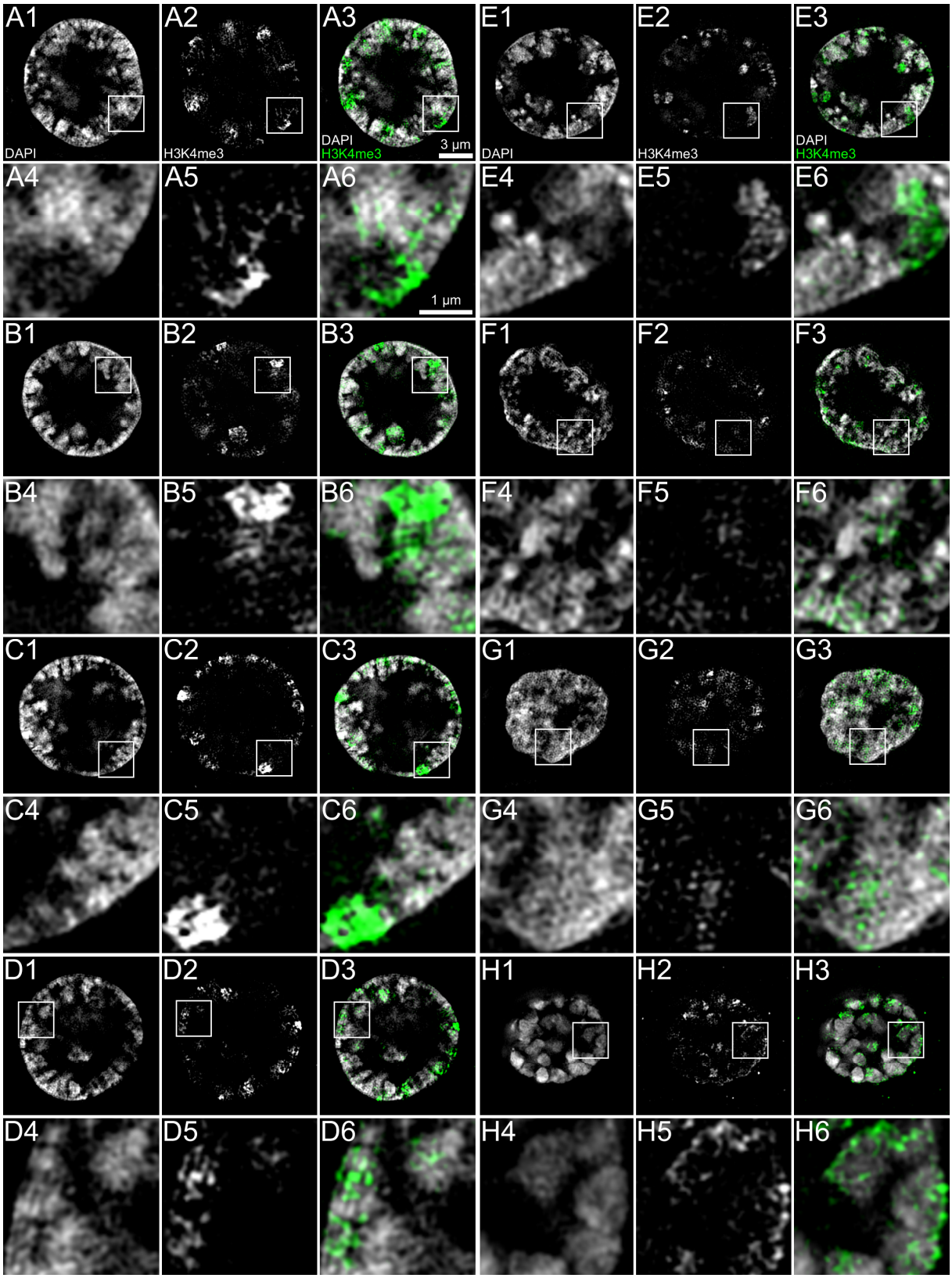

Supplementary Figure 1

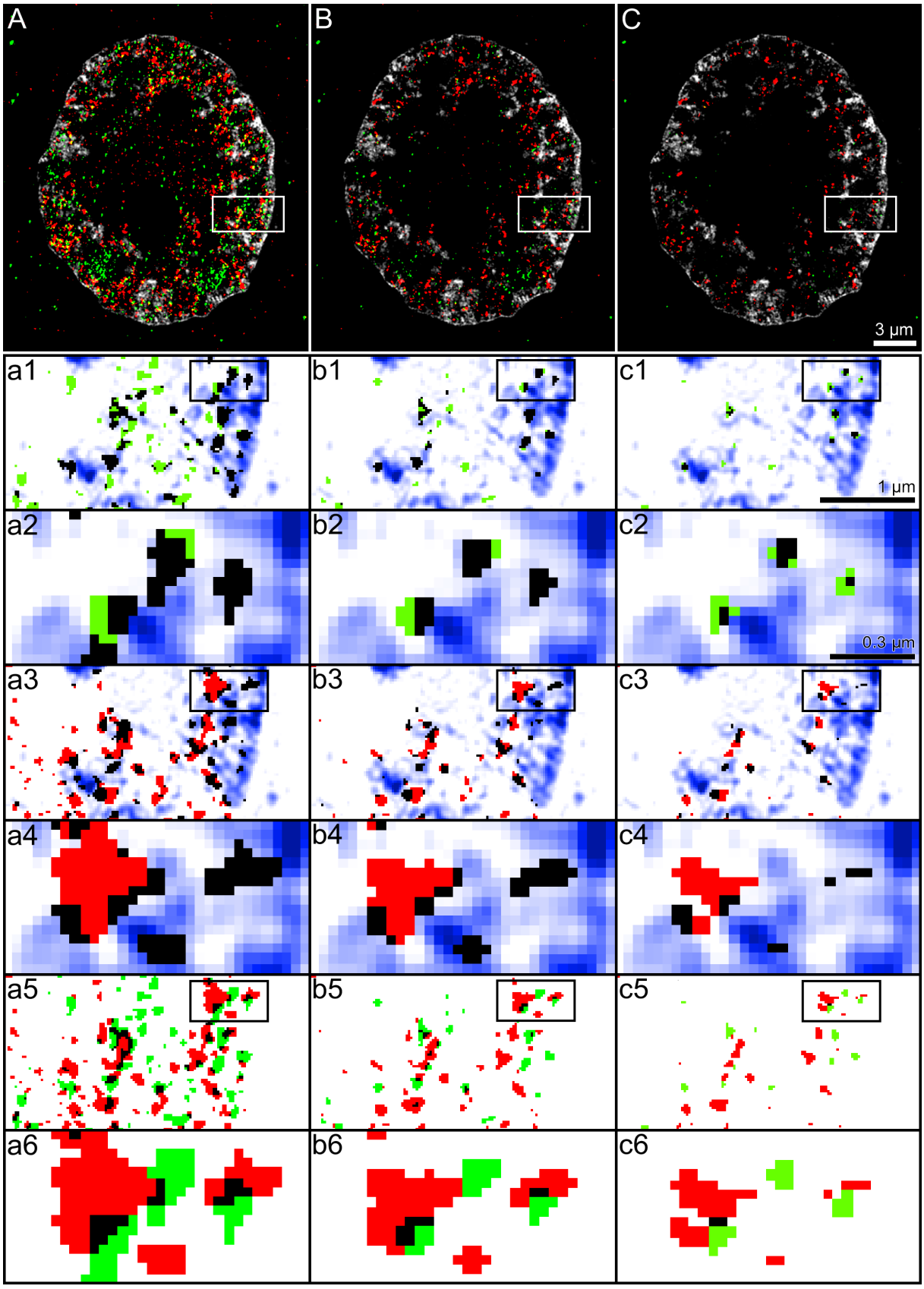

Supplementary Figure 2

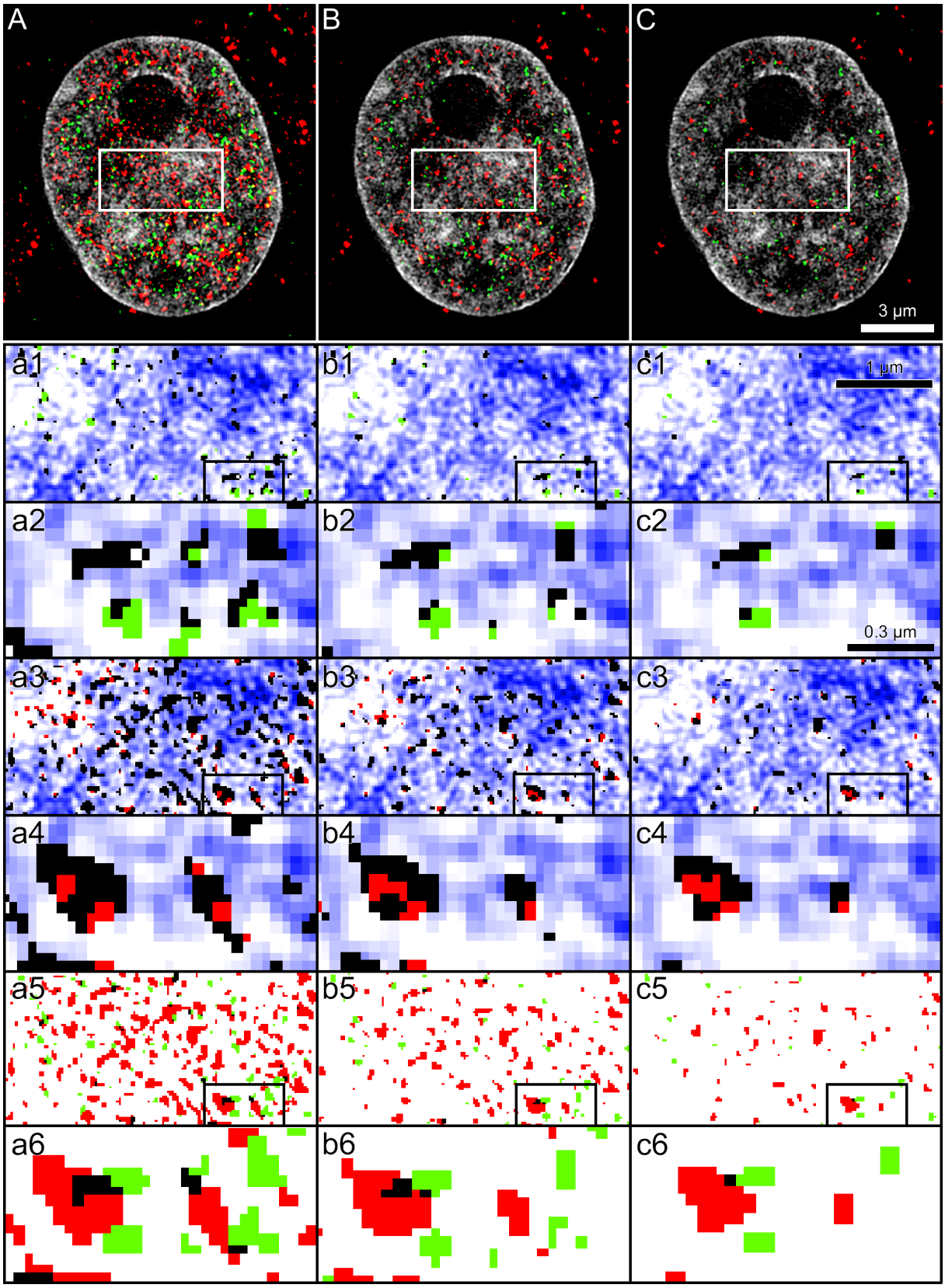

Supplementary Figure 3

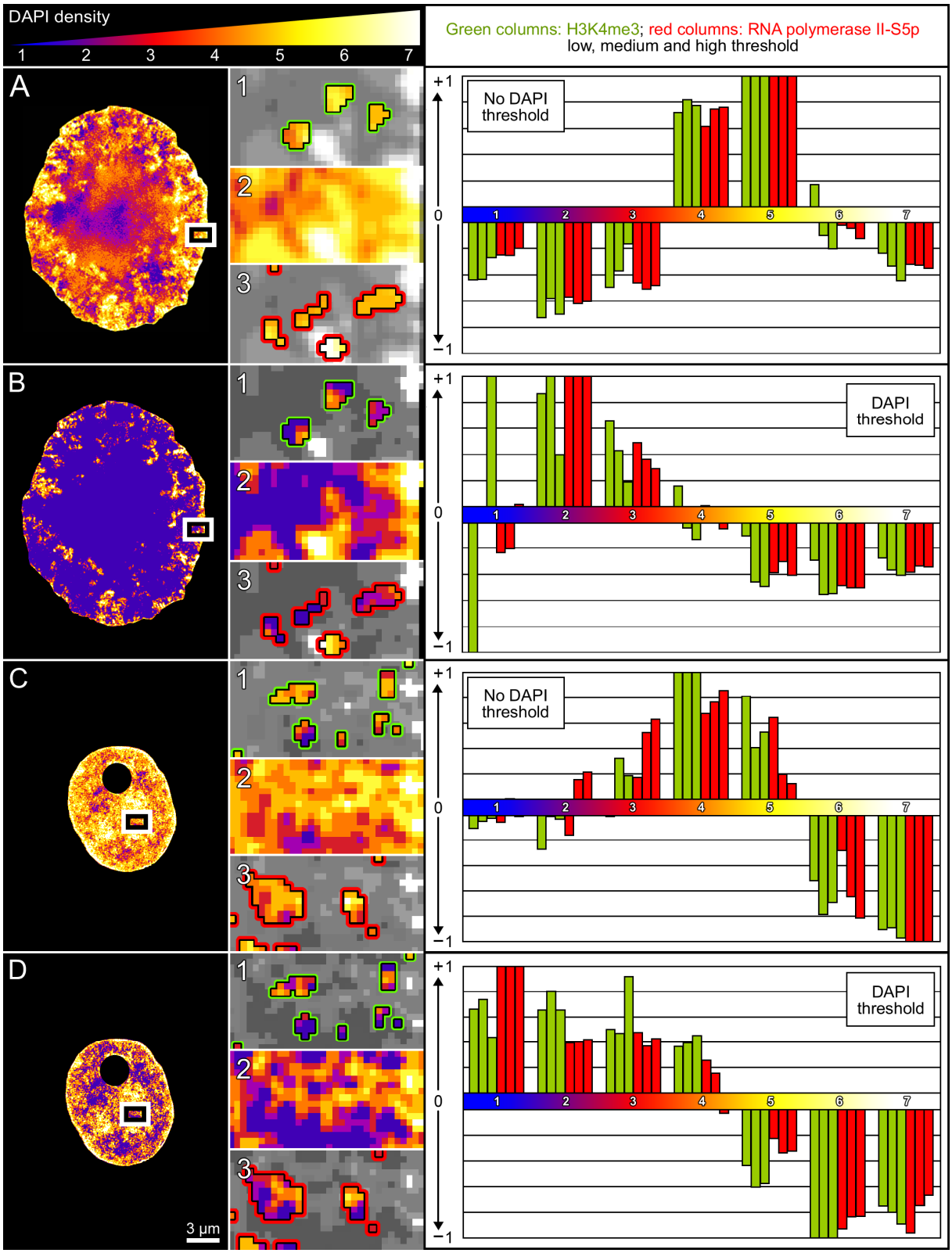

Supplementary Figure 4

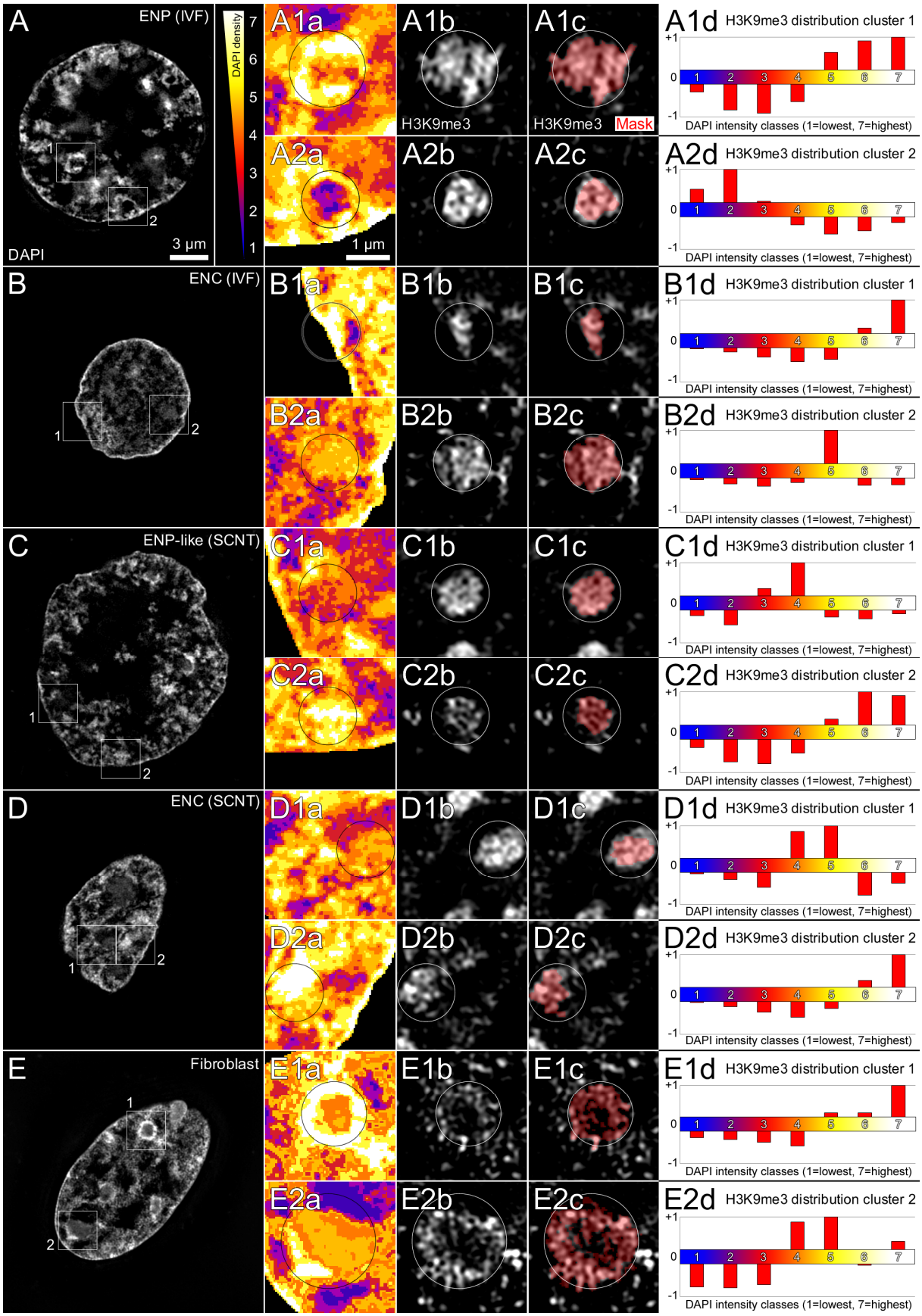

Supplementary Figure 5

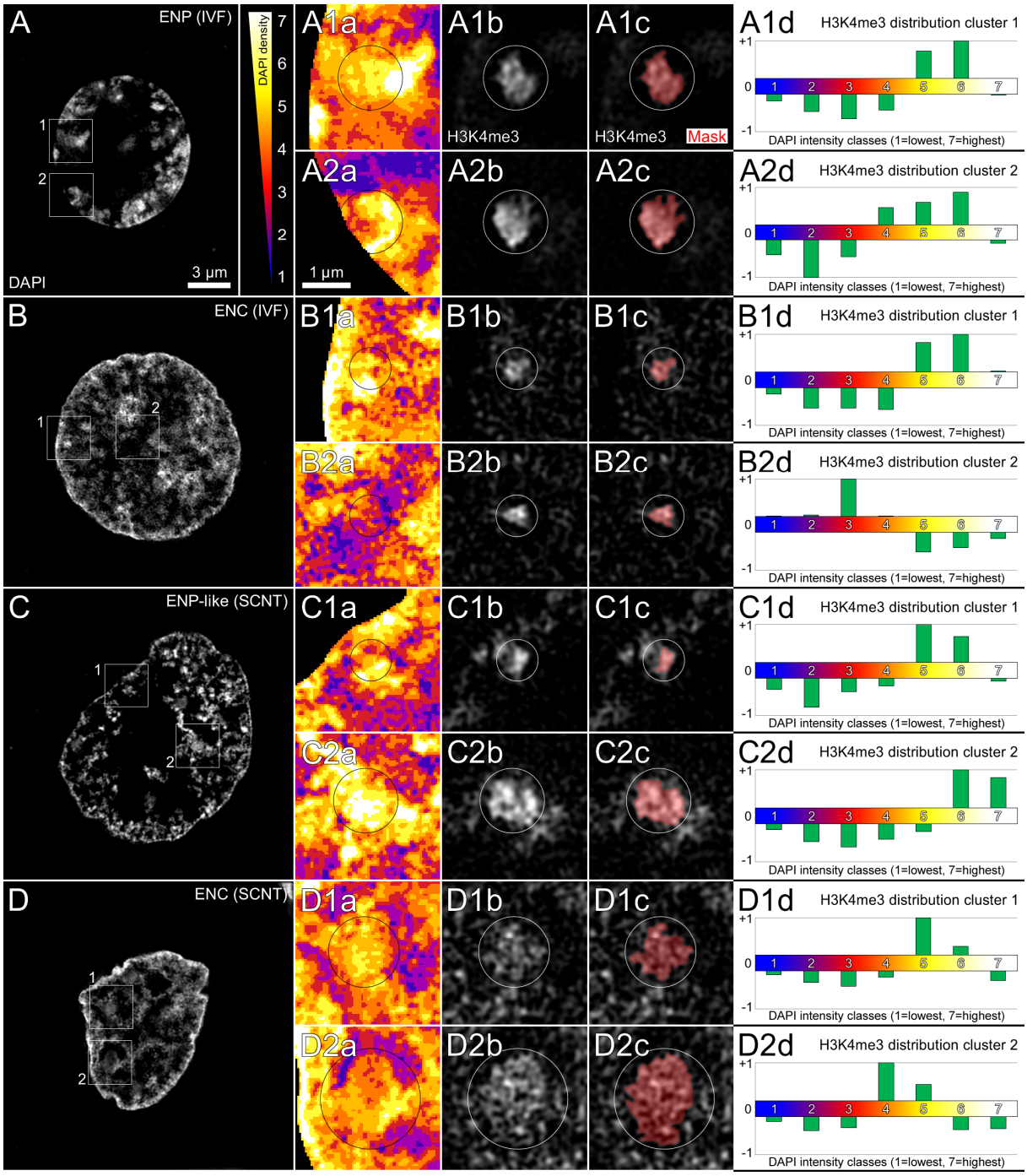

Supplementary Figure 6

2.3. Remodeling of the Nuclear Envelope and Lamina during Bovine Preimplantation Development and Its Functional Implications

PLOS ONE

RESEARCH ARTICLE

Remodeling of the Nuclear Envelope and Lamina during Bovine Preimplantation Development and Its Functional Implications

Jens Popken[1,2]*, Alexander Graf[3], Stefan Krebs[3], Helmut Blum[3], Volker J. Schmid[4], Axel Strauss[5], Tuna Guengoer[2], Valeri Zakhartchenko[2], Eckhard Wolf[2,3]*, Thomas Cremer[1]*

1 Division of Anthropology and Human Genetics, Biocenter, LMU Munich, Planegg-Martinsried, Germany, **2** Chair for Molecular Animal Breeding and Biotechnology, Gene Center, LMU Munich, Munich, Germany, **3** Laboratory for Functional Genome Analysis (LAFUGA), Gene Center, LMU Munich, Munich, Germany, **4** Institute of Statistics, LMU Munich, Munich, Germany, **5** Division of Genetics, Biocenter, LMU Munich, Planegg-Martinsried, Germany

* Jens.Popken@campus.lmu.de (JP); ewolf@lmb.uni-muenchen.de (EW); Thomas.Cremer@lrz.uni-muenchen.de (TC)

Citation: Popken J, Graf A, Krebs S, Blum H, Schmid VJ, Strauss A, et al. (2015) Remodeling of the Nuclear Envelope and Lamina during Bovine Preimplantation Development and Its Functional Implications. PLoS ONE 10(5): e0124619. doi:10.1371/journal.pone.0124619

Received: August 12, 2014

Accepted: March 17, 2015

Published: May 1, 2015

Data Availability Statement: All relevant data are within the paper and its Supporting Information files.

Funding: This study was supported by grants from the Deutsche Forschungsgemeinschaft to T.C, E.W. and V.Z. (CR 59/26, FOR 1041, ZA 425/1-3), In addition, research of E.W. and V.Z. was supported by the EU grant Plurisys, HEALTH-F4-2009-223485 FP7 Health 534 project. The funders had no role in study design, data collection and analysis, decision to publish, or preparation of the manuscript.

Competing Interests: The authors have declared that no competing interests exist.

Abstract

The present study demonstrates a major remodeling of the nuclear envelope and its underlying lamina during bovine preimplantation development. Up to the onset of major embryonic genome activation (MGA) at the 8-cell stage nuclei showed a non-uniform distribution of nuclear pore complexes (NPCs). NPCs were exclusively present at sites where DNA contacted the nuclear lamina. Extended regions of the lamina, which were not contacted by DNA, lacked NPCs. In post-MGA nuclei the whole lamina was contacted rather uniformly by DNA. Accordingly, NPCs became uniformly distributed throughout the entire nuclear envelope. These findings shed new light on the conditions which control the integration of NPCs into the nuclear envelope. The switch from maternal to embryonic production of mRNAs was accompanied by multiple invaginations covered with NPCs, which may serve the increased demands of mRNA export and protein import. Other invaginations, as well as interior nuclear segments and vesicles without contact to the nuclear envelope, were exclusively positive for lamin B. Since the abundance of these invaginations and vesicles increased in concert with a massive nuclear volume reduction, we suggest that they reflect a mechanism for fitting the nuclear envelope and its lamina to a shrinking nuclear size during bovine preimplantation development. In addition, a deposit of extranuclear clusters of NUP153 (a marker for NPCs) without associated lamin B was frequently observed from the zygote stage up to MGA. Corresponding RNA-Seq data revealed deposits of spliced, maternally provided *NUP153* mRNA and little unspliced, newly synthesized RNA prior to MGA, which increased strongly at the initiation of embryonic expression of *NUP153*at MGA.

Introduction

Recently, we observed a massive reorganization of nuclear architecture in bovine preimplantation embryos generated either by *in vitro* fertilization (IVF) or by somatic cell nuclear transfer (SCNT) [1,2]. These changes were most prominent during the transit through minor and major genome activation (mGA and MGA) which occur at the 2-cell stage [3] and at the 8-cell stage [4], respectively. Embryonic nuclei in both IVF and cloned embryos adopted a peripheral localization of chromosome territories (CTs) separated from each other by wide interchromatin (IC) channels, whereas their interior was occupied by a major lacuna deprived of chromatin, but enriched with splicing factors and newly synthesized RNA. Nuclei with this phenotype were termed ENPs (for Embryonic Nuclei with Peripheral chromatin arrangement) and were predominant at MGA. After MGA, CTs were redistributed throughout the nucleus and showed features of nuclear architecture typical for somatic cell types. This conventional nuclear phenotype is characterized by a layer of densely DAPI-stained chromatin beneath the nuclear envelope and around nucleoli, a non-random radial chromatin arrangement with gene-poor chromatin enriched in the nuclear periphery and gene-rich chromatin towards the nuclear center [5–8]. Nuclei with this phenotype were termed ENCs (for Embryonic Nuclei with a Conventional architecture).

The present study was initiated to explore changes of the nuclear envelope and its underlying lamina during these massive changes of the nuclear architecture in bovine preimplantation embryos. The nuclear lamina is located directly beneath the nuclear envelope and is made up of lamins B1 and B2 in developing cells and of lamins A and C in differentiated cells [9]. It serves as an anchoring matrix for chromatin with major implications for chromosome organization and gene expression [10]. Nuclear pore complexes (NPCs) are made up of eight clusters of about 30 nucleoporins (NUPs) [11] building a short tunnel with an inner diameter of ~50 nm [12] and an outer diameter of about 105 nm [13] to 145 nm [14] between a cytoplasmic and a nuclear ring spanning from the outer to the inner membrane of the bi-layer lipid nuclear envelope [15]. Eight fibers connect the nuclear ring with a more interior terminal ring forming the nuclear basket [16]. The 153 kDa nucleoporin NUP153 [17] can be localized at the nuclear ring and at the nuclear basket [18]. Chromatin can be associated with the nuclear basket and with internuclear filaments connected to the terminal ring [16].

Multiple, tubular, double-membraned invaginations of the nuclear envelope carrying NPCs were previously described in nuclei of a wide variety of species, including mammals, and it has been suggested that such invaginations would allow for close topographical relationships between NPCs and chromatin, as well as nucleoli, located in the nuclear interior [19]. In a recent review such invaginations were referred to as type II [20]. In addition, single-membraned invaginations, likely derived from the inner nuclear membrane and lacking NPCs, were described as type I [20]. Patterns of type I and type II invaginations can coexist in the same nucleus with branched type I extensions expanding from type II invaginations forming a nucleoplasmic reticulum (NR), which helps to perform export-import functions of the nuclear envelope not only in the nuclear periphery, but also deep within the nucleus [20].

We performed two-color immunostaining of NUP153 (as a marker for NPCs) and lamin B (as a marker for the lamina) in bovine embryos and recorded light optical serial sections from embryonic nuclei with structured illumination microscopy (3D-SIM). This approach yields a lateral resolution of about 100 nm and an axial resolution of about 300 nm. With conventional confocal laser scanning microscopy (CLSM) the corresponding resolution limits are 200 nm and 600 nm, respectively [21,22]. Accordingly, 3D-SIM provides roughly an eight-fold improvement of the volumetric resolution. Using this novel experimental approach we studied

bovine embryos during preimplantation development with the main focus on changes in the nuclear envelope, its underlying lamina and the distribution of NPCs.

Materials and Methods

Ethics statement

Bovine oocytes for *in vitro* fertilization were obtained from cows slaughtered for meat production at the slaughterhouse Münchner Schlachthof Betriebs GmbH, Munich, Germany in compliance with EU regulations. No animal experiments were conducted.

In vitro fertilization and cultivation of early bovine embryos

In vitro fertilization of bovine oocytes was performed as described in [23]. Cumulus-oocyte complexes (COCs) were obtained by aspiration from ovaries of slaughtered cows. COCs were matured in modified Parker's medium consisting of TCM 199 supplemented with 5% estrous cow serum (ECS) and 0.2 U/ml o-FSH (Ovagen; ICPbio) for 20–22 hours at 39°C in humidified air with 5% CO_2. Matured COCs were washed with the fertilization medium Tyrode's albumin lactate pyruvate (FERT-TALP) supplemented with sodium pyruvate (2.2 mg/ml), heparin sodium salt (2 mg/ml) and bovine serum albumin (BSA; 6 mg/ml) and transferred to 400-µl droplets of medium. Frozen spermatozoa were thawed at 38°C. 100 µl thawed sperm suspension covered by 1 ml capacitation medium was subjected to the swim-up procedure for 60 min. The COCs and spermatozoa (2 x 10^6 cells/ml) were co-incubated for 18 hours at 39°C in humidified air with 5% CO_2. Presumptive zygotes were mechanically denuded by vortexing, washed 3x in SOF culture medium enriched with 5% ECS, BME 100x (20 µl/ml; Invitrogen) and MEM (Minimum Essential Medium) 100x (10 µl/ml, Invitrogen) and transferred to 400-µl droplets of medium covered with mineral oil. Embryos were grown at 39°C in a humidified atmosphere of 5% CO_2, 5% O_2, and 90% N_2 until they reached the appropriate stage for fixation.

Fixation of embryos

Unless noted otherwise fixation of embryos and all subsequent steps were performed at room temperature. Embryos were briefly washed in 38°C PBS, fixed in 2% paraformaldehyde (PFA) in phosphate buffered saline (PBS), washed twice in PBS and then stored at 4°C in PBS until further use.

Immunostaining and embedding

Background caused by PFA was quenched using 20 mM glycine in PBS for 10 min. After washing twice with PBS embryos were permeabilized with 0.5% Triton-X 100 for 15–30 min. After washing twice with PBS unspecific background signals were reduced by incubation in 2% BSA for 2 hours. Embryos were sequentially incubated in 40 µl of primary and secondary antibody solutions, diluted as specified in Tables 1 and 2 in PBS with 2% BSA. Specimens were incubated with primary antibodies overnight at 4°C. After washing 5x in PBS with 2% BSA the appropriate secondary antibodies, diluted in PBS with 2% BSA, were applied for 1 hour, again followed by 5x washing in PBS with 2% BSA and 5x washing without BSA. Thereafter fixation of antibodies was performed with 4% PFA in PBS for 10 min, followed by washing twice in PBS. Before the removal of the zona pellucida chromatin was counterstained with DAPI (4′,6-diamidino-2-phenylindole; Catalog No. D1306, Life Technologies) diluted in PBS (2.5 µg/ml) for 10 min followed by washing twice in PBS. Embryos or individual blastomeres were attached to precision cover glasses (18 mm x 18 mm; 170 ± 5 µm; Carl Roth, Germany; LH22.1) in PBS and embedded in Vectashield (Vector Laboratories).

Table 1. Primary antibodies.

Host	Target	Official name	Dilution	Company	ID
Goat	Epitope at C-terminus of Lamin B1. Detecting Lamin B1 and, to a lesser extent, Lamin B2	Lamin B Antibody (M-20)	1:100	Santa Cruz	SC-6217
Mouse	NUP153	Anti-NUP153 [QE5] antibody	1:200	Abcam	ab24700

doi:10.1371/journal.pone.0124619.t001

Three-dimensional confocal laser scanning microscopy (3D-CLSM)

3D-CLSM was performed using a high aperture, oil immersion objective (63x/1.4 NA). If the working distance of this objective was insufficient an objective with a lower aperture and a longer working distance (20x/0.7 NA) was used. Light optical serial sections of nuclei were recorded with a Leica TCS SP5 using x,y/z voxel sizes of 30–120 nm/200 nm for imaging of selected nuclei. Fluorochromes were excited with blue diode, argon and helium–neon lasers using laser lines at 405 nm, 488 nm and 594 nm respectively.

3D structured illumination microscopy (3D-SIM) and quantitative image evaluation

3D-SIM of embryonic nuclei was performed on a DeltaVision OMX V3 system (Applied Precision Imaging/GE Healthcare) with a lateral (x,y) resolution of ~120 nm and an axial (z) resolution of ~300 nm [7]. The system was equipped with a 100x/1.40 NA PlanApo oil immersion objective (Olympus), Cascade II:512 EMCCD cameras (Photometrics) and 405, 488 and 593 nm diode lasers. Image stacks were acquired with a z-distance of 125 nm and with 15 raw SIM images per plane (5 phases, 3 angles). The SI raw data were computationally reconstructed with channel specific measured OTFs using the softWoRX 4.0 software package (Applied Precision). Images from the different color channels were registered with alignment parameters obtained from calibration measurements with 0.2 μm diameter TetraSpeck beads (Invitrogen). The voxel size of the reconstructed images is 39.5 nm in x,y and 125 nm in z with 32-bit depth. For all subsequent image processing and data analysis, images were converted to 16-bit composite tif-stacks. Image stacks were processed using ImageJ 1.45b (http://rsb.info.nih.gov/ij/). Images are shown after application of a threshold, which removed background, including patterns apparently resulting from SIM imaging/reconstruction [1]. DAPI intensity classes were established as described [7]. The statistical comparisons were performed with the software package for scientific computing R 2.15 (http://www.r-project.org/).

RNA-Seq data analysis

Bovine *in vitro* fertilized embryos were produced as previously described [24] using commercially available semen from a Zebu bull. Visually inspected embryos were picked and snap-frozen in liquid nitrogen after washing in PBS. Denuded oocytes before and after maturation and

Table 2. Secondary antibodies.

Host	Target	Fluorophore	Excitation [nm]	Dilution	Company	ID
Donkey	Mouse IgG (H+L)	Alexa	488	1:400	Invitrogen	A-21202
Donkey	Mouse IgG (H+L)	Alexa	594	1:500	Invitrogen	A-21203
Donkey	Goat IgG (H+L)	Alexa	488	1:400	Invitrogen	A-11055
Donkey	Goat IgG (H+L) preadsorbed	Alexa	594	1:400	Abcam	ab150136

doi:10.1371/journal.pone.0124619.t002

embryos at the 4-cell, 8-cell, 16-cell and blastocyst stages were collected for sequencing. In brief, pools of 10 oocytes or embryos were thawed and lysed in 10 µl of lysis buffer (Prelude kit from NuGEN) and cDNA was generated and amplified with the Ovation RNAseq V2 kit (NuGEN) following the instructions of the manufacturer and as described in [4]. For each stage three replicates were sequenced on an Illumina GAIIx in single-read mode and a read length of 80 bases. Data are available at Gene Expression Omnibus (GEO; GSE52415). Reads were analyzed as described in [4]. Briefly, reads were filtered from the 3' and 5' end with a quality cut-off of 20 and a minimal read length of 30. After filtering, reads were mapped with TopHat2 against the bovine reference genome (UMD 3.1) and the number of reads mapped to intronic positions of the genes *LMNA*, *LMNB1*, *LMNB2*, *NUP35*, *NUP37*, *NUP43*, *NUP50*, *NUP54*, *NUP62*, *NUP85*, *NUP88*, *NUP93*, *NUP98*, *NUP107*, *NUP133*, *NUP153*, *NUP155*, *NUP160*, *NUP188*, *NUP205*, *NUP210*, *NUP210L* and *NUP214* were counted. Reads in intronic regions vs. not-covered positions in intronic regions (RINP) values were calculated as previously described [4]. For the gene expression analysis, the variance stabilized expression values were obtained from the Bioconductor package DESeq.

Results

In our study we combined DAPI staining of DNA with indirect immunostaining of NUP153 (as a marker for the presence of NPCs) and lamin B (as a marker for the nuclear lamina). If not stated otherwise, 3D-SIM was employed to obtain super-resolution light optical serial sections of nuclei.

Nuclear pore complexes (NPCs) show profound changes of distribution patterns during preimplantation development

We demonstrate massive changes of nuclear phenotypes and nuclear pore distributions during different stages of preimplantation development (Fig 1; S1 and S2 Figs). Whereas the lamina showed a contiguously immunopositive staining for lamin B in nuclei at all stages, the distribution of NPCs was strikingly inhomogeneous in the nuclear envelope of male and female pronuclei, as well as in nuclei of 2- to 8-cell embryos. Some regions appeared densely covered with NPCs, whereas others lacked NPCs entirely (Fig 1A and 1B; S1A Fig–S1E Fig and S2A Fig). After MGA the distribution of NPCs became rather uniform over the entire nuclear envelope (Fig 1C and 1D; S1F Fig—S1I Fig and S2B Fig). NPC clusters, which were indicated by confluence of NUP153 signals, appeared more prominent in the large pre-MGA nuclei compared with the smaller post-MGA nuclei (S2 Fig). Visual inspection of 3D-SIM sections suggested that these nuclei also carried the highest total number of NPCs, but limitations of the resolution of 3D-SIM prevented precise counts of individual NPCs in such clusters.

NPCs are restricted to parts of the nuclear envelope in contact with DNA

Regions of the nuclear envelope and its associated nuclear lamina, which lacked NPCs in nuclei from embryos up to the onset of MGA at the 8-cell stage, were characterized by a lack of contacts with DAPI-stained DNA (Fig 1A and 1B). In nuclei of post-MGA embryos DNA apparently contacted the entire envelope with its associated lamina in line with a rather uniform distribution of NPCs (Fig 1C and 1D). Fig 1C presents an exceptionally large post-MGA nucleus from a 19-cell embryo. Some features of its phenotype are similar to the nucleus from an 8-cell embryo shown in Fig 1B. These features include the presence of a major lacuna in the nuclear interior, which is apparently free of DAPI-stained DNA and surrounded by major DAPI-stained chromatin bodies, which are separated by wide interchromatin compartment (IC) channels. In contrast to pre-MGA nuclei (Fig 1A), this post-MGA nucleus revealed a thin rim

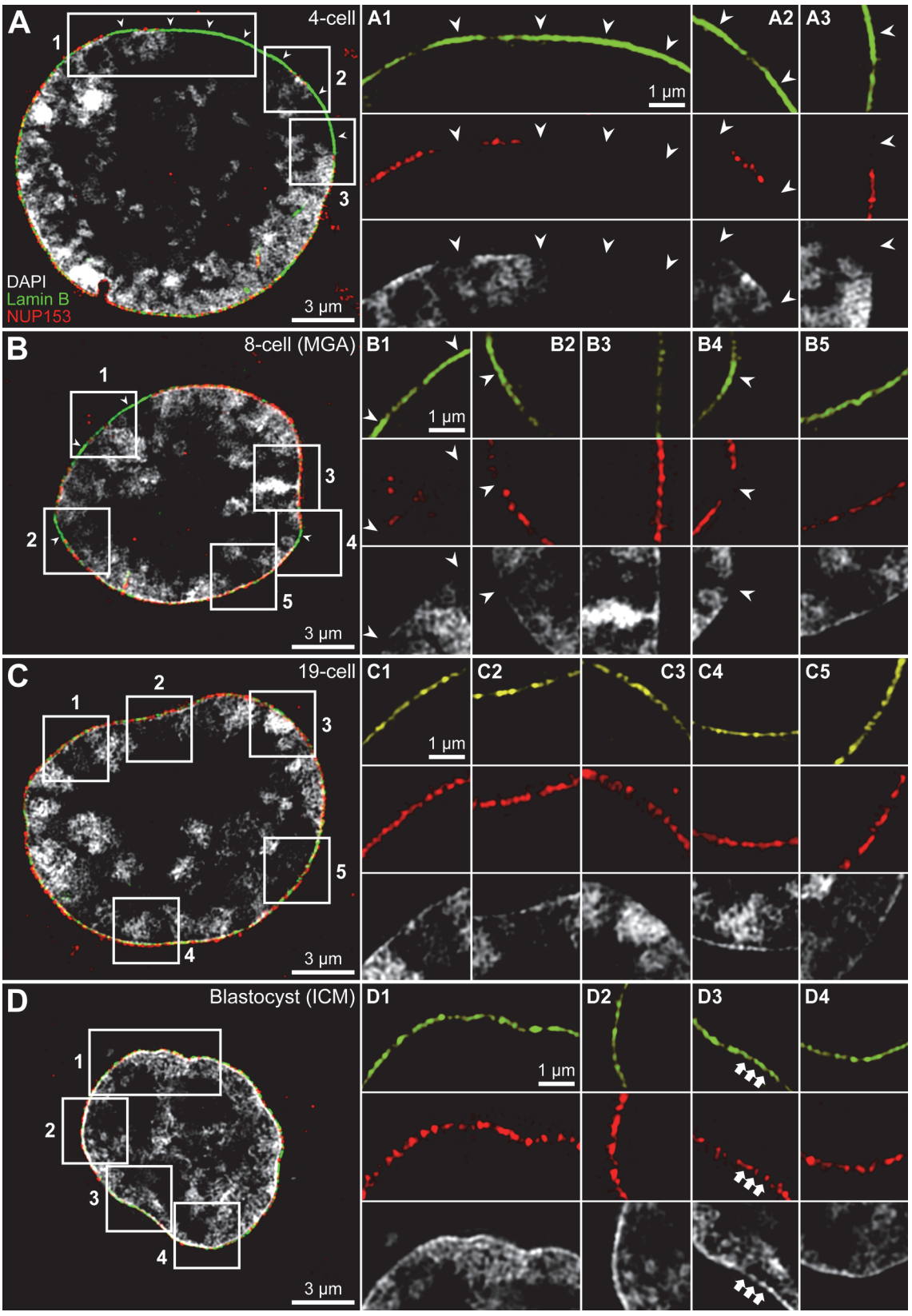
A
4-cell
1
2
3
DAPI
Lamin B
NUP153
3 µm
A1
A2
A3
1 µm
B
8-cell (MGA)
1
2
3
4
5
3 µm
B1
B2
B3
B4
B5
1 µm
C
19-cell
1
2
3
4
5
3 µm
C1
C2
C3
C4
C5
1 µm
D
Blastocyst (ICM)
1
2
3
4
3 µm
D1
D2
D3
D4
1 µm

Fig 1. Presence of NPCs in the nuclear envelope correlates with chromatin contact sites. A and **B.** Midsections of nuclei from a 4-cell embryo (A) and an 8-cell embryo (B) demonstrate a lack of NUP153 signals (red) in regions of the nuclear envelope and associated lamin B (green) without contacts to DAPI-stained DNA (grey). **Panels A1-A3** and **B1-B5** show enlargements of boxed areas in A and B; arrowheads point to lamin B immunopositive, although NUP153 immunonegative regions without demonstrable DAPI-stained DNA. In contrast, the nuclear envelope carries NUP153 signals in regions, where the underlying lamina is contacted by DAPI-stained DNA. **C** and **D.** Midsections of nuclei from a 19-cell embryo (C) and from the inner cell mass of a blastocyst (D) reveal NUP153 signals distributed along the entire nuclear envelope. Enlargements of boxed areas shown in panels **C1-C5** and **D1-D4** demonstrate a strict correlation between contacts of DAPI-stained DNA along the entire lamina and the presence of NPCs. Note that DAPI-stained DNA indicates that the lamina is contacted by extended chromatin masses at some sites, whereas at other sites only a thin lining of chromatin can be noted beneath the lamina. This thin chromatin layer and the associated lamina are perforated by IC channels (D3, arrows). S1 Fig, panels D-F and H, present complete DAPI-, lamin B- and NUP153-stained sections of the nuclei shown in this Figure. Bars: 3 μm for A-D; 1 μm for A1-A3, B1-B5, C1-C5, D1-D4.

doi:10.1371/journal.pone.0124619.g001

of DAPI-stained DNA associated with the entire lamina and a rather uniform distribution of NUP153. A uniform pattern of attachments of DAPI-stained DNA with the lamina was a characteristic feature of nuclei in post-MGA embryos (Fig 1C and 1D; S1F Fig–S1I Fig). These observations suggest that chromatin contacting the nuclear envelope or its lamina is an essential requirement for the presence of NPCs in the corresponding part of the nuclear envelope.

Different types of nuclear invaginations during preimplantation development

Multiple types of nuclear invaginations were another striking finding and could be demonstrated throughout the entire preimplantation period (Fig 2; S1 Movie). Three types of invaginations were distinguished by different patterns of immunostaining with anti-NUP153 and anti-lamin B antibodies (Fig 2A–2C). Throughout all stages of preimplantation development 69% of invaginations studied in a total of 90 nuclei were immunopositive for both NUP153 and lamin B (Fig 2A). We refer to them below as NUP+/lamin B+ invaginations. They could be very short and barely recognizable, but could also penetrate deeply into the nucleus or form tunnels.

Eighteen percent of invaginations were immunopositive for lamin B but negative for NUP153 (Fig 2B). These NUP-/lamin B+ invaginations were not lined by intensely DAPI-stained DNA and may not be involved in import/export functions. SIM serial sections yielded frequent examples of NUP-/lamin B+ intranuclear segments and vesicle-like structures inside the nucleus, which were likely derived from NUP-/lamin B+ invaginations (Fig 2B5). Z-stacks did not reveal any contact with the nuclear envelope suggesting their complete isolation (data not shown). NUP-/lamin B+ extranuclear segments or extranuclear vesicle-like structures were rarely noticed. We argue that NUP-/lamin B+ invaginations are part of a mechanism involved in the reduction of the nuclear envelope, which in turn requires a reduction of the lamina beneath the envelope (see Discussion).

Thirteen percent of invaginations were NUP153 positive but lamin B negative (Fig 2C). These NUP+/lamin B- invaginations, as well as NUP+/lamin B+ invaginations, were typically lined by brightly DAPI-stained chromatin (compare Fig 2C with 2A). Large extrusions, as well as vesicle-like structures of NUP153 positive material were noted outside the nucleus up to the 19-cell stage (Fig 2C2–2C5).

Nuclear volumes decrease during preimplantation development

Nuclear volumes showed a massive decline during preimplantation development (Fig 3A). The largest nuclear volumes were observed at the 2-cell stage, followed by a significant decrease at the 4-cell stage ($p < 10^{-6}$). No further significant change was noted between the 4- and 8-cell stages ($p = 0.7$). A further significant nuclear volume decrease occurred after MGA. Compared with nuclei at the 8-cell stage, nuclear volumes of the 19-cell embryo and morula were

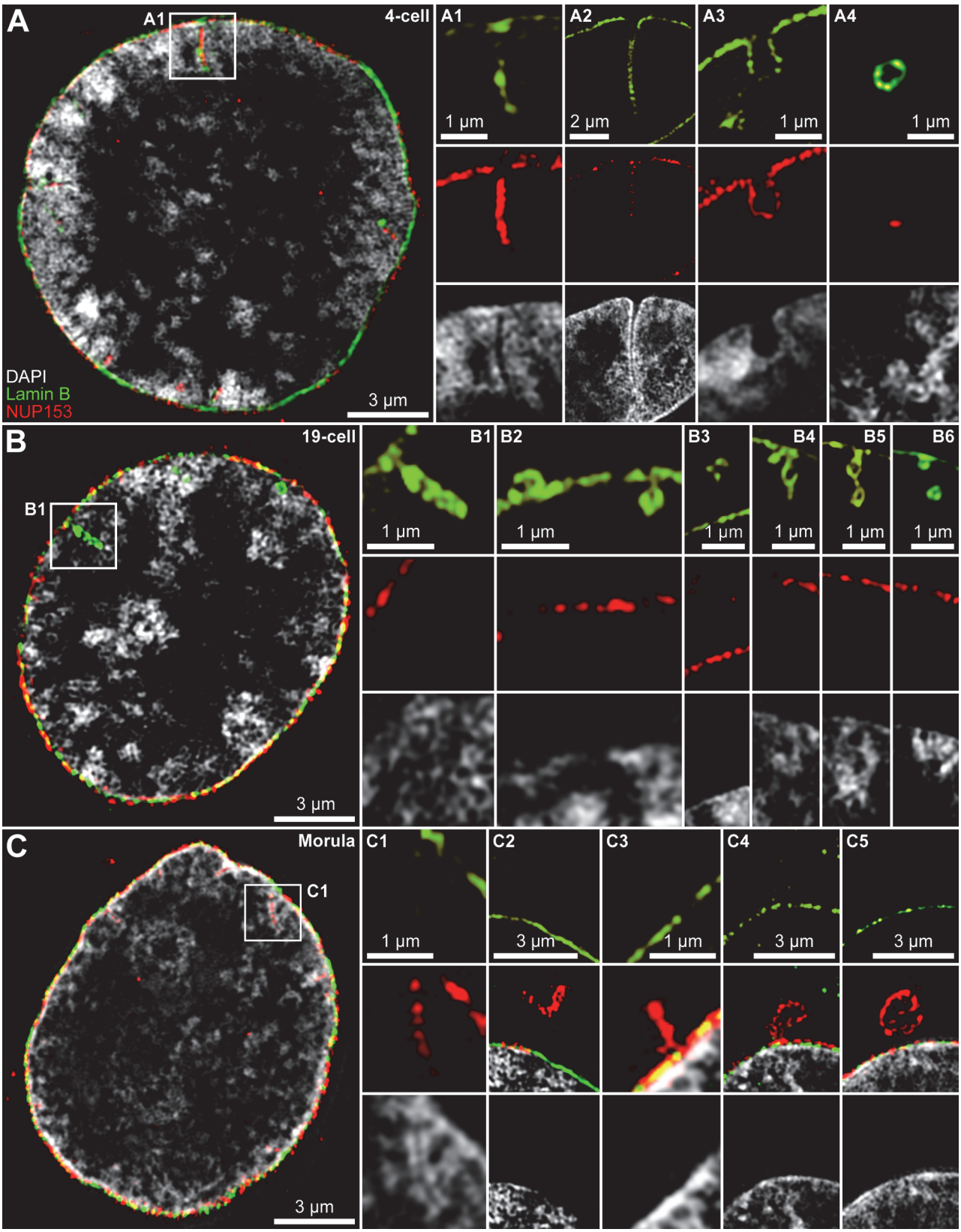
A
A1
4-cell
DAPI
Lamin B
NUP153
3 µm
A1
1 µm
A2
2 µm
A3
1 µm
A4
1 µm
B
19-cell
B1
3 µm
B1
1 µm
B2
1 µm
B3
1 µm
B4
1 µm
B5
1 µm
B6
1 µm
C
Morula
C1
3 µm
C1
1 µm
C2
3 µm
C3
1 µm
C4
3 µm
C5
3 µm

Fig 2. Invaginations, extrusions and excisions of the nuclear envelope/lamina studied by 3D-SIM. A. Midsection through a nucleus from a 4-cell embryo with DAPI-stained DNA (grey) and immunostained NUP153 (red) and lamin B (green). **Panel A1.** Enlarged view of the boxed area in A shows a NUP153+/lamin B+ invagination lined by DAPI-stained chromatin. **Panel A2.** Deep NUP153+/lamin B+ invagination recorded from another nucleus. Other sections (not shown) indicate that this invagination formed part of a tunnel connecting opposite sides of this nucleus. **Panel A3.** Wide NUP153+/lamin B + invagination. **Panel A4.** Vesicle-like, NUP153+/lamin B+ intranuclear structure with sparse NUP153 signal observed in the nuclear interior. **B.** Midsection through a nucleus from a 19-cell embryo. **Panel B1.** Enlarged view of the boxed area in B shows a lamin B positive, but NUP153 negative invagination without a clearly marked border of DAPI-stained chromatin. **Panel B2.** NUP153-/lamin B+ material extruding outward from the nuclear envelope (left) or intruding into the nuclear interior (right). **Panel B3.** Extranuclear NUP153-/lamin B+ segments. **Panel B4-B6.** Intrusions of NUP153-/lamin B+ segments, still connected with the lamina (B4, B5) or entirely disconnected from it (B6; adjacent SIM sections not shown). Notably, invaginations of NUP153-/lamin B + material were not lined by brightly DAPI-stained chromatin in contrast to NUP153 positive invaginations (compare panels A1, A2). **Panel C.** Midsection through a nucleus from a morula. **Panel C1.** Enlarged view of the boxed area in C shows a NUP153 positive, but lamin B negative invagination surrounded by intensely DAPI-stained chromatin. **Panel C2** presents a NUP153+/lamin B- vesicle in a nucleus from a 2-cell pre-MGA embryo lacking association with the nuclear border (see Fig 4 for a projection displaying vast amounts of similar NUP153-clusters seemingly randomly distributed throughout the cytoplasm). **Panel C3**. Small NUP153+/lamin B- extrusion. **Panels C4** and **C5**. NUP153+ extrusions from the nuclear envelope (C4) forming vesicle-like structures that stay in close proximity with the nuclear border in a 19-cell post-MGA embryo nucleus (C5) (for further details see Fig 4, panels A-E and panels 1–4). S3 Fig presents complete DAPI-, lamin B- and NUP153-stained sections of the nuclei shown in this Figure. Bars: 3 μm for A, B, C, C2, C4, C5; 2 μm for A2; 1 μm for A1, A3, A4, B1-B6, C1, C3.

doi:10.1371/journal.pone.0124619.g002

significantly smaller ($p < 0.002$; $p < 0.0005$), whereas no significant volume difference was noted between nuclei of these two embryos ($p = 1$). A further significant decrease was noted between morula stage nuclei and nuclei of the inner cell mass (ICM) ($p < 0.0001$) as well as nuclei of the trophectoderm (TE) of the studied blastocysts ($p < 0.015$). Note that nuclei of the TE were significantly larger than nuclei from the ICM ($p < 0.0001$).

Quantitative evaluation of nuclear invaginations and internal vesicle-like structures

Fig 3B provides a quantitative assessment of nuclear invaginations described above (Fig 2), and of vesicle-like structures observed in the nuclear interior. Whereas invaginations were rare in pronuclei, they became frequent in embryos from the onset of mGA at the 2-cell stage to the morula stage (about 32 cells). In nuclei of 2- to 19-cell embryos the majority of invaginations were NUP+/lamin B+. After MGA, NUP+/lamin B+ invaginations became less frequent. NUP-/lamin B+ invaginations were most frequently observed between the 4-cell and 19-cell stages. This correlates with a major reduction in nuclear volume and surface (compare Fig 3A). NUP+/lamin B- invaginations peaked at the morula stage. Although a similarly sized fraction of NUP+/lamin B+ invaginations was still observed, the lamin B signal was typically weak. At the blastocyst stage invaginations, intranuclear segments and vesicle-like structures were rarely noted.

Extranuclear NUP153 positive clusters

Numerous extranuclear NUP153 positive clusters, located throughout the cytoplasm were noted in nuclei of zygotes, 2-cell and 4-cell embryos (Fig 4A–4C). The distribution pattern of these clusters was markedly changed with the start of MGA in an 8-cell and also in a 19-cell embryo (Fig 4D and 4E). At these stages NUP153 positive extrusions and vesicle-like structures were directly associated with or located very close to the nuclear envelope. No extranuclear NUP153 positive clusters were observed at the morula and blastocyst stages (Fig 4F–4H).

Distribution of NUP153 in mitotic chromosomes

A recent model of postmitotic NPC assembly argues that the NUP107-160 complex assembles at chromatin surfaces and interacts with additional nucleoporins, such as NUP153, for complete NPC assembly [25]. We studied the distribution of NUP153 in DAPI-stained mitoses of bovine 2-cell embryos (Fig 5) together with lamin distributions (Fig 5A1–5A4, 5B1–5B4 and

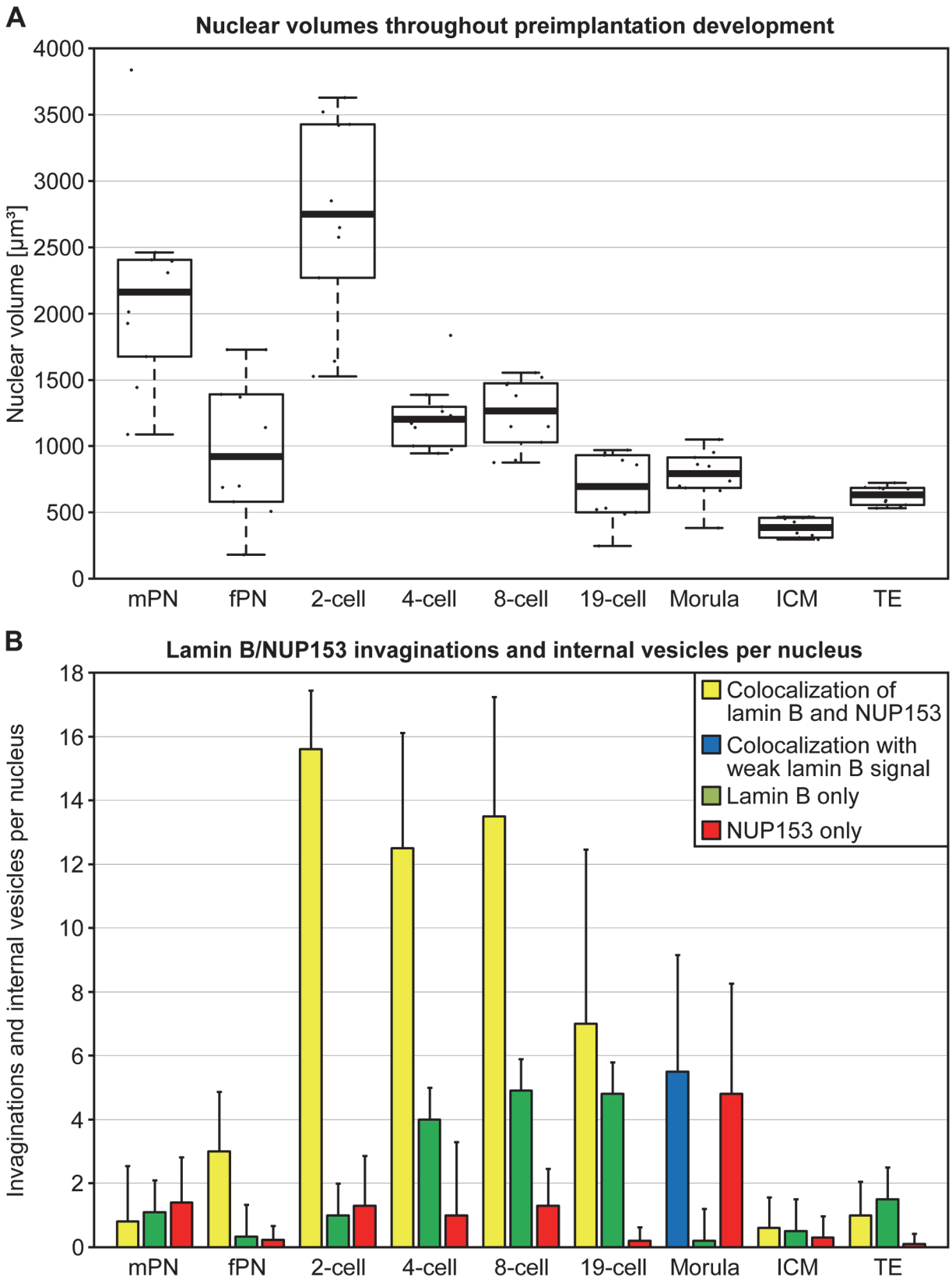
A
Nuclear volumes throughout preimplantation development
Nuclear volume [µm³]
4000
3500
3000
2500
2000
1500
1000
500
0
mPN
fPN
2-cell
4-cell
8-cell
19-cell
Morula
ICM
TE
B
Lamin B/NUP153 invaginations and internal vesicles per nucleus
Invaginations and internal vesicles per nucleus
18
16
14
12
10
8
6
4
2
0
Colocalization of lamin B and NUP153
Colocalization with weak lamin B signal
Lamin B only
NUP153 only
mPN
fPN
2-cell
4-cell
8-cell
19-cell
Morula
ICM
TE

Fig 3. Quantitative evaluation of nuclear volumes (A) and nuclear envelope/lamina invaginations or intranuclear vesicles (B). A. Box-/scatterplots represent volume measurements of nuclei at different stages of preimplantation development. 10 volume measurements were performed for each plot. mPN: male pronuclei; fPN: female pronuclei; ICM: blastocyst nuclei from the inner cell mass; TE: blastocyst nuclei from the trophectoderm. **B.** Bars represent average counts of nuclear invaginations and internal vesicles per nucleus with standard errors of the mean from the zygote to the blastocyst stage performed in nuclei after two-color immunostaining of lamin B and NUP153; see box for the meaning of the color-coded columns. For each stage ten nuclei were evaluated. Counts were performed in nuclei from several embryos up to the 8-cell stage and a single embryo each at the 19-cell, morula and blastocyst stages. Note that invaginations and isolated segments were rare events in zygotic pronuclei and blastocyst nuclei compared to the strong, transient increase of invaginations/vesicles in embryos studied from the 2-cell (mGA) to the morula stages.

doi:10.1371/journal.pone.0124619.g003

5C1–5C4). Contrary to large, cytoplasmic NUP153 positive clusters observed during the interphase of 2-cell stage nuclei (Fig 4B2), only small NUP153 particles were distributed throughout the cytoplasm of mitotic cells together with an apparent enrichment in chromatids. We performed a quantitative analysis of this distribution with respect to mitotic chromosomes in ten serial SIM sections of each mitotic cell (Fig 5A5–5A7, 5B5–5B8 and 5C5–5C8). DAPI-stained DNA was segmented into seven classes with equal intensity variance. This approach allowed a threshold-independent signal intensity classification at the voxel level [26]. Class 1 comprises voxels with intensities close to background level, while class 7 represents voxels with highest intensity. We determined both the number of DAPI pixels and the number of positive pixels for NUP153 present in each DAPI intensity class and tested the null hypothesis of a random distribution of NUP153 positive pixels across the 7 DAPI intensity classes. In this case the fraction of NUP153 pixels should be equal to the fraction of DAPI positive pixels representing each class. This null-hypothesis was rejected with a very high probability ($p < 10^{-15}$). Fig 5 panels A7, B8 and C8 demonstrate a highly significant, relative accumulation of NUP153 signals over chromosomes (classes 2–7) as compared to a relative depletion in the cytoplasm (represented by class 1). The lowest accumulation of NUP153 was noted in class 7. Our analysis indicates that NUP153 could reach the interior of chromosomes, but localization in areas with the highest chromatin density was apparently less pronounced than at the periphery. Many NUP153 particles were located at the chromosome surface. We expect that these particles carried other components of the disassembled NPCs as well and that their location determined the sites where NPCs were reassembled during the telophase/G1 transition in the reconstituted nuclear envelope.

Changes of unspliced and spliced *NUP153* RNA during preimplantation development

RNA-Seq data were recently generated with the goal to characterize the changing patterns of RNA pools already present in oocytes or synthesized *de novo* after major embryonic genome activation [4]. In the present study these data were further analyzed as described in [4] with respect to maternal and embryonic nucleoporin mRNA and more specifically *NUP153* mRNA. At the germinal vesicle and MII stages of oocytes we noted a relatively large pool of spliced nucleoporin mRNA as demonstrated by a high proportion of exonic and a small proportion of intronic reads (Fig 6A and 6B). Spliced nucleoporin mRNA levels remained relatively stable from the germinal vesicle stage to the blastocyst stage. Initiation of embryonic *NUP43*, *NUP107* and *NUP153* expression was detected at MGA at the 8-cell stage by the presence of paternal SNPs. The same approach detected initiation of embryonic expression of *NUP35* and *NUP160* at the 16-cell stage, and of *NUP88* at the blastocyst stage. While the initiation of embryonic expression could not be statistically confirmed for all nucleoporins, a general trend of a higher ratio of reads in intronic regions vs. not-covered positions in intronic regions (RINP, see [4]) was starting at the 8-cell stage for most nucleoporins (Fig 6B). Embryonic *LMNB1* expression started at MGA as suggested by a significant increase of the RINP value (Fig 6C).

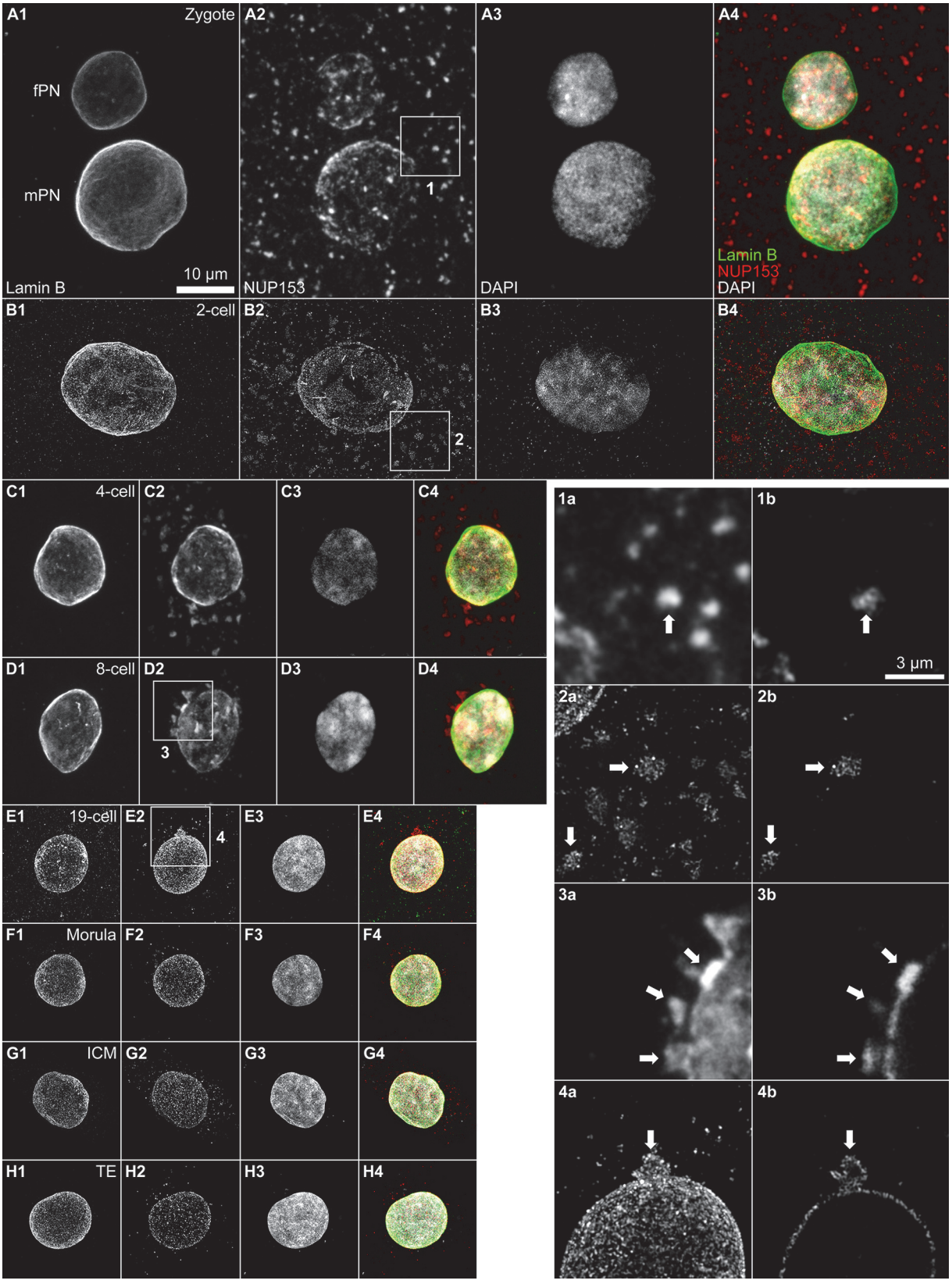
A1
Zygote
fPN
mPN
Lamin B
10 µm
A2
NUP153
1
A3
DAPI
A4
Lamin B
NUP153
DAPI
B1
2-cell
B2
2
B3
B4
C1
4-cell
C2
C3
C4
D1
8-cell
D2
3
D3
D4
E1
19-cell
E2
4
E3
E4
F1
Morula
F2
F3
F4
G1
ICM
G2
G3
G4
H1
TE
H2
H3
H4
1a
1b
3 µm
2a
2b
3a
3b
4a
4b

Fig 4. Panels A-H. Distribution of NUP153 signals during bovine preimplantation development. The panels show projections of light optical serial sections of nuclei recorded with 3D-CLSM (panels A, C, D) and 3D-SIM (panels B, E-H) at different stages of preimplantation development: pronuclei (panel A), 2-cell stage (panel B), 4-cell stage (panel C), 8-cell stage (panel D), 19-cell stage (panel E), morula stage (panel F), blastocyst stage, inner cell mass (ICM; panel G), blastocyst stage, trophectoderm (TE; panel H). All nuclei are shown with identical magnification (bar: 10 μm). Each panel shows from left to right projection images from (1) lamin B, (2) NUP153, (3) DAPI, and (4) overlay of lamin B (green), NUP153 (red) and DAPI (grey). Deposits of NUP153 clusters were randomly distributed throughout the cytoplasm before the onset of MGA at the 8-cell stage. At MGA and shortly after extranuclear NUP153 clusters were located either at or in close proximity to the nuclear periphery. The clusters were no longer present at the morula stage and later (panels F-H). **1a-4a** show enlargements of boxes around clusters (marked with arrows) presented in A, B, D and E. **1b-4b** show single sections of the same clusters. Bars: 10 μm for A-H; 3 μm for 1–4.

doi:10.1371/journal.pone.0124619.g004

While the embryonic expression initiation of *LMNA* coding for lamins A and C and *LMNB2* could not be statistically confirmed, an increase of the RINP value was detected for both genes at the 8-cell stage and later stages as compared to earlier stages (Fig 6D).

Discussion

The nuclear envelope and its underlying lamina play a central role in normal and disease-associated, pathological higher order chromatin organization [27–29]. Our results shed new light on the mechanisms involved in the distribution of NPCs, the role of nuclear invaginations covered with NPCs in nuclear import and export functions and changes of the nuclear envelope and its underlying lamina to fit massive changes of nuclear size. Current evidence does not suffice to provide a coherent scheme of the remodeling of the nuclear envelope and lamina in nuclei during bovine preimplantation development.

Contacts of chromatin with the lamina control the insertion of NPCs into the nuclear envelope

Disassembly of the nuclear envelope at the end of prophase and reassembly of its membranes at the end of mitosis from the endoplasmic reticulum (ER) are accompanied by a corresponding disassembly and reassembly of NPCs into sub-complexes and individual nucleoporins [30,31]. In mitotic cells we found most NUP153 distributed as punctuate fluorescent spots throughout the cytoplasm suggesting their presence in small complexes together with other constituents of NPCs or even to some extent as individual proteins. A prominent enrichment of NUP153 was noted at the periphery of mitotic chromosomes. This enrichment suggests the presence of chromatin binding sites for constituents of NPCs, such as nucleoporins. An active localization at specific chromatin sites is indicated by the fact that attachments of chromatin at the lamina-envelope system generally occur in a highly non-random manner via lamina associated chromatin domains (LADs) [32]. Some enrichment of NUP153 was also detected in the interior of chromatids. The reduced number and/or signal intensity of NUP153 in the interior might indicate either a reduced amount of NUP153 or a reduced clustering.

Bas van Steensel and co-workers [33] visualized the fate of LADs in single cells and found that only about 30% of LADs are in intermittent molecular contact with the nuclear lamina. Upon mitosis, LAD positioning was stochastically reshuffled. This observation indicates that the fraction of chromatin connected to the lamina can change from one cell cycle to the next. Another recent study [34] revealed a homogenous folding state of mitotic chromosomes, which was explained by a model based on a linearly organized, longitudinally compressed array of consecutive chromatin loops. In line with these observations we speculate that binding sites for NPC constituents may be distributed throughout a chromatid and that the fraction of these binding sites exposed at the chromatid periphery may change between subsequent mitoses.

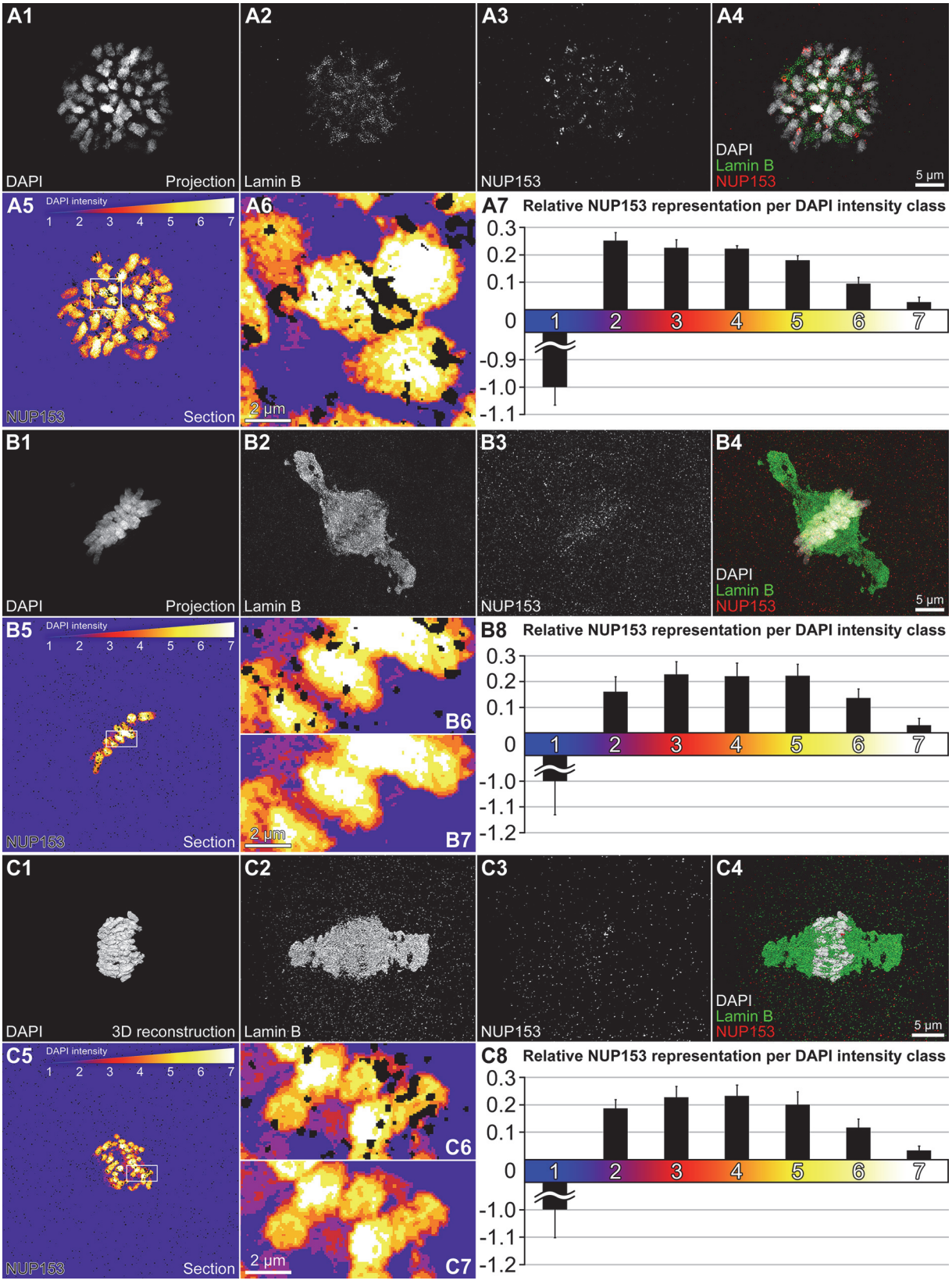
A1
DAPI
Projection
A2
Lamin B
A3
NUP153
A4
DAPI
Lamin B
NUP153
5 µm
A5
DAPI intensity
1 2 3 4 5 6 7
NUP153
Section
A6
2 µm
A7
Relative NUP153 representation per DAPI intensity class
0.3
0.2
0.1
0
-0.9
-1.0
-1.1
1 2 3 4 5 6 7
B1
DAPI
Projection
B2
Lamin B
B3
NUP153
B4
DAPI
Lamin B
NUP153
5 µm
B5
DAPI intensity
1 2 3 4 5 6 7
NUP153
Section
B6
2 µm
B7
B8
Relative NUP153 representation per DAPI intensity class
0.3
0.2
0.1
0
-1.0
-1.1
-1.2
1 2 3 4 5 6 7
C1
DAPI
3D reconstruction
C2
Lamin B
C3
NUP153
C4
DAPI
Lamin B
NUP153
5 µm
C5
DAPI intensity
1 2 3 4 5 6 7
NUP153
Section
C6
2 µm
C7
C8
Relative NUP153 representation per DAPI intensity class
0.3
0.2
0.1
0
-1.0
-1.1
-1.2
1 2 3 4 5 6 7

Fig 5. NUP153 topography during mitosis. A1-A4 and **B1-B4.** Projections of SIM serial sections through metaphase cells of 2-cell embryos stained with DAPI (A1, B1) and immunostained for lamin B (A2, B2) and NUP153 (A3, B3). A4 and B4 show merged images with DAPI (grey), lamin B (green) and NUP153 (red). **C1-C4.** 3D reconstructions of SIM serial sections recorded from an anaphase cell of a 2-cell embryo; DAPI (C1), lamin B (C2), NUP153 (C3), merged image (C4) color-coded as above. 3D reconstructions were rotated in order to provide a view on the two separating anaphase rosettes, which overlapped each other in the original position. Granular lamin B was enriched along the entire mitotic spindle in metaphase and anaphase cells (compare B2 and B4 with C2 and C4). In **A5, B5** and **C5** the metaphase plates (A1, B1) and anaphase rosettes (C1) are presented with seven color-coded DAPI intensity classes. DAPI intensities below the chosen threshold are attributed to class 1 (blue), pixels representing increasing DAPI intensities are color-coded with dark and light red (classes 2 and 3), orange (class 4), dark and light yellow (classes 5 and 6) and white (class 7). NUP153 signals are displayed in black. **A6, B6** and **C6** present enlargements of boxed areas in A5, B5 and C5 with black NUP153 signals. **B7** and **C7** show the same areas as B6 and C6, respectively, without NUP153 signals. A7, B8 and C8 show relative NUP153 accumulations and depletions, respectively, calculated for all seven DAPI classes. In the three mitotic cells the relative numbers of NUP153 positive pixels were significantly enriched in chromatids as compared to the cytoplasm (represented by class 1) ($p < 10^{-15}$). NUP153 was mostly overrepresented in the periphery of chromatids (classes 2 and 3). In the innermost area of chromatids (class 7) NUP153 was reduced compared with the chromatin periphery ($p < 10^{-15}$), but still significantly enriched in comparison with the cytoplasm ($p < 10^{-15}$). Bars: 5 μm for A1-A5, B1-B5, C1-C5; 2 μm for A6, B6 and B7, C6 and C7.

doi:10.1371/journal.pone.0124619.g005

Reconstitution of the nuclear envelope starts with tubules or sheet-like structures of double membranes derived from the ER which expand along chromatin surfaces, fuse into larger segments and finally enclose the mass of chromatids to form a complete new envelope [25]. A current model argues that certain NPC constituents at chromatin surfaces mature into NPCs when they become engulfed by growing ER sheets [25]. However, it is not obvious how large areas of the nuclear envelope can be formed without a direct contact with chromatin. At this point we do not know whether the postmitotic daughter nuclei increased in volume only after a complete nuclear envelope had formed around the relatively small volume of closely associated chromatids present at telophase or whether daughter nuclei were very large from the beginning. According to the first scenario the nuclear envelope was able to form along the surface of closely packaged chromatids and expanded only thereafter together with the expanding nuclear volume. Accordingly, lamin B required for the expanding lamina was imported via already existing NPCs. Areas of the nuclear envelope lacking NPCs may indicate that these parts quickly lost contact with chromatin. The second scenario would imply that it is possible to reassemble large parts of the nuclear envelope at sites located initially remote from chromatin.

In addition to the NPCs formed during reassembly of the nuclear envelope, many more NPCs must be assembled during interphase to approximately double their number before the onset of the next mitosis [35]. The mechanisms for the formation of these additional NPCs may differ from the mechanism for postmitotic NPC assembly [36]. Our data indicate that the interphase formation of NPCs in large pre-MGA nuclei occurred only in parts of the nuclear envelope where the corresponding lamina was in direct contact with chromatin, but was absent in parts of the envelope without such contacts. After MGA both contact sites of chromatin with the lamina and NPCs became much more uniformly distributed.

Role of nuclear envelope remodeling in nuclear volume reduction

Intranuclear envelope segments and vesicles were previously described as intranuclear annulate lamellae in electron microscopy studies of oocytes of numerous species [37,38], as well as in nuclei of mouse preimplantation embryos [39]. Based on our quantitative analysis, we hypothesize that nuclear envelope invaginations without NPCs, as well as isolated intra- and extranuclear segments of the lamina and nuclear envelope, respectively, are part of a mechanism for nuclear envelope reduction during interphase, which accompanies nuclear volume reduction during preimplantation development (interphase hypothesis). As an alternative or in addition to this hypothesis, isolated lamin B and/or NUP153 immunopositive segments and vesicle-like structures may form during mitosis either during the breakdown of the nuclear envelope or during the nuclear envelope reconstitution at late telophase/early G1 phase (mitosis hypothesis). However, both a maximum of NUP153-/lamin B+ invaginations and of NUP153+/lamin

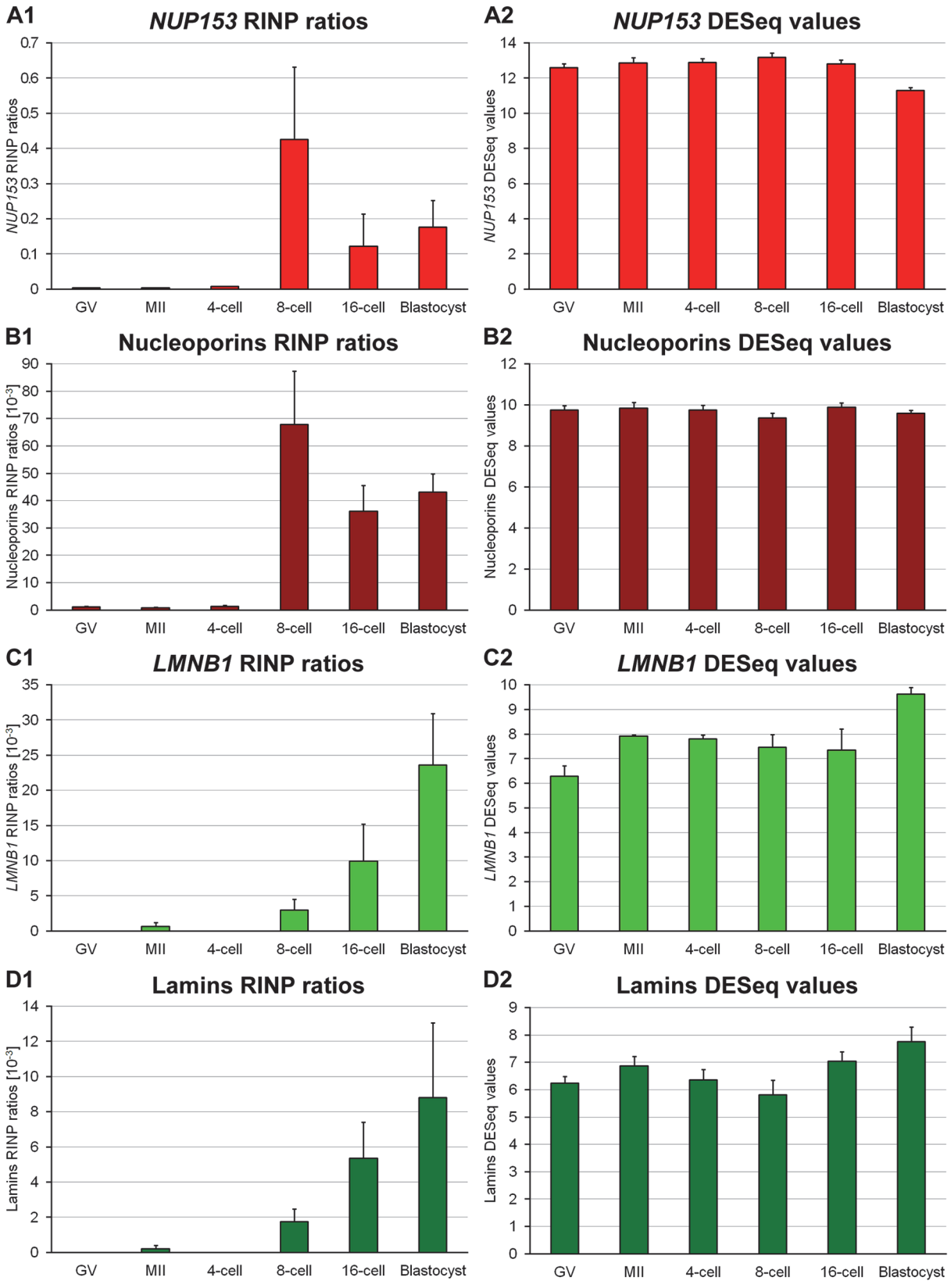
A1
NUP153 RINP ratios
NUP153 RINP ratios
0.7
0.6
0.5
0.4
0.3
0.2
0.1
0
GV
MII
4-cell
8-cell
16-cell
Blastocyst
A2
NUP153 DESeq values
NUP153 DESeq values
14
12
10
8
6
4
2
0
GV
MII
4-cell
8-cell
16-cell
Blastocyst
B1
Nucleoporins RINP ratios
Nucleoporins RINP ratios [10-3]
90
80
70
60
50
40
30
20
10
0
GV
MII
4-cell
8-cell
16-cell
Blastocyst
B2
Nucleoporins DESeq values
Nucleoporins DESeq values
12
10
8
6
4
2
0
GV
MII
4-cell
8-cell
16-cell
Blastocyst
C1
LMNB1 RINP ratios
LMNB1 RINP ratios [10-3]
35
30
25
20
15
10
5
0
GV
MII
4-cell
8-cell
16-cell
Blastocyst
C2
LMNB1 DESeq values
LMNB1 DESeq values
10
9
8
7
6
5
4
3
2
1
0
GV
MII
4-cell
8-cell
16-cell
Blastocyst
D1
Lamins RINP ratios
Lamins RINP ratios [10-3]
14
12
10
8
6
4
2
0
GV
MII
4-cell
8-cell
16-cell
Blastocyst
D2
Lamins DESeq values
Lamins DESeq values
9
8
7
6
5
4
3
2
1
0
GV
MII
4-cell
8-cell
16-cell
Blastocyst

Fig 6. Transcriptome analysis of nucleoporins and lamins. Expression data were generated by Graf et al. [4] and are available at GEO (GSE52415). Data analysis was performed as described [4]. **A1.** Diagram of *NUP153* mRNA ratios of intronic reads to not-covered intronic positions (RINP; see [4]) of three combined replicates for the germinal vesicle (GV) and metaphase II (MII) stages of oocytes as well as the 4-cell, 8-cell, 16-cell and blastocyst stages of embryonic development. **A2.** Diagram of *NUP153* normalized expression values from DESeq for the same stages as shown in A1. The GV and MII stages of oocytes up to the 4-cell stage show a high presence of spliced *NUP153* mRNA compared with a relatively low amount of unspliced, newly synthesized *NUP153* mRNA as shown in A1. Spliced *NUP153* mRNA levels remained stable from the GV to the blastocyst stage (A2). **B1, B2, C1, C2, D1** and **D2** show the diagrams for the same analysis as performed in A1 and A2 for the combined averages of *NUP35*, *NUP37*, *NUP43*, *NUP50*, *NUP54*, *NUP62*, *NUP85*, *NUP88*, *NUP93*, *NUP98*, *NUP107*, *NUP133*, *NUP153*, *NUP155*, *NUP160*, *NUP188*, *NUP205*, *NUP210*, *NUP210L* and *NUP214* (B), *LMNB1* (C) and all lamins (*LMNA*, *LMNB1* and *LMNB2*; D). These results are similar to the results for *NUP153*, indicating that the clustering of NUP153 during interphase is not replicated by lamin B despite its presence in the cytoplasm.

doi:10.1371/journal.pone.0124619.g006

B- extrusions from the nuclear envelope were observed in nuclei at the 8-cell stage. Cells at this stage show the longest interphase length of all stages, and consequently the lowest mitotic rate, during bovine preimplantation development [40]. This supports the interphase hypothesis.

Role of nuclear envelope remodeling in nuclear import/export functions

Our data indicate a particularly high demand for NPCs in embryos preparing for and passing through MGA. During the first cell cycles preceding MGA, such a need may result from the necessity to re-import into newly formed daughter nuclei large amounts of maternally derived proteins or proteins synthesized *de novo* from maternal mRNAs. Invaginations in large nuclei at early preimplantation development covered with NPCs may also help to improve nuclear import and export functions by reducing the average distances of NPCs to chromatin in need of transcription, replication or repair but embedded deep in the nuclear interior [20].

As already noted above (see Results), the clustering of NPCs prevented precise counts of individual nuclear pores even with the improved resolution of 3D-SIM (ca. 100 nm lateral and ca. 300 nm axial). This problem can be overcome by the application of other approaches of super-resolution fluorescence microscopy with still higher resolution (for review see [22]) or alternatively by use of electron microscopy (for review see [41]). One has to take into account that a quantitative determination of NPCs in fixed cells provides only snapshots. New approaches of live cell super-resolution imaging [42] have started to open future avenues for an understanding of the dynamics of NPC formation and distribution. A particularly high need for the synthesis of NPCs was further supported by our RNA-Seq data combined with microscopic observations, which revealed that *de novo* synthesis of nucleoporin mRNAs was initiated at MGA but preceded by large deposits of maternal mRNAs and cytoplasmic NUP153 protein clusters.

The changing distribution of cytoplasmic NUP153 positive clusters

Our microscopic observations demonstrate the presence of NUP153 positive clusters in the cytoplasm of pre-MGA blastomeres. Such NUP153 aggregates may be part of maternally provided NUP building blocks for the formation of NPCs until *de novo* synthesis of nucleoporins is initiated at MGA. In contrast, NUP153 positive nuclear extrusions and vesicle-like structures exclusively located in close proximity to the nuclear envelope observed at and shortly after MGA may reflect a mechanism of nuclear envelope reduction, which occurs in line with nuclear volume reduction during preimplantation development.

Import/export functionality of NPC connections with the interchromatin compartment

In the absence of nuclear envelope invaginations, import/export functions are restricted to NPCs except for occasional observations of ribonucleoprotein particle export based on nuclear

envelope budding [43]. In an envelope smoothly surrounding the nuclear periphery transcription factors entering the nucleus need to overcome distances of several μm in order to reach specific targets located in the nuclear interior. Considering the functional benefits of nuclear envelope invaginations covered with NPCs [20], one wonders why nuclear invaginations decreased in post-MGA embryos and were rarely detected in blastocyst nuclei and as a more general consideration, why such invaginations did not evolve as a structural feature of nuclei in all cell types and under all functional conditions? For an answer it is important to consider the role of NPCs not in isolation but in context with their connection to the interchromatin compartment (IC) [1,26,44]. The IC starts with channels at nuclear pores [45]. These channels penetrate the layer of dense chromatin beneath the lamina and form a three-dimensionally interconnected channel system in the nuclear interior. The IC occupies the nuclear space between chromatin domain clusters (CDCs), which form the building blocks of chromosome territories [5]. Current evidence demonstrates that essential nuclear functions like transcription, DNA replication and repair occur in the periphery of CDCs, called the perichromatin compartment (PR) [26,41].

The potential functional roles of the interconnected NPC-IC system in nuclear import/export have not yet been fully explored. Several lines of experimental evidence, however, suggest a role of the IC in guiding imported proteins, such as proteins involved in transcription, DNA replication, repair and chromatin modifications, towards chromatin embedded deep in the nuclear interior, as well as for the export of ribonucleoprotein particles carrying messenger RNAs towards NPCs. Mor et al. [46] have described evidence in favor of the hypothesis that interchromatin channels ensure "a steady and continuous wave of mRNPs travelling towards the NPC." The observation that green fluorescent protein (GFP) diffuses normally within the IC but shows an anomalous diffusion in compact chromatin [47] is in line with the hypothesis that individual proteins may preferentially move within IC channels. This hypothesis is further supported by high resolution fluorescence correlation spectroscopy (FCS) of the mobility of inert monomers, trimers and pentamers of GFP, as well as GFP fusions with other proteins in nuclei of living cells [48]. Larger nuclear particles with a diameter of 100 nm show an obstructed diffusion in distinct corralled regions surrounded by dense chromatin regions [49].

Conclusions

In conclusion, we argue that the NPC-IC system suffices in nuclei of many cell types to accomplish the needs of nuclear import/export functions even for chromatin embedded deep in the nuclear interior. An additional system of nuclear invaginations covered with NPCs may only be needed in case of extraordinary import/export demands. The case of nuclear envelope remodeling during bovine preimplantation development provides an example for the requirement of nuclear envelope invaginations in the very large nuclei at early preimplantation development but not in the much smaller nuclei at later stages.

Supporting Information

S1 Fig. Changes of nuclear pore distributions during bovine preimplantation development. Midplane sections recorded with confocal laser scanning microscopy (A, B) and 3D-SIM (C-I) from representative nuclei with DAPI-stained DNA (A1–I1), immunostained lamin B (A2-I2) and NUP153 (A3-I3), as well as overlays of DAPI (grey), lamin B (green) and NUP153 (red) (A4-I4). **Panel A**. Male pronucleus. **Panel B**. Female pronucleus. **Panels C-H**. Nuclei from embryos with 2-cells (C), 4-cells (D), 8-cells (E), 19-cells (F), a morula (G) and the inner cell mass (H) and trophectoderm (I) of a blastocyst. Note that lamin B underlines the entire nuclear envelope as a contiguous structure throughout the entire preimplantation development.

NUP153, in contrast, is clustered at some regions of the nuclear envelope, but entirely lacking at others in nuclei until the 8-cell stage, i.e. the stage, where MGA occurs. Such regions are denoted by arrowheads in A-E. In post-MGA nuclei a rather uniform distribution of NUP153 was noted throughout the entire nuclear envelope. Bar shown in A1, represents 5 μm for all images.
(TIF)

S2 Fig. Nuclear pore and lamin B distributions in embryonic pre- and post-MGA nuclei. A1-A3. Top section of a nucleus from a 4-cell embryo immunostained for lamin B (A1) and NUP153 (A2), image overlay (A3; lamin B, green; NUP153, red). Note the strikingly different distribution of lamin B and NPCs with extended lamin B positive areas lacking NPCs in the corresponding part of the envelope. **A4.** Overlay of lamin B signals recorded in SIM serial sections from the nuclear top to the nuclear midplane (half-projection) of the nucleus shown in A1-A3. **A5.** Corresponding half-projection of NUP153 signals from this nucleus. Note large areas free of NUP signals, but filled with lamin B signals in A4. **A6.** Intensity plot of lamin B (black) and NUP153 (red). The area crossed by the plot is marked with a dashed line in A4/A5. The blue lines in A4, A5 and A6 mark the transition from a NUP153 enriched area to a NUP153 depleted area. **B1-B3.** Top section of a nucleus from the 19-cell, post-MGA embryo reveals a more homogeneous distribution pattern: lamin B (B1), NUP153 (B2), image overlay (B3; lamin B, green; NUP153, red). **B4 and B5.** Half-projections of SIM serial sections of lamin B signals (B4) and NUP153 (B5) from a nucleus of the inner cell mass (ICM) recorded in a blastocyst. **B6.** Intensity plots of lamin B (black) and NUP153 (red). The area crossed by each plot is marked with a dashed line in B4/B5.
(TIF)

S3 Fig. Midplane sections of the nuclei shown in Fig 2 stained for lamin B (A1-D1), NUP153 (A2-D2) and DAPI (A3-D3) with overlays (A4-D4) of lamin B (green), NUP153 (red) and DAPI (grey). Bar: 3 μm for A-D.
(TIF)

S1 Movie. This movie presents a view through SIM serial sections of a typical post-MGA nucleus stained with DAPI featuring multiple nuclear invaginations recorded from a morula stage embryo.
(AVI)

Acknowledgments

We are grateful for expert assistance of Myriam Reichenbach, Andrea Beck and Nicolas Saucedo in the generation of IVF embryos used in the present study. We also gratefully acknowledge discussions with Yosef Gruenbaum, Karsten Rippe and Marion Cremer, who helped to improve substantially an earlier version of the manuscript.

Author Contributions

Conceived and designed the experiments: TC JP. Performed the experiments: JP SK TG VZ. Analyzed the data: JP AG. Contributed reagents/materials/analysis tools: TC EW VZ AG SK HB VS AS. Wrote the paper: TC JP AG EW VZ. Designed the software used in the enrichment and depletion analyses: VS. Provided an additional statistical tool for improved visualization of the results of the enrichment and depletion analyses: AS. RNA-Seq data created and analyzed: HB SK AG.

References

1. Popken J, Brero A, Koehler D, Schmid VJ, Strauss A, Wuensch A, et al. (2014) Reprogramming of fibroblast nuclei in cloned bovine embryos involves major structural remodeling with both striking similarities and differences to nuclear phenotypes of *in vitro* fertilized embryos. Nucleus 5: 555–589. doi: 10.4161/19491034.2014.979712 PMID: 25482066
2. Popken J, Koehler D, Brero A, Wuensch A, Guengoer T, Thormeyer T et al. (2014) Positional changes of a pluripotency marker gene during structural reorganization of fibroblast nuclei in cloned early bovine embryos. Nucleus 5: 542–554. doi: 10.4161/19491034.2014.970107 PMID: 25495180
3. Kanka J, Kepkova K, Nemcova L (2009) Gene expression during minor genome activation in preimplantation bovine development. Theriogenology 72: 572–583. doi: 10.1016/j.theriogenology.2009.04.014 PMID: 19501393
4. Graf A, Krebs S, Zakhartchenko V, Schwalb B, Blum H, Wolf E (2014) Fine mapping of genome activation in bovine embryos by RNA sequencing. Proc Natl Acad Sci U S A 111: 4139–4144. doi: 10.1073/pnas.1321569111 PMID: 24591639
5. Cremer T, Cremer M (2010) Chromosome territories. Cold Spring Harb Perspect Biol 2: a003889. doi: 10.1101/cshperspect.a003889 PMID: 20300217
6. Markaki Y, Gunkel M, Schermelleh L, Beichmanis S, Neumann J, Heidemann M, et al. (2010) Functional nuclear organization of transcription and DNA replication: a topographical marriage between chromatin domains and the interchromatin compartment. Cold Spring Harb Symp Quant Biol 75: 475–492. doi: 10.1101/sqb.2010.75.042 PMID: 21467142
7. Markaki Y, Smeets D, Fiedler S, Schmid VJ, Schermelleh L, Cremer T, et al. (2012) The potential of 3D-FISH and super-resolution structured illumination microscopy for studies of 3D nuclear architecture: 3D structured illumination microscopy of defined chromosomal structures visualized by 3D (immuno)-FISH opens new perspectives for studies of nuclear architecture. Bioessays 34: 412–426. doi: 10.1002/bies.201100176 PMID: 22508100
8. Bolzer A, Kreth G, Solovei I, Koehler D, Saracoglu K, Fauth C, et al. (2005) Three-dimensional maps of all chromosomes in human male fibroblast nuclei and prometaphase rosettes. PLoS Biol 3: e157. PMID: 15839726
9. Gruenbaum Y, Margalit A, Goldman RD, Shumaker DK, Wilson KL (2005) The nuclear lamina comes of age. Nat Rev Mol Cell Biol 6: 21–31. PMID: 15688064
10. Amendola M, van Steensel B (2014) Mechanisms and dynamics of nuclear lamina-genome interactions. Curr Opin Cell Biol 28: 61–68. doi: 10.1016/j.ceb.2014.03.003 PMID: 24694724
11. Cronshaw JM, Krutchinsky AN, Zhang W, Chait BT, Matunis MJ (2002) Proteomic analysis of the mammalian nuclear pore complex. J Cell Biol 158: 915–927. PMID: 12196509
12. Doucet CM, Hetzer MW (2010) Nuclear pore biogenesis into an intact nuclear envelope. Chromosoma 119: 469–477. doi: 10.1007/s00412-010-0289-2 PMID: 20721671
13. Maimon T, Elad N, Dahan I, Medalia O (2012) The human nuclear pore complex as revealed by cryo-electron tomography. Structure 20: 998–1006. doi: 10.1016/j.str.2012.03.025 PMID: 22632834
14. Adam SA (2001) The nuclear pore complex. Genome Biol 2: REVIEWS0007.
15. Hinshaw JE, Carragher BO, Milligan RA (1992) Architecture and design of the nuclear pore complex. Cell 69: 1133–1141. PMID: 1617726
16. Arlucea J, Andrade R, Alonso R, Arechaga J (1998) The nuclear basket of the nuclear pore complex is part of a higher-order filamentous network that is related to chromatin. J Struct Biol 124: 51–58. PMID: 9931273
17. Sukegawa J, Blobel G (1993) A nuclear pore complex protein that contains zinc finger motifs, binds DNA, and faces the nucleoplasm. Cell 72: 29–38. PMID: 8422679
18. Ball JR, Ullman KS (2005) Versatility at the nuclear pore complex: lessons learned from the nucleoporin Nup153. Chromosoma 114: 319–330. PMID: 16133350
19. Fricker M, Hollinshead M, White N, Vaux D (1997) Interphase nuclei of many mammalian cell types contain deep, dynamic, tubular membrane-bound invaginations of the nuclear envelope. J Cell Biol 136: 531–544. PMID: 9024685
20. Malhas A, Goulbourne C, Vaux DJ (2011) The nucleoplasmic reticulum: form and function. Trends Cell Biol 21: 362–373. doi: 10.1016/j.tcb.2011.03.008 PMID: 21514163
21. Schermelleh L, Heintzmann R, Leonhardt H (2010) A guide to super-resolution fluorescence microscopy. J Cell Biol 190: 165–175. doi: 10.1083/jcb.201002018 PMID: 20643879
22. Cremer C, Masters BR (2013) Resolution enhancement techniques in microscopy. The European Physical Journal H 38: 281–344.

23. Hiendleder S, Wirtz M, Mund C, Klempt M, Reichenbach HD, Stojkovic M, et al. (2006) Tissue-specific effects of in vitro fertilization procedures on genomic cytosine methylation levels in overgrown and normal sized bovine fetuses. Biol Reprod 75: 17–23. PMID: 16554415

24. Bauersachs S, Ulbrich SE, Zakhartchenko V, Minten M, Reichenbach M, Reichenbach HD, et al. (2009) The endometrium responds differently to cloned versus fertilized embryos. Proc Natl Acad Sci U S A 106: 5681–5686. doi: 10.1073/pnas.0811841106 PMID: 19307558

25. Wandke C, Kutay U (2013) Enclosing chromatin: reassembly of the nucleus after open mitosis. Cell 152: 1222–1225. doi: 10.1016/j.cell.2013.02.046 PMID: 23498932

26. Smeets D, Markaki Y, Schmid VJ, Kraus F, Tattermusch A, Cerase A, et al. (2014) Three-dimensional super-resolution microscopy of the inactive X chromosome territory reveals a collapse of its active nuclear compartment harboring distinct Xist RNA foci. Epigenetics & Chromatin 7: 8.

27. Akhtar A, Gasser SM (2007) The nuclear envelope and transcriptional control. Nat Rev Genet 8: 507–517. PMID: 17549064

28. Shimi T, Butin-Israeli V, Goldman RD (2012) The functions of the nuclear envelope in mediating the molecular crosstalk between the nucleus and the cytoplasm. Curr Opin Cell Biol 24: 71–78. doi: 10.1016/j.ceb.2011.11.007 PMID: 22192274

29. Zuela N, Bar DZ, Gruenbaum Y (2012) Lamins in development, tissue maintenance and stress. EMBO Rep 13: 1070–1078. doi: 10.1038/embor.2012.167 PMID: 23146893

30. Beaudouin J, Gerlich D, Daigle N, Eils R, Ellenberg J (2002) Nuclear envelope breakdown proceeds by microtubule-induced tearing of the lamina. Cell 108: 83–96. PMID: 11792323

31. Hase ME, Cordes VC (2003) Direct interaction with nup153 mediates binding of Tpr to the periphery of the nuclear pore complex. Mol Biol Cell 14: 1923–1940. PMID: 12802065

32. Meuleman W, Peric-Hupkes D, Kind J, Beaudry JB, Pagie L, Kellis M, et al. (2013) Constitutive nuclear lamina-genome interactions are highly conserved and associated with A/T-rich sequence. Genome Res 23: 270–280. doi: 10.1101/gr.141028.112 PMID: 23124521

33. Kind J, Pagie L, Ortabozkoyun H, Boyle S, de Vries SS, Janssen H, et al. (2013) Single-cell dynamics of genome-nuclear lamina interactions. Cell 153: 178–192. doi: 10.1016/j.cell.2013.02.028 PMID: 23523135

34. Naumova N, Imakaev M, Fudenberg G, Zhan Y, Lajoie BR, Mirny LA, et al. (2013) Organization of the mitotic chromosome. Science 342: 948–953. doi: 10.1126/science.1236083 PMID: 24200812

35. Maul GG, Maul HM, Scogna JE, Lieberman MW, Stein GS, Hsu BY, et al. (1972) Time sequence of nuclear pore formation in phytohemagglutinin-stimulated lymphocytes and in HeLa cells during the cell cycle. J Cell Biol 55: 433–447. PMID: 5076782

36. Rothballer A, Kutay U (2013) Poring over pores: nuclear pore complex insertion into the nuclear envelope. Trends Biochem Sci 38: 292–301. doi: 10.1016/j.tibs.2013.04.001 PMID: 23639636

37. Hsu WS (1963) The nuclear envelope in the developing oocytes of the tunicate, boltenia villosa. Z Zellforsch Mikrosk Anat 58: 660–678. PMID: 13955324

38. Everingham JW (1968) Attachment of intranuclear annulate lamellae to the nuclear envelope. J Cell Biol 37: 540–550. PMID: 5656403

39. Fakan S, Odartchenko N (1980) Ultrastructural organization of the cell-nucleus in early mouse embryos. Biologie Cellulaire: 211–217.

40. Holm P, Booth PJ, Callesen H (2002) Kinetics of early in vitro development of bovine in vivo- and in vitro-derived zygotes produced and/or cultured in chemically defined or serum-containing media. Reproduction 123: 553–565. PMID: 11914118

41. Rouquette J, Cremer C, Cremer T, Fakan S (2010) Functional nuclear architecture studied by microscopy: present and future. Int Rev Cell Mol Biol 282: 1–90. doi: 10.1016/S1937-6448(10)82001-5 PMID: 20630466

42. Chen BC, Legant WR, Wang K, Shao L, Milkie DE, Davidson MW, et al. (2014) Lattice light-sheet microscopy: imaging molecules to embryos at high spatiotemporal resolution. Science 346: 1257998. doi: 10.1126/science.1257998 PMID: 25342811

43. Speese SD, Ashley J, Jokhi V, Nunnari J, Barria R, Li Y, et al. (2012) Nuclear envelope budding enables large ribonucleoprotein particle export during synaptic Wnt signaling. Cell 149: 832–846. doi: 10.1016/j.cell.2012.03.032 PMID: 22579286

44. Rouquette J, Genoud C, Vazquez-Nin GH, Kraus B, Cremer T, Fakan S (2009) Revealing the high-resolution three-dimensional network of chromatin and interchromatin space: a novel electron-microscopic approach to reconstructing nuclear architecture. Chromosome Res 17: 801–810. doi: 10.1007/s10577-009-9070-x PMID: 19731052

45. Schermelleh L, Carlton PM, Haase S, Shao L, Winoto L, Kner P, et al. (2008) Subdiffraction multicolor imaging of the nuclear periphery with 3D structured illumination microscopy. Science 320: 1332–1336. doi: 10.1126/science.1156947 PMID: 18535242

46. Mor A, Suliman S, Ben-Yishay R, Yunger S, Brody Y, Shav-Tal Y (2010) Dynamics of single mRNP nucleocytoplasmic transport and export through the nuclear pore in living cells. Nat Cell Biol 12: 543–552. doi: 10.1038/ncb2056 PMID: 20453848

47. Daddysman MK, Fecko CJ (2013) Revisiting point FRAP to quantitatively characterize anomalous diffusion in live cells. J Phys Chem B 117: 1241–1251. doi: 10.1021/jp310348s PMID: 23311513

48. Baum M, Erdel F, Wachsmuth M, Rippe K (2014) Retrieving the intracellular topology from multi-scale protein mobility mapping in living cells. Nat Commun 5: 4494. doi: 10.1038/ncomms5494 PMID: 25058002

49. Bacher CP, Reichenzeller M, Athale C, Herrmann H, Eils R (2004) 4-D single particle tracking of synthetic and proteinaceous microspheres reveals preferential movement of nuclear particles along chromatin—poor tracks. BMC Cell Biol 5: 45. PMID: 15560848

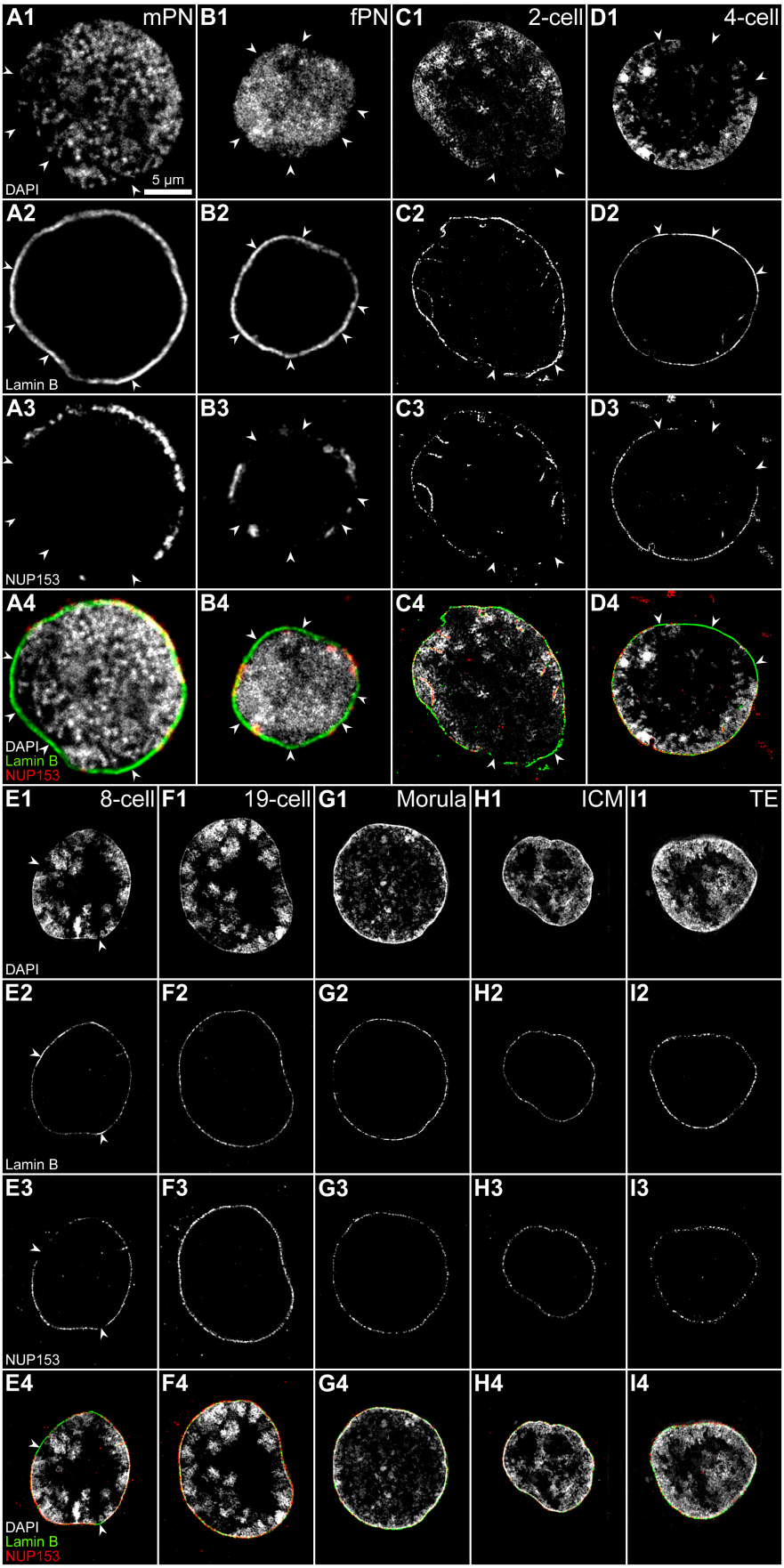
A1
mPN
B1
fPN
C1
2-cell
D1
4-cell
5 µm
DAPI
A2
B2
C2
D2
Lamin B
A3
B3
C3
D3
NUP153
A4
B4
C4
D4
DAPI
Lamin B
NUP153
E1
8-cell
F1
19-cell
G1
Morula
H1
ICM
I1
TE
DAPI
E2
F2
G2
H2
I2
Lamin B
E3
F3
G3
H3
I3
NUP153
E4
F4
G4
H4
I4
DAPI
Lamin B
NUP153

Fig. S1

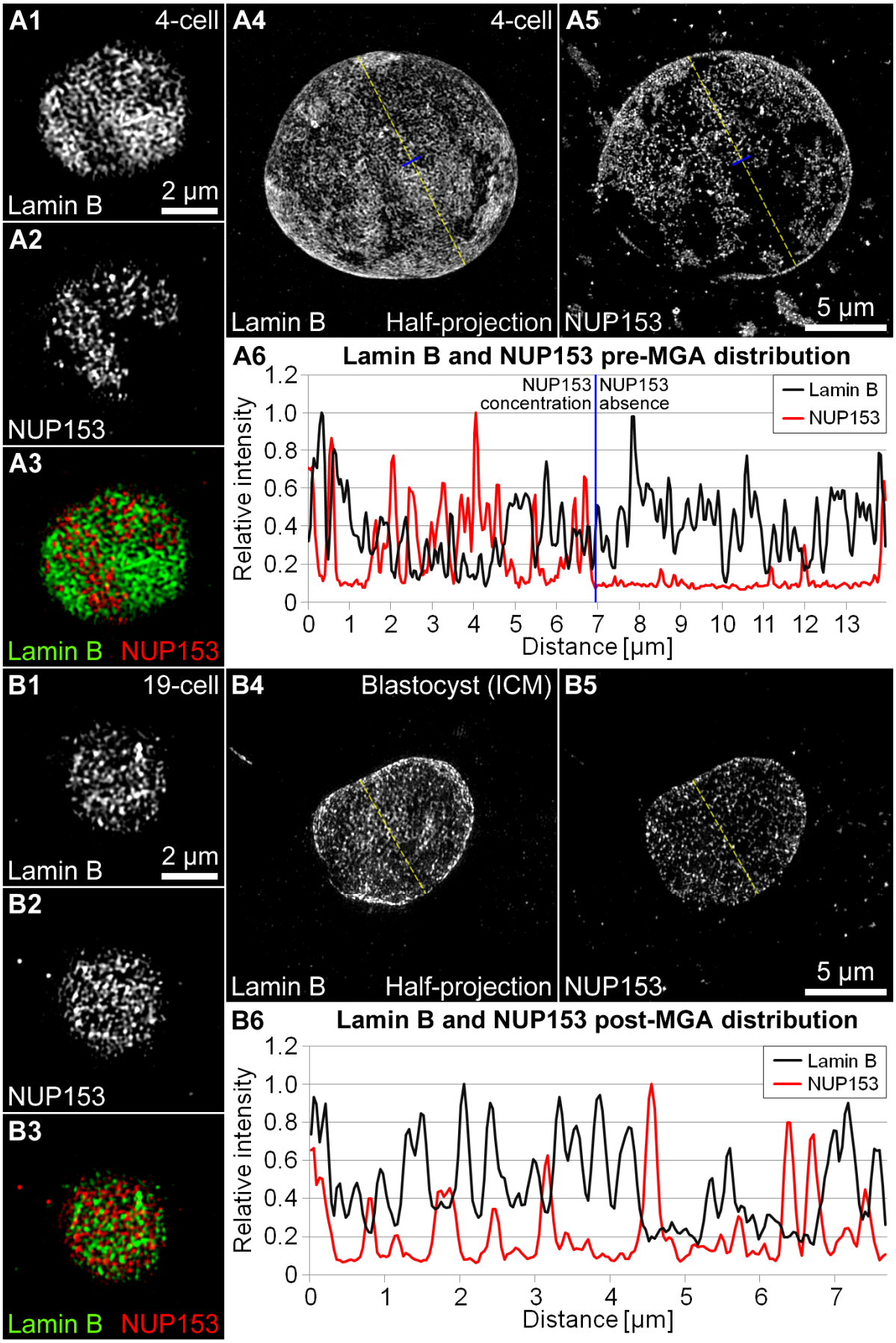
A1
4-cell
Lamin B
2 µm
A2
NUP153
A3
Lamin B NUP153
A4
4-cell
Lamin B
Half-projection
A5
NUP153
5 µm
A6
Lamin B and NUP153 pre-MGA distribution
NUP153 concentration
NUP153 absence
Lamin B
NUP153
Relative intensity
Distance [µm]
B1
19-cell
Lamin B
2 µm
B2
NUP153
B3
Lamin B NUP153
B4
Blastocyst (ICM)
Lamin B
Half-projection
B5
NUP153
5 µm
B6
Lamin B and NUP153 post-MGA distribution
Lamin B
NUP153
Relative intensity
Distance [µm]

Fig. S2

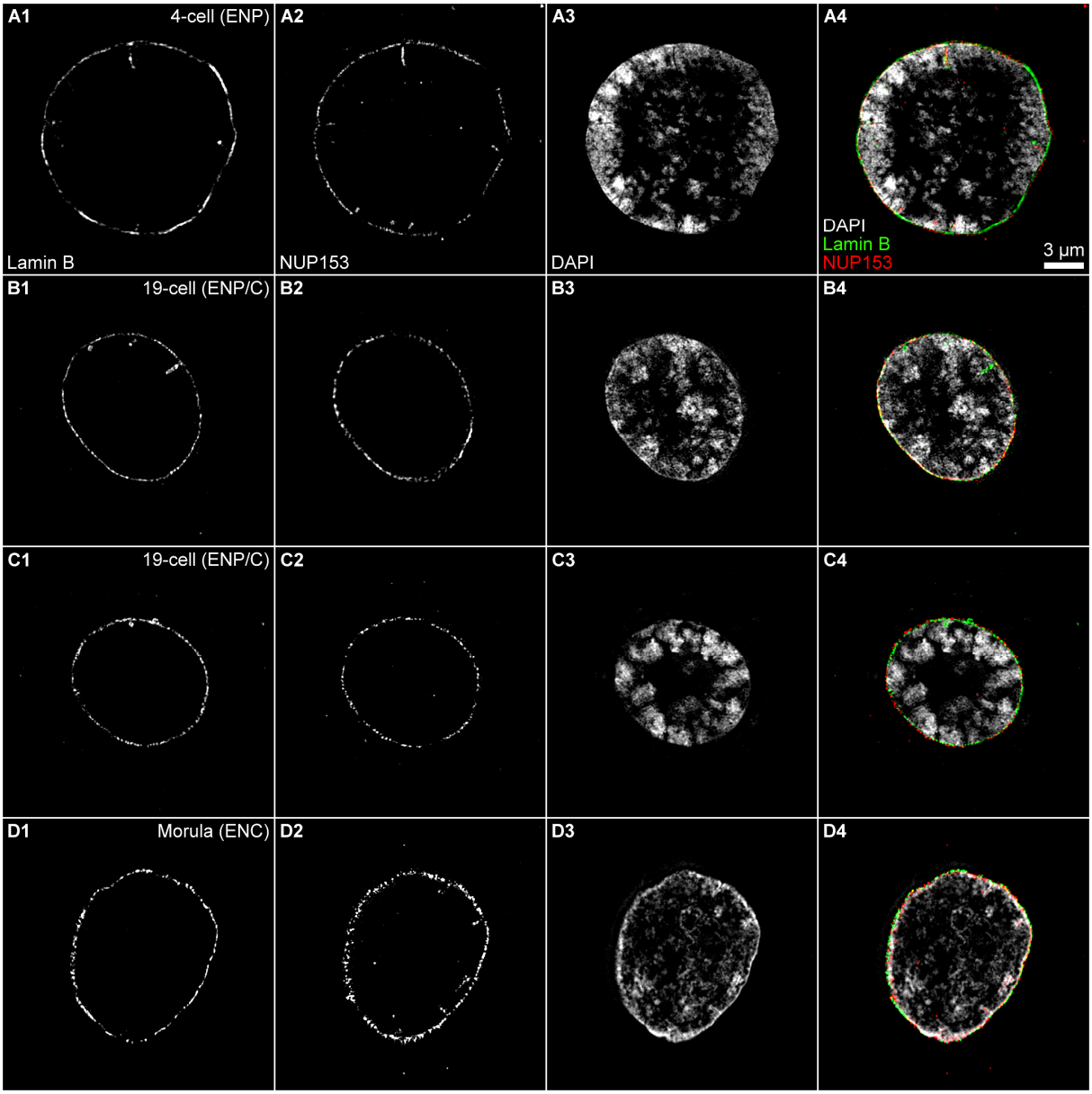
A1
4-cell (ENP)
Lamin B
A2
NUP153
A3
DAPI
A4
DAPI
Lamin B
NUP153
3 µm
B1
19-cell (ENP/C)
B2
B3
B4
C1
19-cell (ENP/C)
C2
C3
C4
D1
Morula (ENC)
D2
D3
D4

Fig. S3

2.4. Stage-dependent remodeling of the nuclear envelope and lamina during rabbit early embryonic development

Journal of Reproduction and Development

Accepted for publication: November 5, 2015
Published online: December 4, 2015

Stage-dependent remodeling of the nuclear envelope and lamina during rabbit early embryonic development

Jens Popken[1,2)], Volker J. Schmid[3)], Axel Strauss[4)], Tuna Guengoer[2)], Eckhard Wolf[2)] and Valeri Zakhartchenko[2)]

[1)]Division of Anthropology and Human Genetics, Biocenter, LMU Munich, Grosshaderner Str. 2, D-82152 Planegg-Martinsried, Germany

[2)]Chair for Molecular Animal Breeding and Biotechnology, and Laboratory for Functional Genome Analysis (*LAFUGA*), Gene Center, LMU Munich, Feodor-Lynen-Str. 25, D-81377 Munich, Germany

[3)]Institute of Statistics, LMU Munich, Ludwigstr. 33, D-80539 Munich, Germany

[4)]Division of Genetics, Biocenter, LMU Munich, Grosshaderner Str. 2, D-82152 Planegg-Martinsried, Germany

Running head: nuclear envelope and lamina remodeling in rabbit embryos

Corresponding author:

*V.Zakhartchenko@gen.vetmed.uni-muenchen.de (VZ)
Chair for Molecular Animal Breeding and Biotechnology, LMU Munich, Hackerstr. 27, D-85764 Oberschleissheim, Germany

Tel.: +49-89-2180-78446

Fax: +49-89-2180-78402

Abstract

Utilizing 3D structured illumination microscopy, we investigated the quality and quantity of nuclear invaginations and the distribution of nuclear pores during rabbit early embryonic development and identified the exact time point of nucleoporin 153 (NUP153) association with chromatin during mitosis. Contrary to bovine early embryonic nuclei, featuring almost exclusively nuclear invaginations containing a small volume of cytoplasm, nuclei in rabbit early embryonic stages contain additionally numerous invaginations containing a large volume of cytoplasm. Small-volume invaginations frequently emanated from large-volume nuclear invaginations but not *vice versa*, indicating a different underlying mechanism. Large- and small-volume nuclear envelope invaginations required the presence of chromatin, as they were restricted to chromatin-positive areas. The chromatin-free contact areas between nucleolar precursor bodies (NPBs) and large-volume invaginations were free of nuclear pores. Small-volume invaginations were not in contact with NPBs. The number of invaginations and isolated intranuclear vesicles per nucleus peaked at the 4-cell stage. At this stage, the nuclear surface showed highly concentrated clusters of nuclear pores surrounded by areas free of nuclear pores. Isolated intranuclear lamina vesicles were usually NUP153 negative. Cytoplasmic, randomly distributed NUP153-positive clusters were highly abundant at the zygote stage and decreased in number until they were almost absent at the 8-cell stage and later. These large NUP153 clusters may represent a maternally provided NUP153 deposit, but they were not visible as clusters during mitosis. Major genome activation at the 8- to 16-cell stage may mark the switch from a necessity for a deposit to on-demand production. NUP153 association with chromatin is initiated during metaphase before the initiation of the regeneration of the lamina. To our knowledge, the present study demonstrates

for the first time major remodeling of the nuclear envelope and its underlying lamina during rabbit preimplantation development.

Key words: Nuclear envelope, Nuclear lamina, Rabbit embryos

Introduction

Preimplantation development of rabbit embryos is accompanied by a reduction of nuclear volumes and activation of the embryonic genome [1]. During oogenesis, maternal mRNAs and proteins are deposited into the developing oocyte. After fertilization, this deposit is used to support the initial stages of embryonic development [2]. Before these deposits are depleted, the embryonic genome is activated to produce embryonic mRNAs and proteins for further development. During early development of rabbit embryos, limited transcriptional activity is initiated at the zygote stage and is progressively increased in subsequent stages [3-5], while most genes get activated during major embryonic genome activation (MGA) at the 8- to 16-cell stage [1].

Nuclear export of newly synthesized mRNA packaged into messenger ribonucleoprotein (mRNP) complexes is mostly facilitated through nuclear pore complexes (NPCs) [6]. Eight clusters, each containing about 30 nucleoporins (NUPs) [7], are combined to form one NPC with an outer diameter of about 120 nm. A short tunnel in the center of NPCs connects the cytoplasmic ring at the outer membrane with the nuclear ring at the inner membrane of the bilayer lipid nuclear envelope [8]. A more interior terminal ring connected to the nuclear ring by fibers forms the nuclear basket [9]. The nucleoporin NUP153 is localized either at the nuclear ring or at the nuclear basket [10]. Chromatin can associate with the nuclear basket and its attached intranuclear filaments [9].

The nuclear envelope is separated from chromatin by the nuclear lamina. In developing cells, the lamina is made up of lamins B1 and B2, whereas differentiated cells feature lamins A and C [11]. The lamina is required by NPCs for nuclear envelope insertion [12]. Invaginations of the nuclear envelope and the nuclear lamina can extend the import/export functionality of nuclear pores to regions remote from the nuclear surface [13,14]. During early embryonic development, the volume and surface of initially large nuclei decline.

Previously, we studied the changes of the nuclear envelope, nuclear pores and nuclear lamina in bovine preimplantation embryos [15]. Major findings included the presence of NPC-free areas in chromatin-free areas of the envelope up to MGA, three different types of invaginations (lamin B+/NUP153+, lamin B+/NUP153- and lamin B-/NUP153+) and large, randomly distributed NUP153 clusters in the cytoplasm before the onset of MGA correlating with NUP153 spliced mRNA deposits in oocytes. In this study, we compared these findings with the situation in rabbits, since rabbit nuclei can have a far more invaginated nuclear envelope than the generally round bovine nuclei.

Materials and Methods

Ethics statement. Rabbits were *in vivo* fertilized and slaughtered for embryo recovery. No animal experiments were conducted.

Embryo culture. *In vivo* fertilized zygotes were flushed from the oviducts 18-20 h post-hCG injection in warm phosphate buffered saline (PBS) supplemented with 4 mg/ml bovine serum albumin and then cultured in Quinn's medium containing 2.5% fetal calf serum in a humidified atmosphere of 5% CO_2 in air at 38.5 C until the appropriate stage for fixation.

Fixation of embryos. Unless noted otherwise, fixation of embryos and all subsequent steps were performed at room temperature. Embryos were briefly washed in 38 C PBS, fixed in 2% paraformaldehyde (PFA) in PBS, washed twice in PBS and then stored at 4 C in PBS until further use.

Immunostaining and embedding. Background caused by PFA was quenched using 20 mM glycine in PBS for 10 min. After washing twice with PBS, embryos were permeabilized with 0.5% Triton-X 100 for 15-30 min. After washing twice with PBS, unspecific background signals were reduced by incubation in 2% BSA for 2 h. Embryos were sequentially incubated in 40 µl of primary and secondary antibody solutions, diluted as specified in Tables 1 and 2 in PBS with 2% BSA. Specimens were incubated with primary antibodies overnight at 4 C. After washing 5x in PBS with 2% BSA, the appropriate secondary antibodies, diluted in PBS with 2% BSA, were applied for 1 h, followed by 5x washing in PBS with 2% BSA and 5x washing without BSA. Thereafter fixation of antibodies was performed with 4% PFA in PBS for 10 min, followed by washing twice in PBS. Before removal of the zona pellucida, chromatin was counterstained with DAPI (4′,6-diamidino-2-phenylindole, catalog No. D1306, Life Technologies) diluted in PBS (2.5 µg/ml) for 10 min followed by washing twice in PBS. Individual blastomeres were attached to precision cover glasses (18 x 18 mm, 170 ± 5 µm, item no. LH22.1, Carl Roth, Karlsruhe, Germany) in PBS and embedded in Vectashield (Vector Laboratories, Lörrach, Germany).

Three-dimensional confocal laser scanning microscopy (3D-CLSM). 3D-CLSM was performed using a large aperture oil immersion objective (63x/1.4 NA). If the working distance of this objective was insufficient, an objective with a lower aperture and a longer working distance (20x/0.7 NA) was used. Light optical serial sections of nuclei were recorded with a Leica TCS SP5 using x,y/z voxel sizes of 30–120

nm/200 nm for imaging of selected nuclei. Fluorochromes were excited with blue diode, argon and helium–neon lasers using laser lines at 405 nm, 488 nm and 594 nm, respectively.

3D structured illumination microscopy (3D-SIM) and quantitative image evaluation. 3D-SIM of embryonic nuclei was performed on a DeltaVision OMX V3 system (Applied Precision Imaging/GE Healthcare) with a lateral (x,y) resolution of ~120 nm and an axial (z) resolution of ~300 nm (Markaki *et al.*, 2012). The system was equipped with a 100x/1.40 NA PlanApo oil immersion objective (Olympus), Cascade II:512 EMCCD cameras (Photometrics) and 405, 488 and 593 nm diode lasers. Image stacks were acquired with a z-distance of 125 nm and with 15 raw SIM images per plane (5 phases, 3 angles). The SI raw data were computationally reconstructed with channel-specific measured OTFs using the softWoRX 4.0 software package (Applied Precision). Images from the different color channels were registered with alignment parameters obtained from calibration measurements with 0.2 µm diameter TetraSpeck beads (Invitrogen). The voxel size of the reconstructed images is 39.5 nm in x and y and 125 nm in z with a 32-bit depth. For all subsequent image processing and data analyses, images were converted to 16-bit composite tiff stacks. Image stacks were processed using ImageJ 1.45b (http://rsb.info.nih.gov/ij/). Images are shown after application of a threshold, which removed background, including patterns apparently resulting from SIM imaging/reconstruction [16]. DAPI intensity classes were established as described previously [17]. Statistical comparisons were performed with the software package for scientific computing R 2.15 (http://www.r-project.org/).

Results

The stage-dependent changes in the distribution of NUP153, NPCs, the nuclear lamina, isolated intranuclear laminar vesicles and nuclear envelope invaginations were studied with 3D-SIM of zygote- to blastocyst-stage embryos stained for chromatin (DAPI) and immunostained for NUP153 and lamin B. We scanned and analyzed 112 pronuclei/nuclei in 28 embryos.

Distribution of chromatin, NUP153 and lamin B changes at the beginning of preimplantation development

Early embryonic development is characterized by profound changes in the distribution of chromatin and nuclear pores (Fig. 1). At the zygote stage, smaller female pronuclei (fPNs) with an evenly shaped nuclear border and larger male pronuclei (mPNs) with a more wave-like nuclear border were always located in close association with each other. Contrary to mPNs, fPNs showed a chromatin gradient from a large concentration at the mPN contact area to a small concentration at the area most remote from the contact site. The nuclear envelope at this remote area was free of NPCs, whereas the nuclear border in contact with the mPN was enriched with NPCs. Both areas of the nuclear border were lamin B positive. Invaginations of the nuclear border were restricted to chromatin-positive areas. Both fPNs and mPNs feature a large amount of short, small-volume invaginations positive for lamin B and NUP153. In addition, fPNs feature the long, large-volume invaginations at the mPN contact site most common for all subsequent stages in the rabbit. Early 2-cell-stage nuclei showed a chromatin-free lacuna, whereas nuclei at the end of the 2-cell stage and subsequent stages no longer showed a round lacuna. With the onset of MGA at the 8- to 16-cell stage, the chromatin was more clustered in individual patches (Fig.

2) until the chromatin distribution became more evenly distributed throughout the nucleus at the blastocyst stage.

Long, voluminous invaginations can ensure proximity to cytoplasm for nucleolar precursor bodies

Rabbit nuclei displayed two types of invaginations. The most common type of invaginations contained large volumes of cytoplasm (Fig. 3A-D). These invaginations could reach across nuclei, connect opposing nuclear borders and subdivide into more voluminous invaginations. The other type of invaginations contained barely any volume (arrowheads in Fig. 3B). In the zygote stage, large-volume invaginations were limited to the area where the two pronuclei were in contact, whereas small-volume invaginations were limited to all chromatin-positive areas of the pronuclei (Fig. 1A). Small-volume invaginations emanated from the nuclear periphery or from large-volume invaginations.

Most nucleolar precursor bodies (NPBs) were located either close to the nuclear border or close to large-volume invaginations (Fig. 3). NPBs located at the nuclear border could be located in close proximity to large invaginations as well. Rarely, NPBs were located in the nuclear interior without any invaginations in their proximity. Multiple large invaginations could be in proximity to a single NPB. Some NPBs were in direct contact with large-volume invaginations. The contact sites between voluminous invaginations and NPBs usually did not contain NPCs, but NPCs could be located at the contacting invagination in close proximity to contact sites. NPBs were not necessarily in contact with an invagination emanating from the closest nuclear border. In some cases, the entire nucleus was crossed by an invagination emanating from the nuclear border most remote from the NPB it was in contact with.

Three types of intranuclear vesicles

Fig. 3E-G presents the three different types of intranuclear vesicles observed. Intranuclear vesicles are defined as voluminous structures inside the nucleus without a connection between their interior and the cytoplasm. The most common vesicles were positive for lamin B but not for NUP153 (Fig. 3E). Far less common were vesicles positive for both lamin B and NUP153 (Fig. 3F). In only a single case, a NUP153-positive but lamin B-negative vesicle-like structure was observed (Fig. 3G; arrow 2). Usually NUP153-positive structures were lined by chromatin (compare with Fig. 1A). This vesicle was not lined by chromatin. The NUP153 signal strength was much lower than the signal strength of NPCs in the nuclear envelope.

Quantification of nuclear volumes

Generally, nuclear volumes declined with later stages from the 2-cell to the blastocyst stage (Fig. 4A). As exceptions, the 2-cell and morula stages featured a wide variety of nuclear volumes. In a morula-stage embryo, the largest nuclei could be larger than the nuclei of an embryo at the 8-cell stage. These nuclei could not simply be stopped/retarded 8-cell stage nuclei, since more than 8 large nuclei were observed in addition to numerous smaller nuclei in the same morula-stage embryo. Small morula nuclei could have the same size as those of blastocysts.

Invaginations peak at the 4-cell stage

The diagram in Fig. 4B reflects the quantification of invaginations and intranuclear vesicles throughout all developmental stages. The most common invaginations and intranuclear vesicles were positive for both lamin B and NUP153. They were present in all stages. Their frequency per nucleus increased at each stage from the zygote to the 4-cell stage. After the 4-cell stage, they became less frequent and stagnated at

the 21-cell stage to blastocyst stage. The second most frequent invaginations and intranuclear vesicles were lamin B positive but NUP153 negative, which peaked in 2-cell stage nuclei. Stagnation at small levels was reached in morula nuclei. NUP153-positive but lamin B-negative structures were rarely observed.

Maternal deposit of extranuclear NUP153-positive clusters up to MGA

Fig. 5A shows a large deposit of NUP153-positive clusters in the zygote stage. These clusters were reduced in size and abundance during the subsequent stages (Fig. 5B-H). At the 4-cell stage, these clusters were usually limited to areas of the cytoplasm located on one side of the nucleus (Fig. 5C1). This deposit was largely depleted at MGA at the 8- to 16-cell stage and subsequent stages (Fig. 5D-H).

Random distribution of NPCs is initiated at MGA

Figure 6 presents nuclei from a pre-MGA 4-cell-stage embryo (Fig. 6A-E) and post-MGA 21-cell-stage embryo (Fig. 6F-H). Extranuclear NUP153 clusters in 4-cell stage blastomeres were only localized in the cytoplasm on one side of the nucleus (see Fig. 5C1 for a full projection including extranuclear clusters). This phenomenon allowed for a half-projection, which included only sections from the half of the nucleus in which almost no external NUP153 clusters were present. This half-projection shows NPCs integrated into the nuclear envelope unobstructed by cytoplasmic NUP153 clusters.

In the pre-MGA nucleus, NPCs were mostly clustered in highly concentrated areas. Some areas in these clusters surpassed the resolution limit of 3D-SIM, and multiple NPCs appeared as combined signal clouds. However, adequately resolved isolated nuclear pores in the vicinity of highly concentrated clusters demonstrated that this signal combination was not an artifact of an insufficient image quality. The

left arrow in Fig. 6D5 marks isolated nuclear pores, and the right arrow marks a group of tightly clustered NPCs. NPC clusters co-localized with areas of low lamin B signal intensity, indicating reduced abundance of lamin B at the NPC integration site (compare Fig. 6B1/2 and D1/2 with B5/6 and D5/6, respectively). However, NUP153 signals were not always found throughout areas of reduced lamin B signals (arrows in Fig. 6B3/4). This might indicate that other parts of NPCs may still or already be present at an NPC integration site while NUP153 is still or already absent. Similar but isolated NUP153-free small lamin B spots were found in post-MGA nuclei (arrow in Fig. 6H4). Pre-MGA NPC clusters were not evenly distributed and were sometimes separated by larger NPC-free areas. NPCs were only present in areas of the nuclear border that featured at least a thin heterochromatin lining under the lamina. While lamin B signals were also present in areas of the nuclear border without an underlying heterochromatin lining, NPCs were absent in the areas (see arrows in Fig. 6E).

NPCs were far less concentrated and no longer isolated as clusters in post-MGA nuclei, while isolated NPCs were more common. However, heterochromatin lining of the nuclear border did not necessarily guarantee NUP153 presence (see arrows in Fig. 6G2).

NUP153 association with chromatids begins at the chromatid periphery during metaphase before reassembly of the nuclear lamina

Fig. 7 displays morula-stage blastomeres during metaphase (A, B) and during anaphase/telophase (C). At one time point during metaphase, both NUP153 and lamin B were enriched in the cytoplasm and underrepresented in chromatids (A8). While the NUP153 distribution in the cytoplasm seems random, multiple lamin B-positive clusters were observed (A3). At another time point during metaphase (B), the

distribution of lamin B remained unchanged, while NUP153 was enriched at the periphery of chromatids but underrepresented in the cytoplasm and inside the chromatid interior (B8). During anaphase/telophase (C), the distribution of lamin B remained unchanged, while NUP153 was underrepresented in the cytoplasm but enriched at the periphery of chromatids and inside the chromatid interior at this stage (C8).

Discussion

This study was initiated to compare the results from our previous investigation on the nuclear envelope, nuclear pores and nuclear lamina in bovine preimplantation embryos [15] with the situation in rabbit embryos, which feature an alternative nuclear phenotype.

Large-volume invaginations provide proximity to cytoplasm for NPBs

While nuclei of bovine early-stage embryos have a round shape with mostly short, small-volume invaginations, early rabbit nuclei feature an amoeba-like shape with mostly large-volume invaginations able to stretch across entire nuclei. A previous study utilizing electron microscopy on *in vivo* and *in vitro* rabbit preimplantation embryos showed similar large-volume invaginations reaching far inside the nucleus [18]. This suggests that these invaginations are not an artifact of the preparation of rabbit embryos for super-resolution fluorescence microscopy. We wanted to compare the composition of nuclear invaginations and the distribution of nuclear pores throughout early embryonic development with the situation we have previously described in the bovine species. Since rabbit embryonic mRNA production peaks at the transition from the morula to blastocyst stage [19, 20], we wanted to investigate whether the increased mRNA production would cause a higher amount of nuclear

invaginations despite having smaller nuclear volumes at these later stages. Our results show that nuclear invaginations did not peak at these stages of highest mRNA production. Instead, invaginations positive for NUP153 and lamin B peaked at the 4-cell stage. This stage is the last stage before a massive volume decline begins at the 8-cell stage. This may suggest that a large nuclear volume is a more important factor for a high abundance of invaginations than increased mRNA export.

However, the number of invaginations positive for NUP153 and lamin B was lower at the 2-cell stage and in male pronuclei at the zygote stage, although these pronuclei/nuclei had larger volumes than those at the 4-cell stage. This may indicate that a larger nuclear volume is not the only factor for an increased abundance of invaginations. Nucleologenesis takes place during the first 4 cell cycles, with the first nucleolus-associated RNA of fully functional nucleoli detected at the morula stage containing about 32 cells [21]. Our data show numerous large-volume invaginations competent for import/export in direct contact with NPBs at the 4-cell stage. This may indicate that large-volume invaginations competent for import/export facilitate cytoplasmic proximity to NPBs. A similar association between invaginations and nucleoli in the form of “nucleolar canals” has been shown previously [22, 23]. Fitting this hypothesis, the zygote, 2-cell, 4-cell, and 8-cell stages show the highest amount of nuclear invaginations competent for import/export throughout preimplantation development. The peak of invaginations positive for NUP153 and lamin B at the 4-cell stage may be the result of a combination of large nuclear volumes and a large protein import requirement of NPBs at that particular stage. While nucleologenesis may have been in full progress at the 21-cell stage, the nuclear volumes had already dropped to blastocyst-like levels, and therefore nucleolar proximity to the cytoplasm may have already been sufficient without additional invaginations.

Invaginations exclusively positive for lamin B were associated with nuclear volume reduction

In our previous study on invaginations in bovine nuclei, we hypothesized that import/export-incompetent invaginations only positive for lamin B may be associated with a volume reduction during interphase [15]. A similar process was previously demonstrated during mosquito spermatogenesis, in which vesicle-like excisions of the lamina into the nuclear interior were associated with a reduction of the nuclear surface during interphase [24]. Our hypothesis was based on the fact that this type of invagination was mostly abundant during the 4-, 8- and 19-cell stages, which exhibited strong volume reductions. However, the results of this study show the highest amount of lamin B-only invaginations at the 2-cell stage and a reduction in the numbers of these invaginations in subsequent stages. The results may not be directly comparable between the two studies, since most invaginations in rabbits are large in volume while almost all invaginations in cattle are small-volume invaginations. Nuclear volumes in 2-cell stage nuclei were more variable than in any other preimplantation stage. Due to the lack of live microscopy data, it is not clear whether the same nuclei can vary drastically in volume over time or if small and large nuclei maintain initial volumes throughout the 2-cell stage. However, nuclei at the early 2-cell stage were on average larger and almost always exhibited one or multiple small or large chromatin-free lacunas, whereas nuclei at the late 2-cell stage were on average smaller and no longer exhibited chromatin-free lacunas. This may indicate that during the rabbit 2-cell stage, interphase nuclear volumes are reduced and the chromatin-free lacuna is removed. In this case, the hypothesis of an increased abundance of invaginations exclusively positive for lamin B during interphase nuclear volume reduction would be further substantiated by the results of this study.

Different mechanisms for small- and large-volume invaginations

Short, small-volume invaginations, which are the almost exclusive nuclear invagination type in the bovine species, did generally not show association with NPBs. This suggests that there may be a different reason and mechanism responsible for large- and small-volume invaginations in the rabbit species. In the bovine species, small-volume invaginations did emanate from the nuclear border and did not emanate from the few large-volume invaginations. In the rabbit species, numerous small-volume invaginations were emanating from large-volume invaginations. This may imply that import/export-competent large-volume invaginations are essentially similar to the nuclear border. The fact that most NPBs were either located at the nuclear border or at large-volume invaginations further supports this hypothesis. The hypothesis of different roles and mechanisms between small- and large-volume invaginations is further substantiated by the finding that small-volume invaginations were frequently emanating from large-volume invaginations but that large-volume invaginations never emanated from small-volume invaginations.

NUP153 clusters

In our previous study on bovine embryos, we showed large, randomly distributed NUP153 clusters before MGA [15]. After MGA at the 8- to 16-cell stage, these clusters greatly decreased in number and were no longer randomly distributed but were mostly located in close proximity to the nuclear envelope until they were no longer present in morula-stage nuclei. RNA-Seq data showed a deposit of spliced, maternally provided mRNA coding for NUP153, other nucleoporins and lamins already present in oocytes with consistent levels up to the blastocyst stage. In this study, we confirmed the existence of a large deposit of NUP153 clusters randomly

distributed throughout the cytoplasm in the rabbit species. Similar to the bovine species, these NUP153 clusters greatly decreased in number at the onset of MGA and were no longer present for the most part at later stages.

NPCs in pre-MGA nuclear envelopes are distributed non-randomly

In a previous study we showed that in nuclei of bovine embryos a large chromatin-free lacuna starts to form at the 4-cell stage and begins to get smaller after MGA at the 8-cell stage [16]. Expansions of this chromatin-free lacuna could be in direct contact with the nuclear border, where we noted a complete lack of nuclear pores. However, chromatin-free areas at the nuclear envelope were already observed at the zygote stage. A similar scenario was noted in this study in rabbit zygotes. A nonhomogeneous chromatin distribution in female pronuclei left half of the nuclear envelope not facing the male pronucleus without visible chromatin. While the entire nuclear envelope was lined by lamin B, this opposing half did not contain NPCs. These chromatin- and NPC-free areas of the nuclear envelope persisted until the 4-cell stage, at which point highly concentrated NPC groups were surrounded by chromatin-free areas exclusively marked by the lamina. This finding confirms the hypothesis that nuclear pores require chromatin.

NUP153 association with chromatids is initiated during metaphase before lamin B association

Previously, the post-mitotic association of NUP153 with chromatin was reported to be initiated at the end of anaphase [25]. In our previous study, this initial association was already observed at metaphase [15]. The difference between these two findings might be explained by increased clustering of NUP153 at the chromatid periphery during anaphase. While a visual inspection using confocal microscopy may suggest

that the initial association occurs during anaphase, our statistical analysis of super-resolution data showed that an overrepresentation of NUP153 at the chromatid periphery occurs already during metaphase. Alternatively, there might be species-specific differences. In this study, we were able to show not only that the association between NUP153 and chromatids is already present during metaphase but also that it is initiated during metaphase. Our data confirm for the rabbit species the previous finding that NUP153 association precedes lamina reassembly [25].

Conclusion

Compared with bovine preimplantation development, we found striking differences and similarities. The most profound difference is that most invaginations in rabbits are large-volume invaginations, whereas most invaginations in cattle are small-volume invaginations. Since small-volume invaginations did regularly emanate from large-volume invaginations but large-volume invaginations did not emanate from small-volume invaginations, the underlying mechanism may differ. This is further substantiated by the observation that only large-volume invaginations directly contacted NPBs. Similarities included the lack of NPCs in chromatin-free areas of the nuclear envelope, an increased abundance of invaginations exclusively positive for lamin B during stages with large nuclear volume alterations, deposition of cytoplasmic NUP153 clusters until the onset of MGA and initiation of association of NUP153 with chromatids during metaphase. To our knowledge, the present study demonstrates for the first time major remodeling of the nuclear envelope and its underlying lamina during rabbit preimplantation development.

Acknowledgments

We gratefully acknowledge the support provided by Thomas Cremer and his critical reading of preliminary versions of the manuscript. This study was supported by grants from the Deutsche Forschungsgemeinschaft to E.W. and V.Z. (CR 59/26, FOR 1041, ZA 425/1-3). In addition, research of E.W. and V.Z. was supported by the EU grant Plurisys, HEALTH-F4-2009-223485 FP7 Health 534 project. The authors are members of COST Action BM1308 - Sharing Advances on Large Animal Models (SALAAM).

References

1. **Leandri RD, Archilla C, Bui LC, Peynot N, Liu Z, Cabau C, Chastellier A, Renard JP, Duranthon V.** Revealing the dynamics of gene expression during embryonic genome activation and first differentiation in the rabbit embryo with a dedicated array screening. *Physiol Genomics* 2009; **36**: 98-113.
2. **Henrion G, Brunet A, Renard JP, Duranthon V.** Identification of maternal transcripts that progressively disappear during the cleavage period of rabbit embryos. *Mol Reprod Dev* 1997; **47**: 353-362.
3. **Christians E, Rao VH, Renard JP.** Sequential acquisition of transcriptional control during early embryonic development in the rabbit. *Dev Biol* 1994; **164**: 160-172.
4. **Brunet-Simon A, Henrion G, Renard JP, Duranthon V.** Onset of zygotic transcription and maternal transcript legacy in the rabbit embryo. *Mol Reprod Dev* 2001; **58**: 127-136.
5. **Cotton R, Manes C, Hamkalo B.** Electron microscopic analysis of RNA transcription in preimplantation rabbit embryos. *Chromosoma* 1980; **79**: 169-178.
6. **Carmody S, Wente S.** mRNA nuclear export at a glance. *J Cell Sci* 2009; **122**: 1933-1937.
7. **Cronshaw J, Krutchinsky A, Zhang W, Chait B, Matunis M.** Proteomic analysis of the mammalian nuclear pore complex. *J Cell Biol* 2002; **158**: 915-927.
8. **Hinshaw J, Carragher B, Milligan R.** Architecture and design of the nuclear pore complex. *Cell* 1992; **69**: 1133-1141.
9. **Arlucea J, Andrade R, Alonso R, Arechaga J.** The nuclear basket of the nuclear pore complex is part of a higher-order filamentous network that is related to chromatin. *J Struct Biol* 1998; **124**: 51-58.
10. **Ball J, Ullman K.** Versatility at the nuclear pore complex: lessons learned from the nucleoporin Nup153. *Chromosoma* 2005; **114**: 319-330.
11. **Gruenbaum Y, Margalit A, Goldman RD, Shumaker DK, Wilson KL.** The nuclear lamina comes of age. *Nat Rev Mol Cell Biol* 2005; **6**: 21-31.
12. **Smythe C, Jenkins HE, Hutchison CJ**. Incorporation of the nuclear pore basket protein nup153 into nuclear pore structures is dependent upon lamina

assembly: evidence from cell-free extracts of Xenopus eggs. *EMBO J* 2000; **19**: 3918-3931.
13. **Legartova S, Stixova L, Laur O, Kozubek S, Sehnalova P, Bartova E.** Nuclear structures surrounding internal lamin invaginations. *J Cell Biochem* 2014; **115**: 476-487.
14. **Malhas A, Goulbourne C, Vaux DJ.** The nucleoplasmic reticulum: form and function. *Trends Cell Biol* 2011; **21**: 362-373.
15. **Popken J, Graf A, Krebs S, Blum H, Schmid VJ, Strauss A, Guengoer T, Zakhartchenko V, Wolf E, Cremer T.** Remodeling of the nuclear envelope and lamina during bovine preimplantation development and its functional implications. *PLOS ONE* 2015; DOI:10.1371/journal.pone.0124619.
16. **Popken J, Brero A, Koehler D, Schmid VJ, Strauss A, Wuensch A, Guengoer T, Graf A, Krebs S, Blum H, Zakhartchenko V, Wolf E, Cremer T.** Functional reprogramming of fibroblast nuclei in cloned bovine embryos is paralleled by major structural remodeling with both striking similarities and differences to nuclear phenotypes of embryos fertilized *in vitro*. *Nucleus* 2014; **5-6**: 555-589.
17. **Markaki Y, Smeets D, Fiedler S, Schmid VJ, Schermelleh L, Cremer T, Cremer M.** The potential of 3D-FISH and super-resolution structured illumination microscopy for studies of 3D nuclear architecture: 3D structured illumination microscopy of defined chromosomal structures visualized by 3D (immuno)-FISH opens new perspectives for studies of nuclear architecture. *Bioessays* 2012; **34**: 412-426.
18. **Van Blerkom J, Manes C, Daniel J C.** Development of preimplantation rabbit embryos in vivo and in vitro: I. An ultrastructural comparison. *Developmental Biology* 1973**; 35.2:** 262-282.

19. **Manes C.** Nucleic acid synthesis in preimplantation rabbit embryos. I. Quantitative aspects, relationship to early morphogenesis and protein synthesis. *J Exp Zool* 1969; **172**: 303-310.
20. **Manes C.** Nucleic acid synthesis in preimplantation rabbit embryos. III. A "dark period" immediately following fertilization, and the early predominance low molecular weight RNA synthesis. *J Exp Zool* 1977; **201**: 247-257.
21. **Baran V, Mercier Y, Renard JP, Flechon JE.** Nucleolar substructures of rabbit cleaving embryos: an immunocytochemical study. *Mol Reprod Dev* 1997; **48**: 34-44.
22. **Collings D, Carter C, Rink J, Scott A, Wyatt S, Allen N.** Plant nuclei can contain extensive grooves and invaginations. *Plant Cell* 2000; **12**: 2425-2440.
23. **Hernandez-Verdun D.** The nucleolus: a model for the organization of nuclear functions. *Histochem Cell Biol* 2006; **126**: 135-148.
24. **Ndiaye M, Mattei X.** Process of nuclear envelope reduction in spermiogenesis of a mosquito, Culex tigripes. *Molecular Reproduction and Development* 1993; **34**: 416-419.
25. **Bodoor K, Shaikh S, Salina D, Raharjo WH, Bastos R, Lohka M, Burke B**. Sequential recruitment of NPC proteins to the nuclear periphery at the end of mitosis. *J Cell Sci* 1999; **112** (Pt 13): 2253-2264.

Figure Legends

Fig. 1. Nuclear volumes and distribution changes of chromatin, NUP153 and lamin B before MGA. Panels A-E. Midsections of pronuclei/nuclei from rabbit IVF embryos immunostained for lamin B (A1-E1; A4-E4, red) and NUP153 (A2-E2; A4-E4, green) and stained for chromatin with DAPI (A3-E3; A4-E4, gray). **A.** Zygote stage with a small female pronucleus (fPN) and a large male pronucleus (mPN). **B.** Early 2-cell stage with a large chromatin-free lacuna. The lacuna is connected to the cytoplasm without a lamin B- or NUP153-positive border. **C**. Early 2-cell stage with a smaller chromatin-free lacuna surrounded by chromatin. **D**. Late 2-cell stage without a chromatin-free lacuna recorded with confocal laser scanning microscopy. **E.** 4-cell stage.

Fig. 2. Nuclear volumes and distribution changes of chromatin, NUP153 and lamin B at the onset of and after MGA. Panels A-E. Midsections of nuclei from rabbit IVF embryos immunostained for lamin B (A1-F1; A4-F4, red) and NUP153 (A2-F2; A4-F4, green) and stained for chromatin with DAPI (A3-F3; A4-F4, gray). **A.** 8-cell stage. **B.** 21-cell stage. **C.** 44-cell morula stage. **D.** Inner cell mass (ICM) nucleus in a blastocyst-stage embryo. **E.** Trophectoderm (TE) nucleus in a blastocyst-stage embryo.

Fig. 3. A-D. Large-volume and small-volume invaginations. A. 4-cell-stage nucleus with a large-volume invagination in contact with a nucleolar precursor body (NPB; the arrow marks the contact site). Note the absence of nuclear pores at the contact site. **B.** 4-cell-stage nucleus with small-volume invaginations (arrowheads) and multiple large-volume invaginations contacting the same centrally located NPB (arrows mark contact sites between invaginations and the nucleolus). **C.** 4-cell-stage nucleus with a large-volume invagination reaching across the nucleus to contact a

NPB (arrow marks contact site). The arrowhead marks a small-volume invagination emanating from a large-volume invagination. The NPB on the right side is not contacted by any invagination. **D.** 4-cell-stage nucleus showing three of the four NPBs in contact with large-volume invaginations (contact sites marked by arrows). The NPB not in contact with invaginations is in contact with the nuclear border in another z-section (not shown). **E-G. Three types of intranuclear vesicles. E1-G1.** Lamin B (3 µm bar). **E2-G2** NUP153. **E3-G3 and E4-G4.** DAPI (gray), NUP153 (green) and Lamin B (red). **E4-G4.** Magnification of the vesicles (500 nm bar). **E.** Lamin B-positive but NUP153-negative intranuclear vesicles are most common. **F.** Lamin B- and NUP153-positive invaginations are far less common. **G.** Arrow 2 marks the only occurrence of a NUP153-positive but lamin B-negative vesicle-like structure. This may not be a NPC-positive vesicle-like structure, since NPCs are normally lined with chromatin but this structure is not.

Fig. 4. A. Quantification of nuclear volumes. fPN, female pronucleus; mPN, male pronucleus; ICM, blastocyst nucleus from the inner cell mass; TE, blastocyst nucleus from the trophectoderm. For each bar, 10 pronuclei/nuclei were measured. **B. Quantification of invaginations and intranuclear vesicles.** For abbreviations, see (A). Exclusively NUP153-positive structures are marked in dark gray. NUP153- and lamin B-positive structures are marked in light gray. Exclusively lamin B-positive structures are marked in black. For each set of bars, invaginations and vesicles in 10 pronuclei/nuclei were counted.

Fig. 5. A maternal deposit of cytoplasmic NUP153 clusters is depleted at the onset of MGA. A1-H1. NUP153. **A2-H2**. Lamin B. **A3-H3**. DAPI. **A4-H4**. Composite (DAPI, gray; NUP153, green; lamin B, red). **A.** Zygote stage with a large male (mPN) and small female pronucleus (fPN). **B.** 2-cell stage. **C.** 4-cell stage. **D.** 8-cell stage. **E.**

21-cell stage. **F.** Morula stage. **G.** Inner cell mass nucleus from a blastocyst. **H** Trophectoderm nucleus from a blastocyst.

Fig. 6. Nuclear pore complex (NPC) and lamina distribution before and after major genome activation (MGA). A. Projection through half of a pre-MGA 4-cell stage nucleus. **A1.** Lamin B. **A2.** Composite with lamin B (gray) and NUP153 (green). **A3.** NUP153. **A4.** DAPI. **B1.** Enlargement of top box in A1**. B2.** Enlargement of box in B1. **B3.** Enlargement of top box in A2. The arrow marks a lamin B-depleted area without NPCs. **B4.** Enlargement of box in B3. The arrow marks a lamin B-depleted area without NPCs. This depleted area is approximately the size of one NPC (120 nm in diameter). **B5.** Enlargement of top box in A3**. B6.** Enlargement of box in B5. **C.** Model of a NPC with potential NUP153 localizations based on the report of Ball and Ullman [10]. NPCs have an outer diameter of about 120 nm and connect the cytoplasm with the nucleoplasm through the nuclear envelope and lamina. The nuclear basket and nuclear filaments connected to the nuclear basket are associated with chromatin. NUP153 is located either at the nuclear ring or at the nuclear basket [10]. **D1.** Enlargement of bottom box in A1. **D2.** Enlargement of box in D1. **D3.** Enlargement of bottom box in A2. **D4.** Enlargement of box in D3. **D5.** Enlargement of bottom box in A3. **D6.** Enlargement of box in B5. **E1-E4.** Midsection of the nucleus shown in A. Arrows mark areas of the nuclear envelope that feature a lamina but that are lacking chromatin and nuclear pores (compare with the fPN in Figure 1A). **F.** Projection through half of a post-MGA 21-cell stage nucleus. **G.** Midsection of the nucleus shown in F. Arrows mark areas of the nuclear envelope that feature a lamina lined by chromatin but that are lacking nuclear pores. **H1, H3, H5**. Enlargements of the box in E. **H2, H4, H6**. Enlargements of the boxes in H1, H3, H5. The arrow in H4

589 marks a lamin B-depleted area without an NPC. This depleted area is approximately
590 the size of one NPC (120 nm in diameter).

591 **Fig. 7. NUP153 associates with chromatids during metaphase before lamina**
592 **reassembly. A.** Lamin B and NUP153 are not associated with chromatids at this
593 time point during metaphase. **A1.** Projection of DAPI. **A2.** Projection of NUP153. **A3.**
594 Projection of lamin B. **A4.** Projection of a composite of DAPI (gray), NUP153 (green)
595 and lamin B (red). **A5.** Section showing 7 DAPI intensity classes from no DAPI
596 intensity in the cytoplasm (dark gray) to large DAPI intensity (white), NUP153
597 (green), lamin B (red) and the colocalization of NUP153 and lamin B (blue). **A6.**
598 Enlargement of the box in A5. **A7.** Same enlargement presented in A6 without
599 NUP153, lamin B or colocalization signals. **A8.** Quantification of over- and
600 underrepresentation of NUP153 (green) and lamin B signals (red) in the 7 DAPI
601 intensity classes. At this stage, NUP153 and lamin B are both strongly
602 overrepresented in the cytoplasm and mostly underrepresented in the chromatin. **B1-**
603 **B8.** The descriptions for A1-A8 above also apply to B1-B8, which represent another
604 time point during metaphase. Lamin B remains unassociated with chromatids, but
605 NUP153 begins to associate with the periphery but not the core parts of chromatids
606 during metaphase. **C1-C8.** The descriptions for A1-A8 above also apply to C1-C8,
607 which represent a time point during anaphase/telophase. Lamin B remains
608 unassociated with chromatids, but NUP153 association stretches into the interior of
609 chromatids during anaphase/telophase.

610

611

612

613

Table 1. Primary antibodies

Host	Target	Official name	Dilution	Company	ID
Goat	Epitope at C-terminus of Lamin B1. Detecting Lamin B1 and, to a lesser extent, Lamin B2	Lamin B Antibody (M-20)	1:100	Santa Cruz	SC-6217
Mouse	NUP153	Anti-NUP153 [QE5] antibody	1:200	Abcam	ab24700

Table 2. Secondary antibodies

Host	Target	Fluorophore	Excitation [nm]	Dilution	Company	ID
Donkey	Mouse IgG (H+L)	Alexa	488	1:400	Invitrogen	A-21202
Donkey	Mouse IgG (H+L)	Alexa	594	1:500	Invitrogen	A-21203
Donkey	Goat IgG (H+L)	Alexa	488	1:400	Invitrogen	A-11055
Donkey	Goat IgG (H+L) preadsorbed	Alexa	594	1:400	Abcam	ab150136

627

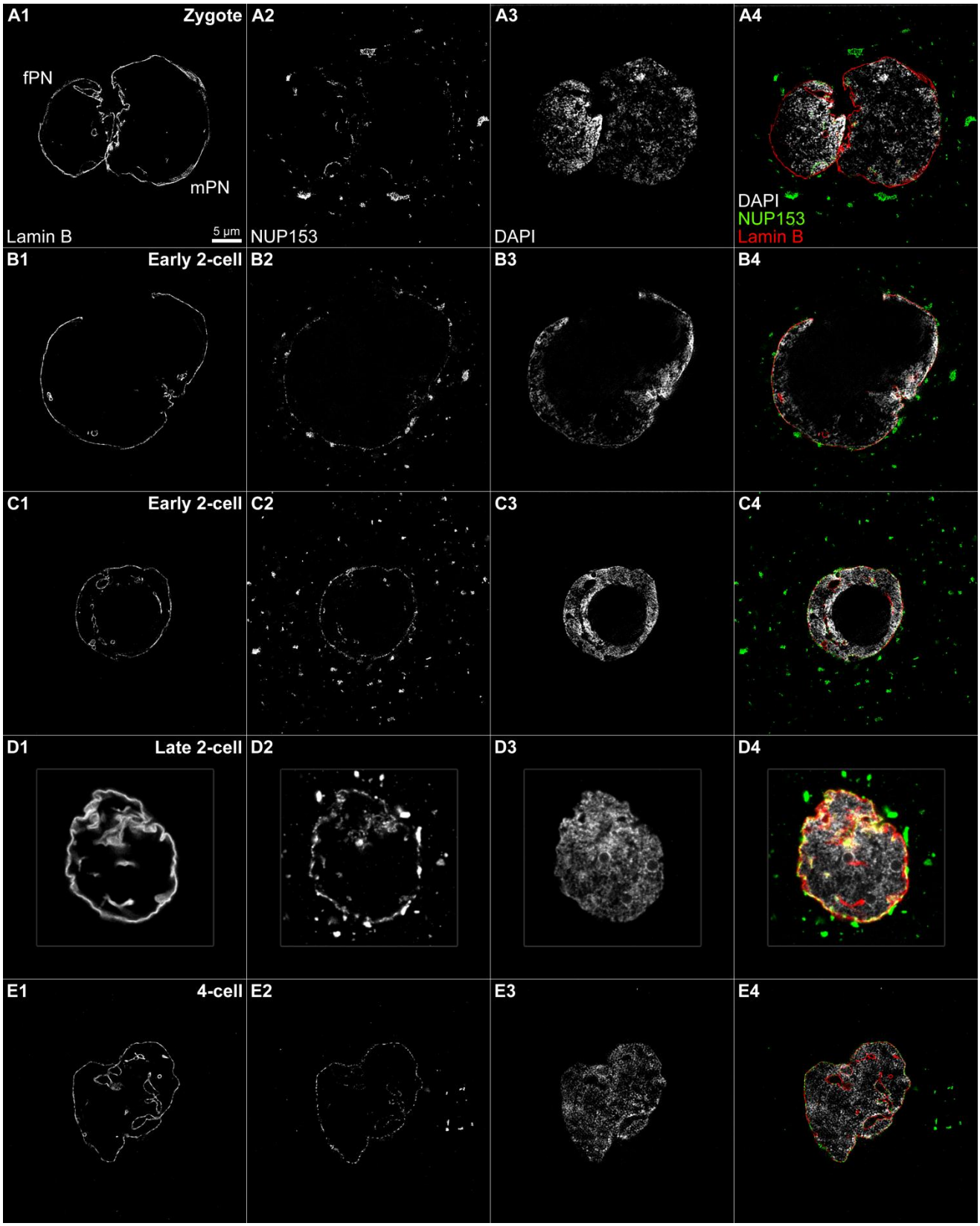

628
629 **Fig. 1.**

630

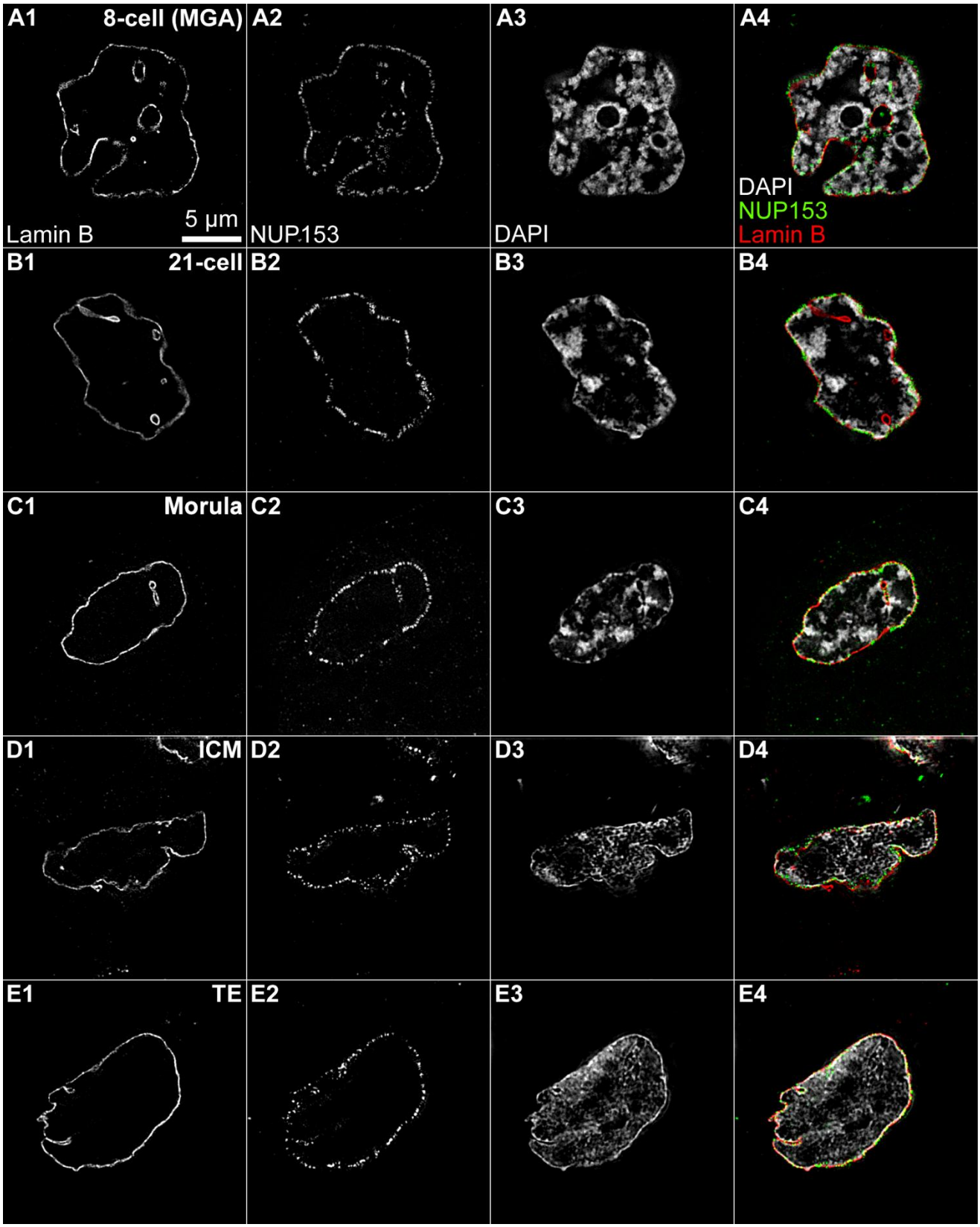
A1
8-cell (MGA)
A2
A3
A4
DAPI
NUP153
Lamin B
5 µm
Lamin B
NUP153
DAPI
B1
21-cell
B2
B3
B4
C1
Morula
C2
C3
C4
D1
ICM
D2
D3
D4
E1
TE
E2
E3
E4

631
632 **Fig. 2.**

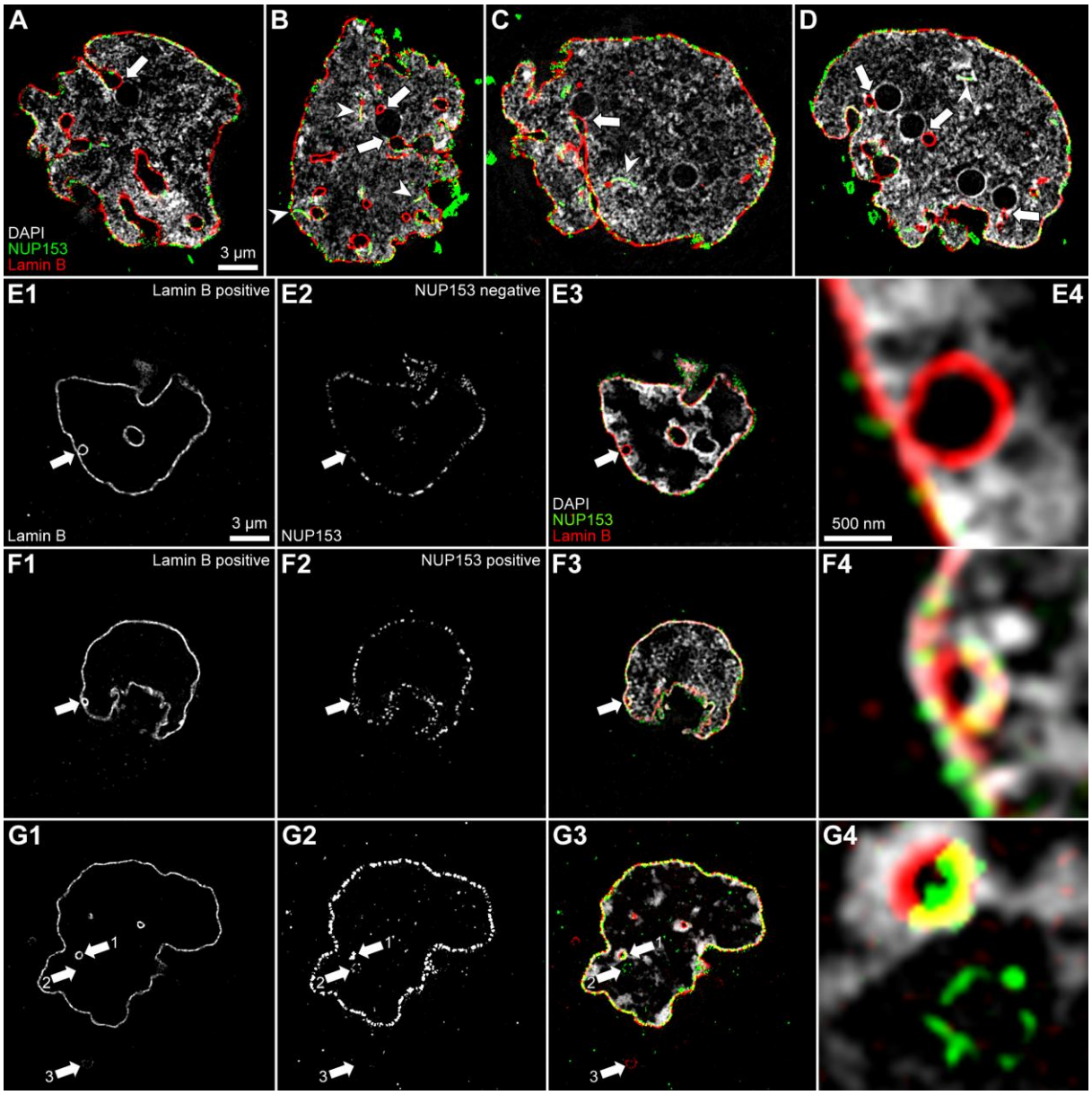
A
B
C
D
DAPI
NUP153
Lamin B
3 µm
E1
Lamin B positive
Lamin B
3 µm
E2
NUP153 negative
NUP153
E3
DAPI
NUP153
Lamin B
E4
500 nm
F1
Lamin B positive
F2
NUP153 positive
F3
F4
G1
G2
G3
G4
1
2
3

Fig. 3.

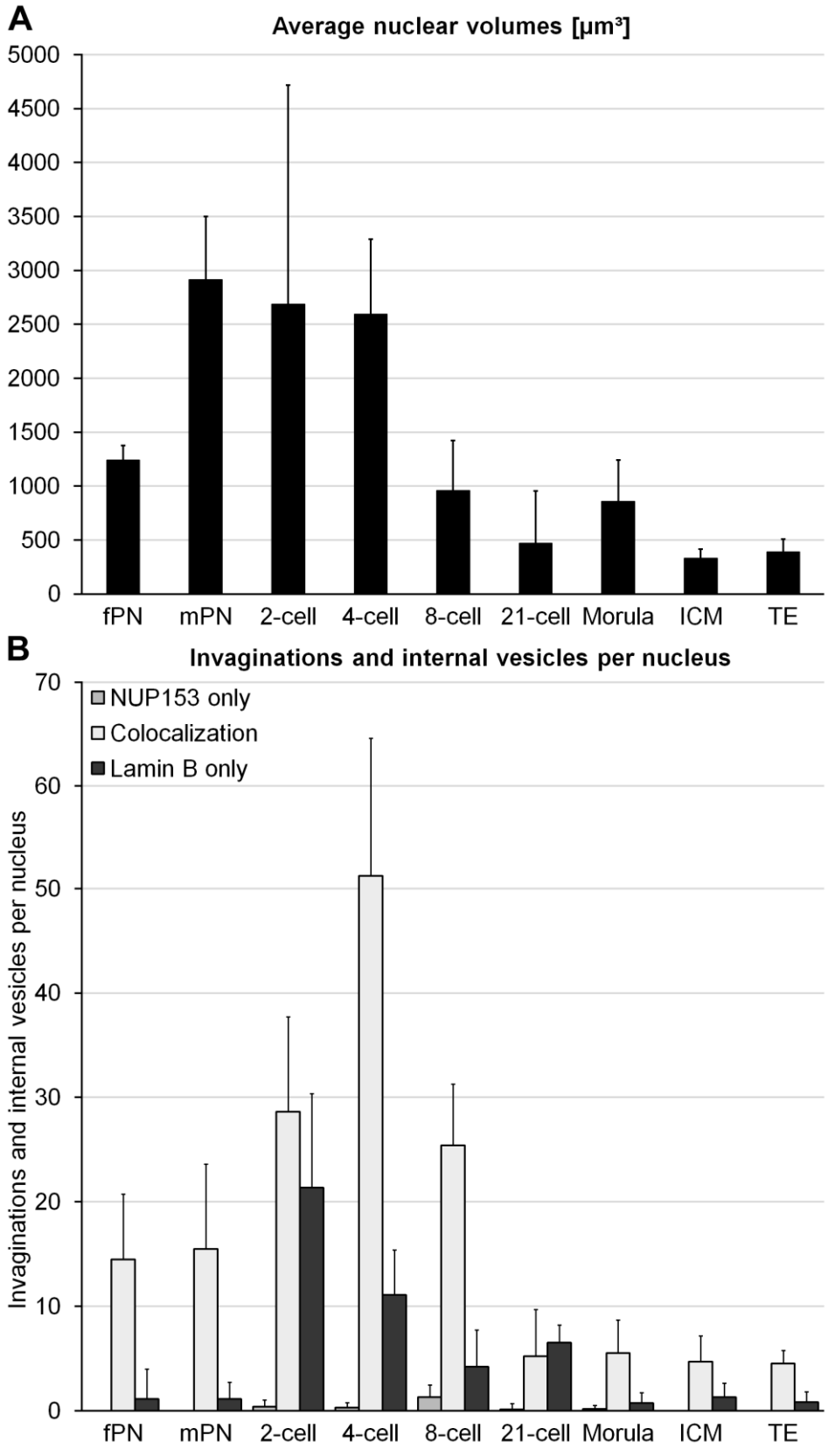
A
Average nuclear volumes [µm³]
5000
4500
4000
3500
3000
2500
2000
1500
1000
500
0
fPN
mPN
2-cell
4-cell
8-cell
21-cell
Morula
ICM
TE
B
Invaginations and internal vesicles per nucleus
NUP153 only
Colocalization
Lamin B only
Invaginations and internal vesicles per nucleus
70
60
50
40
30
20
10
0
fPN
mPN
2-cell
4-cell
8-cell
21-cell
Morula
ICM
TE

Fig. 4.

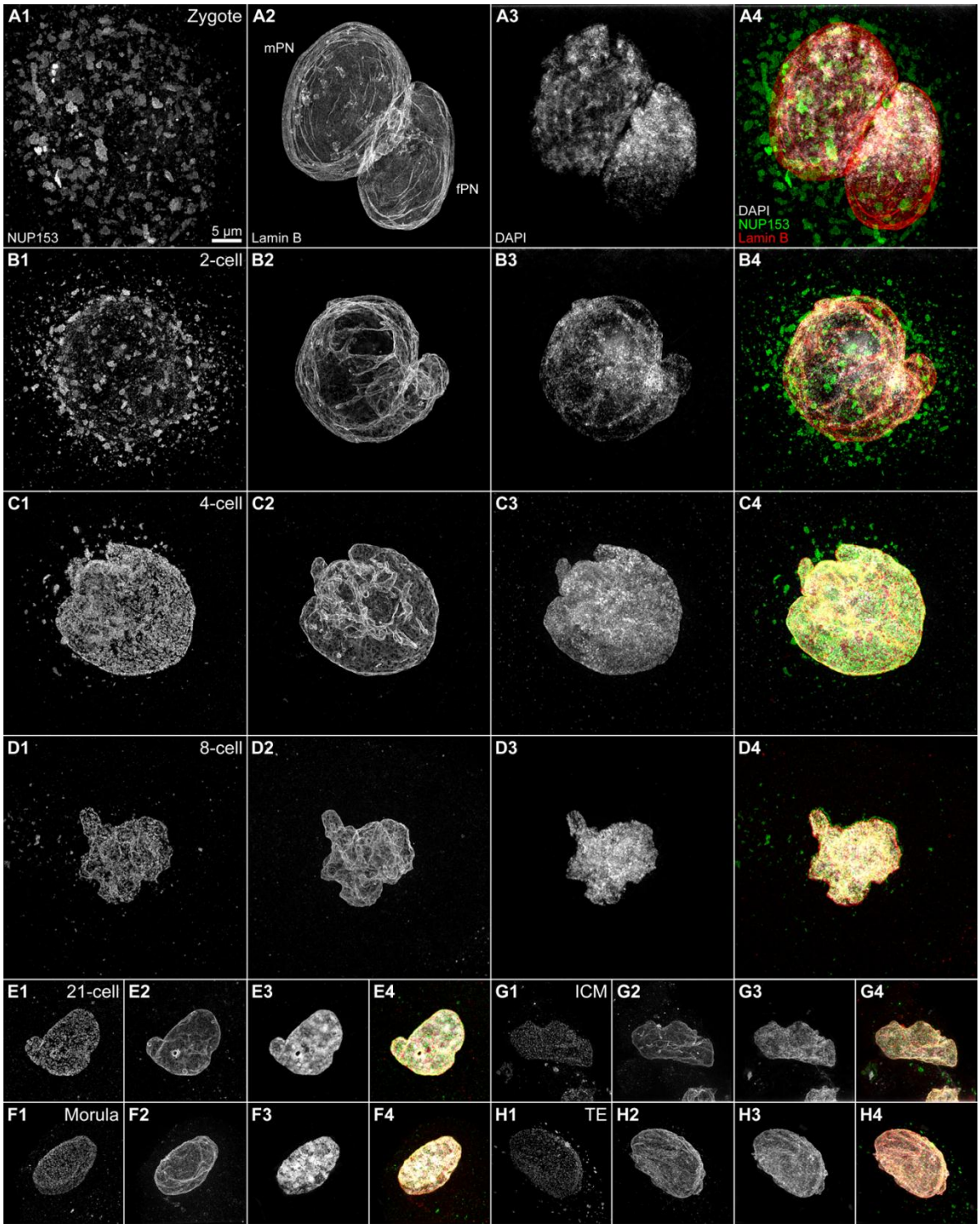
A1
Zygote
NUP153
5 µm
A2
mPN
fPN
Lamin B
A3
DAPI
A4
DAPI
NUP153
Lamin B
B1
2-cell
B2
B3
B4
C1
4-cell
C2
C3
C4
D1
8-cell
D2
D3
D4
E1
21-cell
E2
E3
E4
G1
ICM
G2
G3
G4
F1
Morula
F2
F3
F4
H1
TE
H2
H3
H4

Fig. 5.

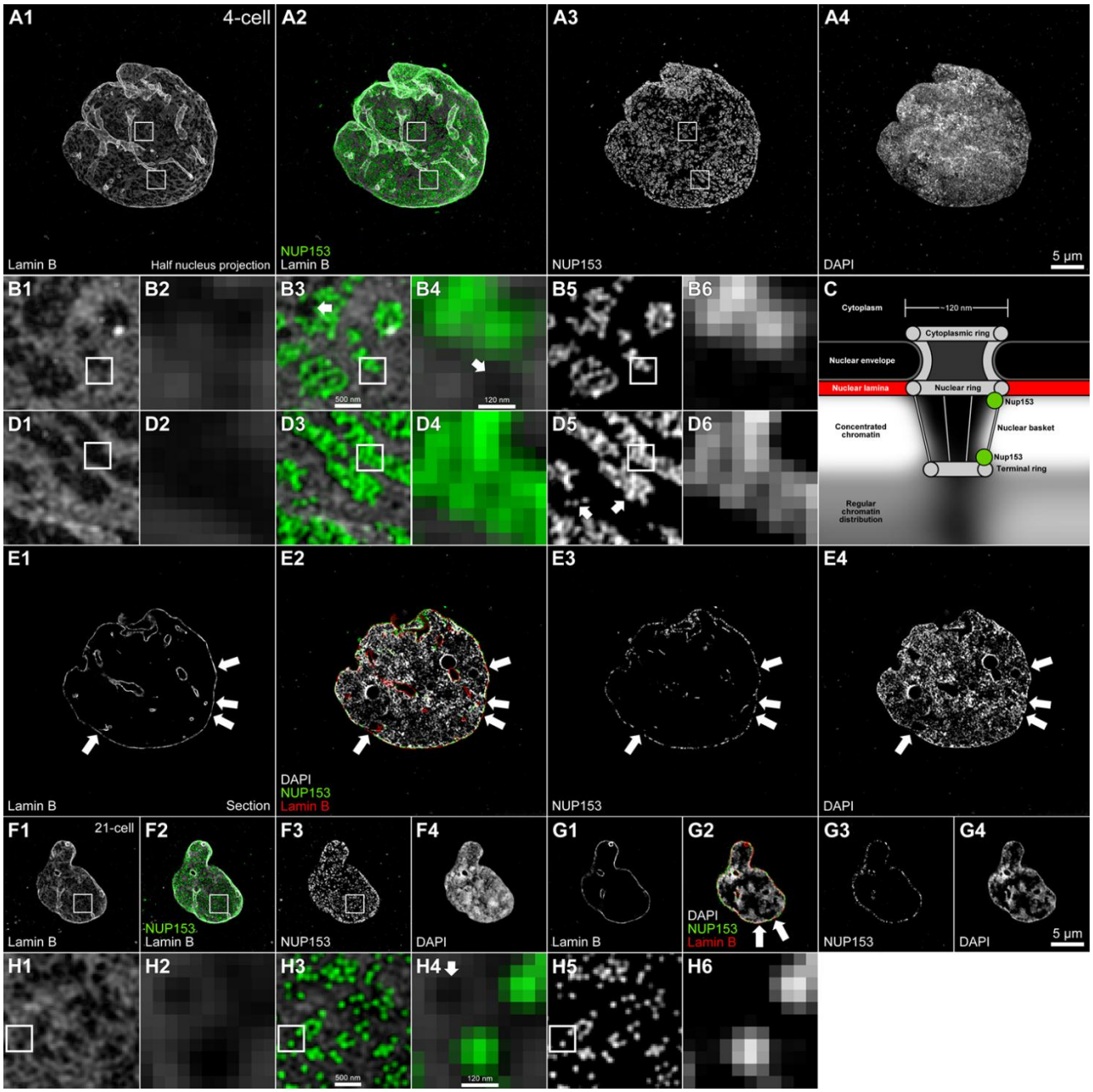
A1
4-cell
Lamin B
Half nucleus projection
A2
NUP153
Lamin B
A3
NUP153
A4
DAPI
5 µm
B1
B2
B3
500 nm
B4
120 nm
B5
B6
C
Cytoplasm
~120 nm
Cytoplasmic ring
Nuclear envelope
Nuclear lamina
Nuclear ring
Nup153
Concentrated chromatin
Nuclear basket
Nup153
Terminal ring
Regular chromatin distribution
D1
D2
D3
D4
D5
D6
E1
Lamin B
Section
E2
DAPI
NUP153
Lamin B
E3
NUP153
E4
DAPI
F1
21-cell
Lamin B
F2
NUP153
Lamin B
F3
NUP153
F4
DAPI
G1
Lamin B
G2
DAPI
NUP153
Lamin B
G3
NUP153
G4
DAPI
5 µm
H1
H2
H3
500 nm
H4
120 nm
H5
H6

Fig. 6.

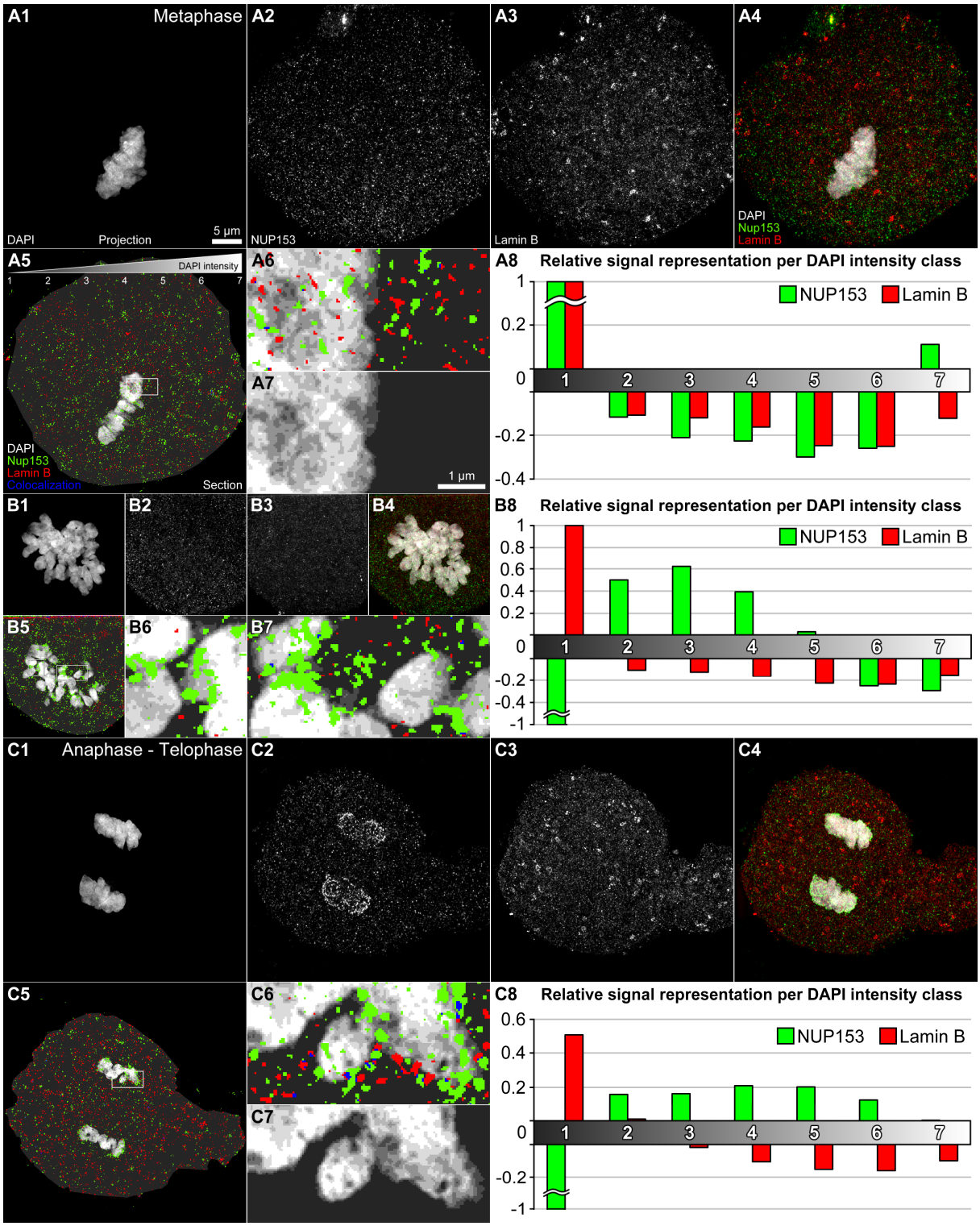
A1
Metaphase
DAPI
Projection
5 µm
A2
NUP153
A3
Lamin B
A4
DAPI
Nup153
Lamin B
A5
DAPI intensity
1 2 3 4 5 6 7
DAPI
Nup153
Lamin B
Colocalization
Section
A6
A7
1 µm
A8
Relative signal representation per DAPI intensity class
NUP153
Lamin B
1
0.2
0
-0.2
-0.4
1 2 3 4 5 6 7
B1
B2
B3
B4
B5
B6
B7
B8
Relative signal representation per DAPI intensity class
NUP153
Lamin B
1
0.8
0.6
0.4
0.2
0
-0.2
-0.4
-1
1 2 3 4 5 6 7
C1
Anaphase - Telophase
C2
C3
C4
C5
C6
C7
C8
Relative signal representation per DAPI intensity class
NUP153
Lamin B
0.6
0.4
0.2
0
-0.2
-1
1 2 3 4 5 6 7

Fig. 7

2.5. Positional changes of a pluripotency marker gene during structural reorganization of fibroblast nuclei in cloned early bovine embryos

RESEARCH PAPER

Nucleus 5:6, 542–554; November/December 2014; Published with license by Taylor & Francis Group

Positional changes of a pluripotency marker gene during structural reorganization of fibroblast nuclei in cloned early bovine embryos

Jens Popken[1,2,†], Daniela Koehler[1,†], Alessandro Brero[1], Annegret Wuensch[2], Tuna Guengoer[2], Tobias Thormeyer[1], Eckhard Wolf[2,*], Thomas Cremer[1,*], and Valeri Zakhartchenko[2,*]

[1]Division of Anthropology and Human Genetics Biocenter; LMU Munich; Martinsried, Germany; [2]Molecular Animal Breeding and Biotechnology; Laboratory for Functional Genome Analysis (LAFUGA); Gene Center; LMU Munich; Munich, Germany

[†]These authors contributed to this work equally.

Keywords: (bovine) preimplantation embryos, chromosome territories, nuclear architecture, nuclear reprogramming, pluripotency gene activation, somatic cell nuclear transfer

Abbreviations: BFF, bovine fetal fibroblasts; BTA, *Bos taurus*; CLSM, confocal laser scanning microscopy; CT, chromosome territory; eADS, enhanced absolute 3D distances to surfaces; IVF, *in vitro* fertilization; MGA, major embryonic genome activation; GOF, Oct4/Pou5f1-EGFP reporter gene; SCNT, somatic cell nuclear transfer.

Cloned bovine preimplantation embryos were generated by somatic cell nuclear transfer (SCNT) of bovine fetal fibroblasts with a silent copy of the pluripotency reporter gene *GOF*, integrated at a single site of a chromosome 13. *GOF* combines the regulatory *Oct4/Pou5f1* sequence with the coding sequence for EGFP. EGFP expression served as a marker for pluripotency gene activation and was consistently detected in preimplantation embryos with 9 and more cells. Three-dimensional radial nuclear positions of *GOF*, its carrier chromosome territory and non-carrier homolog were measured in nuclei of fibroblasts, and of day 2 and day 4 embryos, carrying 2 to 9 and 15 to 22 cells, respectively. We tested, whether transcriptional activation was correlated with repositioning of *GOF* toward the nuclear interior either with a corresponding movement of its carrier chromosome territory 13 or via the formation of a giant chromatin loop. A significant shift of *GOF* away from the nuclear periphery was observed in day 2 embryos together with both carrier and non-carrier chromosome territories. At day 4, *GOF*, its carrier chromosome territory 13 and the non-carrier homolog had moved back toward the nuclear periphery. Similar movements of both chromosome territories ruled out a specific *GOF* effect. Pluripotency gene activation was preceded by a transient, radial shift of *GOF* toward the nuclear interior. The persistent co-localization of *GOF* with its carrier chromosome territory rules out the formation of a giant chromatin loop during *GOF* activation.

Introduction

Early development of mammalian embryos is a critical period characterized by transition of developmental control from RNAs and proteins stored in the oocyte to RNAs and proteins, which are newly synthesized after major embryonic genome activation.[1] This critical event occurs at species-specific times after one or several rounds of blastomere cleavage.[2] In bovine embryos major embryonic genome activation takes place at the 8-cell stage, where the largest proportion of genes becomes active during preimplantation development.[3] Some genes, however, are already activated earlier during minor genome activation.[4] The functional implications of nuclear architecture changes, which occur during this period, are currently not well understood. A number of groups, including ours, have made strong efforts to overcome the methodological obstacles preventing the detailed analysis of nuclear architecture in space and time during early mammalian development.[5-11]

It has been reported that nuclear positions of genes, chromatin domains and even entire chromosome territories can change during development and cell differentiation.[8,12-14] As an alternative to movements of entire chromosome territories, it was suggested that they may occupy the same nuclear place before and after activation of genes carried by them, whereas giant chromatin loops may form upon transcriptional activation and move such genes far away

*Correspondence to: Valeri Zakhartchenko; Email: V.Zakhartchenko@gen.vetmed.uni-muenchen.de; Thomas Cremer; Email: Thomas.Cremer@lrz.uni-muenchen.de; Eckhard Wolf; Email: ewolf@lmb.uni-muenchen.de
Submitted: 06/27/2014; Revised: 09/08/2014; Accepted: 09/15/2014
http://dx.doi.org/10.4161/19491034.2014.970107

from their carrier chromosome territory into a nuclear environment favorable for their transcriptional activation and/or the maintenance of transcription. It was hypothesized that giant loops would even allow the formation of co-regulated, spatial clusters of genes located on different chromosome territories.[15] Based on a protocol that combines chromosome painting in 3-dimensional (3D) preserved *in vitro* fertilized (IVF) bovine embryos with 3D confocal laser scanning microscopy (CLSM) and quantitative 3D image analysis, we have previously studied radial nuclear distributions of the gene-dense BTA 19 and the gene-poor BTA 20 chromosome territories during preimplantation development.[8] Prior to major embryonic genome activation at the 8-cell stage we observed a peripheral, radial distribution of both chromosome territories 19 and 20.[3] After major embryonic genome activation a gene density-related radial distribution of chromosome territories, 19 (more central) and 20 (more peripheral), was established.[8]

The goal of the present investigation was to explore a possible link between pluripotency gene activation and specific radial movements of such genes in nuclei of cloned bovine embryos with the help of a marker gene for pluripotency gene activation (*GOF*).[16] In a previous study we established a model system of cloned bovine embryos based on somatic cell nuclear transfer (SCNT) of bovine fetal fibroblasts with the stably integrated pluripotency marker gene *GOF*.[17] This transgene combines regulatory sequences of the pluripotency gene *Oct4/Pou5f1* with the coding sequence for EGFP.[18] The coding sequence for EGFP synthesis is controlled by a 9-kb fragment of the mouse *Oct4/Pou5f1* regulatory sequence with a deletion in the proximal enhancer.[19] *GOF* is silent in fibroblast nuclei, but EGFP was detected in cloned embryos with $\geq$9 cells.[17] Although causal relationships between pluripotency gene activation and major embryonic genome activation are still not clear, we suggest a temporal correlation of *GOF* activation with major embryonic genome activation in cloned bovine embryos and that this event occurs in both cloned and IVF bovine embryos at the 8-cell stage.[3] This model system was employed for a quantitative 3D-FISH study to answer the question, whether *Oct4/Pou5f1* promoter activation in nuclei of cloned bovine embryos is preceded or followed by changes of the radial nuclear positioning of *GOF* in comparison with the radial positioning of silent *GOF* in fibroblast nuclei. We considered 2 scenarios for a hypothetical repositioning of *GOF*. The marker gene might move on a giant chromatin loop expanding from the carrier chromosome territory into the nuclear interior or *GOF* might move together with its carrier chromosome territory. The analysis of the non-carrier homolog 13 provided a control for possible chromosome territory 13 movements unrelated to the presence and activity of *GOF*.

An accompanying study from our group demonstrated strikingly similar global changes of nuclear landscapes during early development of cloned and *in vitro* fertilized bovine embryos.[11] On their way toward major EGA at the 8-cell stage nuclei of *in vitro* fertilized embryos underwent striking structural changes characterized by the development of a centric or sometimes acentric major lacuna deprived of chromatin and surrounded by rather compact major chromatin bodies. These bodies were located at the nuclear periphery. They were well separated from each other and apparently represent individual chromosome territories. We referred to these nuclei as ENPs (for Embryonic Nuclei with Peripheral chromosome territory distribution). In cloned embryos approaching the 8-cell stage strikingly similar changes were observed. The flat-ellipsoidal shape of nuclei in cultured bovine fetal fibroblasts, used for somatic cell nuclear transfer, changed to a roundish shape. Nuclei increased in size and developed a major lacuna with a peripheral chromatin arrangement. In some cases, the nuclear phenotype noted in cloned 8-cell embryos was indistinguishable from ENPs in IVF embryos. In other cases, the major lacuna and the formation of well separated major chromatin bodies was less pronounced. Accordingly, we referred to such nuclei as ENP-like. During further development of cloned and IVF embryos nuclei became smaller but maintained their roundish shape and adopted a phenotype presenting typical architectural features of somatic cells, characterized by a network of CTs and chromatin clusters throughout the nuclear space, as well as an enrichment of dense chromatin beneath the nuclear lamina and around nucleoli.[20,21] We referred to these nuclei as ENCs (for Embryonic Nuclei with Conventional architecture).[11] These pronounced changes of nuclear architecture have to be taken into consideration in studies of embryonic nuclei focused on potential radial movements, which may accompany the activation of *GOF* or other individual genes (see Discussion).

Results

In a previous study we had demonstrated a single integration site of the pluripotency marker gene *GOF* into an autosome of the bovine fetal fibroblast culture used for SCNT experiments.[17] In the present study this site was mapped more precisely (**Fig. 1**). Three-color FISH to fibroblast metaphase chromosome spreads of the *GOF* probe, a chromosome paint probe for BTA 13 and an α-satellite DNA probe to pericentromeric heterochromatin demonstrated integration of *GOF* into BTA 13q, close to the block of pericentromeric heterochromatin.

Next, we performed 2-color 3D-FISH with BTA 13 paint probes and a differentially labeled *GOF* probe to nuclei of fibroblasts and cloned embryos, fixed at day 2 and day 4 after SCNT. Embryos chosen at day 2 consisted of 2 to 9 cells, embryos at day 4 of 15 to 22 cells. A confocal laser scanning microscope with a high numerical aperture objective was used to record 3D image stacks from 48 BFF nuclei and 127 blastomere nuclei. For high quality 3D imaging we chose embryonic nuclei, located close to the plastic surface onto which day 2 and day 4 embryos were attached.

Whereas parameters, such as the strong volume increase and the roundish shape of nuclei in day 2 embryos were fully maintained after 3D-FISH as compared with nuclei studied immediately after the 3D fixation procedure, we noted that the preservation of nuclei in embryos suffered during the 3D-FISH procedure as indicated by multiple, local disruptions of the nuclear border. Such disruptions were most prominent following 3D-FISH in the large nuclei of day 2 embryos, but were not seen in embryonic nuclei after a 3D fixation and DAPI staining without a FISH treatment.[11] Nuclei of cloned day 2 embryos resembled nuclei of IVF embryos close to major embryonic gene activation.

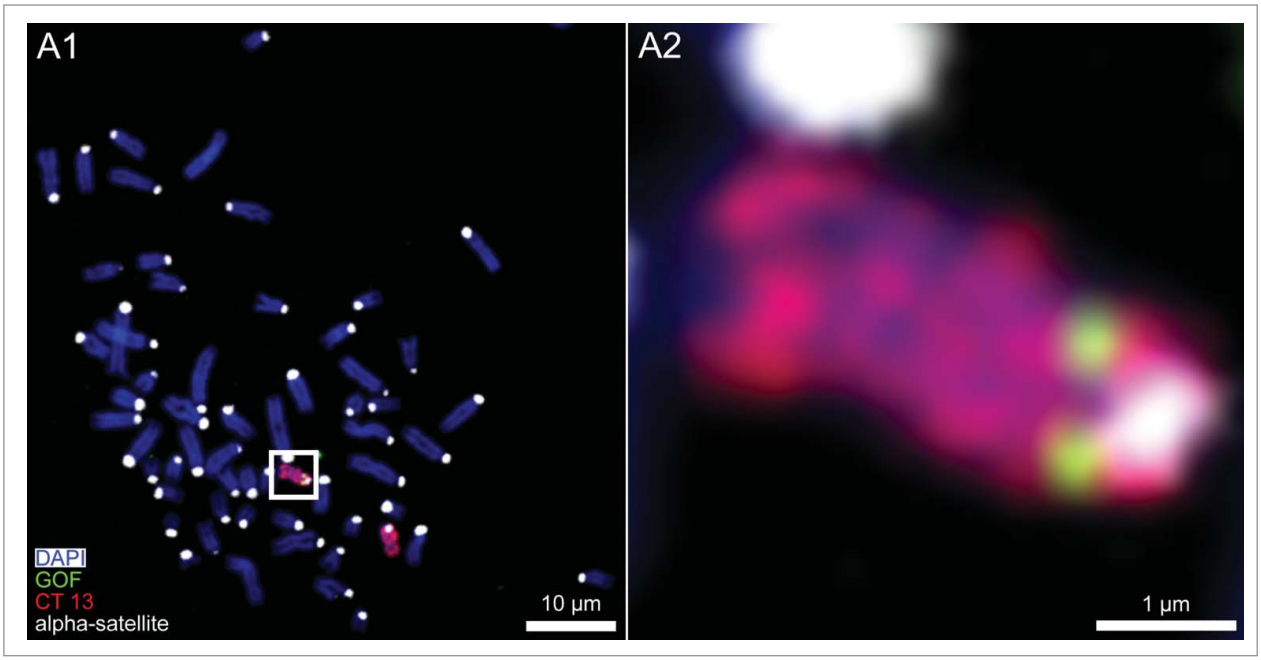

Figure 1. Chromosome 13 painting combined with FISH of the pluripotency marker gene *GOF*. (**A1)** Wide-field, digital, fluorescence microscopy from a bovine fetal fibroblast metaphase spread after 3-color FISH shows DAPI stained chromosomes (blue) painted chromosomes 13 (red), the pluripotency marker gene *GOF* (green) and α-satellite DNA clusters in pericentromeric heterochromatin (white). (**A2**) Magnification of the boxed carrier chromosome 13 demonstrates the integration of *GOF* on 13q near the pericentromeric heterochromatin.

We suggest that the particular vulnerability of such nuclei reflected the lack of a layer of compact chromatin attached to the lamina beneath the nuclear envelope. This layer was typical for the much smaller nuclei of day 4 embryos, which were also less sensitive to damage induced by the 3D-FISH protocol in line with the fact that such damage was also very rarely noted after 3D-FISH of fibroblast nuclei. For a quantitative 3D analysis we chose nuclei showing a reasonable structural preservation with well defined FISH signals. From the 20 nuclei selected from day 2 embryos for a detailed 3D analysis, 3 were chosen from 2 2-cell embryos, 3 from one 3-cell embryo, 5 from 2 6-cell embryos, 2 from 2 7-cell embryos, 5 from 3 8-cell embryos, and 2 from 2 9-cell embryos.

Of the 20 nuclei selected from day 4 embryos, 18 were taken from embryos carrying between 15 and 22 cells. Two nuclei selected from day 4 embryos, whose cell number was not determined, showed a decreased volume within the range of the other 18 nuclei. Significant and non-significant differences between the absolute changes of radial positions of *GOF* and both chromosome territories 13 in day 2 and day 4 embryos were maintained, when these 2 nuclei, as well as the 2 nuclei from 9-cell embryos at day 2 were eliminated from the statistical analysis (data not shown).

Nuclear examples shown in **Figure 2** indicate an impressive internuclear variability of radial positions noted for *GOF*, carrier and non-carrier chromosome territories 13 in fibroblast and embryonic nuclei. *GOF* signals were found either at the border or inside of the carrier chromosome territory 13, but never far away. This finding excludes a role of giant chromatin loops, which would carry away *GOF* from its carrier chromosome territory prior to or during transcriptional activation.

Figure S1 shows examples of nuclei with aberrant numbers of carrier and non-carrier chromosomes 13 in our SCNT experiments. **Table 1** argues for a higher frequency of polyploidization and chromosome missegregation events in cloned embryos compared with IVF embryos. Day 2 cloned embryos displayed a higher frequency of chromosome missegregations compared with day 4 cloned and day 2 IVF embryos. Compared with fibroblast nuclei, a highly significant increase of nuclei with gains of *GOF* and/or chromosome territories 13 was detected in day 2 embryos but not in day 4 embryos, which in comparison with day 2 embryos revealed a significant drop of aberrations.

For a complete 3D reconstruction and 3D evaluation we chose 20 fibroblast nuclei, 20 nuclei from day 2 embryos and 20 nuclei from day 4 embryos with intense painting of both chromosome territories 13 and clearly identifiable *GOF* signals. Compared with nuclei seen in fibroblast cultures, embryonic nuclei revealed a severalfold volume increase at day 2, whereas at day 4 nuclear volumes had decreased again to the range observed for fibroblast nuclei (**Fig. 3A**). For a measure of nuclear roundness we calculated the volume of the largest possible sphere, which could be virtually embedded in a given nucleus and then divided the volume of this sphere by the total nuclear volume (**Fig. 3B**). A strictly spherical cell nucleus is characterized by a roundness factor 1, whereas a roundness factor 0 would indicate a completely flat nucleus with a negligible axial extension. Compared with the flat ellipsoidal shape of nuclei recorded in fibroblast cultures, **Figure 3C** shows a highly significant increase of nuclear roundness in both day 2 and day 4 embryos.

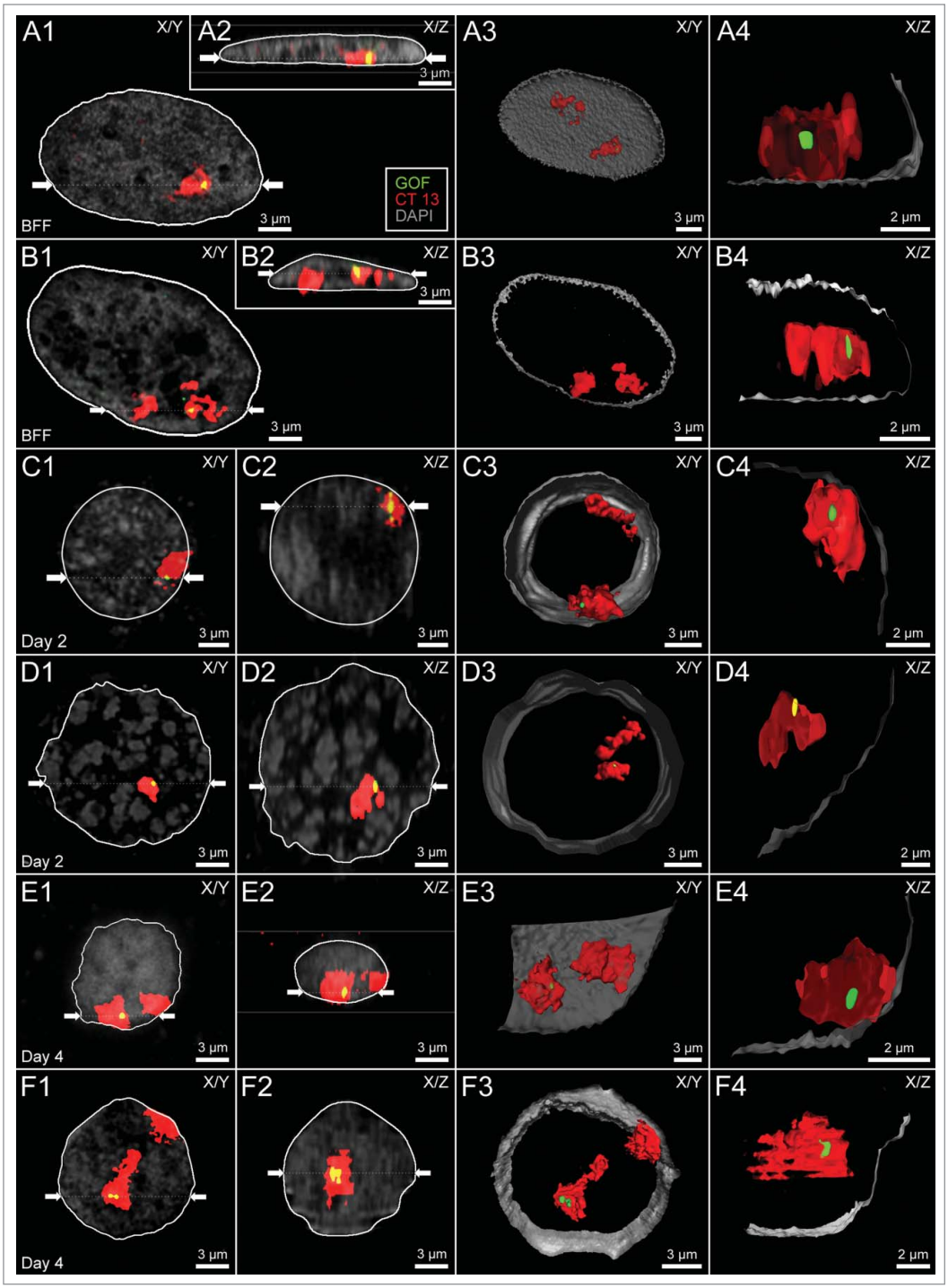

Figure 2. Variability of higher order chromatin arrangements of the pluripotency marker gene *GOF*, its carrier chromosome territory (CT) 13 and the non-carrier homolog. Panels A-F. CSLM images were recorded from 6 nuclei A-F representative for the variability of radial nuclear arrangements of *GOF* (green), its carrier and non-carrier chromosome territories 13 (red): 2 fibroblast nuclei (**A and B**), 2 embryonic nuclei from cloned embryos at day 2 (**C and D**), and 2 nuclei from cloned embryos at day 4 (**E and F**). DAPI stained DNA is presented in gray. X/Y-sections (A1-F1) and X/Z sections (A2-F2) were taken at positions including the painted carrier chromosome territory with the *GOF* signal. Two white arrows in A1-F1 indicate the site, where the X/Z section was taken perpendicular to the X/Y section. Correspondingly, 2 white arrows in A2-F2 indicate the site, where the X/Y section was taken perpendicular to the X/Z section. A3-F3 show partial 3D reconstructions of the same nuclei presenting the location of the carrier and non-carrier chromosome territories 13. A4-F4 show enlarged, virtual sections of the carrier chromosome territory with *GOF* signals representing the nearest position of *GOF* to the DAPI stained nuclear border. Bars: 3 µm for A1-F1, A2-F2, A3-F3; 2 µm for A4-F4.

Table 1. Chromosomal gains and losses in cloned and IVF bovine embryos

					Number of painted CTs per nucleus					Number of GOF signals			
		Painted CT	Embryos analyzed	Nuclei analyzed	1	2	3	4	5	1	2	3	4
This study	BFF	CT 13	-	50	10 (20%)	39 (78%)	0	1 (2%)	0	50 (100%)	0	0	0
	NT D2		25	95	7 (7.4%)	63 (66.3%)	13 (13.7%)	6 (6.3%)	6 (6.3%)	71 (74.7%)	16 (16.8%)	1 (1.1%)	2 (2.1%)
	NT D4		6	32	3 (9.4%)	27 (84.4%)	1 (3.1%)	1 (3.1%)	0	29 (90.6%)	1 (3.1%)	0	0
Koehler et al.[8]	IVF D1	CT 19	7	19	9 (47.4%)	8 (42.1%)	2 (10.5%)	0	0				
	IVF D2		10	37	8 (21.6%)	29 (78.4%)	0	0	0				
	IVF D3		9	58	8 (13.8%)	50 (86.2%)	0	0	0				
	IVF D1	CT 20	7	19	9 (47.4%)	10 (52.6%)	0	0	0				
	IVF D2		10	37	9 (24.3%)	27 (73%)	1 (2.7%)	0	0				
	IVF D3		9	58	4 (6.9%)	54 (93.1%)	0	0	0				

Following 2-color 3D-FISH with a chromosome territory 13 paint probe and a differentially labeled *GOF* probe, numbers of *GOF*, carrier and non-carrier chromosome territories 13 were counted in 3D image stacks recorded from nuclei of bovine fetal fibroblasts, cloned day 2 and day 4 embryos (NT D2 and NT D4, respectively) (compare **Supplemental Figure S1**). In our analysis we included only nuclei, which revealed at least 1 clearly identifiable *GOF* signal together with its painted carrier chromosome territory 13. Possible cases of two, spatially associated CTs 13 could not be identified and were therefore counted as a single territory. As expected for diploid nuclei, most fibroblast nuclei, as well as nuclei from NT D2 and NT D4 embryos, carried two CTs 13, but aberrant numbers of other CTs can, of course, not be excluded. Compared with fibroblast nuclei, a highly significant increase of nuclei ($p < 0.001$) with gains of *GOF* and/or chromosome territories 13 was detected in cloned day 2 embryos. Nuclei of cloned day 4 embryos revealed a significant drop ($p < 0.05$) of aberrations compared with cloned day 2 embryos and did no longer show a significant increase compared with fibroblast nuclei. For comparison with aberration frequencies in bovine IVF embryos at day 1, 2 and 3, we added hitherto unpublished counts of gains and losses of painted chromosomes 19 and 20 from a previous study.[8] A statistical comparison of chromosomal missegregation events counted in cloned and IVF embryos at day 2 was performed under the assumption that chromosomes 13, 19 and 20 shared the same risk of mitotic missegregations. This comparison revealed a highly significantly increased risk of missegregations in cloned over IVF day 2 embryos.

Figure 4 and **Tables 2 and 3** present the results of a quantitative analysis of absolute and relative 3D radial positions of *GOF*, carrier and non-carrier chromosome territories 13 with respect to 3D nuclear borders in fibroblast nuclei and in day 2 and day 4 embryonic nuclei. The absolute radial position of a given FISH signal was defined as the shortest distance (nm) of its intensity gravity center from the nuclear border. Each signal's relative position was determined to be between 1 and 0. A position of 1 represented localization directly at the border and a position of 0 represented localization at the center of the nucleus (for further details see Experimental Procedures). Box/scatter plots in **Figure 4A** show the results of our measurements of absolute, radial positions, whereas box/scatter plots in **Figure 4B** show the calculated relative positions. A statistical analysis of these data is presented in **Table 2**. In comparison with fibroblast nuclei, we observed a significant increase of the mean distance of carrier chromosome territory 13 to the nuclear border in day 2 embryos (**Table 2**, row 1). A significantly larger, absolute, mean distance was also noted for carrier chromosome territory 13 in day 2 nuclei compared with day 4 nuclei (**Table 2**, row 2). Absolute, radial positions of carrier chromosome territory 13 in fibroblast nuclei and in day 4 embryonic nuclei did not differ significantly (**Table 2**, row 3). Absolute *GOF* positions determined in fibroblast nuclei did also not significantly change in day 2 embryonic nuclei (**Table 2**, row 4). A significant, absolute shift of *GOF* toward the nuclear periphery occurred between day 2 and day 4 (**Table 2**, row 5). In line with this finding we also noted a significant decrease of the absolute distance of *GOF* to the nuclear border between fibroblast nuclei and day 4 embryonic nuclei (**Table 2**, row 6).

Most notably, a comparison between absolute, radial positions of carrier and non-carrier chromosome territories 13 measured in nuclei of fibroblasts, day 2 and day 4 embryos did not reveal a significant difference (**Table 2**, rows 7–9). This finding shows that the presence of *GOF* in one of the 2 chromosome territory 13 homologs had no specific influence on their absolute radial positioning. In comparison with fibroblast nuclei the absolute, mean radial position of non-carrier chromosome territory 13 was significantly further removed from the nuclear border in embryonic nuclei at day 2 (**Table 2**, row 10), whereas these positions were neither significantly different between day 2 and day 4 embryonic nuclei (**Table 2**, row 11) nor between fibroblast nuclei and day 4 embryonic nuclei (**Table 2**, row 12).

To account for the large internuclear variability of volumes, we also determined the relative, radial positions of *GOF*, carrier and non-carrier chromosome territories 13 (**Fig. 4B** and **Table 3**). In comparison with BFF nuclei, the mean, relative position of carrier chromosome territory 13 in day 2 and day 4 embryonic nuclei showed a significant shift towards the nuclear periphery (**Table 3**, rows 1 and 3), whereas the mean, relative position of carrier chromosome territory 13 did not change between day 2 and day 4 embryos (**Table 3**, row 2). The observed changes of relative *GOF* positions were in line with the relative, positional changes of carrier chromosome territories (**Table 3**, rows 4–6). In line with the comparisons of the absolute, mean radial positions of carrier vs. non-carrier chromosome territory 13, comparisons of the relative positions did also not reveal a significant difference (**Table 3**, rows 7–9). In contrast, in comparison with fibroblast nuclei the relative

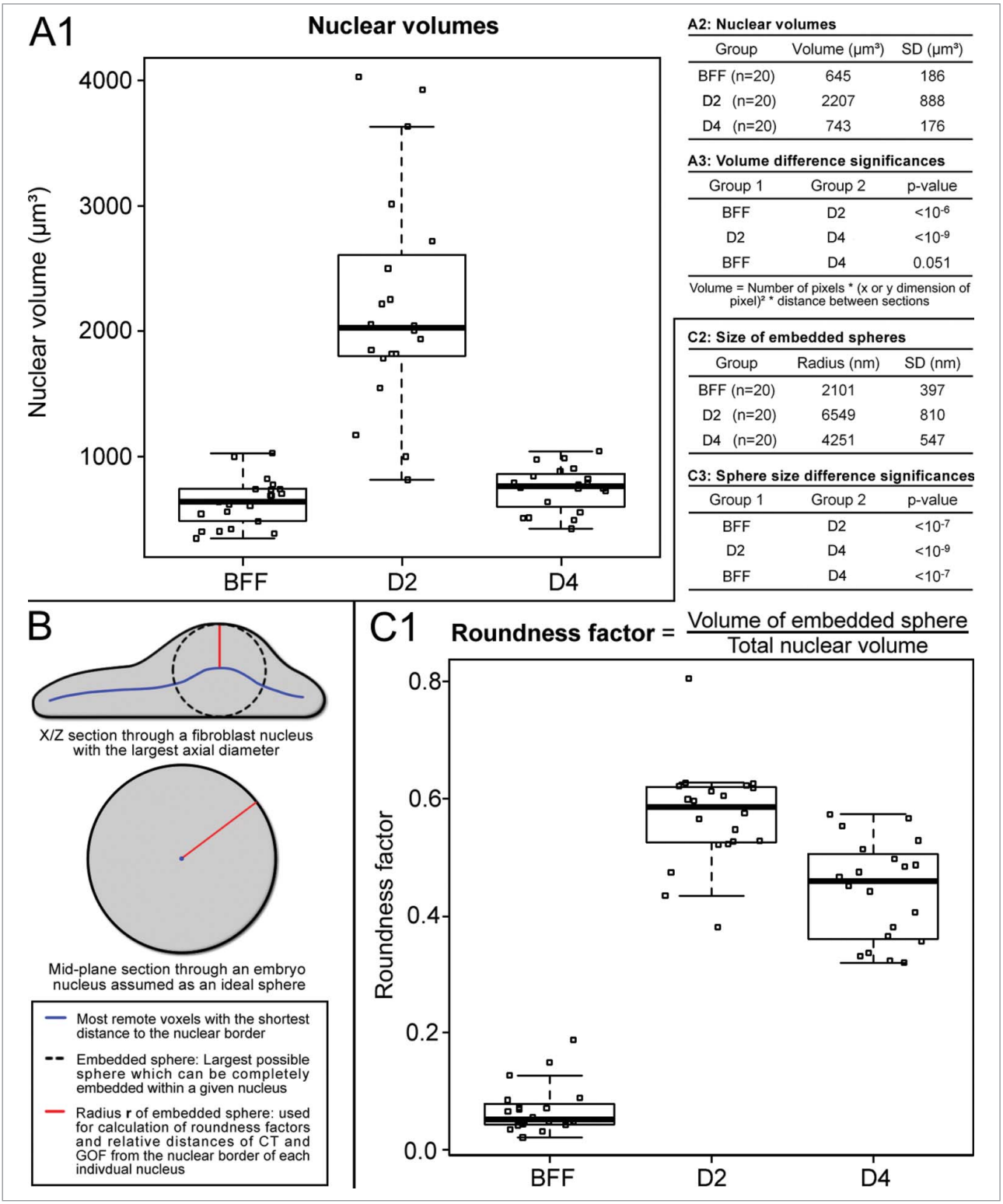

Figure 3. (**A**) Volume measurements of bovine fetal fibroblast (BFF) nuclei, day 2 and day 4 embryonic nuclei. Compared with the volumes of fibroblast nuclei, a severalfold increase was noted for day 2 nuclei, whereas a decrease of nuclear volumes back to the level of fibroblast nuclei was noted in day 4 embryos. (**B and C**) Flat-ellipsoidal shaped fibroblast nuclei adopt a roundish shape in cloned embryos. (**B**) Scheme for the determination of nuclear roundness factors and relative radial distances. A roundness factor (RF) = 0 represents an extremely flat nucleus with zero axial extension, RF = 1 a perfect round shape. (**C**) Compared with RFs of fibroblast nuclei, RFs of nuclei in day 2 and day 4 embryos showed a severalfold increased roundness factor.

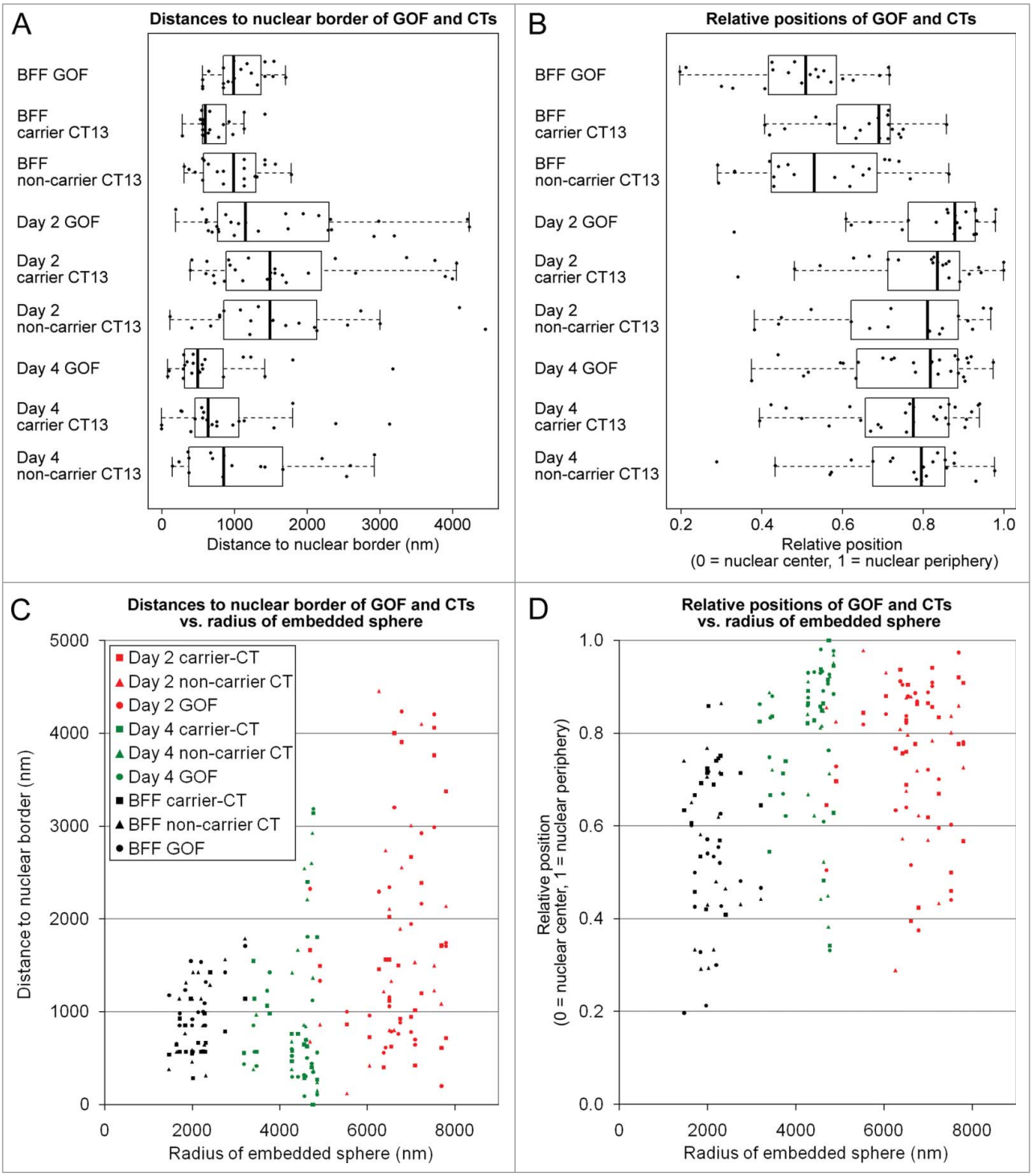

Figure 4. Quantitative analysis of radial nuclear arrangements of the pluripotency reporter gene *GOF*, its carrier chromosome territory (CT) 13 and the non-carrier homolog. (**A**) Absolute 3D distances from the 3D reconstructed nuclear border. (**B**) Relative 3D positions between the center of the nucleus (0) and the 3D reconstructed nuclear border (1). Combined box/scatter plots of *GOF*, the carrier and non-carrier chromosome territories CT 13 in fibroblast nuclei, day 2 embryonic nuclei and day 4 embryonic nuclei observed in cloned embryos at the onset of major embryonic genome activation and shortly thereafter demonstrate an extensive internuclear variability of these measurements. (**C and D**) present the data set shown in (**A and B**), respectively, in relation to the largest sphere, which could be embedded in each given nucleus (compare **Figure 3B and 3C**). Note that the variability of absolute distance measurements increased with the size of the embeddable sphere (**C**), whereas a similar variability was detected with respect to the relative radial positions (**D**).

Table 2. Statistical analysis of differences between absolute, mean distances of GOF and chromosome territory (CT) 13 gravity centers to the nuclear border in bovine fetal fibroblasts (BFFs), day 2 and day 4 cloned embryos

Group 1	Mean distance (nm)	SD	Group 2	Mean distance (nm)	SD	p-value
1. BFF, carrier CT 13	730	272	Day 2, carrier CT 13	1730	1160	<0.0001
2. Day 2, carrier CT 13	1730	1160	Day 4, carrier CT 13	890	774	<0.003
3. BFF, carrier CT 13	730	272	Day 4, carrier CT 13	890	774	1
4. BFF, GOF	1065	349	Day 2, GOF	1635	1119	0.2
5. Day 2, GOF	1635	1119	Day 4, GOF	736	714	<0.0002
6. BFF, GOF	1065	349	Day 4, GOF	736	714	<0.002
			Carrier vs. non-carrier CT (nm)			
7. BFF carrier CT 13	730	272	BFF non-carrier CT	969	426	0.07
8. Day 2, carrier CT 13	1730	1160	Day 2, non-carrier CT	1728	1136	0.8
9. Day 4, carrier CT 13	890	774	Day 4, non-carrier CT	1195	900	0.3
			Non-carrier vs. non-carrier CT (nm)			
10. BFF	969	426	Day 2	1728	1136	<0.02
11. Day 2	1728	1136	Day 4	1195	900	0.1
12. BFF	969	426	Day 4	1195	900	0.9

mean, radial positions of non-carrier chromosome territories were significantly shifted toward the nuclear periphery in embryonic nuclei at day 2 and day 4 (**Table 3**, rows 10 and 12), whereas these positions did not significantly differ in day 2 and day 4 embryos (**Table 3**, row 11).

Figure 4C and D present the same set of absolute and relative measurements shown in **Figure 4A and B** in relation to the largest sphere, which could be embedded in each given nucleus. This presentation further emphasizes the pronounced internuclear variability of *GOF*, carrier and non-carrier chromosome territory 13 positions, which defies a straightforward interpretation, even for the case of normalized positions.

Discussion

The integration of the *GOF* transgene into one of the 2 chromosome territories 13 in bovine fetal fibroblasts and therefore in cloned embryos derived from these cells allowed us to perform 3D-FISH experiments to clarify 3 questions, a) whether GOF activation might be accompanied by a radial movement of this transgene toward the nuclear interior; b) whether a demonstrable movement of *GOF* would occur together with its carrier CT 13 or independent via a giant chromatin loop expanding from the carrier CT; c) whether potential radial movements of the carrier CT would be paralleled by similar movements of the homologous CT 13.

EGFP, the product of transcribed *GOF*, was only detected in embryos with ≥9 cells. Activation of pluripotency genes signifies a major change of the transcriptome during reprogramming of the descendents of a transferred fibroblast nucleus. Notably, *GOF* activation occurred during the same period of preimplantation development as major embryonic gene activation in IVF embryos at the 8-cell stage.[3,17] Apparently major reprogramming of gene expression signified by *GOF* activation was correlated with structural changes of nuclei in cloned embryos, which were strikingly similar with structural changes observed in IVF embryos.[11] Cloned embryos approaching the 8-cell stage adopted

Table 3. Statistical analysis of differences between relative, radial positions of GOF and chromosome territory (CT) 13 gravity centers in bovine fetal fibroblasts (BFFs), day 2 and day 4 cloned embryos

Group 1	Mean position	SD	Group 2	Mean position	SD	p-value
		Relative positions (0 = nuclear center; 1 = nuclear border)				
1. BFF, carrier CT 13	0.65	0.12	Day 2, carrier CT 13	0.74	0.16	<0.01
2. Day 2, carrier CT 13	0.74	0.16	Day 4, carrier CT 13	0.79	0.17	0.3
3. BFF, carrier CT 13	0.65	0.12	Day 4, carrier CT 13	0.79	0.17	<0.003
4. BFF, GOF	0.49	0.15	Day 2, GOF	0.75	0.16	<0.00001
5. Day 2, GOF	0.75	0.16	Day 4, GOF	0.73	0.19	0.06
6. BFF, GOF	0.49	0.15	Day 4, GOF	0.73	0.19	$<10^{-05}$
		Carrier vs. non-carrier CT (0 = nuclear center; 1 = nuclear border)				
7. BFF carrier CT 13	0.65	0.12	BFF non-carrier CT	0.54	0.17	0.06
8. Day 2, carrier CT 13	0.74	0.16	Day 2, non-carrier CT	0.74	0.17	1
9. Day 4, carrier CT 13	0.79	0.17	Day 4, non-carrier CT	0.73	0.19	0.4
		Non-carrier vs. non-carrier CT (0 = nuclear center; 1 = nuclear border)				
10. BFF	0.54	0.17	Day 2	0.74	0.17	<0.001
11. Day 2	0.74	0.17	Day 4	0.73	0.19	0.9
12. BFF	0.54	0.17	Day 4	0.73	0.19	<0.003

a nuclear phenotype, which was termed ENP-like because of its similarities with the ENP phenotype described in 8-cell IVF embryos (the acronym stands for Embryonic Nucleus with Peripheral chromosome territory distribution; see Introduction). After major EGA in IVF embryos and pluripotency gene activation in cloned embryos CTs were redistributed into the nuclear interior resulting in a nuclear phenotype, called ENC for Embryonic Nuclei with Conventional architecture presenting typical architectural features of somatic cells. ENCs are characterized by a network of CTs and chromatin clusters throughout the nuclear space, as well as an enrichment of dense chromatin beneath the nuclear lamina and around nucleoli.[11,22]

Cell numbers counted in cloned embryos at day 2 and day 4 suggest that *GOF* activation had already started in a fraction of day 2 embryos and that *GOF* was active in the large majority, if not all nuclei of embryos studied from day 4 embryos. These nuclei showed predominantly the ENC phenotype, which was also adopted by nuclei of *in vitro* fertilized embryos after major genome activation.[11] At first glance our quantitative analysis of 3D radial nuclear positions of *GOF* in nuclei from fibroblasts and day 2 embryos may argue that a repositioning of this pluripotency marker gene preceded its transcriptional activation. Notably, a comparison of the radial positions of *GOF* and both chromosome territories 13 in day 2 embryos did not indicate a significant correlation with the actual number of cells present in each embryo (data not shown). This finding argues against a gradual repositioning of *GOF* during subsequent cleavage cycles toward the nuclear interior before major embryonic/pluripotency gene activation is occurring around the 8-cell stage. At this point we can neither exclude the possibility that the required detachment of fibroblasts from the plastic surface for SCNT yielded a rounder shape with a change of the radial position of *GOF* nor the possibility that the observed shift in day 2 embryos with 2 to 9 cells was already present in cloned one-cell embryos. A radial shift of genes prior to transcriptional activation makes sense in somatic cell nuclei, where a chromatin environment favorable for transcription together with an enrichment of active genes was noted in the nuclear interior as compared to the less favorable nuclear periphery.[23,24] When applied to the present study, such an interpretation does not take into account the major changes of higher order chromatin architecture, which take place both in IVF and cloned bovine embryos, which pass through the major embryonic/pluripotency gene activation window of preimplantation development.[11] The significant transient shift of *GOF* away from and back to the nuclear periphery observed in our quantitative 3D comparison of fibroblast nuclei with day 2 and day 4 embryonic nuclei was strictly correlated with corresponding movements of the carrier chromosome territory 13 in embryonic nuclei. The persistent colocalization of *GOF* with its carrier chromosome territory rules out the possibility that the repositioning of *GOF* away from the nuclear periphery in day 2 embryos compared with nuclei from fibroblasts depended on the formation of giant chromatin loops. Movements of the non-carrier chromosome territory 13 homolog provided an ideal internal control to decide whether movements of the carrier chromosome territory 13 were triggered by the presence of *GOF*. Our observation, that the same absolute and relative transient movements were observed for carrier and non-carrier chromosome territories 13, rules out a specific influence of *GOF*. In our original hypothesis we predicted that *GOF* may move from the nuclear periphery toward the nuclear interior, because the interior may provide a more convenient environment for active genes. Since *GOF*, once activated around the 8-cell stage, remains transcriptionally active throughout the whole following preimplantation period, one would expect that *GOF* should also retain the more interior nuclear position observed in day 2 embryos. The highly significant absolute shift toward a more peripheral position in day 4 embryos came as an unexpected surprise.

Our findings emphasize that positional changes of genes must be interpreted in the context of changes of the nuclear architecture at large. The apparent differences of absolute and relative distance measurements are a reflection of the complex changes in volume, shape and global chromatin organization between flat ellipsoid fibroblast nuclei, the much larger, roundish nuclei of embryos at the onset of major embryonic gene activation at day 2 and the again much smaller, but still roundish nuclei of day 4 embryos. We do not know yet, when and why the change of nuclear shape actually takes place. Possibly, nuclei already adopt a more roundish shape, when fibroblasts are detached from their growth surface.

Preimplantation development of bovine IVF embryos is prone to chromosomal missegregation and polyploidization events, often leading to embryos consisting of both diploid and polyploid cells.[25,26] Such effects have been observed in various mammalian species, including man, and seem to be even more pronounced in cloned embryos.[27,28] The wide variation of cell numbers observed in our study in day 2 embryos may reflect the particularly high frequency of chromosome missegregations during the first cleavage stages of cloned embryos. The interplay of structural and functional changes of embryonic nuclei during early development provides an unresolved conundrum of developmental biology. The fact that a fibroblast nucleus after SCNT is forced within its new cellular environment to achieve the same, global architecture as nuclei in fertilized IVF embryos and pass through the same sequence of changes, however, strongly suggests that the observed sequence of structural changes should not be belittled as a byproduct of functional reprogramming. We argue that structural reorganization is linked inseparably with changes of nuclear functions.

It is interesting to compare the changes of 3D nuclear architecture observed in our current studies of cloned and IVF bovine embryos with the development of embryos from other mammalian species, such as mouse and rabbit.[5,6,10] For this purpose, one has to take into account that mammalian species differ in the timing of major embryonic gene activation.[2] In rabbit embryos this event apparently starts, like in bovine embryos, at the 8-cell stage. In a previous study of *in vivo* derived and cloned rabbit embryos from our group, only occasional nuclei recorded at this stage showed the peripheral chromatin arrangement phenotype.[6] Immunodetection of H3K4me2/3 was used in this study as a marker for transcriptionally competent chromatin. Although remarkable changes of the nuclear patterns of this marker

occurred between 4-cell and 16-cell rabbit embryos, the resolution of 3D-CLSM was not sufficient to perform the quantitative, high resolution 3D-SIM analyses performed with immunostained H3K4me3 in the accompanying study of bovine embryos during the corresponding window of development.[11] In mouse embryos major embryonic gene activation starts at the 2-cell stage.[29] Merico et al.[10] found stage-specific differences between the nuclear topography of kinetochores, pericentric heterochromatin and the nucleolus in IVF and cloned preimplantation mouse embryos. The time-course of nuclear remodeling events differed during the first blastomere cleavage events, but IVF and cloned embryos achieved the same distinct nuclear organization in the majority of embryos at the 8-cell stage. Aguirre-Lavin et al.[5] combined 3D-FISH, 3D-CLSM and quantitative 3D image analyses to study nuclear arrangements of centromeric (minor satellites), pericentromeric (major satellites), and telomeric genomic sequences, as well as nucleolar precursor bodies and nucleoli in naturally fertilized mouse embryos from the zygote to blastocyst stage. Remarkable changes of nucleolar precursor bodies and pericentromeric heterochromatin were noted during the transition from the mouse 2-cell to the 4-cell stage. Approximately half of the telomeres were localized around the nucleolar precursor bodies or associated with extranucleolar pericentromeric signals. The different probe sets and goals pursued in our studies of cloned and IVF bovine embryos and current studies of mouse and rabbit embryos preclude any direct comparison of the results. The differences of global nuclear architectures are, however, remarkable and emphasize the importance of evolutionary comparisons. Such comparisons will help to identify evolutionary conserved features, which are likely of functional importance for the early development of all mammalian species.

In summary, the 3 questions posed at the beginning of the Discussion can be answered as follows: Compared with silent *GOF* in fibroblast nuclei, we detected a transient shift of *GOF* in embryonic nuclei away from the nuclear periphery at day 2 (question a). At day 4 *GOF* had moved back toward the nuclear periphery. This finding disproves the hypothesis that GOF activation requires a permanent shift of this transgene into the nuclear interior. The observation that *GOF* movements in both directions occurred together with their carrier chromosome territory (CT) 13 rules out the hypothesis a giant chromatin loop was involved in these movements (question b). A specific effect of *GOF* activation on movements of the carrier CT 13 was ruled out by the fact that the same transient shift observed for the *GOF* carrier CT was also observed for the non-carrier homolog (question c). The activation of *GOF* as an indicator of pluripotency gene transcription and translation in cloned day 2 to day 4 embryos seemingly parallels the developmental window, where major embryonic genome activation occurs in IVF embryos. The observed timing of the positional changes of *GOF* may serve as a case in point to emphasize the necessity to interpret positional changes of genes during early embryonic development in the context of changes of the nuclear architecture at large, including complex changes in volume, shape and global chromatin organization.

Experimental Procedures

Ethics statement

No animal experiments were conducted. Oocytes for somatic cell nuclear transfer (SCNT) were recovered from ovaries of heifers and cows slaughtered for meat production.

Bovine fetal fibroblast cultures

Vigorously growing fibroblast cultures stably transfected with the *Pou5f1* reporter construct *GOF18-ΔPE-EGFP* were generated and maintained as previously described.[17] The reporter construct includes the *EGFP* gene flanked by a 9-kb fragment of the murine *Pou5f1* upstream region with a deletion in the proximal enhancer, and a 9-kb fragment containing the non-transcribed murine structural *Pou5f1* gene. *Pou5f1* was previously called *Oct4*. Hence we refer to the transgene as *GOF* (*GFP-Oct-Four*).

Cloned early bovine embryos

Procedures were carried out essentially as described.[17] For details see the thesis of Daniela Koehler.[30] Briefly, embryos were generated by SCNT using fetal fibroblasts carrying the transgene *GOF* described above. Donor cells frozen in small aliquots were thawed approximately one week before SCNT and grown in a 24-well plate in DMEM, supplemented with 20% fetal calf serum. They were usually confluent on the next day and kept in that state until use. After SCNT the cloned embryos were cultured in 100 μl drops of synthetic oviduct fluid supplemented with 5% (v/v) estrous cow serum at 39°C in a humidified atmosphere of 5% CO_2, 5% O_2, and 90% N_2, covered by paraffin oil. Prior to fixation embryos were briefly washed in 1x PBS at 37°C. Embryos were fixed in 3.7% formaldehyde/1x PBS at room temperature and incubated in 0.1N HCl between 30 sec and 2 min until the zona pellucida disappeared, washed again 2 times each for 10 min in 0.05% Triton X-100/1x PBS containing 0.1% BSA, permeabilized for 60 min in 0.5% Triton X-100/1x PBS containing 0.1% BSA, washed again 2 times in 0.05% Triton X-100 in 1x PBS plus 0.1% BSA, incubated in 0.1N HCl for 2 min, washed as above and finally 2 times each for 10 min in 0.01% Triton X-100 in 2x SSC plus 0.1% BSA. Prior to 3D-FISH embryos were incubated in 50% formamide/2x SSC containing 0.1% BSA (pH = 7.0) for at least 2 days and nights.

DNA probes and labeling procedures

The pluripotency reporter gene *GOF* was delineated with a probe consisting of the *EGFP* gene flanked by a 9-kb fragment of the murine *Pou5f1* upstream region with a deletion in the proximal enhancer, and a 9-kb fragment containing the non-transcribed murine structural *Pou5f1* gene, as well as the neomycin resistance cassette FRT-neo-FRT.[18] For visualization of chromosome 13 we used either a chromosome specific paint probe for sheep (*Ovis aries*) chromosome 13, which is homologous to bovine chromosome 13 or a bovine chromosome 13 paint probe.[8,31,32] Chromosomes were sorted by fluorescence activated chromosome sorting (FACS) and their DNA was amplified using degenerate oligonucleotide-primed PCR (DOP-PCR) or a whole

genome amplification kit (GE Healthcare).[31] An α-satellite probe for visualization of pericentromeric heterochromatin on bovine chromosomes was generated by DOP-PCR from bovine genomic DNA using sequence information for bovine satellites III and IV for the synthesis of appropriate primer pairs.[33,34]

Satellite III primers:
5′-AAT CAW GCA GCT CAG CAG GCA RT-3′
5′-GAT CAC GTG ACT GAT CAT GCA CT-3′
Satellite IV primers:
5′-AAG CTT GTG ACA GAT AGA ACG AT-3′
5′-CAA GCT GTC TAG AAT TCA GGG A-3′

For 2- and 3-color FISH experiments probes were labeled appropriately using degenerate oligonucleotide primed polymerase chain reaction (DOP-PCR) or nick-translation protocols. The *GOF* probe was labeled either with TAMRA (tetramethylrhodamine)-dUTP (Bioron) or Cy3-dUTP, chromosome paint probes with DIG (digoxigenin)-11-dUTP and the α-satellite probe with DNP (dinitrophenol)-11-dUTP (PerkinElmer).

Fluorescence *in situ* hybridization and signal detection

FISH experiments were carried out essentially as described by Cremer et al.[35] with modifications described in detail by Koehler et al.[9,30]. Hybridization mixtures contained 50% formamide, 2x SSC, 10% dextran sulfate. In 2D and 3D-FISH experiments carried out with cultured cells probe concentrations were about 20–40 ng/μl for chromosome 13 and *GOF* and 2 ng/μl for the α-satellite probe. In case of 3D experiments to embryos the hybridization mixture contained about 170 ng/μl of the paint and *GOF* probe. This high amount was important firstly, to counteract probe dilution due to medium adherent to the embryo and secondly, to overcome penetration problems. When the paint probe established from sorted bovine chromosomes 13 was used, 500 μg of bovine Cot-1 DNA was added to 1 μg of painting probe to suppress hybridization of repetitive, labeled probe sequences to repetitive DNA sequences dispersed in the entire bovine genome. In case of the paint probe derived from sheep chromosomes 13, this suppression step was not necessary because of the rapid evolutionary divergence of highly repetitive sequences. Both paint probes yielded the same results. For 3D-FISH, embryos were pipetted into a 5 μl drop of hybridization mixture placed in the middle of a metal ring (diameter approximately 2 cm, height 1 mm (Brunel Microscopes Ltd.)) sealed with Fixogum on the surface of a glass slide. For preservation of the 3D shape of embryos and nuclei care was taken to avoid any deforming pressure and to prevent embryos from drying out at any step of the following procedure. The droplet of hybridization mixture was overlaid with mineral oil to avoid air-drying. After at least 2 hours of equilibration of the hybridization mixture with the embryo in a humid environment the glass slide was put on a hot block for 3 min at 76°C to denature nuclear DNA of embryos and probe DNA simultaneously. Hybridization was performed for 2–3 days at 37°C in a humidified atmosphere. For all subsequent washing and probe detection steps, individual embryos were transferred between 1 ml wells carrying the appropriate solutions (for details see Koehler et al.[30]). Embryos were washed twice in 2x SSC followed by stringent washings in 50% formamide/2x SSC and in 0.1% SSC, each for 10 min. After a short incubation in 4x SSC/0.02% Tween 20 (4x SSCT) embryos were placed in 4% BSA for 10 min for blocking unspecific antibody binding sites. Embryos were then incubated overnight at 4°C with monoclonal mouse-anti-digoxigenin (1:500, Sigma). After 2 washings in 4x SSCT secondary antibody solutions were applied for 90 min at room temperature: goat-anti-mouse-alexa488 highly cross adsorbed (1:200, Molecular Probes/Invitrogen) or goat-anti-mouse-Cy5 (1:100, Dianova). After 2 additional 10-min washings in 4x SSCT, embryos were transferred into 0.1 μg/ml DAPI/4x SSCT for 30 min. Embryos were then subjected to an increasing glycerol dilution series (20%, 40% and 60% in 4x SSCT), each for 5 min, and incubated in Vectashield antifade medium (Vector Laboratories) supplemented with DAPI (0.1 μg/ml) and transferred to poly-L-lysinated, 18-well "μ-slides" (Ibidi, Martinsried, Germany). Three-color FISH to metaphase spreads from transgenic BFF cultures with differentially labeled probes for *GOF*, pericentromeric α-satellite sequences and painting of CT 13 was performed according to standard protocols. For detection of the DNP-labeled α-satellite primary polyclonal goat-anti-DNP antibodies (1:250, Sigma) and secondary rabbit anti-goat-FITC (1:200, Sigma) were used.

3D confocal laser scanning microscopy (3D-CLSM) and 3D reconstructions

Embryos attached to μ-slides (see above) were carefully equilibrated prior to microscopy with the antifade Vectashield (Vector Laboratories). Care was taken to avoid uncontrolled changes of the refractive index of Vectashield due to dilution with solutions used for storage of embryos. Bovine embryos maintain a diameter of roughly 150–190 μm throughout their preimplantation development.[36] A Plan Apo 20x/0.7 objective was used for the recording of image stacks from entire embryos. It is important to note that high quality images with high aperture objectives used for quantitative analyses of chromosome territory 13 and *GOF* positions could only be recorded from nuclei located close to the surface of the glass slide. Light optical serial sections were obtained with a Leica TCS SP5 confocal laser scanning microscope using a Plan Apo 63x/1.4 oil immersion objective lens for high resolution image stacks from individual nuclei. Fluorochromes were excited using blue diode, Argon, and Helium-Neon lasers with 405 nm, 488 nm and 594 nm laser lines, respectively. Specimens were imaged using x/y/z voxel sizes of 30–120 nm/200 nm for high-resolution images and 400 nm/500 nm for overview images. 3D reconstructions were done using Amira 5 (Visage Imaging) software. Figures were prepared with Adobe Photoshop CS4 (*http://www.adobe.com/*).

Quantitative analysis of radial positions of *GOF*, its carrier chromosome territory 13 and non-carrier homolog

For quantitative analysis image stacks were processed using Fiji 1.45b (http://fiji.sc/). 3D radial distributions of chromosomes were measured utilizing the software eADS (enhanced

absolute 3D distances to surfaces).[23,37] Briefly, this software measures the shortest absolute distance of each voxel of a previously segmented chromosome territory or *GOF* signal to the border of the corresponding segmented nucleus. The program calculates the median of all measured distances of all voxels. This median value resembles the intensity gravity center, i.e. the highest probability of residence of *GOF*, carrier and non-carrier chromosome territories 13, respectively. To obtain a relative position of this median (1 for localization directly at the border and 0 for a localization at the center) the distance to the closest nuclear border is measured from the center of the nucleus. This distance represents the radius of the largest possible sphere inside the nucleus and serves to determine the relative radial position. The distributions of these absolute distance medians and relative position medians was compared statistically using the Wilcoxon rank-sum test utilizing the software package R 2.15. Final graphs and combined box/scatter plots were generated using R and Microsoft Excel 2003/2007.

Authors' contributions

VZ, EW, TC designed research; DK, VZ, AB, AW, TG, JP performed experiments; JP, DK, AB, TT analyzed data; TC, JP, VZ, EW wrote the paper.

Disclosure of Potential Conflicts of Interest

No potential conflicts of interest were disclosed.

Acknowledgments

Paint probes were kindly provided by Johannes Wienberg (Chrombios, Germany).

Funding

This study was supported by grants from the Deutsche Forschungsgemeinschaft to TC, EW and VZ (CR 59/26, FOR 1041, ZA 425/1–3). In addition, research of EW and VZ was supported by the EU grant Plurisys, HEALTH-F4–2009–223485 FP7 Health 534 project.

Supplemental Materials

Supplemental data for this article can be accessed on the publisher's website: http://www.tandfonline.com/kncl

References

1. Tadros W, Lipshitz HD. The maternal-to-zygotic transition: a play in two acts. Development 2009; 136:3033-42; PMID:19700615; http://dx.doi.org/10.1242/dev.033183
2. Li L, Lu X, Dean J. The maternal to zygotic transition in mammals. Mol Aspects Med 2013; 34: 919-38; PMID:23352575; http://dx.doi.org/10.1016/j.mam.2013.01.003
3. Graf A, Krebs S, Zakhartchenko V, Schwalb B, Blum H, Wolf E. Fine mapping of genome activation in bovine embryos by RNA sequencing. Proc Natl Acad Sci U S A 2014; 111:4139-44; PMID:24591639; http://dx.doi.org/10.1073/pnas.1321569111
4. Kanka J, Kepkova K, Nemcova L. Gene expression during minor genome activation in preimplantation bovine development. Theriogenology 2009; 72:572-83; PMID:19501393; http://dx.doi.org/10.1016/j.theriogenology.2009.04.014
5. Aguirre-Lavin T, Adenot P, Bonnet-Garnier A, Lehmann G, Fleurot R, Boulesteix C, Debey P, Beaujean N. 3D-FISH analysis of embryonic nuclei in mouse highlights several abrupt changes of nuclear organization during preimplantation development. BMC Dev Biol 2012; 12:30; PMID:23095683; http://dx.doi.org/10.1186/1471-213X-12-30
6. Brero A, Hao R, Schieker M, Wierer M, Wolf E, Cremer T, Zakhartchenko V. Reprogramming of active and repressive histone modifications following nuclear transfer with rabbit mesenchymal stem cells and adult fibroblasts. Cloning Stem Cells 2009; 11:319-29; PMID:19508112; http://dx.doi.org/10.1089/clo.2008.0083
7. Cremer T, Zakhartchenko V. Nuclear architecture in developmental biology and cell specialisation. Reprod Fertil Dev 2011; 23:94-106; PMID:21366985; http://dx.doi.org/10.1071/RD10249
8. Koehler D, Zakhartchenko V, Froenicke L, Stone G, Stanyon R, Wolf E, Cremer T, Brero A. Changes of higher order chromatin arrangements during major genome activation in bovine preimplantation embryos. Exp Cell Res 2009; 315:2053-63; PMID:19254712; http://dx.doi.org/10.1016/j.yexcr.2009.02.016
9. Koehler D, Zakhartchenko V, Ketterl N, Wolf E, Cremer T, Brero A. FISH on 3D preserved bovine and murine preimplantation embryos. Methods Mol Biol 2010; 659:437-45; PMID:20809333; http://dx.doi.org/10.1007/978-1-60761-789-1_34
10. Merico V, Barbieri J, Zuccotti M, Joffe B, Cremer T, Redi CA, Solovei I, Garagna S. Epigenomic differentiation in mouse preimplantation nuclei of biparental, parthenote and cloned embryos. Chromosome Res 2007; 15:341-60; PMID:17447149
11. Popken J, Brero A, Koehler D, Schmid VJ, Strauss A, Wuensch A, Guengoer T, Graf A, Krebs S, Blum H, et al. Reprogramming of fibroblast nuclei in cloned bovine embryos involves major structural remodeling with both striking similarities and differences to nuclear phenotypes of *in vitro* fertilized embryos. Nucleus 2014; 5:xx-xx. http://dx.doi.org/10.4161/19491034.2014.979712.
12. Bridger JM. Chromobility: the rapid movement of chromosomes in interphase nuclei. Biochem Soc Trans 2011; 39:1747-51; PMID:22103519; http://dx.doi.org/10.1042/BST20110696
13. Mehta IS, Eskiw CH, Arican HD, Kill IR, Bridger JM. Farnesyltransferase inhibitor treatment restores chromosome territory positions and active chromosome dynamics in Hutchinson-Gilford progeria syndrome cells. Genome Biol 2011; 12:R74; PMID:21838864; http://dx.doi.org/10.1186/gb-2011-12-8-r74
14. Solovei I, Kreysing M, Lanctot C, Kosem S, Peichl L, Cremer T, Guck J, Joffe B. Nuclear architecture of rod photoreceptor cells adapts to vision in mammalian evolution. Cell 2009; 137:356-68; PMID:19379699; http://dx.doi.org/10.1016/j.cell.2009.01.052
15. Gondor A, Ohlsson R. Chromosome crosstalk in three dimensions. Nature 2009; 461:212-7; PMID:19741702; http://dx.doi.org/10.1038/nature08453
16. Shi W, Zakhartchenko V, Wolf E. Epigenetic reprogramming in mammalian nuclear transfer. Differentiation 2003; 71:91-113; PMID:12641564; http://dx.doi.org/10.1046/j.1432-0436.2003.710201.x
17. Wuensch A, Habermann FA, Kurosaka S, Klose R, Zakhartchenko V, Reichenbach HD, Sinowatz F, McLaughlin KJ, Wolf E. Quantitative monitoring of pluripotency gene activation after somatic cloning in cattle. Biol Reprod 2007; 76:983-91.; PMID:17314316; http://dx.doi.org/10.1095/biolreprod.106.058776
18. Niwa H, Miyazaki J, Smith AG. Quantitative expression of Oct-3/4 defines differentiation, dedifferentiation or self-renewal of ES cells. Nat Genet 2000; 24:372-6; PMID:10742100; http://dx.doi.org/10.1038/74199
19. Yoshimizu T, Sugiyama N, De Felice M, Yeom YI, Ohbo K, Masuko K, Obinata M, Abe K, Scholer HR, Matsui Y. Germline-specific expression of the Oct-4/green fluorescent protein (GFP) transgene in mice. Dev Growth Differ 1999; 41:675-84; PMID:10646797; http://dx.doi.org/10.1046/j.1440-169x.1999.00474.x
20. Cremer T, Cremer M. Chromosome territories. Cold Spring Harb Perspect Biol 2010; 2:a003889; PMID:20300217; http://dx.doi.org/10.1101/cshperspect.a003889
21. Smeets D, Markaki Y, Schmid VJ, Kraus F, Tattermusch A, Cerase A, Sterr M, Fiedler S, Demmerle J, Popken J, et al. Three-dimensional super-resolution microscopy of the inactive X chromosome territory reveals a collapse of its active nuclear compartment harboring distinct Xist RNA foci. Epigenetics Chromatin 2014; 7:8; PMID:25057298; http://dx.doi.org/10.1186/1756-8935-7-8
22. Bolzer A, Kreth G, Solovei I, Koehler D, Saracoglu K, Fauth C, Muller S, Eils R, Cremer C, Speicher MR, et al. Three-dimensional maps of all chromosomes in human male fibroblast nuclei and prometaphase rosettes. PLoS Biol 2005; 3:e157; PMID:15839726; http://dx.doi.org/10.1371/journal.pbio.0030157
23. Kupper K, Kolbl A, Biener D, Dittrich S, von Hase J, Thormeyer T, Fiegler H, Carter NP, Speicher MR, Cremer T, et al. Radial chromatin positioning is shaped by local gene density, not by gene expression. Chromosoma 2007; 116:285-306; PMID:17333233; http://dx.doi.org/10.1007/s00412-007-0098-4
24. Kolbl AC, Weigl D, Mulaw M, Thormeyer T, Bohlander SK, Cremer T, Dietzel S. The radial nuclear positioning of genes correlates with features of megabase-sized chromatin domains. Chromosome Res 2012; 20:735-52; PMID:23053570; http://dx.doi.org/10.1007/s10577-012-9309-9

25. Demyda-Peyras S, Dorado J, Hidalgo M, Anter J, De Luca L, Genero E, Moreno-Millan M. Effects of oocyte quality, incubation time and maturation environment on the number of chromosomal abnormalities in IVF-derived early bovine embryos. Reprod Fertil Dev 2013; 25:1077-84; PMID:23182337; http://dx.doi.org/10.1071/RD12140
26. Viuff D, Rickords L, Offenberg H, Hyttel P, Avery B, Greve T, Olsaker I, Williams JL, Callesen H, Thomsen PD. A high proportion of bovine blastocysts produced in vitro are mixoploid. Biol Reprod 1999; 60:1273-8; PMID:10330080; http://dx.doi.org/10.1095/biolreprod60.6.1273
27. Terashita Y, Yamagata K, Tokoro M, Itoi F, Wakayama S, Li C, Sato E, Tanemura K, Wakayama T. Latrunculin A treatment prevents abnormal chromosome segregation for successful development of cloned embryos. PloS One 2013; 8:e78380; PMID:24205216; http://dx.doi.org/10.1371/journal.pone.0078380
28. Mertzanidou A, Wilton L, Cheng J, Spits C, Vanneste E, Moreau Y, Vermeesch JR, Sermon K. Microarray analysis reveals abnormal chromosomal complements in over 70% of 14 normally developing human embryos. Hum Reprod 2013; 28:256-64; PMID:23054067; http://dx.doi.org/10.1093/humrep/des362
29. Sawicki JA, Magnuson T, Epstein CJ. Evidence for expression of the paternal genome in the two-cell mouse embryo. Nature 1981; 294:450-1; PMID:6171732; http://dx.doi.org/10.1038/294450a0
30. Koehler D. Cloning in Cattle: Nuclear architecture and epigenetic status of chromatin during reprogramming of donor cell nuclei. Munich: Ludwig-Maximilians-University; 2009. Available from http: /edoc.ub.uni-muenchen.de1487;99151487
31. Burkin DJ, O'Brien PC, Broad TE, Hill DF, Jones CA, Wienberg J, Ferguson-Smith MA. Isolation of chromosome-specific paints from high-resolution flow karyotypes of the sheep (Ovis aries). Chromosome Res 1997; 5:102-8; PMID:9146913; http://dx.doi.org/10.1023/A:1018414123751
32. Ansari HA, Bosma AA, Broad TE, Bunch TD, Long SE, Maher DW, Pearce PD, Popescu CP. Standard G-, Q-, and R-banded ideograms of the domestic sheep (Ovis aries): homology with cattle (Bos taurus). Report of the committee for the standardization of the sheep karyotype. Cytogenet Cell Genet 1999; 87:134-42; PMID:10640834; http://dx.doi.org/10.1159/000015380
33. Singer MF. Highly repeated sequences in mammalian genomes. Int Rev Cytol 1982; 76:67-112; PMID:6749748; http://dx.doi.org/10.1016/S0074-7696(08)61789-1
34. Adega F, Chaves R, Guedes-Pinto H, Heslop-Harrison JS. Physical organization of the 1.709 satellite IV DNA family in Bovini and Tragelaphini tribes of the Bovidae: sequence and chromosomal evolution. Cytogenet Genome Res 2006; 114:140-6; PMID:16825766; http://dx.doi.org/10.1159/000093330
35. Cremer M, Grasser F, Lanctot C, Muller S, Neusser M, Zinner R, Solovei I, Cremer T. Multicolor 3D fluorescence in situ hybridization for imaging interphase chromosomes. Methods Mol Biol 2008; 463:205-39; PMID:18951171; http://dx.doi.org/10.1007/978-1-59745-406-3_15
36. Bó G, Mapletoft R. Evaluation and classification of bovine embryos. Anim Reprod 2013; 10:344-8.
37. Albiez H, Cremer M, Tiberi C, Vecchio L, Schermelleh L, Dittrich S, Kupper K, Joffe B, Thormeyer T, von Hase J, et al. Chromatin domains and the interchromatin compartment form structurally defined and functionally interacting nuclear networks. Chromosome Res 2006; 14:707-33; PMID:17115328; http://dx.doi.org/10.1007/s10577-006-1086-x

Supplementary Information

Supplementary Figure 1. Missegregation of carrier and non-carrier chromosomes in cloned day 2 and day 4 bovine embryos. Panels A and B. Nuclei from two day 2 embryos recorded by 3D-CLSM. Panel A shows the respective light optical sections of a nucleus from a 2-cell embryo with three chromosome territories 13 (red), including one carrier chromosome territory 13, identified by the *GOF* signal (green) and two non-carrier chromosome territories 13. Light optical sections of the nucleus presented in panel B indicate three non-carrier chromosome territories in addition to the carrier chromosome territory 13 with the *GOF* signal. DAPI stained nuclear DNA is shown in blue or grey. Note that the DAPI images of both day 2 nuclei show large clusters of DAPI stained DNA separated by wide, unstained regions, which we consider as part of the interchromatin compartment.[11] These clusters apparently represent individual chromosome territories as indicated by the correspondence of some clusters with painted chromosome territories 13. In panel A we noted a peripheral location of all chromosome territories surrounding a large central lacuna, called the major interchromatin compartment lacuna, which lacks DAPI stained DNA entirely. Such nuclei were predominantly noted around major embryonic gene activation in both IVF and cloned embryos.[11] The presence of this phenotype in a 2-cell embryo is an unusual observation and may indicate that despite the growth delay of this embryo the nucleus was able to adopt a phenotype typical for 8-cell embryos with an undisturbed growth. **Panel B** shows a nucleus from an 8-cell embryo. Chromosome territories were distributed throughout the interior and separated by wide interchromatin channels, although this nucleus lacked the huge major interchromatin lacuna shown in panel A. In IVF embryos this phenotype was often noted after the onset of major embryonic gene activation. **Panel C.** Projection of light optical sections of a nucleus from a day 4 embryo with four chromosome territories, including two carrier chromosome territories 13, each showing one *GOF* signal, and two non-carrier chromosome territories 13. This nucleus may represent a polyploidization event. DAPI stained DNA was

distributed throughout the nuclear space and chromosome territories were no longer separated by wide interchromatin channels and could only be demarcated as individuals after chromosome painting.

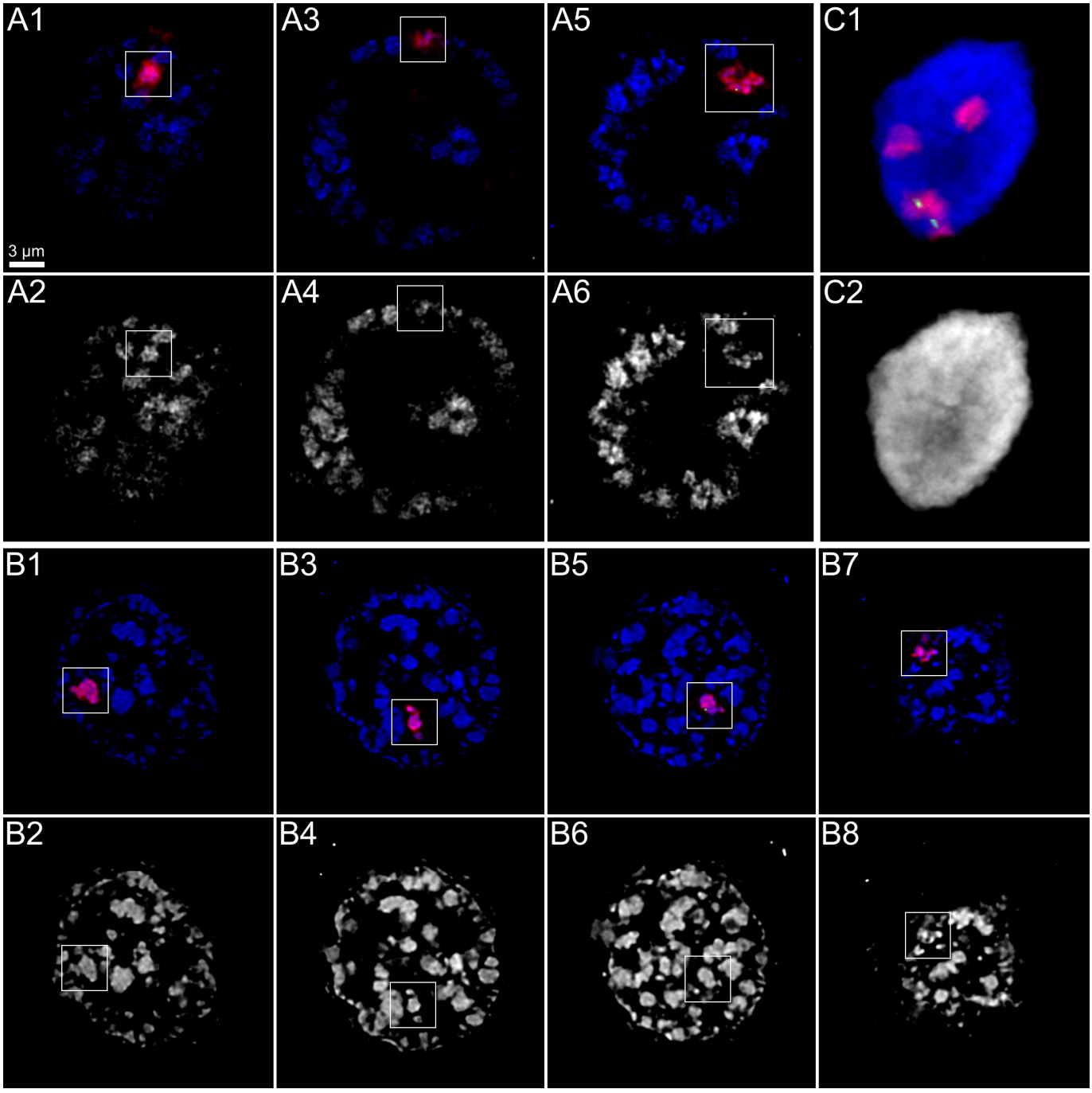

Supplementary Figure 1

2.6. Ultra-Structural Alterations in In Vitro Produced Four-Cell Bovine Embryos Following Controlled Slow Freezing or Vitrification

ANATOMIA HISTOLOGIA EMBRYOLOGIA
JOURNAL OF VETERINARY MEDICINE
Anatomia, Histologia, Embryologia

ORIGINAL ARTICLE

Ultra-Structural Alterations in *In Vitro* Produced Four-Cell Bovine Embryos Following Controlled Slow Freezing or Vitrification

T. Cavusoglu[1,2]*, J. Popken[3], T. Guengoer[4], O. Yilmaz[1,2], Y. Uyanikgil[1,2], U. Ates[5], M. Baka[1,2], E. Oztas[6] and V. Zakhartchenko[4]*

Addresses of authors: [1] Department of Histology and Embryology, Ege University, 35100, Izmir, Turkey;
[2] Cord Blood, Cell-Tissue Application and Research Center, Ege University, 35100, Izmir, Turkey;
[3] Division of Anthropology and Human Genetics, Biocenter, Ludwig-Maximilian-University of Munich, Grosshadernerstrasse 2, 82152, Planegg-Martinsried, Germany;
[4] Department of Molecular Animal Breeding and Biotechnology, Ludwig-Maximilian-University of Munich, Hackerstr. 27, 85764, Oberschleissheim Germany;
[5] Department of Histology and Embryology, Bilim University School of Medicine, 34349, Istanbul, Turkey;
[6] Department of Histology and Embryology, Gulhane Military Medical Academy, 06010, Ankara, Turkey

***Correspondence:**
Tel.: +90 232 3905911;
fax: +90 232 3901649;
e-mail: mdturkercavusoglu@gmail.com (T. Cavusoglu)
Tel.: +49 089 2180 78446;
fax: +49 089 2180 78402;
e-mail: v.zakhartchenko@gen.vetmed.uni-muenchen.de (V. Zakhartchenko)

With 7 figures and 3 tables

Received February 2015; accepted for publication July 2015

doi: 10.1111/ahe.12197

Summary

Cryopreservation is the process of freezing and preserving cells and tissues at low temperatures. Controlled slow freezing and vitrification have successfully been used for cryopreservation of mammalian embryos. We investigated the effect of these two cryopreservation methods on *in vitro* produced four-cell stage bovine embryos which were classified according to their quality and separated into three groups. The first group was maintained as untreated controls ($n = 350$). Embryos of the second ($n = 385$) and the third ($n = 385$) groups were cryopreserved either by controlled slow freezing or by vitrification. Embryos in groups 2 and 3 were thawed after 1 day. Hundred embryos were randomly selected from the control group, and 100 morphologically intact embryos from the second and third group were thawed after 1 day and cultured to observe the development up to the blastocyst stage. The blastocyst development rate was 22% in the control group, 1% in the slow-freezing group and 3% in the vitrification group. Remaining embryos of all three groups were examined by light microscopy, transmission electron microscopy and immunofluorescence confocal microscopy with subsequent histological staining procedures. Cryopreservation caused degenerative changes at the ultra-structural level. Compared with vitrification, slow freezing caused an increased mitochondrial degeneration, cytoplasmic vacuolization, disruption of the nuclear and plasma membrane integrity, organelle disintegration, cytoskeletal damage, a reduced thickness of the zona pellucida and a formation of fractures in the zona pellucida. Further studies are required to understand and decrease the harmful effects of cryopreservation.

Introduction

Cryopreservation is the process of freezing and preserving cells and tissues using cryoprotectants at low temperatures (Fahy, 1986). Successful freezing of sperm by glycerol (Polge et al., 1949) marks the beginning of research on embryo cryopreservation. Embryo cryopreservation was first established on murine embryos by Whittingham in 1972 (Whittingham et al., 1972). Subsequently, embryos of the cow (Wilmut and Rowson, 1973), rabbit (Bank and Maurer, 1974; Whittingham and Adams, 1976), sheep (Willadsen et al., 1976), horse (Yamamoto et al., 1982), human (Trounson and Mohr, 1983), pig (Hayashi et al., 1989) and dog (Suzuki et al., 2009) were successfully cry-

opreserved. This technique was utilized in assisted reproduction to solve reproductive problems. Assisted reproductive techniques used in the livestock industry combine embryo production, embryo cryopreservation and embryo transfer in addition to artificial insemination. Embryo cryopreservation has been widely used in the recent years due to the increase in embryo transfer applications. Controlled slow freezing and vitrification are two different methods used for cryopreservation of mammalian embryos (Naik et al., 2005). Embryos can then be stored after the freezing process at −196°C in liquid nitrogen until thawing. Controlled slow freezing was introduced before vitrification and remains the most common technique used for livestock, domestic animals and human embryos (Vajta and Kuwayama, 2006; Saragusty and Arav, 2011). During slow freezing, embryos are frozen gradually with a programmable freezing device while using cryoprotectants at a lower concentration than in vitrification (Hendriks et al., 2014). Glycerol and ethylene glycol (EG) is the most efficient cryoprotectant for *in vitro* production (IVP) bovine embryos for slow-freezing method (Sommerfeld and Niemann, 1999).

Controlled slow freezing requires equilibration, seeding, gradual cooling and ultimately exposure to liquid nitrogen (Sagırkaya and Bagış, 2003). Rall and Fahy introduced the method of vitrification to cryopreserve mammalian embryos (Rall and Fahy, 1985). During vitrification, embryos are frozen with fast cooling ratios before ice crystallization forms a structure similar to glass (Campos-Chillon et al., 2006). Vitrification solutions contain cryoprotectants at high concentrations with an increased viscosity (Kasai, 1997). Vitrification of *in vitro* produced bovine embryos can be successful with the use of various cryoprotectants such as glycerol and propanediol (Kuwayama et al., 1994), EG, ficoll and sucrose (Tachikawa et al., 1993; Mahmoudzadeh et al., 1995), EG and dimethyl sulphoxide (Ishimori et al., 1993), glycerol and EG (Agca et al., 1994; Donnay et al., 1998). Vitrification has many advantages such as cost-effectiveness (no requirement for expensive devices such as programmable freezer), short application time (instant freezing requires neither ice seeding nor slow cooling) and being easily applicable at all suitable laboratories (Sagırkaya and Bagış, 2003; Kızıl et al., 2007). Controlled slow freezing and vitrification induce different types of defects in bovine embryos (Uysal, 2007). Embryo viability decreases after freezing and thawing processes, because of physical and chemical damage induced by cryopreservation procedure (Park et al., 2006). Intracellular formation of ice crystals occurring during the freezing process can induce damage to the cytoskeleton (Tharasanit et al., 2005) and to nuclear and plasma membranes (Mohr and Trounson, 1981) that may lead to abnormalities of chromosomes and DNA (Magli et al., 1999; Moradi et al., 2013), disruption of mitochondria and the zona pellucida (ZP, Mohr and Trounson, 1981) and accumulation of cellular debris at the perivitelline space (Hyttel et al., 1986). This leads to a degeneration of cells and eventually causes cell death by apoptosis or necrosis (Baguisi et al., 1999). The main challenge of cryopreservation is to maintain a high developmental competence of thawed embryos (Martinez et al., 1998). The freezing process can negatively affect the metabolic activity and vitality of cells (Rieger et al., 1993). During freezing process, freezing-associated embryo viability loss can be influenced by many causes such as freezing protocol, type and concentration of cryoprotectant, embryo production procedure, species of animal and the stage of embryos during cryopreservation (Pereira and Marques, 2008; Bettencourt et al., 2009). The optimal developmental stage and protocol for cryopreservation is still not determined. Similar cryopreservation protocols applied to multiple species may result in different results (Rall, 1992; Hredzák et al., 2005; Pereira and Marques, 2008).

In this study, we aimed to investigate the effects of controlled slow freezing and vitrification on the ultra-structure of *in vitro* produced four-cell bovine embryos. We have chosen this stage of development because it is a transcriptionally quiet period (Baroux et al., 2008) which precedes the most critical stage in pre-implantation development, major embryonic genome activation, which occurs in 8- to 16-cell bovine embryos (Graf et al., 2014) and is characterized by a developmental block (reviewed in Lequarre et al., 2003) and is associated with a structural reorganization of embryonic nuclei (Popken et al., 2014).

Materials and Methods

Chemicals

All chemicals were obtained from Sigma-Aldrich (St. Louis, MO, USA) unless indicated otherwise. Serum in IVP experiments were obtained from oestrus cow, heat-inactivated (56°C, 30 min), pooled, filtered with a 0.22-mm membrane and frozen in 1.5-ml Eppendorf vials (Mucci et al., 2006) until used. The same batch of estrous cow serum (ECS) was used in all experiments.

Experimental design

Immature oocytes were obtained at laboratory conditions by follicle aspiration from ovaries collected from cows slaughtered for meat production. Oocytes were classified according to the classification described (Mucci et al., 2006). Recovered oocytes were matured and fertilized *in vitro* according to the standardized protocol (see

below) and then cultured in synthetic oviduct fluid (SOF), supplemented with ECS, essential amino acids (EAA), non-essential amino acids (N-EAA) and pyruvic acid (PA) in an incubator with 5% CO_2, 5% O_2 and 90% N_2 at 39°C until the four-cell stage. Only four-cell embryos with an excellent or good quality (Bó and Mapletoft, 2013) were used in the study and divided into three groups. The first group was maintained as a control group ($n = 350$). Embryos from the second group ($n = 385$) and the third group ($n = 385$) were cryopreserved either by controlled slow freezing or by vitrification. Frozen embryos were stored in straws in liquid nitrogen and thawed after 1 day. Subsequent culture was performed in SOF medium for 2 h. Afterwards, the morphological integrity of thawed embryos was examined under a stereomicroscope. From all three groups, 100 four-cell embryos were cultured for 4 days to determine blastocyst rates. The other four-cell embryos of groups 2 and 3 whose morphological integrity was preserved and the four-cell embryos of group 1 were examined by light microscopy, transmission electron microscopy (TEM) and confocal microscopy. After this analysis, histological follow-up and staining procedures were performed to further investigate the effects of cryopreservation. This study design is indicated in Table 1.

In vitro production of bovine embryos

The standardized protocol for IVP of bovine embryos was described previously (Boelhauve et al., 2005). Bovine ovaries were collected at a local slaughter house and transported to the laboratory (within 3 h) in phosphate-buffered saline (PBS) solution containing penicillin (50-100 IU/ml) and amphotericin-B (50 ng/ml) at 30°C. Ovaries were washed two times with 0.9% NaCl at 30°C to remove blood debris and dried lightly on sterile filter paper. Cumulus–oocyte complexes (COCs) were recovered by aspiration of 2- to 10-mm follicles using a sterile 21-gauge needle attached to a sterile 10-ml syringe and classified using a stereomicroscope. Only COCs with homogenous cytoplasm that included more than three layers of compact cumulus cells were selected (Mucci et al., 2006) for the experiments and washed twice in oocyte maturation medium [TCM-199 with Earle's salts, supplemented with 5% ECS, 0.025 IU/ml follicle-stimulating hormone (FSH) (Sioux Biochemical Inc. IA, USA) and 0.025 IU/ml luteinizing hormone (LH) (Sioux Biochemical, Inc. IA, USA)]. Groups of 40 COCs were matured *in vitro* for 24 h in 400 μl oocyte maturation medium at 39°C at an atmosphere of 5% CO_2 in humidified air. After *in vitro* maturation (IVM), COCs were washed with IVF-TALP (modified Tyrode's solution supplemented with 6 mg/ml bovine serum albumin (BSA), 0.022 mg/ml PA and 0.01 mg/ml heparin) and transferred to four-well plates that contained 400 μl of IVF-TALP per well. Frozen semen from the same bull was used for all *in vitro* fertilization (IVF) experiments. Motile spermatozoa were selected by swim-up in Sperm-TALP (modified Tyrode's solution supplemented with 6 mg/ml BSA and 0.11 mg/ml PA) at 39°C at an atmosphere of 5% CO_2 in humidified air. Approximately 18 h after the addition of spermatozoa suspension (~1×10^6 spermatozoa/ml), the cumulus cells were removed by gently vortexing for 3 min. Groups of 40 presumptive zygotes were transferred to 400 μl drops of SOF supplemented with 5% (v/v) ECS, 40 μl/ml EAA and 10 μl/ml N-EAA, 0.363 mg/ml PA covered with mineral oil and cultured at 39°C in a humidified atmosphere of 5% CO_2, 5% O_2 and 90% N_2. Embryos were collected for analysis on day 1 (24 h) and day 2 (48 h) after the addition of sperm.

Freezing and thawing

For slow freezing, EG solution (Vigro Ethylene Glycol Freeze Plus with sucrose; Bioniche Animal Health Belleville, Ontario, Canada) was used as the freezing solution. Handling of embryos was performed at room temperature (RT). Slow freezing was performed as described (Voelkel and Hu, 1992) with modifications. Embryos were immersed in the cryopreservation solution for 5 min. Ten embryos were then loaded into the middle 15 portion of each of the 90-mm straws (cryopreservation solution- air bubble- cryopreservation solution with embryos- air bubble- cryopreservation solution). Straws were sealed with plastic plugs (Quicklock), placed vertically in the cooling chamber of a programmable freezer (Consarctic CL-5500) and kept at −6°C for 4 min for manual ice crystal seeding. Embryos were cooled at 0.5°C/min rate until reach-

Table 1. Study groups and experimental design

Study groups	Total number of embryos	Embryos with preserved morphology after thawing	Four-cell embryos cultured to blastocyst	Four-cell embryos used for TEM analysis	Four-cell embryos used for confocal analysis
Control	350	–	100	230	10
Slow freezing	385	362	100	242	10
Vitrification	385	370	100	250	10

ing −35°C and then rapidly immersed in liquid nitrogen. Straws were first left at RT for 10 s, then for 10 s at a 37°C water bath and finally dried lightly on sterile filter paper for thawing. Solutions were enabled to mix well by shaking the straws. Straws were cut and their contents were dispensed into a sterile 35-mm Petri dish. After 10-min duration of subsequent waiting, they were evaluated as equilibrium was reached. Thawed embryos were washed with culture medium at the end of this duration.

Vitrification and warming

All solutions were obtained from the BOVIPRO Vit-Kit™ (Minitüb Abfüll und Labortechnik GmbH& Co. KG Haupstrasse, Tiefenbach, Germany), and embryos were vitrified by the BOVIPRO Embryo Vitrification Kit's protocol. Liquid nitrogen was added to the foam box at a height of about 15 cm. The Goblet-Cane Holder apparatus was hung over the foam box maintaining a distance of 2.5 cm with the liquid nitrogen. Attention was paid to prevent contact of liquid nitrogen with the inner part of the Goblet-Cane Holder apparatus. As the liquid nitrogen level inside the foam box decreased, liquid nitrogen was added to adjust this distance constantly to 2.5 cm. All the media of the vitrification kit [holding medium (HM), equilibration medium-A, equilibration medium-B, vitrification medium (VM), dilution medium (DM)] were warmed up to RT before the vitrification procedure started. The chambers of a 5-chamber Petri dish were numbered and named according to the mediums used in the respective chambers. One millilitre of HM was applied to the first chamber. One millilitre of equilibration medium-A was applied to the second chamber. One millilitre of equilibration medium-B was added to the third chamber. The fourth chamber was left empty. One millilitre of DM was added to the fifth chamber. The level of 0.25 ml straws to which DM was determined to be retracted and to which the air was to be retracted was marked. The embryos that were planned to be frozen by vitrification were removed from the incubator at each application and moved to the PBS in groups of five. The embryos in PBS were washed with PBS in groups of five and were moved to the HM in the first chamber. During this time, 90 μl of DM was retracted on the straw for the addition of embryos until the point marked before. Then, 1.5 cm of air was added until the next marked point. The embryos in the first chamber were moved to the second chamber (inside the equilibration medium-A) for 5 min. Then, they were moved from the second to the third chamber (inside the equilibration medium-B) for 5 min. During these 5 min, a 30 μl drop of VM per embryo was added to the fourth chamber. After these 5 min, the embryos of the third division were transferred to the drops in the fourth division one by one. The embryos of the fourth division inside the drops of VM were transferred in 1 min one by one to the straws pre-filled with DM and air. The straws were supplied with ~1.5 cm air and 90 μl DM while ensuring that embryos stay in between those two layers of DM and air. The straws were sealed by plugs and cooled at the vapour phase by being put inside the Goblet-Cane Holder apparatus for 1-min duration. They were then removed out of the apparatus and stored in the tank of −196°C liquid nitrogen until thawing.

Thawing or warming

Immediately after an initial warming, all straws were held at the sealed end and flicked 3–5 times, dislodging the air pockets to mix the contents. Embryos were allowed to rehydrate via in-straw dilution for up to 1 min before the sealed end of the straw was cut and its contents emptied into a Petri dish. Finally, the embryos were moved into culture medium.

Post-cryopreservation survival rate determination

After thawing or warming, embryos were washed and cultured in SOF supplemented with ECS, EAA, NEAA and PA and covered with mineral oil at 39°C in a humidified atmosphere of 5% CO_2, 5% O_2 and 90% N_2 for 2 h to allow embryo re-expansion. Survival was defined according to the re-expansion and the morphology of embryos. Fresh day 2 embryos and re-expanded embryos produced in each media were used as controls.

Light and electron microscopy

Fresh embryos (n = 230), thawed embryos after controlled slow freezing (n = 242) and thawed embryos after vitrification (n = 250) were scored and then fixed within 2 h after collection or thawing and warming. Embryos were fixed overnight at 4°C in 2% glutaraldehyde in 0.1 M cacodylate buffer (pH 7.2; 480–500 mOsm). Post-fixation was performed for 30 min by osmium tetroxide (OsO_4). OsO_4 plus cacodylate tampon mixture (1:1) was used for the post-fixation procedure in a dark chamber. Embryos were left in a cacodylate tampon for 5 min after post-fixation. They were then dehydrated through a graded series of ethanol (2 × 50%, 70%, 95%, 2 × 100%; 5 min each), followed by alcohol: propylene oxide (1:1, 10 min) and propylene oxide (2 × 10 min) and impregnated with propylene oxide/Epon (2:1, 30 min and 1:2, 30 min). They were then embedded in epoxy resin (without DMP-30, overnight at 4°C, later with DMP-30, 1 day at 37°C, 1 day at 45°C, 1 day at 60°C). Resin blocks were solidified at RT

for 3 days. Serial semi-thin (1 μm) sections were cut with an ultramicrotome (Reichert, Austria) and stained with methylene blue-azure II-basic fuchsin and toluidine blue for examination under the light microscope, ultra-thin sectioning and lipid quantification. Ultra-thin sections (0.5 μm) from selected areas were then picked up on copper grids, counter-stained with uranyl acetate and lead citrate and examined by a Libra 120 Plus Transmission Electron Microscope (Carl Zeiss, Germany) at 120 kV.

Fixation of embryos for immunofluorescence

Fixation, immunostaining, embedding and confocal microscopy were essentially performed as described in Popken et al. (2014). All steps were performed at RT unless noted otherwise. Embryos were briefly washed in 38°C PBS, fixed in 2% paraformaldehyde (PFA) in PBS, washed twice in PBS and then stored at 4°C in PBS until further use.

Immunostaining procedures

Unspecific background was quenched by incubating embryos in 20 mM glycine in PBS for 10 min. After washing twice with PBS, embryos were permeabilized with 0.5% Triton X-100 for 15–30 min. Embryos were stained with phalloidin-tetramethylrhodamine B isothiocyanate (50 mg/ml, P1951; Sigma-Aldrich) for 40 min in PBS. embryos were stained with phalloidin–tetramethylrhodamine B isothiocyanate (50 mg/ml, P1951; Sigma-Aldrich) for 40 min in PBS. After washing twice with PBS, unspecific background signals were reduced by incubation in PBS with 2% BSA for 2 h. Embryos were incubated with monoclonal mouse anti-a-tubulin overnight at 4°C (1:2000, clone B-5-1-2; Sigma-Aldrich) diluted in PBS with 2% BSA. After washing 5× in PBS with 2% BSA, the secondary antibody goat anti-mouse IgG (H&L) fluorescein conjugated (1:100, AP124F; Chemicon, Life Technologies, Vector Laboratories: Temecula, CA, USA) diluted in PBS with 2% BSA, was applied for 1 h, again followed by 5× washing in PBS with 2% BSA and 5× without. Fixation of antibodies was performed with 4% PFA in PBS for 10 min, followed by washing twice in PBS and twice in PBS with 0.05% Tween-20 (PBST). Chromatin was counterstained with DAPI (Life Technologies, Carlsbad, CA, USA D1306; 4′,6-diamidino-2-phenylindole) and 2.5 μg/ml diluted in PBST for 10 min, followed by washing twice in PBS.

Embedding for three-dimensional confocal laser scanning microscopy (3D-CLSM)

Embryos were attached to cover glasses and equilibrated with the anti-fade Vectashield (Vector Laboratories). 3D-CLSM of whole embryos was performed with a Leica TCS SP5 and an objective with a low aperture and a long working distance (20×/0.7 NA) using oil immersion. Fluorochromes were excited with blue diode, argon and helium–neon lasers using laser lines at 405, 488 and 594 nm, respectively.

Statistical analysis

The control of normal distribution at each group in the ZP thickness (variable) was performed by the Shapiro–Wilk test. Nonparametric tests were used to compare the groups because variable (ZP thickness) was not distributed normally. First, a significant difference is found with the Kruskal–Wallis test between the three groups, and then, the Bonferroni correction was used for comparing the pairs of group (pairwise) with the Mann–Whitney *U*-test.

Results

Oocyte aspiration and IVM

On average, 6.47 oocytes per ovary were recovered by follicle aspiration from 374 ovaries. In total, 2423 oocytes were obtained. A total of 2140 oocytes containing three or more cumulus cell layers were selected for the IVM procedure. The resulting 1840 mature oocytes (maturation ratio: 85.98%) were divided into three groups: control, slow freezing and vitrification (Table 2).

In vitro culture

From 1840 mature oocytes, 1193 four-cell embryos were obtained after *in vitro* fertilization and culture (Table 3). Twenty-two blastocysts were obtained from 100 embryos

Table 2. Ovaries and oocytes used, with maturation and oocyte ratio per ovary

Groups	Ovaries used	Immature oocytes	Oocytes per ovary	Number of oocytes with three or more cumulus cell layers	Matured oocytes	Maturation ratio (%)
Control	118	766	6.49	671	572	85.24
Slow freezing	130	840	6.46	749	650	86.78
Vitrification	126	817	6.48	720	618	85.83
Total	374	2423	6.47	2140	1840	85.98

Table 3. Development of matured and fertilized oocytes to the four-cell stage

Study Groups	Matured oocytes used for fertilization	Four-cell stage embryos	Cleavage rates
Control	572	368	64.33
Slow freezing	650	420	64.61
Vitrification	618	405	64.53
Total	1840	1193	64.49

of group 1 which were cultured for blastocyst development. A total of 362 embryos with full morphological integrity were determined after thawing of 385 embryos which were frozen by the slow-freezing method (group 2). In this group, one blastocyst was obtained from 100 thawed embryos. A total of 370 embryos with full morphological integrity were determined after the thawing of 385 embryos frozen by vitrification (group 3). In this group, 3 blastocysts developed from 100 thawed embryos.

Morphology of untreated oocytes, untreated embryos and thawed embryos

Oocytes collected by follicle aspiration were surrounded by various amounts of cumulus cell layers and had a sandy ooplasm texture. Some oocytes were devoid of any cumulus cell layers. Matured oocytes were surrounded by expanded cumulus cell layers. Oocytes with an acceptable quality were round and colourless. They had a slightly granular cytoplasm with a sandy texture and were surrounded by an uninterrupted ZP containing an unfragmented first polar body inside the narrow perivitelline space (Fig. 1).

At the four-cell stage, high-quality embryos not exposed to any cryopreservation treatment were expected to be comprised of four blastomeres of an approximately equal size. The margins of the blastomeres were expected to be free of fragmentation. The ZP was usually intact and a large subzonal space was observed (Fig. 2a). When embryos were exposed to the cryopreservation solutions,

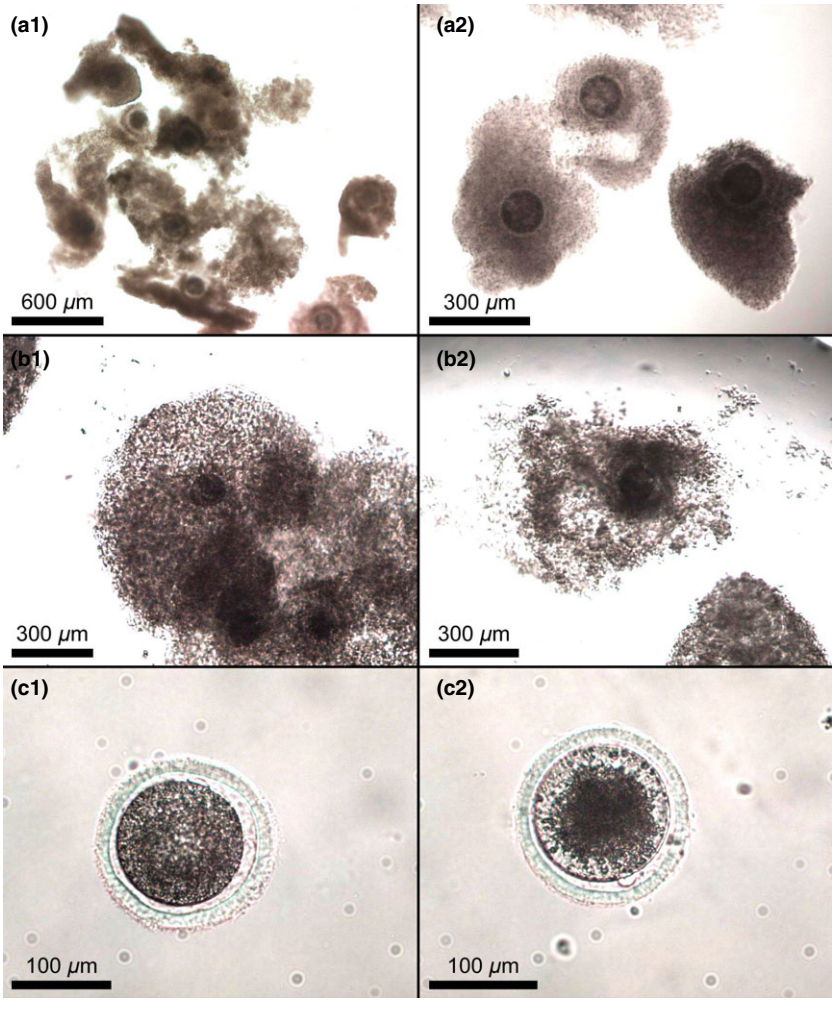

Fig. 1. Bovine oocytes. (a) Immature oocytes recovered from ovaries surrounded by cumulus cells. (b) Matured oocytes after IVM surrounded by cumulus cells. (c) Matured oocytes after the removal of cumulus cell layers.

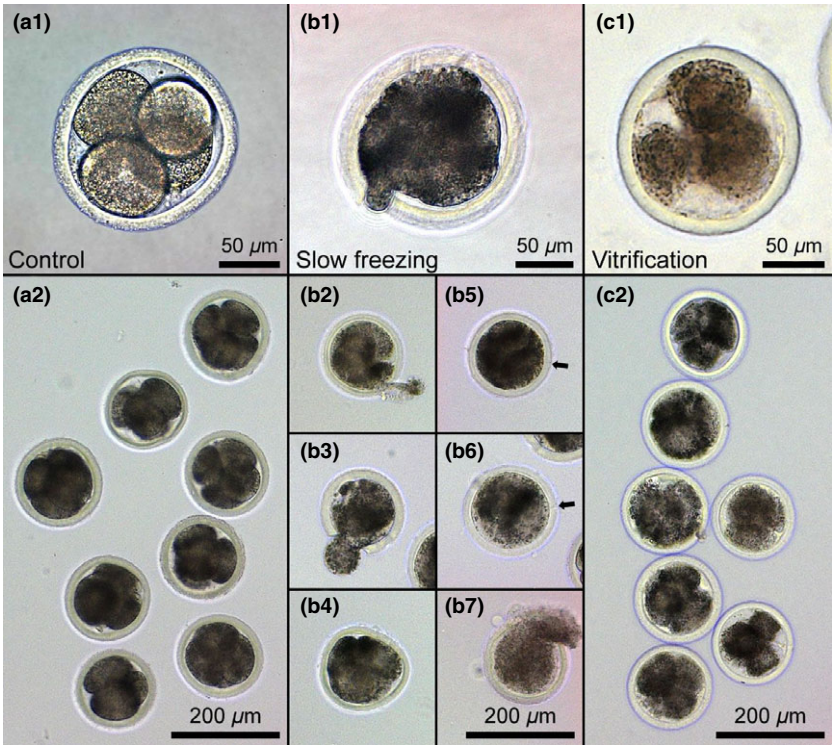

Fig. 2. Four-cell embryos. (a) Untreated control group. (b) Thawed after slow freezing. (c) Thawed after vitrification.

their blastomeres were shrinking to the point that a space between them and the ZP was visible and they were losing their round appearance. The gap between individual blastomeres and the ZP disappeared after thawing or warming (Fig. 2b,c), and some blastomeres were degenerated. ZP damages were observed in some embryos of both group 2 and group 3. However, these damages occurred more often in the slow-freezing group (Fig. 2b).

Cytoskeleton analysis

Embryos of the control group consisted of equally sized, unfragmented blastomeres and were surrounded by an intact ZP. DAPI-stained nuclei were not centrally localized inside the blastomeres. The generally diffuse actin signals were more concentrated at blastomere membranes facing adjacent blastomeres and around the nucleus. Tubulins were widely dispersed throughout the cytoplasm, and higher concentrations were noted at regions close to blastomere membranes facing the ZP.

Embryos of the slow-freezing group showed fragmented and/or degenerated blastomeres with a compromised membrane integrity, surrounded by a smooth ZP with a narrower subzonal space. The inter-cellular area between blastomeres was enlarged compared with the control and vitrification groups. Degenerated blastomere particles were positive both for actin and for tubulin. DAPI-stained nuclei were not centrally localized inside the blastomeres. Actin filaments were generally diffuse throughout the cytoplasm but were occasionally dense. Actins were more concentrated under the blastomere membrane adjacent to inter-cellular areas between blastomeres. Actin condensation around the nucleus in the control group was reduced in this group. Tubulins generally diffuse throughout the cytoplasm were more concentrated at the periphery of blastomeres adjacent to the ZP. Occasional disruptions of tubulins were observed in fragmented and degenerated blastomeres.

Degeneration of embryos of the vitrification group varied greatly. Some blastomeres displayed disintegrated blastomere membranes while other blastomeres were morphologically normal. All blastomeres were surrounded by a ZP with a smooth margin and displayed narrower subzonal spaces compared with the control group. Degenerated blastomere particles were positive for actin and tubulin. DAPI-stained nuclei were not centrally localized inside the blastomeres. Actins generally diffusely distributed throughout the cytoplasm were concentrated at the periphery of blastomeres adjacent to the inter-cellular space. Actins were absent at the periphery of blastomeres in the vicinity of the ZP. Tubulins were generally diffuse throughout the cytoplasm. The tubulin density at adjacent blastomere regions close to the ZP which are visible at control and slow-freezing groups was not observed with this group (Fig. 3).

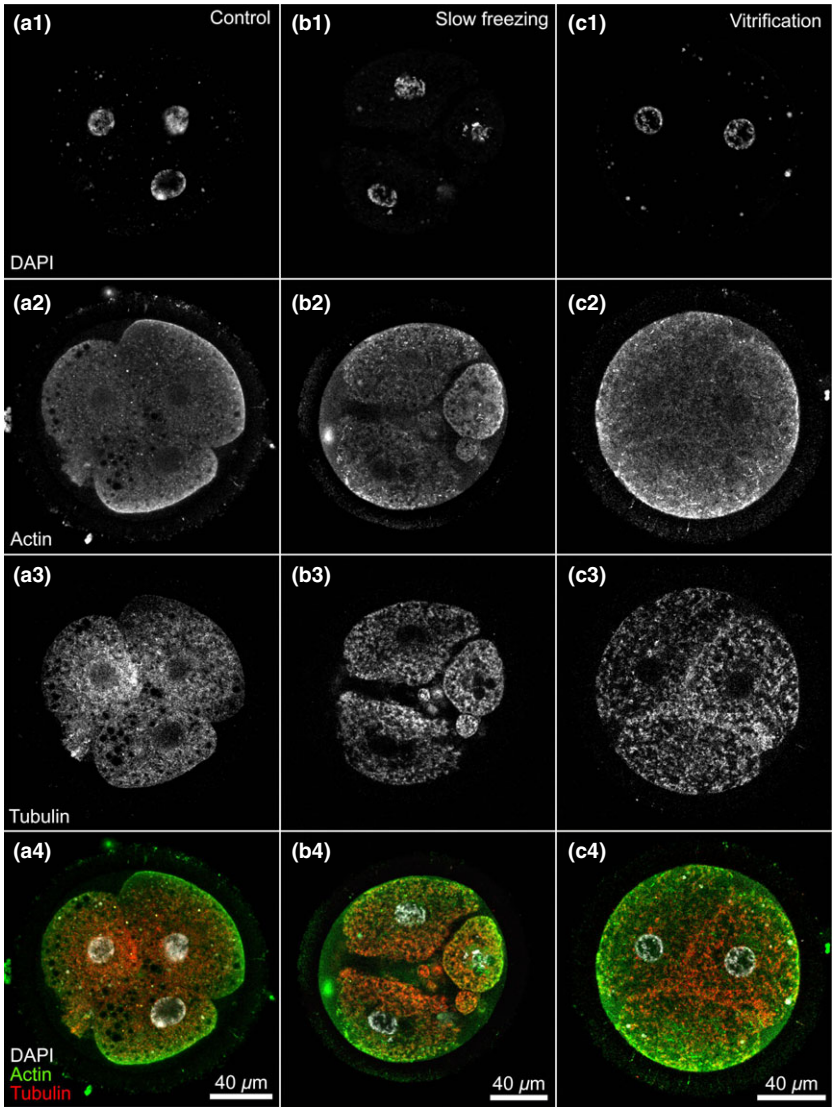

Fig. 3. Cytoskeleton of 4-cell embryos. (a) Untreated control group. (b) Thawed after slow freezing. (c) Thawed after vitrification. a1–c1. DAPI. a2–c2. Actin. a3–c3. Tubulin. a4–c4. Composite of DAPI (grey), actin (green) and tubulin (red).

Evaluation of methylene blue-azure II-basic fuchsin and toluidine blue stainings

Semi-thin epon slices (1 μm) of all three study groups stained by methylene blue-azure II-basic fuchsin (Fig. 4) and toluidine blue (Fig. 5) were examined using light microscopy. Control group embryos showed equal-sized, unfragmented blastomeres with clear margins. Large subzonal spaces were observed only between blastomeres but not between the ZP and individual blastomeres. The borders of blastomeres in contact to the ZP were undamaged. Nuclear borders were smooth and round. Lipid drops with different sizes were dispersed throughout the cytoplasm. Embryos of the slow-freezing and vitrification group showed mostly irregular blastomere margins while some maintained a smooth appearance. Some blastomeres showed fragmentations and/or degenerations. ZPs of the slow-freezing group were thicker when compared with the vitrification group. This finding was confirmed via measurements performed on TEM scans. The subzonal spaces between blastomeres in the slow-freezing group were found to be narrower when compared with the vitrification group. Both groups showed vacuolizations within the cytoplasms and cellular debris between blastomeres in subzonal spaces. However, the slow-freezing group displayed more of such debris. Nuclei maintained their round shapes and smooth nuclear borders. Numerous lipid drops at various sizes dispersed throughout the cytoplasm were observed (Figs 4 and 5).

Ultra-structural changes

Figure 6a shows TEM scans of blastomeres of the control group. The nucleus featured the double-membrane struc-

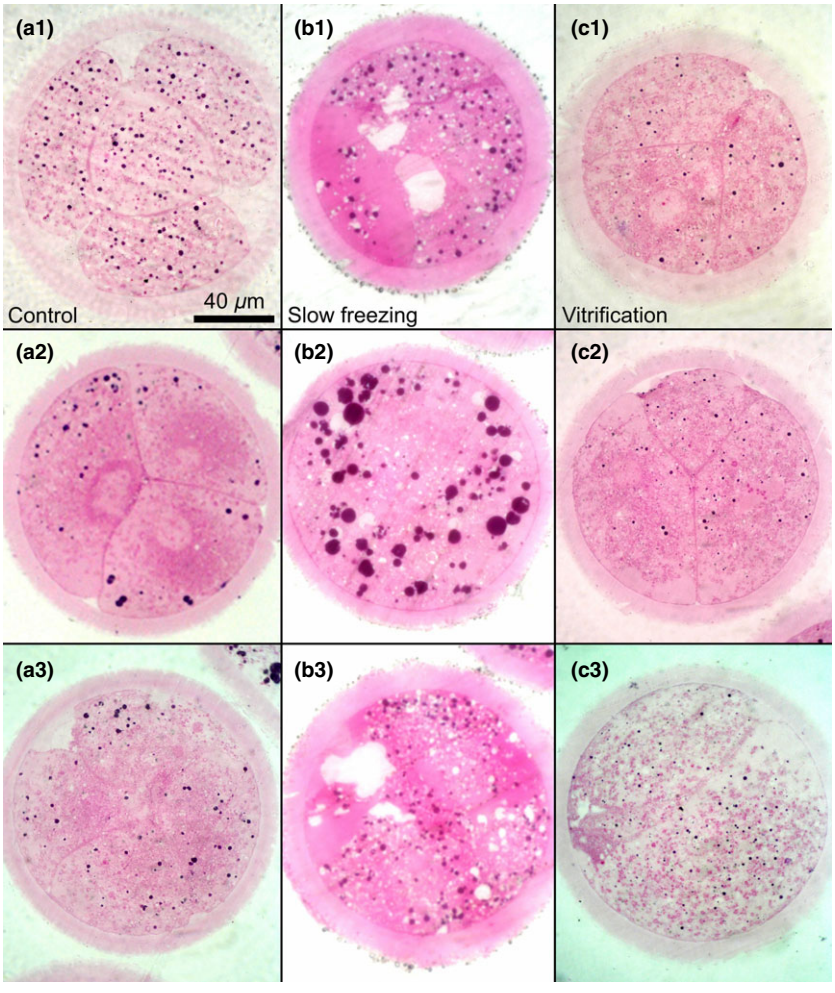

Fig. 4. Four-cell embryos stained by methylene blue-azure II-basic fuchsin. (a) Untreated control group. (b) Thawed after slow freezing. (c) Thawed after vitrification.

ture of the nuclear membrane. Mature mitochondrial structures and numerous immature developing mitochondria were observed at the perinuclear area. Pouch-shaped RER (Rough Endoplasmic Reticulum) cisternas were mostly in their developing state and were surrounded by the endoplasmic reticulum. Ribosomes were located at the cytoplasmic side of its membrane. The semi-transparent, vesicular, smooth endoplasmic reticulum was accompanying mitochondria during development. In these rapidly developing cells, annulate lamellae are connected with the nuclear membrane. These could be enriched with tightly packed nuclear pore complexes (NPC) and could emanate from flattened clusters of membrane cisternas. Big, electron-dense, round, primary lysosomes were observed inside the cytoplasm, and smaller secondary lysosomes were observed. Conjugation complexes were absent among blastomeres. Short, obtuse microvilli structures were interlocked with each other at the inter-cellular space. Electron-dense vesicular debris resided at the inter-cellular space. Small, coated vesicles for endocytosis and exocytosis were noted close to the blastomere membrane. Microtubule structures with round, smooth walls and long, thin appearance with a higher density at organelles at their transverse sections were noticed in vicinity of the blastomere membrane. Cross-sections of dot-like microfilaments form the skeleton of microvilli and provide endurance to the blastomere membrane. They were fractured under the blastomere membrane at longitudinal sections. The subzonal space contained cytoplasmic particles and debris with various shapes and sizes between the blastomere membrane and the ZP. The smooth surface of the ZP and its homogenous nature surrounded the embryo. It is observed that the average thickness of the ZP is thicker than that in the vitrification and slow-freezing groups.

The nuclear membrane of slow-freezing group nuclei was irregularly shaped (Fig. 6b). When compared with the control group, numerous degenerated mitochondria showed an electron-dense matrix at the periphery and had a degenerated cristae and matrix at the centre. Trans-

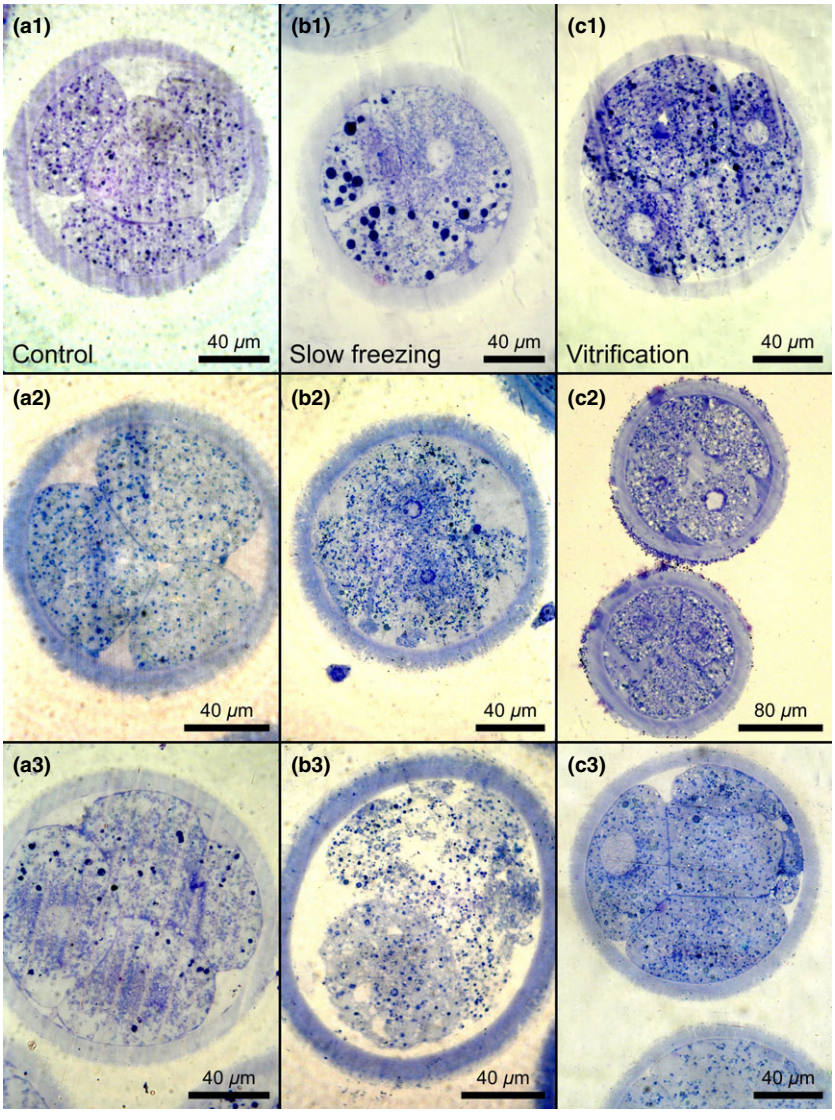

Fig. 5. Four-cell embryos stained by toluidine blue. (a) Untreated control group. (b) Thawed after slow freezing. (c) Thawed after vitrification.

parent, dilated cisternae of the endoplasmic reticulum, as well as annulate lamellae and lipid drops, were observed accompanying the electron-dense lysosomes, vesicles and mitochondria within the cytoplasm. The subzonal space was reduced in volume. Compared with the control group, a presence of cellular debris inside the subzonal space was noted. The ZP was thinner when compared with the control group but thicker when compared with the vitrification group. Microfilaments were observed to get denser at locations closer to the blastomere membrane and dispersed within the cytoplasm. Microfilaments decreased in general when compared with the control and vitrification groups. Microtubules around the organelles at control group were shown to be decreasing in density but were in higher abundance at cell membranes in the vicinity of the ZP.

Embryos of the vitrification group were also analysed by TEM (Fig. 6c). Non-centrally localized nuclei had an ovoid shape. Inner and outer membranes were clearly defined. The nuclear membrane was largely folded. Bleps containing nucleoplasma were formed by a dilated outer membrane. Next to mature mitochondria dispersed throughout the cytoplasm, irregular, non-ovoid-shaped degenerated mitochondria were observed. They showed a partially disrupted cristae, matrix, inner and outer membranes. Big, irregular and round-shaped, electron-dense secondary lysosomes; smaller primary lysosomes; dilated annulate lamellae; SERs (Smooth endoplasmic reticulum) accompanying vesicular, degenerated mitochondria; and lipid drops that were either big or small were observed as being randomly localized throughout the cytoplasm. The subzonal space between the blastomere membrane and the ZP contained cytoplasmic

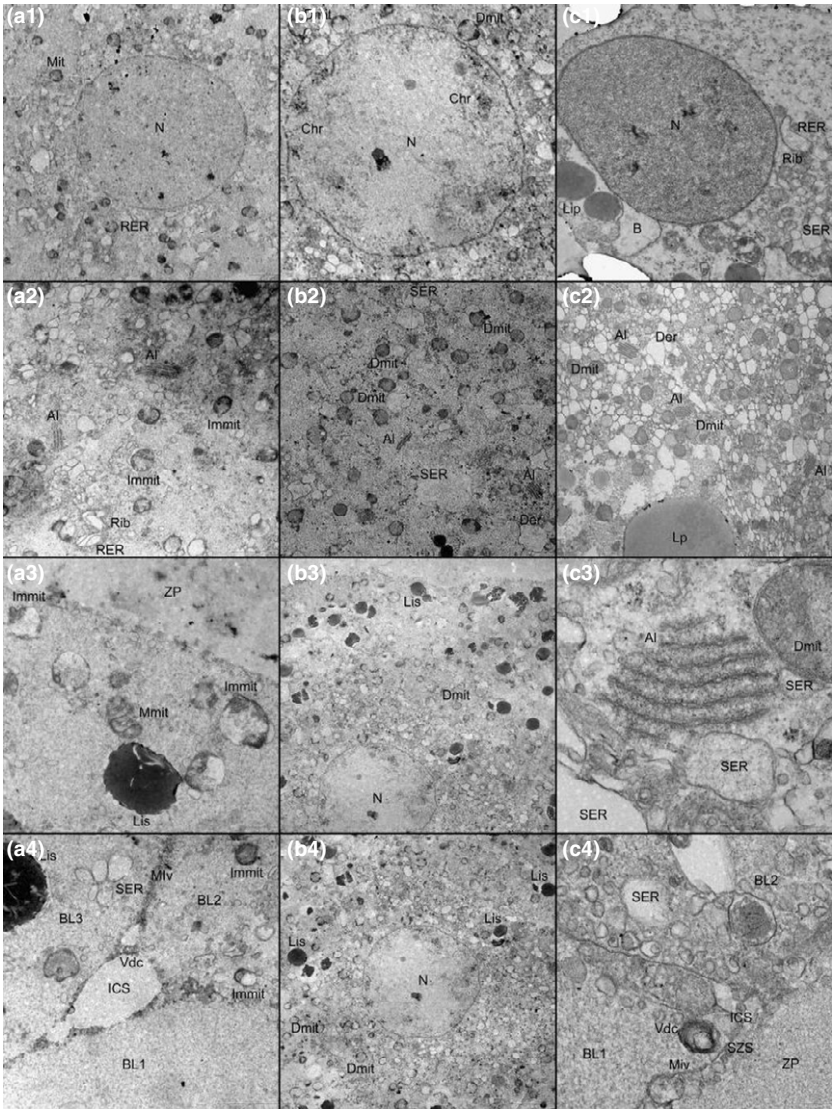

Fig. 6. Four-cell embryo TEM scans. (a) Untreated control group. (b) Thawed after slow freezing. (c) Thawed after vitrification. N, nucleus; Chr, chromatin; SER, smooth endoplasmic reticulum; RER, rough endoplasmic reticulum; Rib, ribosome; Lis, lysosome; AL, annulate lamellae; B, Blep; Mmit, mature mitochondria; Immit, immature mitochondria; Dmit, degenerated mitochondria; Vdc, vesicular debris body; Lip, lipid drop; BL, blastomere; SZS, subzonal space; ICS, intercellular space; Miv, microvillus; ZP, zona pellucida.

particles. The distribution of microvilli at the blastomere membrane and their microfilaments were shown to be relatively decreased when compare with the control group. Microtubules inside the blastomeres were found to be distributed throughout the cytoplasm. Blastomeres were decreased in density at their periphery. The thickness of the ZP of four-cell bovine embryos was significantly reduced in the slow-freezing group ($n = 15$) compared with the control group ($n = 15$; $P < 0.001$). This thickness was even more reduced in the vitrification group ($n = 15$) compared with the control group ($P < 0.001$) and the slow-freezing group ($P < 0.004$).

Statistical results

The comparison of the effect of cryopreservation at four-cell bovine embryo between the groups was performed. The results are as follows: Kruskal–Wallis test: $P < 0.001$; when control and slow freezing were compared, $P < 0.001$; when control and vitrification were compared, $P < 0.001$; and when slow freezing and vitrification were compared, $P = 0.004$ (Fig. 7).

Discussion

Previous studies reported that cryopreservation has negative effects on embryonic development. However, the effects of cryopreservation may differ between species and may vary depending on the quality of embryos, the developmental stage during freezing, the cryoprotectants used, the cryopreservation method applied and whether the embryos are generated *in vivo* or *in vitro* (Vincent and Johnson, 1992; Weber et al., 1992; Palasz and Mapletoft, 1996; Desai et al., 2007). In our study, it was first and

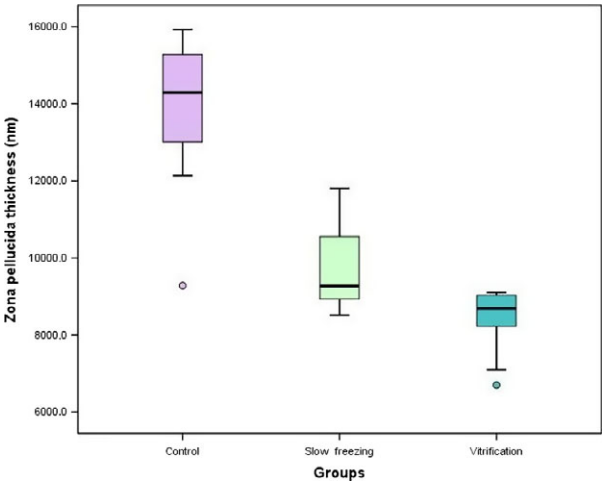

Fig. 7. The thickness of the zona pellucida statistical comparison between the experimental and control groups.

foremost intended to obtain the quality of embryos under *in vitro* conditions in order to analyse the effects of cryopreservation, and thus, care was taken to ensure that the study was carried out at a certain standard. To attain this standard, ovaries of healthy cows of the same species and age range were included in the study and frozen spermatozoa of the bulls of the same species which are checked and sold commercially were used in the fertilization process. The processes of ovary preparation, oocyte aspiration, IVM and IVF, culture, cryopreservation and thawing were undertaken by the same researcher, and same techniques were used during each application. One of the key factors in obtaining quality embryos under *in vitro* conditions is oocyte maturation. The fact that the media used for the IVM of oocytes affect the IVF and the subsequent embryonic development rates was demonstrated in various studies (Bavister et al., 1992; Goto and Iritani, 1992; Zuelke and Brackett, 1993). In the maturation of bovine oocytes, two types of media are used. Defined media contain basic physiological salts with bicarbonate buffering systems. Complex media contain the contents of defined media with the addition of materials such as amino acids, purine and vitamins. The most commonly used complex maturation medium is TCM-199 (Akyol, 2006). Greve and Madison indicated that after using TCM-199 medium supplemented with 10% fetal calf serum (FCS) in oocyte maturation, the maturation rate was 80% (Greve and Madison, 1991). MacCallum et al. (1997) used TCM-199 medium without any supplements in oocyte maturation and reported that the maturation rate was 39% following an 18-h incubation. Leibfried-Rutledge et al. (1989) indicated that the maturation rate rose to 90% after the addition of various hormones such as LH, FSH and oestrogen to TCM-199. Greve et al. (1993), on the other hand, stated that they used the medium TCM-199 supplemented with 20% oestrus cow serum (OCS) in their study and that the rate of oocyte maturation was 83%. In our study, oocytes were selected in line with the method described by Brackett and Zuelke (1993). After follicle aspiration from ovaries, the oocytes were maturated by being incubated for 24 h in TCM-199 medium supplemented with 5 μl/ml FSH, 5 μl/ml LH and 50 μl/ml OCS. Maturation of oocytes was confirmed if cumulus cells were expanded and if the perivitelline space contained polar bodies. Our oocyte maturation rate of 86% was higher than the results obtained by Greve and Avery who used the TCM-199 medium supplemented with 20% OCS. The fact that we obtained a higher oocyte maturation rate although the medium we used contained less OCS showed that the LH and the FSH added to the medium had positive effects on oocyte maturation as stated by Leibfried-Rutledge et al. (1989). Our results were also better than the results of Greve and Madison (1991) who used TCM-199 supplemented with 10% FCS as maturation medium, indicating that OCS was more effective than FCS in *in vitro* oocyte maturation. While these serum supplementations support the IVM process of oocytes, they have both negative and positive effects on bovine embryonic development decreasing early-stage embryo development (Bavister, 1995) by inhibiting the initial cleavage divisions (Pinyopummintr and Bavister, 1991) but stimulating blastocyst development (Van Langendonckt et al., 1997). The addition of a serum to the culture medium to obtain *in vitro* embryos may result in metabolic and morphological deviations during later development (Gardner, 1994; Thompson et al., 1995). Abe et al. (1999) reported that while high survival rates were maintained by standard cryopreservation methods in *in vivo* produced bovine embryos, survival rates for *in vitro* developed embryos were found to be low and that those embryos were more sensitive to cryopreservation. Hasler et al. (1995) demonstrated that media containing serum used for *in vitro* embryos caused the formation of intense lipid droplets of all sizes in embryos and that those lipid droplets increased the sensitivity to cryopreservation. While the role of intracellular lipids is not fully understood, some researchers claimed that the intracellular lipids either in embryos or in oocytes were being used as an energy source for the developing oocytes and embryos and that they were necessary for cell division as a lipid source (Pugh et al., 1998; Sturmey et al., 2009). Studies involving pigs showed that porcine embryos, which include dispersed intracellular lipids in high concentrations in their blastomeres, have increased sensitivity to cryopreservation and that intracellular lipids may induce heterogenous intracellular ice nucleation or lipid phase changes (Toner et al., 1986; Kashiwazaki et al.,

1991). Romek et al. (2009) indicated that the intracellular lipid content was dependent on the embryo development stage and showed a dramatic decrease following the morula stage. They also expressed that accordingly, early development stages became more sensitive to low temperatures in comparison with advanced stages. In another study, it was indicated that the tolerance to cold and cryopreservation of bovine embryos obtained under *in vitro* conditions after being cultured in a serum-added medium can be increased after the cytoplasmic lipid droplets are centrifuged and isolated, which indicated that cytoplasmic lipid droplets may directly influence the sensitivity of embryos to cold and cryopreservation (Ushijima et al., 1999). In our study, both during TEM analyses and during light microscopy analyses of semi-thin Epon sections following toluidine blue and methylene blue-azure II-basic fuchsin staining, lipid droplets of all sizes were found in embryo blastomeres. Twenty-two embryos reached the blastocyst stage in the control group, one in the slow-freezing group and three in the vitrification group. A light microscopy analysis of the embryos that did not reach the blastocyst stage revealed that some embryos were degenerated, some were still at the four-cell stage and demonstrated no development, and some failed to reach the stage of blastocyst despite reaching further stages. These results may indicate that the intracellular lipid droplets formed in *in vitro* produced embryos using serum-containing media increased the sensitivity to cryopreservation. Embryos at early developmental stages may have been more sensitive to freezing. These results are consistent with the reports by Abe H. et al., Hasler JF. et al. and Romek M. et al. Cryopreservation may have extremely destructive effects on the cellular organization of embryos. The formation of ice crystallization may pierce plasma membranes. The cellular plasma membrane is very sensitive to cooling and often shows damages following cryopreservation (Zeron et al., 2002). Cryopreservation damages are able to induce cell deaths and may be associated with cryoprotectant toxicity, cold shock, osmotic stress, freeze damage and ice crystallization (Quinn, 1985; Saragusty et al., 2009). During freezing process, cryoprotectants protect cells from the damage caused by cold shock and ice crystallization formation. On the other hand, they have their own chemical toxicity or osmotic effect which may also cause damage on cells (Dobrinsky, 1996). Such effects of cryoprotectants may cause damages in the cytoskeleton structure of embryos (Dobrinsky et al., 2000). If the cytoskeleton is damaged or destabilized, the embryo may lose this intracellular communication path and an irreparable destruction may take place. The growth, maturation and fertilization of the oocyte require proper localization and active movement of cellular organelles which is realized by the reorganization of tubule and actin structures (Sun and Schatten, 2006). It was reported that due to cryopreservation, the intracellular functions of cells may be deteriorated, their organelles may be denatured, plasma membranes may be pierced, and the central cellular structure of the embryo may be damaged (Dobrinsky, 1996).

While some researchers reported that cryoprotectants prevent the irreparable damages to the cytoskeleton components via depolymerization of cellular microstructures such as microfilaments and microtubules prior to cryopreservation (Overstrom et al., 1993; Dobrinsky, 1996), the others argued that certain cryoprotectants used in cryopreservation such as glycerol and EG may be toxic via inducing the irreversible deterioration of microstructures inside the cell (Weber et al., 1992; Dobrinsky, 1996). It was reported that cryoprotectants do not always have the same effect, and variations could be seen in the interaction of cellular organelles and embryos with the cytoskeleton with respect to different species and different embryonic development stages (Parks and Ruffing, 1992; Vincent and Johnson, 1992). It was expressed that the irreversible damages in porcine embryos at morula and early blastocyst stages are associated with freezing at -196°C and not with being subjected to the cryoprotectants used (Dobrinsky, 1996). In another study carried out using equine embryos, it was reported that in the cryopreservation of embryos at blastocyst stage, deformation at cytoskeleton and significant cell deaths were observed after thawing where glycerol was used. It was expressed that the damage in actin structures encountered in embryos was due to freezing and thawing rather than glycerol toxicity (Tharasanit et al., 2005). In the TEM and confocal microscopy analyses carried out during our study, structures of the cytoskeleton components actin and tubulin were compromised in embryos of the slow-freezing and vitrification groups due to the effects of cryopreservation. This deterioration in actin and tubulin structures may have led to a disruption of metabolic functions, which may have resulted in the cell death observed in embryos.

Degeneration of blastomere structures and fractures in the ZP may be linked with cold damage and freezing–thawing procedures rather than the toxic effects of cryoprotectants. In cryopreservation studies with oocytes, premature cortical granule exocytosis and a hardened ZP occurred as a result of freezing–thawing (Carroll et al., 1990; Mavrides and Morroll, 2005). Cryopreservation also hardened the ZP of embryos (Schiewe et al., 1995). In our study, the average thickness of the ZP was decreased in embryos of the 'slow-freezing' group and was even more decreased in the 'vitrification' group. The thinning of the ZP may have

resulted either from the dehydration during cryopreservation or from freezing in very low temperatures. Fair et al. (2001) indicated that after cryopreservation of bovine embryos, ultrastructural changes could be seen, such as debris in expanded subzonal space and the microvilli disintegration and the dispersion deterioration, swelling in RER and mitochondria and erasure in mitochondrial cristae, thinner ZP compared to in vivo embryos, degenerated nuclei and apoptotic bodies and cell losses. after cryopreservation of bovine embryos, ultrastructural changes could be seen, such as debris in expanded subzonal space and the microvilli disintegration and the dispersion deterioration, swelling in RER and mitochondria and erasure in mitochondrial cristae, thinner ZP compared to *in vivo* embryos, degenerated nuclei and apoptotic bodies and cell losses. From the observation of apoptotic body formation and nuclear degeneration in cells, Fair et al. (2001) linked these cell death findings observed in embryos to apoptosis. However, in our study these apoptosis symptoms were not encountered following the cryopreservation of four-cell bovine embryos. The emergence of apoptosis in bovine, mouse and human embryos and the initial embryonic genome activity corresponds to the same period in the 9- to 16-cell stage (Brison, 2000). The earliest findings of bovine apoptosis were observed around eight-cell stage by using TUNEL and/or nuclear morphology (Neuber et al., 2002; Gjørret et al., 2005, 2007).

Ultra-structural alterations including cytoplasmic vacuolization, mitochondrial degeneration, disintegration of plasma membrane and cellular organelles observed in *in vitro* four-cell bovine embryos cryopreserved by controlled slow freezing or vitrification indicate that these procedures have harmful effects on embryonic viability and need further improvements.

Acknowledgements

This project was supported by an Ege University Grant (2011-Tıp-064), Ege University Local Animal Ethics Committee (Decision Number: 2009/25).

Conflict of Interest

None.

References

Abe, H., T. Otoi, S. Tachikawa, S. Yamashita, T. Satoh, and H. Hoshi, 1999: Fine structure of bovine morulae and blastocysts *in vivo* and *in vitro*. Anat. Embryol. **199**, 519–527.

Agca, Y., R. Monson, D. Northey, O. A. Mazni, and J. Rutledge, 1994: Post-thaw survival and pregnancy rates of *in vitro* produced bovine embryos after vitrification. Theriogenology **41**, 154.

Akyol, N., 2006: Sığırlarda *in vitro* oosit maturasyonu (*In vitro* maturation of bovine oocytes). Lalahan Hay. Araşt. Enst. Derg. (Lalahan Livestock Research Institute) **46**, 59–69.

Baguisi, A., P. Lonergan, E. Overstrom, and M. Boland, 1999: Vitrification of bovine embryos: incidence of necrosis and apoptosis. Theriogenology **51**, 162.

Bank, H., and R. R. Maurer, 1974: Survival of frozen rabbit embryos. Exp. Cell Res. **89**, 188–196.

Baroux, C., D. Autran, C. S. Gillmor, D. Grimanelli, and U. Grossniklaus, 2008: The maternal to zygotic transition in animals and plants. Cold Spring Harb. Symp. Quant. Biol. **73**, 89–100.

Bavister, B. D., 1995: Culture of preimplantation embryos: facts and artifacts. Hum. Reprod. Update **1**, 91–148.

Bavister, B. D., T. A. Rose-Hellekant, and T. Pinyopummintr, 1992: Development of *in vitro* matured/*in vitro* fertilized bovine embryos into morulae and blastocysts in defined culture media. Theriogenology **37**, 127–146.

Bettencourt, E., C. Bettencourt, J. Silva, P. Ferreira, C. De Matos, E. Oliveira, R. J. Romão, A. Rocha, and M. Sousa, 2009: Ultrastructural characterization of fresh and cryopreserved *in vivo* produced ovine embryos. Theriogenology **71**, 947–958.

Bó, G., and R. Mapletoft, 2013: Evaluation and classification of bovine embryos. Anim. Reprod. **10**, 344–348.

Boelhauve, M., F. Sinowatz, E. Wolf, and F. F. Paula-Lopes, 2005: Maturation of bovine oocytes in the presence of leptin improves development and reduces apoptosis of *in vitro*-produced blastocysts. Biol. Reprod. **73**, 737–744.

Brackett, B. G., and K. A. Zuelke, 1993: Analysis of factors involved in the *in vitro* production of bovine embryos. Theriogenology **39**, 43–64.

Brison, D. R., 2000: Apoptosis in mammalian preimplantation embryos: regulation by survival factors. Hum. Fertil. (Camb) **3**, 36–47.

Campos-Chillon, L. F., D. J. Wlaker, J. De La Torre-Sanchez, and G. E. Jr Seidel, 2006: *In vitro* assessment of a direct transfer vitrification procedure for bovine embryos. Theriogenology **65**, 1200–1214.

Carroll, J., H. Depypere, and C. D. Matthews, 1990: Freeze-thaw-induced changes of the zona pellucida explains decreased rates of fertilization in frozen-thawed mouse oocytes. J. Reprod. Fertil. **90**, 547–553.

Desai, N., H. Blackmon, J. Szeptycki, and J. Goldfarb, 2007: Cryoloop vitrification of human day 3 cleavage-stage embryos: post-vitrification development, pregnancy outcomes and live births. Reprod. Biomed. Online **14**, 208–213.

Dobrinsky, J., 1996: Cellular approach to cryopreservation of embryos. Theriogenology **45**, 17–26.

Dobrinsky, J. R., V. G. Pursel, C. R. Long, and L. A. Johnson, 2000: Birth of piglets after transfer of embryos cryopreserved

by cytoskeletal stabilization and vitrification. Biol. Reprod. **62**, 564–570.

Donnay, I., P. Auquier, S. Kaidi, C. Carolan, P. Lonergan, P. Mermillod, and A. Massip, 1998: Vitrification of *in vitro* produced bovine blastocysts: methodological studies and developmental capacity. Anim. Reprod. Sci **52**, 93–104.

Fahy, G. M., 1986: The relevance of cryoprotectant "toxicity" to cryobiology. Cryobiology **23**, 1–13.

Fair, T., P. Lonergan, A. Dinnyes, D. C. Cottell, P. Hyttel, F. A. Ward, and M. P. Boland, 2001: Ultrastructure of bovine blastocysts following cryopreservation: effect of method of blastocyst production. Mol. Reprod. Dev. **58**, 186–195.

Gardner, D. K., 1994: Mammalian embryo culture in the absence of serum or somatic cell support. Cell Biol. Int. **18**, 1163–1179.

Gjørret, J. O., J. Wengle, P. Maddox-Hyttel, and W. A. King, 2005: Chronological appearance of apoptosis in bovine embryos reconstructed by somatic cell nuclear transfer from quiescent granulosa cells. Reprod. Domest. Anim. **40**, 210–216.

Gjørret, J. O., D. Fabian, B. Avery, and P. Maddox-Hyttel, 2007: Active caspase-3 and ultrastructural evidence of apoptosis in spontaneous and induced cell death in bovine *in vitro* produced pre-implantation embryos. Mol. Reprod. Dev. **74**, 961–971.

Goto, K., and A. Iritani, 1992: Oocyte maturation and fertilization. Anim. Reprod. Sci **28**, 407–413.

Graf, A., S. Krebs, M. Heininen-Brown, V. Zakhartchenko, H. Blum, and E. Wolf, 2014: Genome activation in bovine embryos: review of the literature and new insights from RNA sequencing experiments. Anim. Reprod. Sci. **149**(1–2), 46–58.

Greve, T., and V. Madison, 1991: *In vitro* fertilization in cattle: a review. Reprod. Nutr. Dev. **31**, 147–157.

Greve, T., B. Avery, and H. Callesen, 1993: Viability of *in vivo* and *in vitro* produced bovine embryos. Reprod. Domest. Anim. **28**, 164–169.

Hasler, J., W. Henderson, P. Hurtgen, Z. Jin, A. McCauley, S. Mower, B. Neerly, L. Shuey, J. Stokes, and S. Trimmer, 1995: Production, freezing and transfer of bovine IVF embryos and subsequent calving results. Theriogenology **43**, 141–152.

Hayashi, S., K. Kobayashi, J. Mizuno, K. Saitoh, and S. Hirano, 1989: Birth of piglets from frozen embryos. Vet. Rec. **125**, 43–44.

Hendriks, W. K., B. A. J. Roelen, B. Colenbrander, and T. A. E. Stout, 2014: Cellular damage suffered by equine embryos after exposure to cryoprotectants or cryopreservation by slow-freezing or vitrification. Equine Vet. J.. DOI: 10.1111/evj.12341. [Epub ahead of print] PMID: 25187202.

Hredzák, R., A. Ostró, I. Maracek, J. Kacmárik, V. Zdilová, and J. Veselá, 2005: Influence of slow-rate freezing and vitrification on mouse embryos. Acta Vet. Brno **74**, 23–27.

Hyttel, P., H. Lehn-Jensen, and T. Greve, 1986: Ultrastructure of bovine embryos frozen and thawed by a two-step freezing method. Acta Anat. **125**, 27–31.

Ishimori, H., K. Saeki, M. Inai, Y. Nagao, J. Itasaka, Y. Miki, N. Seike, and H. Kainuma, 1993: Vitrification of bovine embryos in a mixture of ethylene glycol and dimethyl sulfoxide. Theriogenology **40**, 427–433.

Kasai, M., 1997: Cryopreservation of mammalian embryos. Mol. Biotechnol. **7**, 173–179.

Kashiwazaki, N., S. Ohtani, K. Miyamoto, and S. Ogawa, 1991: Production of normal piglets from hatched blastocysts frozen at -196 degrees C. Vet. Rec. **128**, 256–257.

Kızıl, S. H., N. Akyol, T. Karasahin, and M. Satılmıs, 2007: 7 günlük in-vitro sığır embriyolarının vitrifikasyonla dondurulması (The vitrification of *in vitro* fertilized bovine embryos after 7 days cultured). Lalahan Hay. Araşt. Enst. Derg. (Lalahan Livestock Research Institute) **47**, 1–5.

Kuwayama, M., S. Fujikawa, and T. Nagai, 1994: Ultrastructure of IVM-IVF bovine blastocysts vitrified after equilibration in glycerol 1, 2-propanediol using 2-step and 16-step procedures. Cryobiology **31**, 415–422.

Leibfried-Rutledge, M., E. Critser, J. Parrish, and N. First, 1989: *In vitro* maturation and fertilization of bovine oocytes. Theriogenology **31**, 61–74.

Lequarre, A. S., J. Marchandise, B. Moreau, A. Massip, and I. Donnay, 2003: Cell cycle duration at the time of maternal zygotic transition for in vitro produced bovine embryos: effect of oxygen tension and transcription inhibition. Biol. Reprod. **69**(5), 1707–1713.

MacCallum, C., D. Salamone, and A. T. Palasz, 1997: Effect of maturation medium supplements on bovine oocyte fertilization and embryo development. Theriogenology **47**, 193.

Magli, M. C., L. Gianaroli, D. Fortini, A. P. Ferraretti, and S. MunneÂ, 1999: Impact of blastomere biopsy and cryopreservation techniques on human embryo viability. Hum. Reprod. **14**, 770–773.

Mahmoudzadeh, A., A. Van Soom, P. Bols, M. Ysebaert, and A. de Kruif, 1995: Optimization of a simple vitrification procedure for bovine embryos produced *in vitro*: effect of developmental stage, two-step addition of cryoprotectant and sucrose dilution on embryonic survival. J. Reprod. Fertil. **103**, 33–39.

Martinez, A., D. De Matos, C. Furnus, and G. Brogliatti, 1998: *In vitro* evaluation and pregnancy rates after vitrification of *in vitro* produced bovine embryos. Theriogenology **50**, 757–767.

Mavrides, A., and D. Morroll, 2005: Bypassing the effect of zona pellucida changes on embryo formation following cryopreservation of bovine oocytes. Eur. J. Obstet. Gynecol. Reprod. Biol. **118**, 66–70.

Mohr, Lr, and A. Trounson, 1981: Structural changes associated with freezing of bovine embryos. Biol. Reprod. **25**, 1009–1025.

Moradi, S. Z., A. M. Meybodi, H. Gourabi, H. Mozdarani, and Z. Mansouri, 2013: Chromosome abnormalities and viability of vitrified eight-cell mouse embryos at presence of two different cryoprotectants at different storage durations. Cell J. (Yakhteh) **14**, 254–263.

Mucci, N., J. Aller, G. G. Kaiser, F. Hozbor, J. Cabodevila, and R. H. Alberio, 2006: Effect of estrous cow serum during bovine embryo culture on blastocyst development and cryotolerance after slow freezing or vitrification. Theriogenology **65**, 1551–1562.

Naik, B., B. Rao, R. Vagdevi, M. Gnanprakash, D. Amarnath, and V. H. Rao, 2005: Conventional slow freezing, vitrification and open pulled straw (OPS) vitrification of rabbit embryos. Anim. Reprod. Sci **86**, 329–338.

Neuber, E., C. Luetjens, A. Chan, and G. Schatten, 2002: Analysis of DNA fragmentation of *in vitro* cultured bovine blastocysts using TUNEL. Theriogenology **57**, 2193–2202.

Overstrom, E., R. Duby, J. Dobrinsky, J. Robl, A. Baguisi, P. Lonergan, P. Duffy, J. H. Walsh, J. F. Roche, and M. P. Boland, 1993: Cytoskeletal damage in vitrified or frozen bovine embryos. Theriogenology **39**, 276.

Palasz, A. T., and R. J. Mapletoft, 1996: Cryopreservation of mammalian embryos and oocytes: recent advances. Biotechnol. Adv. **14**, 127–149.

Park, S. Y., E. Y. Kim, X. S. Cui, J. C. Tae, W. D. Lee, N. H. Kim, S. P. Park, and J. H. Lim, 2006: Increase in DNA fragmentation and apoptosis-related gene expression in frozen-thawed bovine blastocysts. Zygote **14**, 125–131.

Parks, J. E., and N. A. Ruffing, 1992: Factors affecting low temperature survival of mammalian oocytes. Theriogenology **37**, 59–73.

Pereira, R. M., and C. C. Marques, 2008: Animal oocyte and embryo cryopreservation. Cell Tissue Bank. **9**, 267–277.

Pinyopummintr, T., and B. D. Bavister, 1991: *In vitro*-matured/*in vitro*-fertilized bovine oocytes can develop into morulae/blastocysts in chemically defined, protein-free culture media. Biol. Reprod. **45**, 736–742.

Polge, C., A. Smith, and A. Parkes, 1949: Revival of spermatozoa after vitrification and dehydration at low temperatures. Nature **164**, 666.

Popken, J., A. Brero, D. Koehler, V. J. Schmid, A. Strauss, A. Wuensch, T. Guengoer, A. Graf, S. Krebs, H. Blum, V. Zakhartchenko, E. Wolf, and T. Cremer, 2014: Reprogramming of fibroblast nuclei in cloned bovine embryos involves major structural remodeling with both striking similarities and differences to nuclear phenotypes of *in vitro* fertilized embryos. Nucleus **5**, 555–589.

Pugh, P., A. Ankersmit, L. McGowan, and H. Tervit, 1998: Cryopreservation of *in vitro*-produced bovine embryos: effects of protein type and concentration during freezing or of liposomes during culture on post-thaw survival. Theriogenology **50**, 495–506.

Quinn, P. J., 1985: A lipid-phase separation model of low-temperature damage to biological membranes. Cryobiology **22**, 128–146.

Rall, W. F., 1992: Cryopreservation of oocytes and embryos: methods and applications. Anim. Reprod. Sci. **28**, 237–245.

Rall, W. F., and G. M. Fahy, 1985: Ice-free cryopreservation of mouse embryos at −196 °C by vitrification. Nature **313**, 573–575.

Rieger, D., J. Pollard, and S. Leibo, 1993: The effect of cryopreservation on the metabolic activity of *in vitro* produced cattle blastocyst. Cryobiology **30**, 631.

Romek, M., B. Gajda, E. Krzysztofowicz, and Z. Smorag, 2009: Lipid content of non-cultured and cultured pig embryo. Reprod. Domest. Anim. **44**, 24–32.

Sagırkaya, H., and H. Bagış, 2003: Cryopreservation of mammalian embryos. Uludag Univ. J. Fac. Vet. Med. **22**, 127–135.

Saragusty, J., and A. Arav, 2011: Current progress in oocyte and embryo cryopreservation by slow freezing and vitrification. Reproduction **141**, 1–19.

Saragusty, J., H. Gacitua, I. Rozenboim, and A. Arav, 2009: Do physical forces contribute to cryodamage? Biotechnol. Bioeng. **104**, 719–728.

Schiewe, M., N. Hazeleger, C. Sclimenti, and J. Balmaceda, 1995: Physiological characterization of blastocyst hatching mechanisms by use of a mouse antihatching model. Fertil. Steril. **63**, 288–294.

Sommerfeld, V., and H. Niemann, 1999: Cryopreservation of bovine in vitro produced embryos using ethylene glycol in controlled freezing or vitrification. Cryobiology. **38**, 95–105.

Sturmey, R., A. Reis, H. Leese, and T. McEvoy, 2009: Role of fatty acids in energy provision during oocyte maturation and early embryo development. Reprod. Domest. Anim. **44**, 50–58.

Sun, Q. Y., and H. Schatten, 2006: Regulation of dynamic events by microfilaments during oocyte maturation and fertilization. Reproduction **131**, 193–205.

Suzuki, H., T. Asano, Y. Suwa, and Y. Abe, 2009: Successful delivery of pups from cryopreserved canine embryos. Biol. Reprod. **81**, 84, 363–368.

Tachikawa, S., T. Otoi, S. Kondo, T. Machida, and M. Kasai, 1993: Successful vitrification of bovine blastocysts, derived by *in vitro* maturation and fertilization. Mol. Reprod. Dev. **34**, 266–271.

Tharasanit, T., B. Colenbrander, and T. A. E. Stout, 2005: Effect of cryopreservation on the cellular integrity of equine embryos. Reproduction **129**, 789–798.

Thompson, J. G., D. K. Gardner, P. A. Pugh, W. H. McMillan, and H. R. Tervit, 1995: Lamb birth weight is affected by culture system utilized during *in vitro* pre-elongation development of ovine embryos. Biol. Reprod. **53**, 1385–1391.

Toner, M., E. Cravalho, K. Ebert, and E. Overström, 1986: Cryobiophysical properties of porcine embryos. Biol. Reprod. **34**, 98.

Trounson, A., and L. Mohr, 1983: Human pregnancy following cryopreservation, thawing and transfer of an eight-cell embryo. Nature **305**, 707–709.

Ushijima, H., H. Yamakawa, and H. Nagashima, 1999: Cryopreservation of bovine pre-morula-stage *in vitro* matured/*in vitro* fertilized embryos after delipidation and before use in nucleus transfer. Biol. Reprod. **60**, 534–539.

Uysal, O., 2007: Sığır embriyolarının vitrifikasyonu (Vitrification of bovine embryos). Vet. Hekim. Der. Derg. **78**, 45–50.

Vajta, G., and M. Kuwayama, 2006: Improving cryopreservation systems. Theriogenology **65**, 236–244.

Van Langendonckt, A., I. Donnay, N. Schuurbiers, P. Auquier, C. Carolan, A. Massip, and F. Dessy, 1997: Effects of supplementation with fetal calf serum on development of bovine embryos in synthetic oviduct fluid medium. J. Reprod. Fertil. **109**, 87–93.

Vincent, C., and M. H. Johnson, 1992: Cooling, cryoprotectants, and the cytoskeleton of the mammalian oocyte. Oxf. Rev. Reprod. Biol. **14**, 73–100.

Voelkel, S., and Y. Hu, 1992: Use of ethylene glycol as a cryoprotectant for bovine embryos allowing direct transfer of frozen-thawed embryos to recipient females. Theriogenology **37**, 687–697.

Weber, P. K., L. K. McGinni, and C. R. Youngs, 1992: An evaluation of potential vitrification solutions for cryopreservation of porcine embryos. Theriogenology **37**, 321.

Whittingham, D. G., and C. E. Adams, 1976: Low temperature preservation of rabbit embryos. J. Reprod. Fertil. **47**, 269–274.

Whittingham, D. G., S. P. Leibo, and P. Mazur, 1972: Survival of mouse embryos frozen to -196 degrees and -269 degrees C. Science **178**, 411–414.

Willadsen, S. M., C. Polge, L. E. Rowson, and R. M. Moor, 1976: Deep freezing of sheep embryos. J. Reprod. Fertil. **46**, 151–154.

Wilmut, I., and L. E. Rowson, 1973: Experiments on the low-temperature preservation of cow embryos. Vet. Rec. **92**, 686–690.

Yamamoto, Y., N. Oguri, Y. Tsutsumi, and Y. Hachinohe, 1982: Experiments in the freezing and storage of equine embryos. J. Reprod. Fertil. Suppl. **32**, 399–403.

Zeron, Y., M. Tomczak, J. Crowe, and A. Arav, 2002: The effect of liposomes on thermotropic membrane phase transitions of bovine spermatozoa and oocytes: implications for reducing chilling sensitivity. Cryobiology **45**, 143–152.

Zuelke, K. A., and B. G. Brackett, 1993: Increased glutamine metabolism in bovine cumulus cell-enclosed and denuded oocytes after *in vitro* maturation with luteinizing hormone. Biol. Reprod. **48**, 815–820.

3. Discussion

3.1. Changes of nuclear landscapes during preimplantation development

The study “Reprogramming of fibroblast nuclei in cloned bovine embryos involves major structural remodeling with both striking similarities and differences to nuclear phenotypes of *in vitro* fertilized embryos” shows that before and shortly after the onset of major EGA at the 8-cell stage (Graf et al., 2014) major chromatin bodies (MCBs), representing individual chromosome territories, were typically located at the nuclear periphery surrounding a large major IC lacuna (MICL) located in the nuclear interior. For nuclei with this phenotype we introduced the term ENP (Embryonic Nucleus with Peripheral CT distribution). In ENPs major chromatin bodies were often separated by wide interchromatin compartment (IC) channels connected with the major lacuna, whereas smaller channels often pervaded throughout their interior. Except for occasional MCBs extending into the MICL, it lacked DNA detectable by DAPI staining. Since DAPI has a preference for AT-rich DNA (Kapuscinski, 1995), we could not exclude the presence of chromatin loops with GC-rich DNA expanding throughout the MICL. Lack of DNA in the MICL of ENPs was confirmed using the DNA sequence independent DNA counterstain TO-PRO-3 (Bink et al., 2001). Additionally, the restriction of EdU incorporation to DAPI positive areas confirmed the lack of chromatin within the major lacuna. After major EGA the major lacuna became smaller until Embryonic Nuclei displayed a Conventional nuclear architecture (ENC) featuring a 3D chromatin network with a co-aligned IC network distributed throughout the nuclear interior. In ENCs chromatin-free spaces under the nuclear lamina between major chromatin bodies were replaced by a ubiquitously present chromatin lining. Similarly, nucleolar precursor bodies or early nucleoli not lined by chromatin before major EGA displayed a concentrated chromatin lining after major EGA.

Evidence for strong RNA synthesis in nucleoli after the 8-cell stage and a significant increase in the expression of genes coding for ribosomal proteins at the 8-cell stage suggests full nucleolar functionality after major EGA (Pederson, 2011).

A significant decrease of nuclear volumes takes place during early bovine development. In addition, a significant volume difference was noted between the larger nuclei of trophectoderm cells and the smaller nuclei of the inner cell mass. Although differences in gene expression were found between the two cell lineages (Ozawa et al., 2012), the central question, whether causal relationships exist between differences of gene expression patterns and structural differences of nuclei provides a challenge for future studies. Detailed knowledge of the dynamics of nuclear organization during development and differentiation is indispensable to overcome this challenge and requires biophysical in addition to molecular biological approaches (Hampoelz and Lecuit, 2011; Martins et al., 2012).

The structural transformation, which was observed in fertilized embryos, when pre-ENPs at the 2-cell stage were transformed into typical ENPs at the 8-cell stage clearly precedes EGA, whereas it remains to be seen whether structural changes during the differentiation of ENPs into ENCs precedes or follows functional changes triggered by MGA or whether structural reorganization is an event, which may occur even in the absence of functional reprogramming or *vice versa*.

In our study “Stage-dependent remodeling of the nuclear envelope and lamina during rabbit early embryonic development” the occurrence of a chromatin-free central lacuna was observed in rabbit embryos at the early 2-cell stage, but not around major EGA at 8- to 16-cell stage. This further substantiates the hypothesis, that the formation of a central lacuna is not initialized at major EGA. The phenomenon of nuclear volume decline throughout preimplantation development also occurred in rabbit embryos.

3.2. Massive global changes of nuclear architecture in cloned embryos correspond with changes observed in fertilized bovine embryos

Most strikingly, the results of this study and the study “Positional changes of a pluripotency marker gene during structural reorganization of fibroblast nuclei in cloned early bovine embryos“ demonstrate that global changes of nuclear architecture observed during pluripotency gene activation (PGA) of cloned bovine embryos closely resemble changes discovered in embryos with corresponding sizes generated by *in vitro* fertilization (IVF) (Popken et al., 2014a; Popken et al., 2014b). The occurrence of a major lacuna at the 8-cell stage of cloned bovine embryos confirms that the major lacuna is not an artifact of the *in vitro* fertilization process and again raises the question, how structural and functional changes are related with each other (Cao et al., 2013; Kosak and Groudine, 2004). Normal preimplantation development is frequently prohibited already in fertilized embryos as a consequence of chromosomal missegregations taking place during the first cleavage stages (Huang et al., 2009). Such events are even more frequent in cloned embryos (Popken et al., 2014b). It will be of particular interest to correlate changes of transcriptomes with changes of nuclear architecture in fertilized and cloned preimplantation embryos with a normal chromosome complement. It will also be of interest to study embryos, whose growth is delayed or blocked for genetic or environmental reasons and explore, whether certain changes of nuclear architecture and gene expression patterns occur in a strictly coordinated manner or independently from each other. Like cloned embryos, fertilized embryos presented nuclei with the ENP phenotype at the onset of major embryonic genome activation (EGA) and most ENPs were transformed into ENCs during the transition from the 8- to the 16-cell stage and adopted the typical phenotype of somatic cell nuclei characterized by an

enrichment of dense chromatin beneath the nuclear lamina and around nucleoli (Bolzer et al., 2005). As in fertilized embryos, the structural transformation of ENPs into ENCs was accompanied by a major reduction of nuclear size. ENCs maintained the roundish shape of ENPs and did not convert back to the flat-ellipsoidal shape of fibroblast nuclei. However, this shape of fibroblasts may have been caused by their adherence to a surface rather than their cell type and may have already converted to spherical nuclei after disassociation from the surface of culture wells.

The reason(s) for the massive and apparently identical changes of global nuclear architecture in fertilized and cloned, early bovine embryos are not obvious. Since ENPs were already observed in embryos, which had not yet reached the 8-cell stage, where major EGA occurs, we assume that the formation of ENPs reflects the preparation of nuclei for the critical period, where development is shifted from maternal gene products to embryonic ones. During this process maternal RNAs are used to provide ENPs with a rich amount of proteins functionally required for this maternal-to-embryonic transition (MET) (Graf et al., 2014). Storage of a massive amount of proteins to meet the embryo’s needs before the onset of major EGA may enforce the large volume of ENPs, including the formation of the major lacuna and wide IC channels separating individual CTs from each other as preferential storage sites. During the first cell cycles after major EGA coding maternal RNAs disappear. The onset of EGA, which occurs at the 8-cell stage of fertilized and cloned bovine embryos, guarantees the embryo's further supply both with household proteins, as well as proteins for the special needs of further normal development. Our study of early development of bovine embryos generated by *in vitro* fertilization (IVF) showed splicing factors distributed throughout the major lacuna of ENPs (Popken et al., 2014a). Possibly, the synthesis and storage of numerous factors based on coding maternal RNAs is essential for the preparation of nuclei for EGA and enforces the

formation of the major lacuna and wide IC channels separating individual CTs from each other. The subsequent global structural transformation of ENPs into ENCs after the onset of EGA may be necessary to ensure the long-term replicative potential of embryonic cells after EGA. The latter prediction is supported by evidence that nuclei with a persistent ENP phenotype are prone to apoptosis (Leidenfrost, 2009) and rarely seen in blastocysts (Leidenfrost et al., 2011; Popken et al., 2014a).

Rabbit preimplantation embryos do not feature the initiation of a major lacuna at the 4-cell stage. Instead, large volume invaginations in direct contact with nucleoli were most abundant at the 4-cell stage. These large volume invaginations were rarely observed in the bovine species. It is possible, that the two species solve the hypothetical problem of an increased import necessity for nucleogenesis prior to major EGA in two different ways. In bovine embryos, nucleoli precursor bodies (NPBs) or early nucleoli at the 4-cell and 8-cell stage were located mostly either at the nuclear border or at the edge of the central lacuna. In rabbit 4-cell stages, nucleoli were mostly located at the nuclear border or in the proximity to invaginations carrying a large volume of cytoplasm. If the cytoplasm and the central lacuna contained factors important for NPBs or early nucleoli then they were located close to those factors in both species either by the solution of a lacuna or invaginations.

3.3. Evidence for profound variability of higher order CT arrangements in ENPs and ENCs

In a previous study on CT movements in bovine IVF embryos, at major EGA the gene-dense CT 19 moved towards the center of the nucleus whereas the gene-poor CT 20 was unaffected (Koehler et al., 2009). In our study, compared with fibroblast nuclei from BFF cultures 3D mean radial distances of *GOF* to the nuclear border increased in cloned pre-PGA embryos but decreased again in post-PGA embryos.

This movement back towards the periphery while still being activated argues against a general movement of this activated gene towards the center of the nucleus. Throughout this process co-localization of *GOF* with its carrier CT 13 was maintained and a difference between radial nuclear movements of carrier and non-carrier CTs was not detected. These findings indicate that *GOF* did not have an effect on the position of its carrier-CT and that *GOF* was not moved by a giant loop. Possible functional implications of average radial *GOF* and CT arrangements remain unclear at this point and must be considered in the light of an impressive inter-nuclear variability for absolute and radial nuclear positions of *GOF*, carrier and non-carrier CTs.

Our study underlines the necessity of single cell analyses in addition to molecular, high-throughput analyses of the higher order chromatin organization performed with cell populations (Bickmore and van Steensel, 2013; de Graaf and van Steensel, 2013; de Wit et al., 2013; Dixon et al., 2012; Gibcus and Dekker, 2013). Recently, strong efforts have been made to establish a Hi-C protocol fit for use at the single cell level (Nagano et al., 2013). These major advancements, however, will not render microscopic analyses superfluous, which have also taken a dramatic turn during the last decade by the emergence of super-resolution fluorescence microscope in combination with further advancements of electron microscopy (Rouquette et al., 2010). Correlative microscopy has provided opportunities to employ different microscopic techniques in a sequential manner following individual cells from the live to the fixed state with ever increasing resolution (Huebner et al., 2013). Current progress has greatly enriched the toolbox necessary to merge molecular approaches with microscopy in a way undreamed of even a few years ago.

3.4. Structural similarities between ENPs carried by replicative competent embryonic cells and nuclei from senescent fibroblasts

The observed coincidence of rather compact CTs and MGA in 8-cell embryos (Graf et al., 2014) was an unexpected finding. Surprisingly, replicative viable ENPs share major structural similarities with nuclei observed in fibroblast cultures at the end of their replicative life span (Chandra et al., 2012; Funayama et al., 2006) as well as in fibroblast cultures driven prematurely into a senescence-like state as a result of drug exposure (Illner et al., 2010). Nuclei in these terminal cultures also form major chromatin bodies (mCBs), called senescence associated heterochromatic foci (SAHFs). In line with mCBs in embryonic cell nuclei SAHFs co-localize for the most part with individual painted CTs separated from each other by broad interchromatin channels, although chromatin connections between SAHFs and mCBs apparently exist.

Lack of DNA in the IC channel system expanding between chromatin clusters was supported by electron microscopic studies based on the selective visualization of DNA both with an osmium ammine staining procedure and immunodetection with primary anti-DNA antibodies and secondary gold-labeled antibodies (Huebner et al., 2013; Illner et al., 2010). Like the formation of ENPs in cloned embryos, the formation of SAHFs or drug induced SAHF-like structures requires a major structural reorganization of CTs. (Chandra et al., 2012) described a concentric chromatin architecture of SAHFs with H3K9me3 accumulated in the core region, surrounded by a layer of chromatin with H3K27me3, and an additional layer enriched in H3K36me3, a marker for transcriptionally active chromatin. (Illner et al., 2010) reported mCB/SAHF like structures with nascent RNA produced at their surface. Gene-poor chromatin was located in the interior of these structures together with H3K9me3 and H3K27me3, whereas gene-dense chromatin was enriched at their periphery together

with H4K8ac. Some CTs studied in typical ENPs presented a compact core with H3K9me3, surrounded by H3K4me3-labeled, peripheral chromatin, others were highly enriched in H3K4me3 distributed throughout the entire territory and still others revealed little H3K4me3 and H3K9me3 immunopositive labeling. Further studies are required to determine possible similarities and differences between mCBs noted in senescent fibroblast nuclei and in replication competent embryonic cell nuclei.

3.5. ENPs/ENCs fit to a model of nuclear architecture based on co-aligned, three-dimensional networks of inactive and active nuclear compartments

CTs are built up from about 500 kb to 1 Mb large chromatin domains (~1-Mbp CDs), which were originally identified as replication foci during S-phase (Nakamura et al., 1986), but later identified as basic structures of higher chromatin organization present at all stages of interphase (Walter et al., 2003). Multiple, interconnected CDs form larger chromatin domain clusters (CDCs). Multiple CDCs contribute to the formation of chromosome band domains, which in turn form chromosome arm domains up to individual CTs. The network character of higher order chromatin organization complicates a distinction of defined subsets of this organization. For this reason the discovery of individual replication foci had to await the development of pulse-labeling of DNA, whereas the unequivocal identification of individual CTs in somatic cell nuclei and ENCs became only possible after the development of chromosome painting protocols. ENPs represent a rare case of nuclear architecture, where individual CTs are widely separated and thus can be distinguished as major chromatin bodies (MCBs).

Direct evidence for the formation of nascent RNA in the PR was first provided by electron microscopic observations following pulse-labeling with BrUTP (Cmarko et al., 1999) and recently by fluorescence labeling strategies for the detection of UTP-

enriched transcription compartments in living cells (Maharana et al., 2012). Based on 3D-SIM, we performed a rigorous quantitative analysis of the nuclear topography of DAPI-stained chromatin, histone markers for transcriptionally competent chromatin (H3K4me3) and silent chromatin (H3K9me3), as well as RNAPII. We chose RNAPII carrying a phosphorylated serine 5 in its carboxy-terminal domain (S5p) as epitope for immunodetection, because RNAPII-S5p is recruited at the 5' prime site of genes and essential for successful gene transcription (Eick and Geyer, 2013; Heidemann et al., 2013). It should be noted, however, that RNAPII-S5p can also bind at numerous other sites including heterochromatic regions and can be involved in the transcription of non-coding sequences. The repetitive, heptapeptide sequences of the CTD undergo dynamic modifications "written and read as signatures to orchestrate the recruitment of factors with the transcribing RNAPII", including other sites of potential phosphorylation (Heidemann et al., 2013).

Our analysis provides robust evidence for highly significant enrichments of H3K4me3 and RNAPII clusters at the periphery of CDCs, whereas H3K9me3 was enriched in their interior. Multiple RNA polymerases II have been described as integrative parts of transcription factories (Papantonis and Cook, 2013). Our high-resolution analysis does not support a simple black and white picture with transcriptionally silent chromatin exclusively in the interior and competent chromatin exclusively in the periphery of CDCs, since chromatin enriched in H3K9me3 was found to expand occasionally into the PR, whereas some chromatin enriched in H3K4me3 was occasionally noted in the interior of CDCs as well. Furthermore, large H3K4me3 or H3K9me3 positive clusters were observed in chromatin concentrations that do not necessarily reflect the predictions of the CT-IC model.

The PR lines a 3D network of interchromatin compartment (IC) channels and lacunas (Albiez et al., 2006). 3D-SIM suggests that the fraction of the nuclear space

occupied by the IC was strongly reduced during structural transformation of ENPs into ENCs. The wide IC channels, which separated individual CTs and entered the major IC lacuna in the nuclear interior of ENPs disappeared during structural transformation of nuclei into ENC. Conclusive evidence for an IC network, which starts at nuclear pores, pervades the entire nuclear space between CTs and CDCs, and occupies a major part of the nuclear volume was provided in other cell types both by super-resolution fluorescence microscopy (Cremer and Cremer, 2010; Markaki et al., 2010; Markaki et al., 2012; Schermelleh et al., 2008) and electron microscopic studies using procedures for a highly specific visualization of DNA (Huebner et al., 2013; Illner et al., 2010; Kizilyaprak et al., 2010; Rouquette et al., 2010; Rouquette et al., 2009). The smallest IC channels may invade the interior of CDCs and extend between or even expand into the interior of individual 1-Mbp CDs. Models have considered the possibility that 1-Mbp CDs may be built up either from intermingling, 30 nm thick chromatin loops or from smaller CDs with a DNA content in the order of ~100 kbp (Cremer et al., 2000; Mirny, 2011). In addition, differences of the extent and width of IC channels and lacunas in ENPs and ENCs may reflect the storage of different amounts of macromolecules in the IC, which in turn may hinder an expansion of the chromatin compartment.

3.6. Nuclear volume and surface reduction

Bovine preimplantation development involves a massive nuclear volume reduction. The largest nuclei were seen in 2-cell stage embryos, the smallest in blastocysts. In search for the mechanism(s) underlying this volume reduction it is important to decide whether nuclear reconfiguration occurs as a result of mitosis or during interphase or by a combination of events during the entire cell cycle. Our observation that ENP/Cs showed MCBs/CTs and nucleoli throughout the nuclear interior but still

retained nuclear volumes in the range of typical ENPs indicates that long-range CT movements from the nuclear periphery to the interior occurred within interphase nuclei and suggests the possibility that the ENP-ENC transition occurs at least in part during interphase. A global reorganization of nuclei during interphase or in postmitotic cells is not without precedence. Mammalian rod cell nuclei provide a case for a massive reorganization during postmitotic terminal cell differentiation (Solovei et al., 2009). Several studies report large scale movements of specific chromatin segments in interphase nuclei within time scales in the order of minutes (Chuang et al., 2006; Osborne et al., 2007; Roukos et al., 2013). The mechanisms necessary for these movements have not yet been clarified and may act both from inside and outside of the nucleus. (Mehta et al., 2011) proposed a mechanism based on intra-nuclear actin and myosin. Forces for large-scale chromatin movements, however, may also act from the cytoplasm (Strickfaden et al., 2010). For a mechanism of nuclear volume reduction acting from the outside, one could envisage the formation of a contractile network around the nucleus but evidence for this is lacking. Alternatively, an energy dependent fluid export out of the cell could create a hypertonic cytoplasmic environment, which in turn could lead to a shift of fluids from the nucleus to the cytoplasm (Albiez et al., 2006). The loss of fluid from the major lacuna in combination with a degradation of excessive amounts of proteins could result in a collapse of the major lacuna and enforce movements of CTs into the nuclear interior.

In the rabbit species, one or more chromatin-free lacunas in the center or nuclei were observed at the early 2-cell stage but no longer at the late 2-cell stage. This suggests that these lacunas were removed during interphase of 2-cell stage rabbit embryos. Late 2-cell stage nuclei were on average smaller than early 2-cell nuclei. This is counter-intuitive since duplication of the genomic content in somatic

cells rather increases their volumes (Maeshima et al., 2010). Bovine lacunas were always separated from the cytoplasm with a lamina. In rabbit embryonic nuclei this lamina lining of the lacuna was frequently missing.

3.7. Potential mechanisms of nuclear envelope reduction

The nuclear envelope and its underlying lamina play a central role in normal and disease-associated, pathological higher order chromatin organization (Akhtar and Gasser, 2007; Shimi et al., 2012; Zuela et al., 2012). Bovine embryonic development between the zygote and the blastocyst stage was characterized by major changes of the nuclear envelope and underlying lamina. The dynamics of nuclear envelope synthesis and degradation during preimplantation development may be exceedingly complex. On the one side cell multiplication requires the synthesis of ever more nuclear envelopes. On the other side the strong decrease of nuclear volumes requires the elimination of redundant nuclear envelope at the level of individual nuclei.

In the bovine and the rabbit species large deposits of NUP153 clusters were observed throughout the cytoplasm. In both species these randomly located deposits were largely depleted shortly after major EGA. This may indicate that the production of new nuclear pores was matching demand after major EGA in both cases. However, in the bovine species at major EGA and shortly thereafter, large NUP153 clusters continued to exist in direct contact with the nuclear envelope. This may indicate an export mechanism of nuclear envelope and its NPCs during nuclear surface reduction at the 8- and 19-cell stage.

Nuclear invaginations featuring NPCs may facilitate the rapid export of mRNA newly synthesized at sites remote from the nuclear border as well as the import of proteins newly synthesized in the cytoplasm to such sites (Legartova et al., 2014;

Malhas et al., 2011). These invaginations were observed in increased abundance in bovine and rabbit embryonic nuclei until the initiation of major EGA. This may indicate a supporting role in supplying large nuclei with factors in preparation for major EGA. Numerous invaginations containing large volumes of cytoplasm in direct contact with nucleoli or NPBs in rabbit embryos further substantiate this hypothesis. On the contrary, nuclear invaginations positive for lamin B but lacking NPCs may not be involved in import/export. In the bovine species import/export incompetent invaginations were most abundant at stages with nuclear volume reductions. In the rabbit species these invaginations were most abundant at the 2-cell stage at which nuclei showed the largest variability of nuclear volumes throughout preimplantation development. This may indicate a mechanism of short term nuclear lamina storage during interphase nuclear surface reductions.

Although differentiation-dependent changes of nuclear volumes and shapes, as well as global and locus-specific changes of chromatin arrangements are now well established phenomena, the mechanisms, necessary to bring about such changes remain to be elucidated. Advances in super-resolution fluorescence microscopy of living cells will open new avenues to distinguish between effects seen during interphase and effects implying mitosis.

3.8. Considerations on a mechanism, which controls the positions of NPCs in the nuclear envelope

In bovine and rabbit embryos prior to major EGA a direct contact of chromatin, identified by DAPI-stained DNA, with the lamina, identified by immunostaining of lamin B, was not established on all parts of the lamina. We discovered that NPCs, identified by immunostaining of NUP153, were restricted to areas of the nuclear envelope and lamina that were in contact with chromatin. Other parts of the nuclear

envelope, whose underlying lamina was not in contact with chromatin, did not reveal NPCs. After major EGA both chromatin contact sites at the lamina and NPCs became much more uniformly distributed. The present results indicate that a direct contact of chromatin at the nuclear lamina is an essential condition for the formation of an NPC at this site. This condition seems plausible, when we consider that disassembled parts of NPCs, including nucleoporins, such as NUP153, were observed in close association with the periphery of mitotic chromosomes. Accordingly, a direct contact of chromatin to the lamina may allow the local transfer of these components to a corresponding site of the nuclear envelope. It is not known yet, what factors may be causally responsible to initiate the formation of an NPC and it may be that the NUP153 may only be a “bystander” in this respect.

Electron microscopic studies show chromatin association with the nuclear basket and its attached intranuclear filaments (Arlucea et al., 1998). The absence of NUP153 in chromatin-free areas at stages of high mRNA export demand such as major EGA at the 8-cell stage suggests that NPCs require the presence of chromatin. This is further supported by our observations, that NUP153 positive invaginations were usually lined by concentrated chromatin and that no such invaginations were found remote from chromatin within the major chromatin-free IC lacuna. Our study on the content of the major interchromatin lacuna (MICL) in bovine embryos confirmed the presence of newly synthesized mRNA throughout the MICL (Popken et al., 2014a). Therefore, mRNA export functionality at the border in contact with the MICL at MGA would be beneficial but is apparently not possible. The few nuclei after MGA with MICL extensions in contact with the nuclear border displayed a thin layer of heterochromatin below the entire nuclear lamina and no large NPC-free areas.

3.9. 3D structured illumination microscopy (3D-SIM) on mammalian embryos

The study “3D structured illumination microscopy of mammalian embryos and spermatozoa” demonstrates a robust and practical way to achieve super-resolution fluorescence microscopy on mammalian embryos. This was achieved by essentially simulating in blastomeres the properties of adherence and proximity to the cover glass of adherent cells, which work well with 3D-SIM (Markaki et al., 2012). This solution may not necessarily exclusively apply to 3D-SIM but could be compatible with alternative microscopy solutions such as photoactivated localization microscopy (PALM) (Zhong, 2010), stochastic optical reconstruction microscopy (STORM) (Rust et al., 2006) and stimulated-emission-depletion microscopy STED (Hell and Wichmann, 1994), which also rely on specimens not or only minimally moving during scanning. Furthermore, due to the signal reducing properties of the embedding medium the signal intensity and therefore the image quality should increase with proximity to the cover glass of scanned sections. Reconstruction algorithms configured via fluorescent beads directly attached to the cover glass also work better with sections scanned as close to the cover glass as possible, as this resembles the situation of the fluorescent beads better. Additionally, the demonstration of 3D-SIM on spermatozoa attached to the cover glass under the blanket of the transparent zona pellucida shows that theoretically even specimens that do not attach at all to a cover glass could be scanned with this protocol if they are similarly immobilized under the blanket of a transparent film attached to the cover glass.

Potential drawbacks of this novel protocol are the additional necessity for at least one micromanipulator and sufficient training to handle sticky embryos. Mouse and rabbit embryos can be particularly challenging in this regard, since most commercially available antibodies are produced in mouse or rabbit. Staining with a

primary antibody produced in the same host species as the species of the embryo requires the removal of the zona pellucida prior to staining. Otherwise, the zona pellucida will filter out antibodies and the blastomeres inside the zona pellucida will not receive the appropriate antibody concentration. However, removal of the zona pellucida early in the protocol has two disadvantages. Firstly, if the blastomeres are not well attached to each other, they may get lost when transporting the embryo. Individual blastomeres can be too small to identify in a stereomicroscope. This is especially problematic, if other particles such as dust are located in the medium. Secondly, the risk of a loss of the entire embryo due to accidental attachment of the embryo at the bottom of a well or at the inside wall of the pipette is greatly increased without a zona pellucida. Embryos protected by a zona pellucida can be recovered by strongly blowing medium against them. However, blowing strongly against unprotected attached embryos can easily result in the fragmentation of the embryo into individual blastomeres. Therefore it is strongly recommended to search for antibodies from a different host if rabbit or mouse embryos have to be stained and scanned.

Our study has shown that stainings against highly concentrated proteins such as NUP153 or lamin B were possible even after two years of storage of fixed embryos in PBS with useful results. Therefore, embryos can be produced and fixed in larger quantities once and then used in small groups for training and for experiments saving the time for embryo production. Embryos only need to be produced fresh, stained and scanned right away if the target proteins are either only present in low concentrations such as histones or if their concentration needs to be quantified by their original signal intensity. However, intensity quantifications should not be performed with microscopy requiring subsequent reconstruction since algorithms alter signal intensities. Confocal laser scanning microscopy without

deconvolution would be more appropriate for such a task.

Compared with live imaging, fixed embryos have disadvantages and advantages. The main disadvantage is the lack of data of the same specimen throughout a specific time window. In our bovine embryo nuclear architecture study it would have been beneficial to follow the development of the large central lacuna. Similarly, the removal of the central chromatin-free lacuna during the 2-cell stage in rabbit embryos could have been visualized. Nuclear volumes could have been measured at the beginning and the end of the 2-cell stage to identify a nuclear volume decrease per nucleus. In the nuclear envelope and lamina studies one could have quantified whether mitosis has an impact on the numbers of invaginations throughout the cell cycle. However, there are also clear advantages in fixing specimens. Firstly, any expression of fluorescent proteins in the sample would have required diverting from the unaltered natural situation and could have triggered abnormal phenomena. Our live cell experiments on human primary fibroblasts (data not shown) have shown that most DNA constructs that work well with established cell lines like HeLa cells do not work in primary fibroblasts. This hints at an increased sensibility of unaltered primary cells compared with cell lines who have adapted to cell culture conditions for years or even decades (Gartler, 1968). The desired protein/fluorescent protein construct may simply not be compatible with mammalian embryos. Secondly, not all antibody targets can be made visible via plasmids. For instance, specific histone modifications are not possible to mark with a transgene for the histone on a plasmid. Furthermore, only the highest wave-lengths of the visible spectrum are preferred for time-lapse microscopy to minimize the potential harmful effects of short wavelength rays such as UV radiation known to damage DNA (Kleiman et al., 1990). Embryonic development may be affected negatively by the generation of reactive oxygen species (ROS) due to light exposure (Agarwal et al.,

2014). With fixed samples, the unaltered, natural situation can be investigated with the entire spectrum of the visible light.

3.10. Slow freezing causes more damage than vitrification

Previous studies have shown that the survival rate of embryos warmed after vitrification surpasses that of embryos thawed after slow freezing (Saragusty and Arav, 2011). Our study of the effects of both methods on 4-cell stage bovine embryos demonstrates that slow freezing causes more damage to the zona pellucida and blastomeres than vitrification. While the damages caused to the zona pellucida would affect all pre-hatching stages similarly, the amount of destruction caused in blastomeres may be higher in early developmental stages of embryos, since oocytes and early embryonic stages contain a deposit of energy reserves in form of lipid drops provided by the mother animal (Abe et al., 2002). These lipid drops have a high rate of ice crystal formation during slow freezing. Additionally, the survival rate of embryos after any method of freezing is higher at later stages such as the blastocyst stage, since the higher amount of blastomeres in later stages makes embryo recovery more likely, if the destructive effects of freezing have triggered apoptosis or necrosis in a certain amount of blastomeres. The remaining abundance of blastomeres can easily divide and replace lost blastomeres, whereas the destruction of the single cell of the zygote or oocyte stage would be fatal for further development. Furthermore, damages caused by freezing prior to major EGA may trigger the developmental stop of the oocyte-to-embryo transition at major EGA, whereas damages after this checkpoint do not (Meirelles et al., 2004).

However, ice crystal formation is not the only negative factor introduced by slow freezing. Cryoprotectants, while beneficial to an embryo in the frozen state, may have toxic side effects before freezing is accomplished (Sommerfeld and Niemann,

1999). Thus, during the initial steps of slow freezing embryos are generally longer exposed to the toxic environment of cryoprotectants than during the short moment they come in contact with cryoprotectants during vitrification.

In fertility clinics vitrification of blastocysts has already become the state of the art due to its superior success rates (Stehlik et al., 2005). The relatively new trend of “social” freezing (Mertes and Pennings, 2011), the freezing of oocytes of younger patients for fertilization and transfer at a higher age, would be far less successful using slow freezing due to the ice crystal formation of maternal lipid deposits at this early stage (Cao et al., 2009). Vitrified oocytes can have the same developmental competence as fresh oocytes (Cobo et al., 2008; Trokoudes et al., 2011).

4. Annex

4.1. References

Abe, H., Otoi, T., Tachikawa, S., Yamashita, S., Satoh, T., and Hoshi, H. (1999). Fine structure of bovine morulae and blastocysts in vivo and in vitro. Anatomy and embryology *199*, 519-527.

Abe, H., Yamashita, S., Satoh, T., and Hoshi, H. (2002). Accumulation of cytoplasmic lipid droplets in bovine embryos and cryotolerance of embryos developed in different culture systems using serum-free or serum-containing media. Molecular reproduction and development *61*, 57-66.

Agarwal, A., Durairajanayagam, D., and du Plessis, S.S. (2014). Utility of antioxidants during assisted reproductive techniques: an evidence based review. Reproductive biology and endocrinology : RB&E *12*, 112.

Ahn, S.H., Kim, M., and Buratowski, S. (2004). Phosphorylation of serine 2 within the RNA polymerase II C-terminal domain couples transcription and 3′ end processing. Molecular cell *13*, 67-76.

Akhtar, A., and Gasser, S.M. (2007). The nuclear envelope and transcriptional control. Nature reviews Genetics *8*, 507-517.

Albiez, H., Cremer, M., Tiberi, C., Vecchio, L., Schermelleh, L., Dittrich, S., Kupper, K., Joffe, B., Thormeyer, T., von Hase, J.*, et al.* (2006). Chromatin domains and the interchromatin compartment form structurally defined and functionally interacting nuclear networks. Chromosome research : an international journal on the molecular, supramolecular and evolutionary aspects of chromosome biology *14*, 707-733.

Antonin, W., Franz, C., Haselmann, U., Antony, C., and Mattaj, I.W. (2005). The integral membrane nucleoporin pom121 functionally links nuclear pore complex assembly and nuclear envelope formation. Molecular cell *17*, 83-92.

Arav, A., Yavin, S., Zeron, Y., Natan, D., Dekel, I., and Gacitua, H. (2002). New trends in gamete's cryopreservation. Molecular and cellular endocrinology *187*, 77-81.

Arlucea, J., Andrade, R., Alonso, R., and Arechaga, J. (1998). The nuclear basket of the nuclear pore complex is part of a higher-order filamentous network that is related to chromatin. Journal of structural biology *124*, 51-58.

Badr, H., Bongioni, G., Abdoon, A.S., Kandil, O., and Puglisi, R. (2007). Gene expression in the in vitro-produced preimplantation bovine embryos. Zygote *15*, 355-367.

Ball, J.R., and Ullman, K.S. (2005). Versatility at the nuclear pore complex: lessons learned from the nucleoporin Nup153. Chromosoma *114*, 319-330.

Bannister, A.J., and Kouzarides, T. (2011). Regulation of chromatin by histone modifications. Cell research *21*, 381-395.

Baskaran, R., Dahmus, M.E., and Wang, J.Y. (1993). Tyrosine phosphorylation of mammalian RNA polymerase II carboxyl-terminal domain. Proceedings of the National Academy of Sciences of the United States of America *90*, 11167-11171.

Beaudouin, J., Gerlich, D., Daigle, N., Eils, R., and Ellenberg, J. (2002). Nuclear envelope breakdown proceeds by microtubule-induced tearing of the lamina. Cell *108*, 83-96.

Bernstein, B.E., Humphrey, E.L., Erlich, R.L., Schneider, R., Bouman, P., Liu, J.S., Kouzarides, T., and Schreiber, S.L. (2002). Methylation of histone H3 Lys 4 in coding regions of active genes. Proceedings of the National Academy of Sciences of the United States of America *99*, 8695-8700.

Bickmore, W.A., and van Steensel, B. (2013). Genome architecture: domain organization of interphase chromosomes. Cell *152*, 1270-1284.

Bink, K., Walch, A., Feuchtinger, A., Eisenmann, H., Hutzler, P., Hofler, H., and Werner, M. (2001). TO-PRO-3 is an optimal fluorescent dye for nuclear counterstaining in dual-colour FISH on paraffin sections. Histochemistry and cell biology *115*, 293-299.

Bó, G., and Mapletoft, R. (2013). Evaluation and classification of bovine embryos. Anim Reprod *10*, 344-348.

Bolzer, A., Kreth, G., Solovei, I., Koehler, D., Saracoglu, K., Fauth, C., Muller, S., Eils, R., Cremer, C., Speicher, M.R.*, et al.* (2005). Three-dimensional maps of all chromosomes in human male fibroblast nuclei and prometaphase rosettes. PLoS Biol *3*, e157.

Brunet-Simon, A., Henrion, G., Renard, J.P., and Duranthon, V. (2001). Onset of zygotic transcription and maternal transcript legacy in the rabbit embryo. Molecular reproduction and development *58*, 127-136.

Camous, S., Kopecny, V., and Flechon, J.E. (1986). Autoradiographic detection of the earliest stage of [3H]-uridine incorporation into the cow embryo. Biol Cell *58*, 195-200.

Campos, E.I., and Reinberg, D. (2009). Histones: annotating chromatin. Annual review of genetics *43*, 559-599.

Cao, F., Fukuda, A., Watanabe, H., and Kono, T. (2013). The transcriptomic architecture of mouse Sertoli cell clone embryos reveals temporal-spatial-specific reprogramming. Reproduction *145*, 277-288.

Cao, Y.X., Xing, Q., Li, L., Cong, L., Zhang, Z.G., Wei, Z.L., and Zhou, P. (2009). Comparison of survival and embryonic development in human oocytes cryopreserved by slow-freezing and vitrification. Fertility and sterility *92*, 1306-1311.

Carmody, S.R., and Wente, S.R. (2009). mRNA nuclear export at a glance. Journal of cell science *122*, 1933-1937.

Chandra, T., Kirschner, K., Thuret, J.Y., Pope, B.D., Ryba, T., Newman, S., Ahmed, K., Samarajiwa, S.A., Salama, R., Carroll, T.*, et al.* (2012). Independence of

repressive histone marks and chromatin compaction during senescent heterochromatic layer formation. Molecular cell *47*, 203-214.

Christians, E., Rao, V.H., and Renard, J.P. (1994). Sequential acquisition of transcriptional control during early embryonic development in the rabbit. Developmental biology *164*, 160-172.

Chuang, C.H., Carpenter, A.E., Fuchsova, B., Johnson, T., de Lanerolle, P., and Belmont, A.S. (2006). Long-range directional movement of an interphase chromosome site. Curr Biol *16*, 825-831.

Cmarko, D., Verschure, P.J., Martin, T.E., Dahmus, M.E., Krause, S., Fu, X.D., van Driel, R., and Fakan, S. (1999). Ultrastructural analysis of transcription and splicing in the cell nucleus after bromo-UTP microinjection. Molecular biology of the cell *10*, 211-223.

Cobo, A., Kuwayama, M., Perez, S., Ruiz, A., Pellicer, A., and Remohi, J. (2008). Comparison of concomitant outcome achieved with fresh and cryopreserved donor oocytes vitrified by the Cryotop method. Fertility and sterility *89*, 1657-1664.

Cremer, C. (2012). Optics Far Beyond the Diffraction Limit. In Springer Handbook of Lasers and Optics, F. Traeger, ed. (Springer Berlin Heidelberg), pp. 1359-1397.

Cremer, T., and Cremer, M. (2010). Chromosome territories. Cold Spring Harb Perspect Biol *2*, a003889.

Cremer, T., Kreth, G., Koester, H., Fink, R.H., Heintzmann, R., Cremer, M., Solovei, I., Zink, D., and Cremer, C. (2000). Chromosome territories, interchromatin domain compartment, and nuclear matrix: an integrated view of the functional nuclear architecture. Critical reviews in eukaryotic gene expression *10*, 179-212.

Croken, M.M., Nardelli, S.C., and Kim, K. (2012). Chromatin modifications, epigenetics, and how protozoan parasites regulate their lives. Trends in parasitology *28*, 202-213.

Cronshaw, J.M., Krutchinsky, A.N., Zhang, W., Chait, B.T., and Matunis, M.J. (2002). Proteomic analysis of the mammalian nuclear pore complex. The Journal of cell biology *158*, 915-927.

D'Angelo, M.A., Anderson, D.J., Richard, E., and Hetzer, M.W. (2006). Nuclear pores form de novo from both sides of the nuclear envelope. Science *312*, 440-443.

de Graaf, C.A., and van Steensel, B. (2013). Chromatin organization: form to function. Current opinion in genetics & development *23*, 185-190.

De Ruijter, A., Van Gennip, A., Caron, H., Kemp, S., and van Kuilenburg, A. (2003). Histone deacetylases (HDACs): characterization of the classical HDAC family. Biochem J *370*, 737-749.

de Wit, E., Bouwman, B.A., Zhu, Y., Klous, P., Splinter, E., Verstegen, M.J., Krijger, P.H., Festuccia, N., Nora, E.P., Welling, M.*, et al.* (2013). The pluripotent genome in three dimensions is shaped around pluripotency factors. Nature *501*, 227-231.

Dixon, J.R., Selvaraj, S., Yue, F., Kim, A., Li, Y., Shen, Y., Hu, M., Liu, J.S., and Ren, B. (2012). Topological domains in mammalian genomes identified by analysis of chromatin interactions. Nature *485*, 376-380.

Doucet, C.M., and Hetzer, M.W. (2010). Nuclear pore biogenesis into an intact nuclear envelope. Chromosoma *119*, 469-477.

Dreger, M., Bengtsson, L., Schoneberg, T., Otto, H., and Hucho, F. (2001). Nuclear envelope proteomics: novel integral membrane proteins of the inner nuclear membrane. Proceedings of the National Academy of Sciences of the United States of America *98*, 11943-11948.

Dultz, E., Zanin, E., Wurzenberger, C., Braun, M., Rabut, G., Sironi, L., and Ellenberg, J. (2008). Systematic kinetic analysis of mitotic dis- and reassembly of the nuclear pore in living cells. The Journal of cell biology *180*, 857-865.

Eick, D., and Geyer, M. (2013). The RNA Polymerase II Carboxy-Terminal Domain (CTD) Code. Chemical reviews.

Franz, C., Walczak, R., Yavuz, S., Santarella, R., Gentzel, M., Askjaer, P., Galy, V., Hetzer, M., Mattaj, I.W., and Antonin, W. (2007). MEL-28/ELYS is required for the recruitment of nucleoporins to chromatin and postmitotic nuclear pore complex assembly. EMBO reports *8*, 165-172.

Funayama, R., Saito, M., Tanobe, H., and Ishikawa, F. (2006). Loss of linker histone H1 in cellular senescence. The Journal of cell biology *175*, 869-880.

Garcia Verdugo, J.M., Regidor Garcia, J., Castellano Lopez, B., and Lopez Garcia, C. (1983). Ultrastructure of neuronal cell bodies in the dorsal cortex of Lacerta galloti. Journal fur Hirnforschung *24*, 485-494.

Gartler, S.M. (1968). Apparent Hela cell contamination of human heteroploid cell lines. Nature *217*, 750-751.

Gibcus, J.H., and Dekker, J. (2013). The hierarchy of the 3D genome. Molecular cell *49*, 773-782.

Graf, A., Krebs, S., Zakhartchenko, V., Schwalb, B., Blum, H., and Wolf, E. (2014). Fine mapping of genome activation in bovine embryos by RNA sequencing. Proceedings of the National Academy of Sciences of the United States of America.

Grisart, B., Massip, A., and Dessy, F. (1994). Cinematographic analysis of bovine embryo development in serum-free oviduct-conditioned medium. Journal of reproduction and fertility *101*, 257-264.

Gruenbaum, Y., Margalit, A., Goldman, R.D., Shumaker, D.K., and Wilson, K.L. (2005). The nuclear lamina comes of age. Nature reviews Molecular cell biology *6*, 21-31.

Gustafsson, M.G. (1999). Extended resolution fluorescence microscopy. Curr Opin Struct Biol *9*, 627-634.

Gustafsson, M.G. (2000). Surpassing the lateral resolution limit by a factor of two using structured illumination microscopy. J Microsc *198*, 82-87.

Hahn, S. (2004). Structure and mechanism of the RNA polymerase II transcription machinery. Nat Struct Mol Biol *11*, 394-403.

Hampoelz, B., and Lecuit, T. (2011). Nuclear mechanics in differentiation and development. Current opinion in cell biology *23*, 668-675.

Han, Z., Chung, Y.G., Gao, S., and Latham, K.E. (2005). Maternal factors controlling blastomere fragmentation in early mouse embryos. Biology of reproduction *72*, 612-618.

Hase, M.E., and Cordes, V.C. (2003). Direct interaction with nup153 mediates binding of Tpr to the periphery of the nuclear pore complex. Molecular biology of the cell *14*, 1923-1940.

Hebbes, T.R., Thorne, A.W., and Crane-Robinson, C. (1988). A direct link between core histone acetylation and transcriptionally active chromatin. The EMBO journal *7*, 1395.

Heidemann, M., Hintermair, C., Voss, K., and Eick, D. (2013). Dynamic phosphorylation patterns of RNA polymerase II CTD during transcription. Biochimica et biophysica acta *1829*, 55-62.

Heintzmann, R., and Cremer, C.G. (1999). Laterally modulated excitation microscopy: improvement of resolution by using a diffraction grating. Paper presented at: BiOS Europe'98 (International Society for Optics and Photonics).

Hell, S.W., and Wichmann, J. (1994). Breaking the diffraction resolution limit by stimulated emission: stimulated-emission-depletion fluorescence microscopy. Optics letters *19*, 780-782.

Hinshaw, J.E., Carragher, B.O., and Milligan, R.A. (1992). Architecture and design of the nuclear pore complex. Cell *69*, 1133-1141.

Huang, X., Andreu-Vieyra, C.V., Wang, M., Cooney, A.J., Matzuk, M.M., and Zhang, P. (2009). Preimplantation mouse embryos depend on inhibitory phosphorylation of separase to prevent chromosome missegregation. Mol Cell Biol *29*, 1498-1505.

Huebner, B., Cremer, T., and Neumann, J. (2013). Correlative Microscopy of Individual Cells: Sequential Application of Microscopic Systems with Increasing Resolution to Study the Nuclear Landscape. Methods in molecular biology *1042*, 299 - 336.

Illner, D., Zinner, R., Handtke, V., Rouquette, J., Strickfaden, H., Lanctot, C., Conrad, M., Seiler, A., Imhof, A., Cremer, T.*, et al.* (2010). Remodeling of nuclear architecture by the thiodioxoxpiperazine metabolite chaetocin. Experimental cell research *316*, 1662-1680.

Iqbal, K., Barg-Kues, B., Broll, S., Bode, J., Niemann, H., and Kues, W. (2009). Cytoplasmic injection of circular plasmids allows targeted expression in mammalian embryos. BioTechniques *47*, 959-968.

Jaenisch, R., and Bird, A. (2003). Epigenetic regulation of gene expression: how the genome integrates intrinsic and environmental signals. Nature genetics *33 Suppl*, 245-254.

Kapuscinski, J. (1995). DAPI: a DNA-specific fluorescent probe. Biotechnic & histochemistry : official publication of the Biological Stain Commission *70*, 220-233.

Kizilyaprak, C., Spehner, D., Devys, D., and Schultz, P. (2010). In vivo chromatin organization of mouse rod photoreceptors correlates with histone modifications. PloS one *5*, e11039.

Kleiman, N.J., Wang, R.R., and Spector, A. (1990). Ultraviolet light induced DNA damage and repair in bovine lens epithelial cells. Current eye research *9*, 1185-1193.

Koehler, D., Zakhartchenko, V., Froenicke, L., Stone, G., Stanyon, R., Wolf, E., Cremer, T., and Brero, A. (2009). Changes of higher order chromatin arrangements during major genome activation in bovine preimplantation embryos. Experimental cell research *315*, 2053-2063.

Kosak, S.T., and Groudine, M. (2004). Form follows function: The genomic organization of cellular differentiation. Genes & development *18*, 1371-1384.

Kouzarides, T. (2007). Chromatin modifications and their function. Cell *128*, 693-705.

Kues, W.A., Sudheer, S., Herrmann, D., Carnwath, J.W., Havlicek, V., Besenfelder, U., Lehrach, H., Adjaye, J., and Niemann, H. (2008). Genome-wide expression profiling reveals distinct clusters of transcriptional regulation during bovine preimplantation development in vivo. Proceedings of the National Academy of Sciences of the United States of America *105*, 19768-19773.

Kutay, U., and Hetzer, M.W. (2008). Reorganization of the nuclear envelope during open mitosis. Current opinion in cell biology *20*, 669-677.

Leandri, R.D., Archilla, C., Bui, L.C., Peynot, N., Liu, Z., Cabau, C., Chastellier, A., Renard, J.P., and Duranthon, V. (2009). Revealing the dynamics of gene expression during embryonic genome activation and first differentiation in the rabbit embryo with a dedicated array screening. Physiological genomics *36*, 98-113.

Legartova, S., Stixova, L., Laur, O., Kozubek, S., Sehnalova, P., and Bartova, E. (2014). Nuclear structures surrounding internal lamin invaginations. Journal of cellular biochemistry *115*, 476-487.

Leidenfrost, S. (2009). Zellentwicklung, Zelltod und die Expression Apoptose-assoziierter Gene in der frühen Embryogenese beim Rind. In Lehrstuhl für Allgemeine Anatomie, Histologie und Embryologie (Munich: Ludwig-Maximilians-University, http://edoc.ub.uni-muenchen.de/11663/).

Leidenfrost, S., Boelhauve, M., Reichenbach, M., Gungor, T., Reichenbach, H.D., Sinowatz, F., Wolf, E., and Habermann, F.A. (2011). Cell arrest and cell death in mammalian preimplantation development: lessons from the bovine model. PloS one *6*, e22121.

Lenart, P., Rabut, G., Daigle, N., Hand, A.R., Terasaki, M., and Ellenberg, J. (2003). Nuclear envelope breakdown in starfish oocytes proceeds by partial NPC disassembly followed by a rapidly spreading fenestration of nuclear membranes. The Journal of cell biology *160*, 1055-1068.

Li, L., Lu, X., and Dean, J. (2013). The maternal to zygotic transition in mammals. Molecular aspects of medicine *34*, 919-938.

Maeshima, K., Iino, H., Hihara, S., Funakoshi, T., Watanabe, A., Nishimura, M., Nakatomi, R., Yahata, K., Imamoto, F., and Hashikawa, T. (2010). Nuclear pore formation but not nuclear growth is governed by cyclin-dependent kinases (Cdks) during interphase. Nature structural & molecular biology *17*, 1065-1071.

Maharana, S., Sharma, D., Shi, X., and Shivashankar, G.V. (2012). Dynamic organization of transcription compartments is dependent on functional nuclear architecture. Biophys J *103*, 851-859.

Malhas, A., Goulbourne, C., and Vaux, D.J. (2011). The nucleoplasmic reticulum: form and function. Trends in cell biology *21*, 362-373.

Mansfeld, J., Guttinger, S., Hawryluk-Gara, L.A., Pante, N., Mall, M., Galy, V., Haselmann, U., Muhlhausser, P., Wozniak, R.W., Mattaj, I.W*., et al.* (2006). The conserved transmembrane nucleoporin NDC1 is required for nuclear pore complex assembly in vertebrate cells. Molecular cell *22*, 93-103.

Markaki, Y., Gunkel, M., Schermelleh, L., Beichmanis, S., Neumann, J., Heidemann, M., Leonhardt, H., Eick, D., Cremer, C., and Cremer, T. (2010). Functional nuclear organization of transcription and DNA replication: a topographical marriage between chromatin domains and the interchromatin compartment. Cold Spring Harbor symposia on quantitative biology *75*, 475-492.

Markaki, Y., Smeets, D., Fiedler, S., Schmid, V.J., Schermelleh, L., Cremer, T., and Cremer, M. (2012). The potential of 3D-FISH and super-resolution structured illumination microscopy for studies of 3D nuclear architecture: 3D structured illumination microscopy of defined chromosomal structures visualized by 3D (immuno)-FISH opens new perspectives for studies of nuclear architecture. BioEssays : news and reviews in molecular, cellular and developmental biology *34*, 412-426.

Martins, R.P., Finan, J.D., Guilak, F., and Lee, D.A. (2012). Mechanical regulation of nuclear structure and function. Annu Rev Biomed Eng *14*, 431-455.

Maul, G.G., Maul, H.M., Scogna, J.E., Lieberman, M.W., Stein, G.S., Hsu, B.Y., and Borun, T.W. (1972). Time sequence of nuclear pore formation in phytohemagglutinin-stimulated lymphocytes and in HeLa cells during the cell cycle. The Journal of cell biology *55*, 433-447.

McManus, M.T., and Sharp, P.A. (2002). Gene silencing in mammals by small interfering RNAs. Nature reviews Genetics *3*, 737-747.

Mehta, I.S., Eskiw, C.H., Arican, H.D., Kill, I.R., and Bridger, J.M. (2011). Farnesyltransferase inhibitor treatment restores chromosome territory positions and

active chromosome dynamics in Hutchinson-Gilford progeria syndrome cells. Genome biology *12*, R74.

Meirelles, F.V., Caetano, A.R., Watanabe, Y.F., Ripamonte, P., Carambula, S.F., Merighe, G.K., and Garcia, S.M. (2004). Genome activation and developmental block in bovine embryos. Animal reproduction science *82-83*, 13-20.

Memili, E., and First, N.L. (2000). Zygotic and embryonic gene expression in cow: a review of timing and mechanisms of early gene expression as compared with other species. Zygote *8*, 87-96.

Mertes, H., and Pennings, G. (2011). Social egg freezing: for better, not for worse. Reproductive biomedicine online *23*, 824-829.

Meshreky, S.Z., Fahim, H.N., Abdel-Aal, E., and Ibrahim, S. (2012). EFFECT OF VITRIFICATION AND CRYOSTORAGE LENGTH ON VIABILITY OF RABBIT EMBRYOS AFTER THAWING.

Mirny, L.A. (2011). The fractal globule as a model of chromatin architecture in the cell. Chromosome research : an international journal on the molecular, supramolecular and evolutionary aspects of chromosome biology *19*, 37-51.

Misirlioglu, M., Page, G.P., Sagirkaya, H., Kaya, A., Parrish, J.J., First, N.L., and Memili, E. (2006). Dynamics of global transcriptome in bovine matured oocytes and preimplantation embryos. Proceedings of the National Academy of Sciences of the United States of America *103*, 18905-18910.

Mor, A., Suliman, S., Ben-Yishay, R., Yunger, S., Brody, Y., and Shav-Tal, Y. (2010). Dynamics of single mRNP nucleocytoplasmic transport and export through the nuclear pore in living cells. Nature cell biology *12*, 543-552.

Murayama, Y., Mizuno, J., Kamakura, H., Fueta, Y., Nakamura, H., Akaishi, K., Anzai, K., Watanabe, A., Inui, H., and Omata, S. (2006). Mouse zona pellucida dynamically changes its elasticity during oocyte maturation, fertilization and early embryo development. Human cell *19*, 119-125.

Nagano, T., Lubling, Y., Stevens, T.J., Schoenfelder, S., Yaffe, E., Dean, W., Laue, E.D., Tanay, A., and Fraser, P. (2013). Single-cell Hi-C reveals cell-to-cell variability in chromosome structure. Nature *502*, 59-64.

Nakamura, H., Morita, T., and Sato, C. (1986). Structural organizations of replicon domains during DNA synthetic phase in the mammalian nucleus. Experimental cell research *165*, 291-297.

Nakayama, J., Rice, J.C., Strahl, B.D., Allis, C.D., and Grewal, S.I. (2001). Role of histone H3 lysine 9 methylation in epigenetic control of heterochromatin assembly. Science *292*, 110-113.

Ndiaye, M., and Mattei, X. (1993). Process of nuclear envelope reduction in spermiogenesis of a mosquito, Culex tigripes. Molecular reproduction and development *34*, 416-419.

Niwa, H., Miyazaki, J., and Smith, A.G. (2000). Quantitative expression of Oct-3/4 defines differentiation, dedifferentiation or self-renewal of ES cells. Nature genetics *24*, 372-376.

Ooi, S.K., and Bestor, T.H. (2008). The colorful history of active DNA demethylation. Cell *133*, 1145-1148.

Osborne, C.S., Chakalova, L., Mitchell, J.A., Horton, A., Wood, A.L., Bolland, D.J., Corcoran, A.E., and Fraser, P. (2007). Myc dynamically and preferentially relocates to a transcription factory occupied by Igh. PLoS Biol *5*, e192.

Ozawa, M., Sakatani, M., Yao, J., Shanker, S., Yu, F., Yamashita, R., Wakabayashi, S., Nakai, K., Dobbs, K.B., Sudano, M.J.*, et al.* (2012). Global gene expression of the inner cell mass and trophectoderm of the bovine blastocyst. BMC developmental biology *12*, 33.

Pacheco-Trigon, S., Hennequet-Antier, C., Oudin, J.-F., Piumi, F., Renard, J.-P., and Duranthon, V. (2002). Molecular characterization of genomic activities at the onset of zygotic transcription in mammals. Biology of reproduction *67*, 1907-1918.

Palancade, B., and Bensaude, O. (2003). Investigating RNA polymerase II carboxyl-terminal domain (CTD) phosphorylation. European journal of biochemistry / FEBS *270*, 3859-3870.

Papantonis, A., and Cook, P.R. (2013). Transcription factories: genome organization and gene regulation. Chemical reviews *113*, 8683-8705.

Parrish, J.J. (2014). Bovine in vitro fertilization: in vitro oocyte maturation and sperm capacitation with heparin. Theriogenology *81*, 67-73.

Pederson, T. (2011). The nucleolus. Cold Spring Harb Perspect Biol *3*.

Popken, J., Brero, A., Koehler, D., Schmid, V.J., Strauss, A., Wuensch, A., Guengoer, T., Graf, A., Krebs, S., Blum, H.*, et al.* (2014a). Functional reprogramming of fibroblast nuclei in cloned bovine embryos is paralleled by major structural remodeling with both striking similarities and differences to nuclear phenotypes of embryos fertilized *in vitro*. Nucleus (in press).

Popken, J., Koehler, D., Brero, A., Wuensch, A., Guengoer, T., Thormeyer, T., Wolf, E., Cremer, T., and Zakhartchenko, V. (2014b). Positional changes of a pluripotency marker gene during structural reorganization of fibroblast nuclei in cloned early bovine embryos. Nucleus (in press).

Pradhan, S., and Esteve, P.O. (2003). Mammalian DNA (cytosine-5) methyltransferases and their expression. Clinical immunology *109*, 6-16.

Ramakrishnan, V. (1997). Histone structure and the organization of the nucleosome. Annual review of biophysics and biomolecular structure *26*, 83-112.

Ridsdale, J.A., Hendzel, M.J., Delcuve, G.P., and Davie, J.R. (1990). Histone acetylation alters the capacity of the H1 histones to condense transcriptionally active/competent chromatin. The Journal of biological chemistry *265*, 5150-5156.

Rizos, D., Ward, F., Duffy, P., Boland, M.P., and Lonergan, P. (2002). Consequences of bovine oocyte maturation, fertilization or early embryo development in vitro versus in vivo: implications for blastocyst yield and blastocyst quality. Molecular reproduction and development *61*, 234-248.

Ross, P.J., and Cibelli, J.B. (2010). Bovine somatic cell nuclear transfer. Methods in molecular biology *636*, 155-177.

Roth, S.Y., Denu, J.M., and Allis, C.D. (2001). Histone acetyltransferases. Annual review of biochemistry *70*, 81-120.

Roukos, V., Voss, T.C., Schmidt, C.K., Lee, S., Wangsa, D., and Misteli, T. (2013). Spatial dynamics of chromosome translocations in living cells. Science *341*, 660-664.

Rouquette, J., Cremer, C., Cremer, T., and Fakan, S. (2010). Functional nuclear architecture studied by microscopy: present and future. Int Rev Cell Mol Biol *282*, 1-90.

Rouquette, J., Genoud, C., Vazquez-Nin, G.H., Kraus, B., Cremer, T., and Fakan, S. (2009). Revealing the high-resolution three-dimensional network of chromatin and interchromatin space: a novel electron-microscopic approach to reconstructing nuclear architecture. Chromosome research : an international journal on the molecular, supramolecular and evolutionary aspects of chromosome biology *17*, 801-810.

Rust, M.J., Bates, M., and Zhuang, X. (2006). Sub-diffraction-limit imaging by stochastic optical reconstruction microscopy (STORM). Nature methods *3*, 793-795.

Saragusty, J., and Arav, A. (2011). Current progress in oocyte and embryo cryopreservation by slow freezing and vitrification. Reproduction *141*, 1-19.

Sathananthan, H., Menezes, J., and Gunasheela, S. (2003). Mechanics of human blastocyst hatching in vitro. Reproductive biomedicine online *7*, 228-234.

Schermelleh, L., Carlton, P.M., Haase, S., Shao, L., Winoto, L., Kner, P., Burke, B., Cardoso, M.C., Agard, D.A., Gustafsson, M.G.*, et al.* (2008). Subdiffraction multicolor imaging of the nuclear periphery with 3D structured illumination microscopy. Science *320*, 1332-1336.

Schermelleh, L., Heintzmann, R., and Leonhardt, H. (2010). A guide to super-resolution fluorescence microscopy. The Journal of cell biology *190*, 165-175.

Shi, W., Zakhartchenko, V., and Wolf, E. (2003). Epigenetic reprogramming in mammalian nuclear transfer. Differentiation *71*, 91-113.

Shimi, T., Butin-Israeli, V., and Goldman, R.D. (2012). The functions of the nuclear envelope in mediating the molecular crosstalk between the nucleus and the cytoplasm. Current opinion in cell biology *24*, 71-78.

Smeets, D., Markaki, Y., Schmid, V.J., Kraus, F., Tattermusch, A., Cerase, A., Sterr, M., Fiedler, S., Demmerle, J., Popken, J.*, et al.* (2014). Three-dimensional super-resolution microscopy of the inactive X chromosome territory reveals a collapse of its

active nuclear compartment harboring distinct Xist RNA foci. Epigenetics & Chromatin *7*, 8.

Smythe, C., Jenkins, H.E., and Hutchison, C.J. (2000). Incorporation of the nuclear pore basket protein nup153 into nuclear pore structures is dependent upon lamina assembly: evidence from cell-free extracts of Xenopus eggs. The EMBO journal *19*, 3918-3931.

Solovei, I., Kreysing, M., Lanctot, C., Kosem, S., Peichl, L., Cremer, T., Guck, J., and Joffe, B. (2009). Nuclear architecture of rod photoreceptor cells adapts to vision in mammalian evolution. Cell *137*, 356-368.

Sommerfeld, V., and Niemann, H. (1999). Cryopreservation of bovine in vitro produced embryos using ethylene glycol in controlled freezing or vitrification. Cryobiology *38*, 95-105.

Stasevich, T.J., Hayashi-Takanaka, Y., Sato, Y., Maehara, K., Ohkawa, Y., Sakata-Sogawa, K., Tokunaga, M., Nagase, T., Nozaki, N., McNally, J.G*., et al.* (2014). Regulation of RNA polymerase II activation by histone acetylation in single living cells. Nature *516*, 272-275.

Stehlik, E., Stehlik, J., Katayama, K.P., Kuwayama, M., Jambor, V., Brohammer, R., and Kato, O. (2005). Vitrification demonstrates significant improvement versus slow freezing of human blastocysts. Reproductive biomedicine online *11*, 53-57.

Storch, K.N., Taatjes, D.J., Bouffard, N.A., Locknar, S., Bishop, N.M., and Langevin, H.M. (2007). Alpha smooth muscle actin distribution in cytoplasm and nuclear invaginations of connective tissue fibroblasts. Histochemistry and cell biology *127*, 523-530.

Strambio-De-Castillia, C., Niepel, M., and Rout, M.P. (2010). The nuclear pore complex: bridging nuclear transport and gene regulation. Nature reviews Molecular cell biology *11*, 490-501.

Strickfaden, H., Zunhammer, A., van Koningsbruggen, S., Kohler, D., and Cremer, T. (2010). 4D chromatin dynamics in cycling cells: Theodor Boveri's hypotheses revisited. Nucleus *1*, 284-297.

Sukegawa, J., and Blobel, G. (1993). A nuclear pore complex protein that contains zinc finger motifs, binds DNA, and faces the nucleoplasm. Cell *72*, 29-38.

Sunba, M.S., Rahi, A.H., and Morgan, G. (1980). Tumours of the anterior uvea. II. Intranuclear cytoplasmic inclusions in malignant melanoma of the iris. The British journal of ophthalmology *64*, 453-456.

Tadros, W., and Lipshitz, H.D. (2009). The maternal-to-zygotic transition: a play in two acts. Development *136*, 3033-3042.

Trokoudes, K.M., Pavlides, C., and Zhang, X. (2011). Comparison outcome of fresh and vitrified donor oocytes in an egg-sharing donation program. Fertility and sterility *95*, 1996-2000.

Vigneault, C., Gravel, C., Vallee, M., McGraw, S., and Sirard, M.A. (2009). Unveiling the bovine embryo transcriptome during the maternal-to-embryonic transition. Reproduction *137*, 245-257.

Walter, J., Schermelleh, L., Cremer, M., Tashiro, S., and Cremer, T. (2003). Chromosome order in HeLa cells changes during mitosis and early G1, but is stably maintained during subsequent interphase stages. The Journal of cell biology *160*, 685-697.

Watson, M.L. (1955). The nuclear envelope; its structure and relation to cytoplasmic membranes. J Biophys Biochem Cytol *1*, 257-270.

Wilmut, I., Schnieke, A.E., McWhir, J., Kind, A.J., and Campbell, K.H. (1997). Viable offspring derived from fetal and adult mammalian cells. Nature *385*, 810-813.

Wowk, B., Leitl, E., Rasch, C.M., Mesbah-Karimi, N., Harris, S.B., and Fahy, G.M. (2000). Vitrification enhancement by synthetic ice blocking agents. Cryobiology *40*, 228-236.

Wuensch, A., Habermann, F.A., Kurosaka, S., Klose, R., Zakhartchenko, V., Reichenbach, H.D., Sinowatz, F., McLaughlin, K.J., and Wolf, E. (2007). Quantitative monitoring of pluripotency gene activation after somatic cloning in cattle. Biology of reproduction *76*, 983-991.

Yoshimizu, T., Sugiyama, N., De Felice, M., Yeom, Y.I., Ohbo, K., Masuko, K., Obinata, M., Abe, K., Scholer, H.R., and Matsui, Y. (1999). Germline-specific expression of the Oct-4/green fluorescent protein (GFP) transgene in mice. Development, growth & differentiation *41*, 675-684.

Zander-Fox, D., Lane, M., and Hamilton, H. (2013). Slow freezing and vitrification of mouse morula and early blastocysts. Journal of assisted reproduction and genetics *30*, 1091-1098.

Zernicka-Goetz, M., Pines, J., McLean Hunter, S., Dixon, J.P., Siemering, K.R., Haseloff, J., and Evans, M.J. (1997). Following cell fate in the living mouse embryo. Development *124*, 1133-1137.

Zhong, H. (2010). Photoactivated localization microscopy (PALM): an optical technique for achieving ~10-nm resolution. Cold Spring Harbor protocols *2010*, pdb top91.

Zuela, N., Bar, D.Z., and Gruenbaum, Y. (2012). Lamins in development, tissue maintenance and stress. EMBO reports *13*, 1070-1078.

4.2. Acknowledgements

This doctorate thesis would not have been possible without the hard word, time dedication and resources of many highly skilled and engaged contributors. I would like to thank:

Prof. Thomas Cremer and Prof. Eckhard Wolf for their leadership, guidance, contribution and support. Prof. Cremer was contributing intensively in the creation of most of our manuscripts.

Valery Zakhartchenko who was very supportive and was also contributing intensively in the finalization of manuscripts.

Tuna Güngör for his countless contributions to all of our studies, for IVF training and for initiating the cooperation with the Department of Histology and Embryology, Ege University, Izmir, Turkey.

Daniela Köhler for generating the data for the study on localization changes of GOF and CTs 13 and for earlier additional developmental work on challenging blastomere DNA/RNA labeling protocols.

Tobias Thormeyer for the eADS software and personal support on how to use the software correctly.

Alessandro Brero for his contributions to the study on localization changes of GOF and CTs 13 and earlier developmental work on challenging blastomere DNA/RNA labeling protocols.

Annegret Wünsch for her cell culture training and her pioneering work and advice on GOF.

Felix Habermann for his pioneering work and advice on GOF and sharing his experience and observations with fluorescent microscopy on bovine embryos.

Marion Cremer for her critical reading of our first manuscripts, for helping to improve substantially an earlier version of the bovine nuclear envelope and lamina manuscript and her support, advice and guidance.

Yolanda Markaki and Barbara Hübner for their support, advice and guidance.

Daniel Smeets for discussions on 3D-SIM experiences.

Michael Sterr for our multiple testing sessions of various whole-mount approaches.

Türker Çavuşoğlu and Yiğit Uyanıkgil for their close collaboration on the cryopreservation study.

Erica de Monte for her support and assistance in the IVF lab.

Myriam Reichenbach, Horst-Dieter Reichenbach, Andrea Beck, Nicolas Saucedo, Kilian Simmet, Eva-Maria Jemiller, Prof. Bernhard Aigner, Andrea Bähr, Elisabeth Kemter, Barbara Keßler, Nikolai Klymiuk, Mayuko Kurome for insightful discussions, assistance and support.

Maik Dahlhoff for providing mouse embryos.

Pauline Fezert for her kind insights and support.

Alexander Graf, Stefan Krebs, Helmut Blum for the great support and collaboration on RNA-Seq data.

Prof. Volker J. Schmid for developing the statistical software to analyze the positioning of signals throughout the DAPI gradient.

Axel Strauss for developing additional statistical algorithms for our studies.

Irina Solovei and Boris Joffe for kind encouragement, constant help and support and many insightful suggestions.

Katrin Schneider for her introduction to and her maintenance of the spinning disk confocal microscope.

Olga Alexandrova for ensuring optimal confocal microscopy conditions.

Prof. Heinrich Leonhardt for providing access to and ensuring a high quality of the 3D-SIM microscope.

Andreas Meiser for many discussions about improving the image quality in 3D-SIM and for maintaining the 3D-SIM microscope.

Jürgen Neumann for maintaining the 3D-SIM microscope in optimal working conditions and his suggestions on optic phenomena around spherical nuclei.

Hartmann Harz for various 3D-SIM discussions.

Daniela Meilinger and Andrea Rottach for supporting me greatly by allowing me to participate in many insightful seminars during the PhD.

Katharina Thanisch for insightful discussions.

Martin Heß for being part of my thesis advisory committee and for his suggestions for improving the image quality.

Prof. Charles David for the opportunity to perform live cell hydra microscopy on the spinning disk microscope and for being a member of my rigorosum.

Michael Bögle for greatly supporting my transfer from Freie University Berlin to the LMU Munich, for constantly supporting me in Munich and without whom I would not have been able to be where I am today.

Irini Bassios for providing support during challenging times.

Prof. Elisabeth Weiß for allowing me to compete for the Bavarian Elite Academy and for advising me on the legal background for starting the Phd directly after the Bachelor.

Prof. Andreas Klingl for being part of the rigorosum.

Johannes Wienberg (Chrombios, Germany) for providing paint probes.

Dirk Eick for providing RNA polymerase II antibodies.

Yosef Gruenbaum and Karsten Rippe for helping to improve substantially an earlier version of the bovine nuclear envelope and lamina manuscript.

Christina Grimm for many insightful discussions.

4.3. Statutory declaration and statement

Hiermit versichere ich ehrenwörtlich, dass meine Dissertation selbständig und ohne unerlaubte Hilfsmittel angefertigt worden ist.

Die vorliegende Dissertation wurde weder ganz, noch teilweise bei einer anderen Prüfungskommission vorgelegt.

Ich habe noch zu keinem früheren Zeitpunkt versucht, eine Dissertation einzureichen oder an einer Doktorprüfung teilzunehmen.

München, den 1.2.2015

4.4. Contribution in manuscripts with co-authorship

In the manuscript “Cryopreservation of *in vitro* produced four-cell stage bovine embryos: effects of controlled slow freezing and vitrification” I have prepared (fixing, staining and embedding) and performed all confocal microscopy scans, have created the Figure showing the confocal scans and have improved all other Figures and the original text.